Establishing the performances of the NanoBioAnalytical platform for extracellular vesicles detection and characterization : Exploration of neuroprotective human platelet lysates

Balasubramaniam Namasivayam

THESE DE DOCTORAT DE L'ETABLISSEMENT UNIVERSITE BOURGOGNE FRANCHE-COMTE

PREPAREE A L'UNIVERSITE BOURGOGNE FRANCHE-COMTE

École doctorale n°37

Doctorat de Sciences Pour l'Ingénieur et Microtechniques

Par

M.NAMASIVAYAM Balasubramaniam

Détermination des performances de la plateforme NanoBioAnalytique pour la détection et la caractérisation de vésicules extracellulaires : Exploration de lysats plaquettaires humain à visée neuroprotectrice

Establishing the performances of the NanoBioAnalytical platform for Extracellular Vesicles detection and characterization : Exploration of neuroprotective Human Platelet Lysates

Thèse présentée et soutenue à Besançon, le 23/07/2021

Composition du Jury :

M. Luc BUEE	Directeur de Recherche	INSERM, Université Lille	Président
M. Rienk NIEUWLAND	Assistant Professor	Amsterdam UMC	Rapporteur
M. Jérôme DEJEU	Maître de Conférences	Université Grenoble Alpes	Rapporteur
Mme. Jessica GOBBO	Clinical Research Scientist	Centre Georges-François Leclerc, Dijon	Invitée
Mme. Céline ELIE-CAILLE	Maître de Conférences	Institut FEMTO-ST	Co-superviseur
M. Thierry BURNOUF	Vice Dean	Université Médicale de Taipei	Co-directeur
M. Wilfrid BOIREAU	Directeur de Recherche	Institut FEMTO-ST	Directeur

Dedicated to

Mr. Namasivayam Govindaperumal

Mrs. Vasuki Namasivayam

&

In the loving memory of

Mr. Govindaraj Namasivayam

Acknowledgments

This work was accomplished in the facilities of the BioMicroDevices (BMD) team at the Micro-NanoSciences and Systems (MN2S) department in the Institut Femto-ST, Besançon, France. I sincerely thank the director of the institute Pr. Laurent LARGER, and the director of MN2S department Dr. Vincent LAUDE. I wish to express my distinguished gratitude to Pr. Thérèse LEBLOIS, head of the BMD group and director of SPIM doctoral school. I respect your splendid support to me dealing with various matters and thank you so much for being such a great listener and willing to help all the PhD students of the institute.

I am fortunate to be nurtured by the valuable guidance of my thesis supervisors, Dr. Wilfrid BOIREAU, principal researcher, CNRS, and Prof. Thierry BURNOUF vice-dean of the college of biomedical engineering, Taipei Medical University, Taiwan and Dr. Céline ELIE-CAILLE HDR, Scientific deputy director of the MN2S, associate professor ISIFC engineering school. This thesis work would not have been possible without all your support, solicitude, and generosity.

Wilfrid, I am particularly thankful for your wonderful support at various times during this thesis. Thank you for your trust in me and for always there for helping me to carry out my work effectively. Thank you also for the various opportunities you have provided me to interact with colleagues and with collaborators. I sincerely appreciate your kindness. Your support always made it easier to overcome the obstacles.

Celine, it is my great pleasure to have the opportunity to work with your close supervision. I must mention your confidence in me helped me to learn and make advancements of many things in the research subject. In particular, I am thankful to you for listening to my inputs and improving them. Whenever I discuss with you, I am always left with new ideas and information's that made me a curious learner.

Thierry, I am so much indebted to you for your precious support throughout my thesis, I am at a loss of words to express my gratitude for your compassion and immensity. I enjoyed the warm welcome at your facilities at the TMU and will forever cherish this period. Thank you for providing us various precious samples and this helped to advance my understanding of the EVs research subject to a greater extent. Thank you for all the remarkable opportunities to interact and network with the peers from academia and industry.

I sincerely appreciate the members of the BMD team. My cordial acknowledgements to Alain for being friendly and extending your help throughout my tenure. I always could count on you for the support needed. My sincere thanks to Vincent, I enjoyed working with you on the pilot studies in IR spectroscopy observation of EVs. Your vast knowledge is an inspiration to me and thank you for your humbleness. I also thank for the fruitful interactions with Bruno, Jean-François, and Franck.

Thank you Rabah, our friendship is highly valuable to me, and I always enjoyed interacting with you. Thanks for those high-quality biochips that helped me in my experimentations.

My earnest gratefulness goes to Oliver, Sarah, Magali, Nicolas, Jean-Baptiste, Franck, Florian for their solidarity and support.

I dedicate my sincere thanks to Jocelyne, Sophie, Sandrine, Axelle, Tamina and Mireille for their warm personalities.

I thank the supportive and amiable colleagues of the department Achraf, Charalampos, Marc, Yida, Amar, Charles, Julien, Raya, Alexandr, Aymen, Daniel, Sylvain, Fernando, Mohammad, Saber, Geetika, Paresh, Dakmak, Emma, Adeleine, Olivia, Florian, and all others.

I also cherish the wonderful time in the past with the alumni of the institute. Special thanks to Benoit, Audrey, Anthony, Deborah, Clarisse, Fabien and Maya. All of you have been incredibly supportive to me.

I extend my sincere acknowledgment to my colleagues in Taiwan. My distinguished gratitude to Ivy, thank you for helping my stay in Taipei easier. Needless to mention your patience in teaching me some advanced research stuff. I have learnt so much from you. Thank you Ouada, Liling for your friendliness and the fruitful exchanges throughout my thesis. I fondly remember our visit to the Yangmingshan trails in Taiwan.

I especially thank Anji, Lassina, Daniel, Rifa, Praveen, Sangeetha, Manthosh, Santhosh, Vincent, Amber, Candy, and many other friends in TMU for all of their welcome, assistance, and kindness.

Finally, yet importantly, I am grateful for the never-ending support and love of my parents, family members, and friends.

The true splendour of humankind is self-respect and knowledge

-Periyar.

Abstract

Extracellular Vesicles (EVs) are small lipid enclosed structures of size ranging from 50-5000 nm. They are released by almost all types of cells as a medium of intracellular communication. The EVs can be isolated from various body fluids such as blood, urine, cerebrospinal fluid, saliva, etc. There are three types of EVs namely Exosomes, Microparticles, and Apoptotic bodies. They are categorized based on their biogenesis. EVs express several membrane markers on their surface and contain effective bioactive molecules potentially to be delivered into distant cells and thereby modulate the property of the recipient cells.

EVs are challenging to be distinguished because of their heterogeneity, overlap in the physical properties with the other components in the complex media such as protein aggregates, lipid fragments, lipoproteins, etc.

The NanoBioAnalytical (NBA) platform has been developed as a label-free, multiplexed analytical solution for the effective characterization of EVs. It is a multi-biophysical characterization technique composed of Surface Plasmon Resonance-imaging (SPRi), Atomic Force Microscopy (AFM), and Mass spectrometry (MS).

The first axis of this Ph.D. work is to assess the analytical performance of the NBA platform for a complex biological EV sample. The Platelet-derived EVs (PEVs) were obtained from Taipei Medical University (TMU) and used in this project to determine the limit of detection (LOD) and dynamic range (DR) of NBA. A specific multiplex format of a biochip was designed using antibodies against CD41 protein commonly expressed in the PEVs. EVs are captured in the biochip of antibodies bio interface grafted at two different densities. EVs are captured on this surface at various orders of magnitude of PEVs concentration. These biochips are then characterized in an AFM to study the structural and morphological characteristics. Quantitative EVs analysis is also performed such as EVs counting and metrological analysis. An improved data analysis method was also developed for treating and analyzing SPRi and AFM data. A dynamic threshold selection method was developed to optimize the AFM quantification parameters. The results demonstrated that the NBA platform is sensitive at 10^6/mL concentration range without any signal amplification strategy. It is also shown that the NBA platform has a linear dynamic range of at least up to 10^9/mL.

The second aspect of the work dealt with characterizing EVs from a set of Human Platelet Lysates (HPLs) preparations used for studying neuroprotection. Three different types of HPLs

namely Heat-treated Platelet Pellet Lysates (HPPL), Platelet Pellet Lysates (PPL), and Serum Converted Platelet Lysates (SCPL) were obtained from TMU. Different HPL preparations were proven to be neuroprotective against *in* vitro cellular toxicity and *in* vivo Parkinson's disease as well as Traumatic Brain Injury (TBI) models. The goal of this axis of the project is to evaluate the presence of EVs in HPPL, PPL, and SCPL. A dedicated multiplexed pattern of 7 different markers and negative control was designed for the study in the NBA platform. Differential phenotyping, as well as differential EVs characterization, were performed in SPRi and AFM. The comparative studies indicated that there is a difference in expression of phenotypes and EVs in varying levels between these HPLs.

These studies indicated that the NBA platform is capable of characterizing EVs in complex media in a label-free manner as well as in a multiplexed format. The observations also indicated NBA platform can help in progressing not only in EVs research in a diagnostic, therapeutic perspective but also bring meaningful contributions for the EVs standardization research.

Keywords: EVs characterization, EVs nanometrology, Human Platelet Lysates, Label-free EVs sensing, Neuroprotection, Platelet-EVs.

Résumé

Les vésicules extracellulaires (VE) sont des petites structures sphériques fermées par des lipides d'une taille allant de 50 à 5 000 nm. Elles sont libérées par presque tous les types de cellules en tant que moyen de communication intracellulaire. Les vésicules extracellulaires peuvent être isolées de divers fluides corporels tels que le sang, l'urine, le liquide cérébrospinal, la salive, etc. Il existe trois types de vésicules extracellulaires, à savoir les exosomes, les microparticules et les corps apoptotiques. Ils sont classés en fonction de leur biogenèse. Les vésicules extracellulaires expriment plusieurs marqueurs membranaires à leur surface et contiennent des molécules bioactives efficaces pouvant potentiellement être délivrées dans des cellules distantes et ainsi moduler la propriété des cellules réceptrices.

Les vésicules extracellulaires sont difficiles à distinguer en raison de leur hétérogénéité, du chevauchement des propriétés physiques avec les autres composants des milieux complexes tels que les agrégats de protéines, les fragments lipidiques, les lipoprotéines, etc.

La plate-forme NanoBioAnalytique (NBA) a été développée en tant que solution analytique multiplexée sans marquage pour une caractérisation efficace des vésicules extracellulaires. Il s'agit d'une technique de caractérisation multi-biophysique composée d'imagerie par résonance plasmonique de surface (SPRi), de microscopie à force atomique (AFM) et de spectrométrie de masse (MS).

Le premier axe de ce travail consiste à évaluer les performances analytiques de la plateforme NBA pour un échantillon biologique complexe de VE dérivées des plaquettes (PEV) obtenus de l'Université Médicale de Taipei (TMU) et utilisé dans ce projet pour déterminer la limite de détection et la plage dynamique de la NBA. Une biopuce en format multiplex spécifique a été conçue en utilisant des anticorps contre la protéine CD41 couramment exprimée dans les PEV. Les VEs sont immuno-capturés dans la biopuce grâce à une bio interface présentant deux densités différentes d'anticorps. Les VE sont capturées sur cette surface à divers ordres de grandeur de concentration de PEV. Ces biopuces sont ensuite caractérisées dans un AFM pour en étudier leurs caractéristiques structurales et morphologiques. L'analyse quantitative des VE est également effectuée comme le dénombrement des VE, l'analyse métrologique et la densité de surface. Une méthode améliorée d'analyse des données a également été développée pour le traitement et l'analyse des données SPRi et AFM. Une méthode de sélection de seuil dynamique a été développée pour optimiser les paramètres de quantification de l'AFM. Les résultats ont démontré que la plate-forme NBA présente une limite de détection de 10^6 VE/mL sans aucune

stratégie d'amplification du signal. Il est également démontré que la plate-forme NBA a une plage dynamique linéaire couvrant 3 décades (10^6 -10^9 VE/mL).

Le deuxième axe du travail porte sur la caractérisation des VE à partir d'un ensemble de préparations de lysats plaquettaires humains (HPL) utilisés pour l'étude de la neuroprotection. Trois types différents de HPL, à savoir les lysats de plaquettes traités thermiquement (HPPL), les lysats de plaquettes standard (PPL) et les lysats de plaquettes convertis en sérum (SCPL) ont été obtenus. A TMU, ces différentes préparations de HPL se sont avérées neuroprotectrices contre la toxicité cellulaire in vitro et la maladie de Parkinson in vivo ainsi que les modèles de traumatisme crânien (TBI). L'objectif de cet axe du projet est d'évaluer au sein des échantillons HPPL, PPL et SCPL la présence de VE et de les qualifier. Un modèle de biopuce multiplexés comprenant 7 ligands différents et un contrôle négatif a été conçu pour l'étude dans la plateforme NBA. Le phénotypage différentiel ainsi que la caractérisation différentielle des VEs ont été réalisés dans SPRi et AFM. Les études comparatives ont indiqué qu'il existe une différence dans l'expression des phénotypes et des VEs à des niveaux variables entre ces HPL.

Les résultats obtenus au cours de cette thèse établissent la plate-forme NBA comme une solution analytique sensible et spécifique pour la caractérisation des vésicules extracellulaires dans des échantillons complexes à partir d'un format multiplex et sans marquage. Les observations ont également indiqué que la plate-forme NBA peut apporter une contribution majeure sur la métrologie des VEs et la méthodologie analytique qui permettra une qualification fine et robuste des VEs dans une perspective diagnostique et thérapeutique.

Mots clés : SPRi, AFM, vésicules extracellulaires, microparticules plaquettaires, nanométrologie, Lysats de plaquettes, Neuroprotection.

Table of contents

List of Acronyms

Acronym	Phrase
AD	Alzheimer's Disease
ADP	Adenosine diphosphate
AF4	Asymmetric Flow Field-Flow Fractionation
AFM	Atomic Force Microscopy
ALS	Amyotrophic Lateral Sclerosis
ATP	Adenosine triphosphate
BCA	Bicinchoninic Acid Assay
BDNF	Brain Derived Neurotrophic Factor
BIA	Biomolecular Interaction Assay
BSA	Bovine Serum Albumin
CBME	College Of Biomedical Engineering
CCD	Charge Coupled Diode
CNS	Central Nervous System
COVID	Corona Virus Disease
CPC	Charged-Carboxylic-coated Particles for Calibration
CSF	Cerebrospinal Fluid
DLS	Dynamic Light Scattering
DNA	Deoxyribonucleic Acid
DR	Dynamic Range
EDC	1-Ethyl-3-(3-dimethylaminopropyl) carbodiimide
EGF	Epidermal Growth Factor
EGFR	Epidermal Growth Factor Receptor
EM	Electron Microscopy
ESCRT	Endosomal Sorting Complex Required for Transport
EV	Extracellular Vesicles
EVCI	Extracellular Vesicles Consistency Index
FACS	Fluorescence Assisted Cell Sorting
FC	Flow Cytometry
FCM	Flow Cytometer
FCS	Fetal Calf Serum
FESEM	Field Emission Scanning Electron Microscope
FGF	Fibroblast Growth Factor
GE	General Electric
GP	Glycoprotein
HEPES	4-(2-hydroxyethyl)-1-piperazineethanesulfonic acid)
HER	Human Epidermal growth factor Receptor
HIV	Human Immunodeficiency Virus
HPC	Human Platelet Concentrates
HPL	Human Platelet Lysates

HPPL	Heat-Treated Human Platelet Lysates
IBM	International Business Machines
IFC	Integrated Microfluidic Channels
IGF	Insulin-Like Growth Factor
IR	Infrared
ISEV	International Society for Extracellular Vesicles
LAG3	Lymphocyte-Activation Gene 3
LED	Light Emitting Diode
LOB	Limit of Blank
LOD	Limit of Detection
LSPR	Localized Surface Plasmon Resonance
LUHMES	Lund Human Mesencephalic
MALDI	Matrix Assisted Laser Desorption Ionization
MCF7	Michigan Cancer Foundation-7,
MHCII	Major Histocompatibility Complex Class II
MIMENTO	MIcrofabrication for MEcanics, Nanosciences, Thermal and Optics
MISEV	Minimum Informations for Studies of Extracellular Vesicles
MS	Multiple Sclerosis
MSC	Mesenchymal Stem Cell
MV	Microvesicles
MVB	Multivesicular Body
MVE	Multivesicular Endosome
NBA	NanoBioAnalytical Platform
NHS	National Health Services
NKT	Natural Killer T Cells
nPMPs	Naturally occurring Platelet Microparticles
NTA	Nanoparticles Tracking Analysis
OG	Octyl Glucoside
PBS	Phosphate Buffered Saline
PC	Platelet Concentrates
PD	Parkinson’s Disease
PDGF	Platelet-Derived Growth Factor
PEG	Polyethylene glycol
PEV	Platelet derived Extracellular Vesicles
PM	Plasma Membrane
PPL	Platelet Pellet Lysates
PRP	Platelet Rich Plasma
PS	Phosphatidylserine
PVD	Physical Vapor Deposition
QCM	Quartz Crystal Microbalance
RI	Refractive Index

RMS	Root Mean Square
RNA	Ribonucleic Acid
ROI	Region of Interest
RPS	Resistive Pulse Sensing
RSA	Rat Serum Albumin
RT-qPCR	Reverse Transcriptase quantitative Polymerase Chain Reaction
RU	Resonance Units
SAM	Self-Assembled Monolayer
SCPL	Serum Converted Platelet Lysates
SD	Standard Deviation
SEC	Size Exclusion Chromatography
SEM	Scanning Electron Microscope
SERS	Surface Enhanced Raman Spectroscopy
SPM	Scanning Probe Microscopy
SPR	Surface Plasmon Resonance
SUPRA-MS	SUrface Plasmon Resonance in Array combined with Mass Spectrometry
TDDS	Targeted Drug Delivery System
TEM	Transmission Electron Microscopy
TERS	Tip Enhanced Raman Spectroscopy
TF	Tissue Factor
TGF	Transforming Growth Factor
TMU	Taipei Medical University
TRPS	Tunable Resistive Pulse Sensing
UC	Ultracentrifugation
UV	Ultraviolet
VEGF	Vascular Endothelial Growth Factor
VPM	Variable Pressure Module

Table 1 List of acronyms used in the manuscript

1. Introduction to EVs

1.1 Extracellular vesicles

Cells transport and release bilayer membrane-enclosed vesicular structures with characteristic cargo and surface profiles ranging from 50-5000 nm in size collectively described as Extracellular Vesicles (EVs).[1,2] EVs are broadly classified into three categories namely exosomes, microvesicles (MV), and apoptotic bodies. In humans, the EVs are commonly found in various body fluids such as blood, saliva, tears, cerebrospinal fluid, breast milk, urine, semen, etc.[3–8] They usually carry various bioactive molecules such as lipids, metabolites, proteins, mRNA, chemokines, miRNA, etc. EVs were historically considered cellular debris.[9] After the discovery that they contain potent cargo molecules, EVs are recently appreciated as cellular messengers. The release and uptake of EVs play a role in intracellular communication. Microvesicles originate in a process of direct pinching from the plasma membrane and the exosomes are generated in an endocytic pathway. Although the EVs subsets differ in biogenesis, the physical properties such as size, density, and inner composition are shared between each subpopulation.[10,11] Some physical properties of the EVs also have an overlap with other components such as protein aggregates, viruses. The development of tools and techniques to isolate, enrich and characterize these sub-populations in various body fluids continues to evolve. Regardless of the challenges involved, EVs have attracted progressive interest among academic researchers for their diverse role in various domains of immunology, cancer, tissue regeneration. The clinical research community is mainly interested in the potential uses of EVs ranging from a non-invasive biomarker to novel drug delivery agents.[12]

2. Discovery of EVs

2.1.1 Microvesicles

MVs may be the first subset of Extracellular Vesicles to have been discovered. In 1946, it was observed that the platelet-free plasma, centrifuged at 31,000x*g* showed a considerable extension in the clotting time compared to platelet-free plasma. The investigators determined that the "pellet of coagulant material" (MVs) had resulted in reduced clotting ability. This provided an idea for the first time that there are components in plasma other than platelets that promote blood coagulation.[13] The first electron microscopy observation of vesicles and of their heterogeneity was published in the 1960s.[10,14]

2.1.2 Exosomes

The early description of exosomes and their biogenesis originate from a work that focused on the pathways of receptor-mediated endocytosis. The author investigated how the transferrin receptor is recycled between the plasma membrane and the endocytic compartments in rat reticulocytes.[15] Electron microscopy (EM) surprisingly revealed the accumulation of (vesicles containing) Functionalized gold nanoparticles conjugated transferrin have been predominantly localized inside the multivesicular bodies. They were named multivesicular endosomes (MVE). Moreover, the multivesicular bodies were found to fuse with the plasma membrane and undergo a release as exocytosis vesicles,[16] which were later renamed as "exosomes". A recent investigation suggests exosomes themselves could be heterogeneous and suggested two subpopulations of exosomes namely Exo-S and Exo-L.[17]

2.1.3 Exomeres

Exomeres are the latest class of EVs which were discovered in various cell lines using asymmetric flow field flow fractionation (AF4) technique. They are generally less than 50nm in size and currently no known biological function.[17,18]

2.2 EVs in intracellular communication

2.2.1 Microvesicles

Versatile roles of MVs in the cellular communication process are identified. They participate in activating other cells by acting as a signaling complex.[19] MVs also exert various functions such as transferring surface markers between cells,[20] regulating the cell adhesion of the recipient cell,[21] delivering a bioactive cargo comprised of nucleic acids, proteins,[22] and other biomolecules to the recipient cells, a shuttle for the infectious particles such as HIV,[23] prions,[24] relocating intact organelles such as mitochondria to a distant cell.[25,26]

2.2.2 **Exosomes**

A decade after the presentation of exosome biogenesis in 1983, the major histocompatibility complex class II-enriched compartment (MHCII) were demonstrated to fuse with the plasma membrane with a concomitant release of exosomes. Exosomes produced from the antigen-presenting cells were shown to transfer the antigens both *in* vivo and *in* vitro. This paved the way for continuous research on exosomes as a novel mediator of intracellular communication.[27,28]

Nearly after 20 years of the discovery of exosomes, exosome-mediated intracellular communication is demonstrated.[27] Exosomes from mouse and human mast cell lines were assessed using DNA microarray, revealing that the cargo contents of the exosomes contained mRNA and miRNAs. When the human and rat mast cells are co-cultured, the proteins previously identified in rat mast cells are discovered in human mast cells. This work first demonstrated the exosome-mediated transfer of RNAs that remained functional and induced recipient cellular phenotypic plasticity. [29]

2.3 Overview of biogenesis

2.3.1 **Microvesicles**

MVs are directly shed outwardly from the plasma membrane through membrane blebbing, cargo trafficking, and scission. The whole mechanisms of vesicle formation and release are not fully understood. The literature describes several mechanisms of how the MVs are formed and released. Membrane blebbing could be involved in the relocation of tumor susceptibility gene 101 (TSG101) from the late endosome to the plasma membrane and subsequent membrane curvature and pinching. This leads to release in the extracellular space as an intact vesicle.[30] Alternatively, protein-protein crowding can occur at the periphery of the plasma membrane and pressure generated with the interaction of proteins and collision with one another, leading to reform of the plasma membrane to curvature and subsequent release.[31] Reorganization of lipids in the plasma membrane mediated by lipid pumping enzymes such as floppase and scramblase contributes to changes to the membrane asymmetry that leads to MV formation and release. This is one of the widely known mechanisms of MV biogenesis.

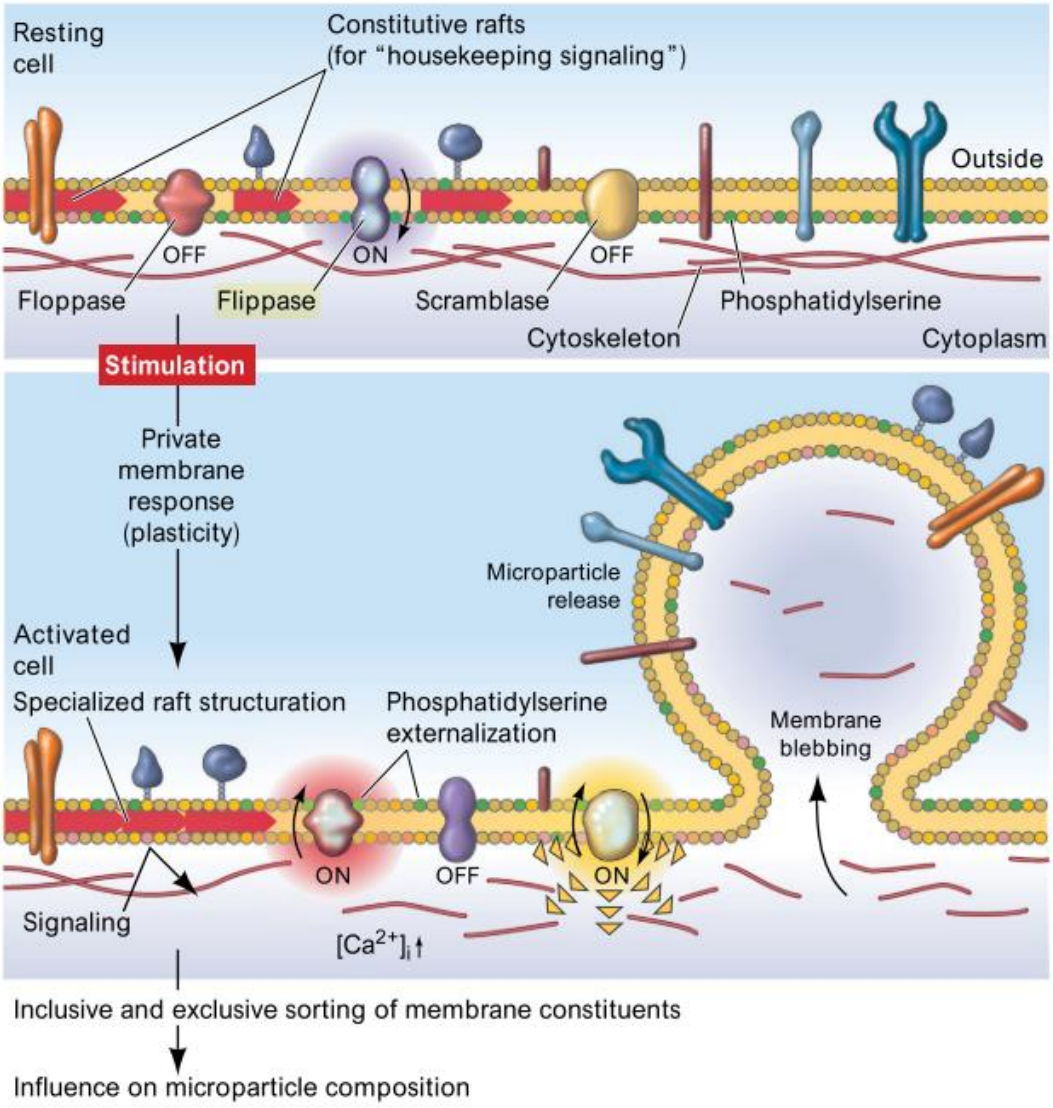

Figure 1 Biogenesis of a Microvesicle. The biogenesis is stimulated by various factors. When there is an increase in the concentration of Ca2+ in the cytosol, signals are transmitted, and the externalization of the Phosphatidylserine takes place. This action is regulated by floppase and scramblase enzymes. Further maturation leads to blebbing of the plasma membrane and pinching and released as MVs in the extracellular milieu. Picture reference: Hugel et al.[32]

2.3.2 **Exosomes**

Exosome biogenesis begins with the inward budding of the plasma membrane. It is regulated by the so-called endocytic pathway.[11,33] Many pathways are reported such as clathrin-mediated endocytosis, lipid-raft mediated endocytosis, macropinocytosis, caveolin-mediated endocytosis, etc.[34]

In receptor-mediated endocytosis, the ligand-receptor interaction results in generating clathrin-coated pits. The deposition of hair-like structures of clathrin beneath the plasma membrane matures into early endosomes. The endosomal membrane invaginates further and forms small intraluminal vesicles.

The structure surrounding these intraluminal vesicles is called a multivesicular body (MVB). The MVB can either progress into lysosomal degradation through the MVB pathway or it can fuse with the plasma membrane and the vesicles are released as exosomes.[33,34] In cancer, as another way of biogenesis, small GTPases such as RAB5, RAB 21 are involved in the early biogenesis of endosomes.[35] The cargo is selectively sorted and loaded to the endosomes by ESCRT (Endosomal Sorting Complex Required for Transport) machinery. They eventually mature into late endosomes and further fuse to the plasma membrane to the delivery of exosomes in the extracellular space.[36]

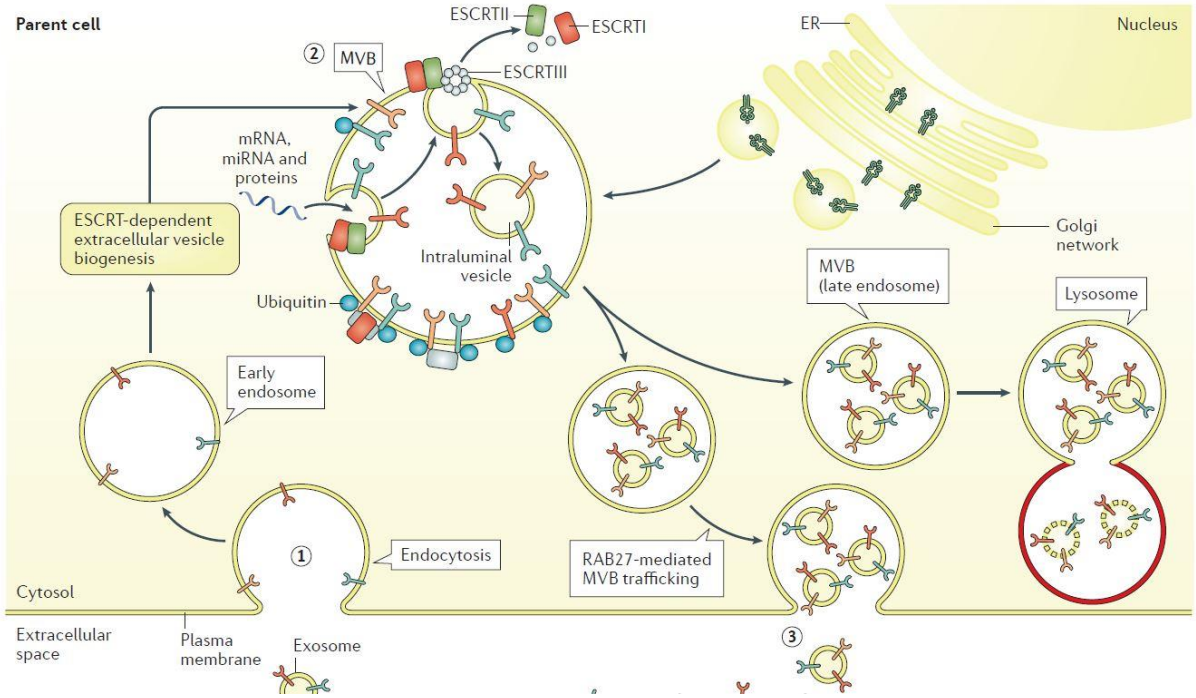

Figure 2 Biogenesis of Exosomes by ESCRT dependent pathway. The degradative pathway of MVB –Lysosome fusion is also shown. Picture ref. G. Szabo et al.[224]

2.4 Properties of Extracellular vesicles

2.4.1 Evolution of the nomenclature and subtypes of EVs

Upon their discovery in 1946, then considered as platelet dust, EVs were later renamed platelet microparticles. In 1999, Heijnen et al reported that platelets also release exosomes.[37]

The EVs are described in the literature under various names including ectosomes, oncosomes, exosomes, large dense-core vesicles, nanovesicles, outer membrane vesicles, matrix vesicles, synaptic vesicles, exosomes, prostasomes, and apoptotic bodies.[38,39] They are usually named after the cells from where they originate. In 2018, a new class of EV structure

of size <50nm, named exomeres, was discovered in different cell lines.[40] Exomeres are non-membranous nanoparticle structures with a cargo of lipids and nucleic acids.[18]

Collective names referring to exosomes, MVs, and apoptotic bodies as EVs are proposed by the international society for EVs (ISEV) in 2011.[39] ISEV has also recommended using the term EVs unless the biogenesis method is proven with images. In its updated guidelines, ISEV recommended using small, medium, and large EVs with a user-defined range for each class. It is suggested small EVs may be classified with a size range less than 100 or 200nm and more than 200nm could be known as medium or large EVs. Similarly, EVs could be discriminated with their density such as low-density EVs, high-density EVs, etc. Additionally, EVs may also be called with their associated markers such as CD41 EVs, CD81 positive EVs, etc. It is also recommended to attribute the EVs with their origin or a condition such as blood-derived EVs, hypoxic EVs, etc. [2]

2.4.2 Physical characteristics of EVs

2.4.2.1 Microvesicles

MVs are comparatively bigger than exosomes although the smallest MV could have a size identical to or even smaller than that of an exosome. The MVs could range from 100-1000 -nm in diameter and are characterized by markers associated with the cell of origin. Some MVs also express phosphatidylserine (PS) on the surface. The MVs have a density between 1.14-1.20 g/mL and are relatively denser than the exosomes. MVs are conventionally isolated at 10,000x*g* to 20,000x*g*. These microparticles are known to have spherical, ellipsoidal, or cylindrical structures.[41,42]

2.4.2.2 Exosomes

The exosomes are small in size and most reports describe them to be less than or up to 50-150 nm. The exosomes are characterized, although not uniquely, by the presence of proteins involved in membrane transport and fusion, such as GTPases, annexins, and flotillin, components of the endosomal sorting complex required for transport (ESCRT) complex such as Alix, tumor susceptibility gene 101 (TSG101), heat shock proteins (HSPs), integrins, and tetraspanins, including CD63, CD81, and CD82.[39] The exosomes are isolated using ultracentrifugation at strong centrifugal forces typically at 100,000x*g* to 200,000x*g*. The exosomes have a density of 1.10-1.20 g/mL and are observed to have circular,[16] spherical, and cup-shaped morphology in the transmission electron microscope (TEM).[41,43,44]

2.4.2.3 *Apoptotic bodies*

The apoptotic bodies range from 100-5000nm. They arise as a result of cellular degradation during apoptosis. One might think fragments resulting in the cell death process could follow a chaotic or a random process. Conversely, the generation of apoptotic bodies is controlled in several morphological steps known as apoptotic cell disassembly.[45] The density of apoptotic vesicles is between 1.16 to 1.28 g/mL, which is partly overlapping with that of MVs and exosomes, and their morphology is typically more heterogeneous than that of other cell-derived vesicles as seen in TEM.[39]

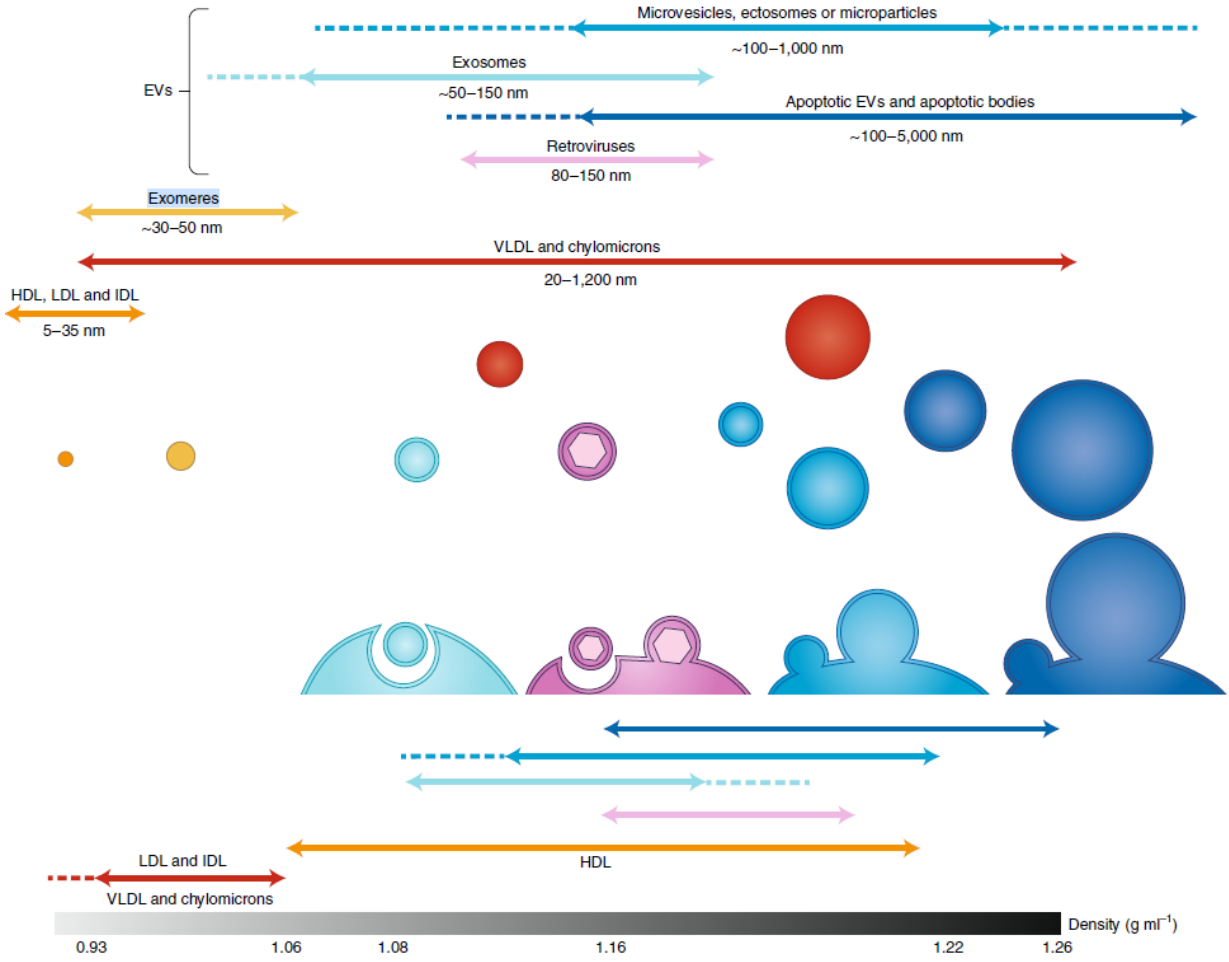

Figure 3 Comparison of physical properties of EVs. The nature of the EVs subpopulations is shared among different subpopulations as well as various other biological entities such as very-low-density lipoproteins (VLDL), retrovirus particles. LDL: low-density lipoprotein, HDL: High-density lipoprotein, IDL: Intermediate-density lipoprotein. Image credits Mathilde Mathieu et al.[225]

3. Significance of Platelet-derived EVs

Platelet-derived EVs (PEVs) attracted interest from scientific and clinical researchers for their multifaceted role in promoting and regulating physiological and pathological functions. They are also a potential disease diagnosis marker including but not limited to infectious diseases, cancer, cardiological and neurodegenerative disorders.

Owing to their small size, biocompatibility, and migratory capacity to cross important biological barriers such as the blood-brain barrier,[46] EVs are attractive candidates for targeted drug delivery applications. Since platelet contains various growth factors and immune regulators, they are also used as intrinsic therapeutic mediators with an emphasis in regenerative medicine. It is reported that PEVs constitute around 80% of the order of abundance of all EVs in the blood plasma.[25] Some reports claim PEVs constitute 70-90% of all EVs.[47,48] Recent estimates suggest PEVs could contain around 50% and a proportion of the EVs might be of megakaryocytes origin.[49–51]. With the evolution of infrastructures and advancements in the measurement techniques, a study by Berkman's et al argues that around 50% EVs in plasma is of platelets origin together with erythrocyte EVs and leukocytes EVs which accounts for 29% and 20% respectively. The difference in the total amount of EVs between an earlier study in 2001 and a recent study in 2019 revealed an increase by 264-fold in the total concentration of EVs in plasma.[52] For use in clinical applications, cell-derived EVs must be cultured in an *in* vitro or ex vivo setup. Compared to cell-derived EVs, the manufacturing of the PEVs is easier and simpler. The process of blood collection and apheresis are widely regulated thus providing a suitable means to extract, safe, scalable, and quality source of the EVs as a resource in diagnostic, therapeutic applications.[49]

3.1 Functional role of PEVs

The circulating PEVs have various functional roles including mediating intracellular communication, transporting pro or anti-coagulatory/inflammatory modulators (depending upon the destiny of the target cells), acting as a waste container for the disposal of broken components of the platelet that is undergoing a natural death. The functions of PEVs are shared with that of platelets. Interestingly, PEVs are also identified in body fluids other than blood such as lymph, synovial fluid, and bone marrow where they are often associated with pro-inflammatory conditions, as well as observed to have distinct functions than that of blood PEVs. This suggests that PEVs may have potential involvements in distributing platelet contents to tissues impenetrable by platelets themselves.[53]

3.2 PEVs as potential biomarkers

The relative abundance, phenotype, and cargo of nucleic acids, proteins, and other molecules are the main hallmarks of PEVs that are often used to control disease conditions or progression. Changes in the abundance of EVs are reported in several diseases such as hematological disorders, atherothrombotic disorders, autoimmune diseases, infectious diseases, and many types of cancer, or neurological ailments. A summary table of various diseases and the relative up or downregulation of PEVs can be found in the article by Gaseka et al. [54]

3.2.1 PEVs in Blood diseases diagnosis

Hematological disorders affect blood and blood-forming organs and the involvement of PEVs in these disorders is attributed to their angiogenic, thrombotic, and inflammatory properties. PEVs could potentially serve as delivering the various essential growth regulators for the attributed function.

Atherosclerosis is caused by structural changes in the internal arteries by atherosclerotic plaque build-up. The induced structural damage of the blood vessel forms the thrombus and results in clotting. This causes reduced blood flow to the heart and causes acute coronary syndromes. The thrombus could also migrate to the brain where it could manifest as an ischemic stroke or to the kidneys and result in renal artery stenosis. The involvement of PEVs in these disorders is comparable to the role of PEVs in thrombosis. The PEVs are expected to have a role in promoting cell adhesion. *in* vitro studies suggest that PEVs treated monocytes and endothelial cells demonstrated increased cell interaction and adhesion.[55,56] Activated endothelial cells release endothelial EVs bearing tissue factor (TF). These TF-positive EVs in turn activates the platelets and could result in the accumulation of PEVs. Nomura has detailed various PEV associated blood diseases and described the above mechanism in detail.[57]

3.2.2 Diagnosis of neurological diseases using PEVs

PEVs are being studied as biomarkers in various diseases like Huntington's disease, Alzheimer’s disease (AD), Parkinson’s disease (PD), and Amyotrophic lateral sclerosis (ALS). Neurogranin, a brain associated protein, was found to be downregulated in blood exosomes and cerebrospinal fluid (CSF) of patients with AD.[58] Neuroscience researchers are also interested in EVs mediated mi-RNA transfer after it was discovered that seeds of misfolded proteins such as α-synuclein (α-syn), tau, and amyloid β (Aβ) are mediated by exosomes to non-disease areas and accelerating the progress of the neurodegeneration.[59] Detection of mi-

RNAs associated with these proteins could be potentially used as a diagnostic tool of various neurodegenerative diseases.[60]

3.2.3 PEVs as potential biomarkers of immunological disorders

Autoimmune diseases are caused by the imbalance of immune response. Multiple sclerosis (MS) is one of the autoimmune diseases which is characterized by inflammation and demyelination of the central nervous system (CNS). During MS pathological progression, the upregulation of PEVs is reported together with the endothelial and the leukocyte EVs. The contribution of PEVs to the MS disease progression is linked to the increased metalloproteinase activity.[61–63] EVs contain these metalloproteinase markers on their surface.

In a study between HIV-infected patients and the control group, Vincente et al found a significant upregulation of PEVs in HIV-infected subjects.[64] Cappellano et al suggested that PEVs could be used as a diagnostic biomarker of (SARS- Corona-Virus-2 disease) COVID infections.[65]

3.2.4 PEVs as cancer biomarkers

Interaction of tumor cells and platelets EVs are widely studied. Therefore, this aspect of research attracted prevalent interest. The biomarker discovery in cancer research is crucial since early detection leads to better clinical outcomes. PEVs contribute to angiogenesis, migration, invasion, and metastasis.[66] Studies also highlight that PEVs supply essential growth factors for cellular survival.[21] Since the upregulation of PEVs due to increased proliferative, pro-coagulant, cell growth, survival, and maintenance properties, also increased apoptosis, the PEVs abundance is being studied as a potential cancer diagnostic feature.[66]

Nonetheless, the functional understanding of PEVs in most disease conditions is still limited. For example, Scott syndrome, which is a disorder caused by low or defective platelet count, or the castaman syndrome which is a bleeding disorder affected by the inability of the platelet to generate EVs (MVs).[67] In such cases, the downregulation of the PEVs is difficult to be associated with the disease condition. It is also noteworthy that the lack of standardized characterization and validation techniques might also have resulted in a systematic difference in the reported concentrations of the PEVs in the above-mentioned studies.[54]

3.2.5 PEVs in Liquid biopsy and precision oncology

PEVs are also being investigated for their potential applications in liquid biopsy and precision oncology. Liquid biopsy techniques rely on detecting circulating biomarkers in the

body fluids. Non-small-cell lung cancer, breast cancer, pancreatic cancer, colorectal cancer, ovarian cancer, and nasopharyngeal carcinoma can be detected based on blood-derived EVs. The advantage of using PEVs as a liquid biopsy tool is that PEVs can provide information in both protein and transcript levels. It has been suggested a multi-faceted diagnosis of both protein and mi-RNA is particularly effective in non-small cell lung cancer.[68] Liquid biopsy is also expected to make advancements in the precision medicine field. Cancer therapeutics could make use of the personalized information to tailor-make effective drugs and help to circumvent some of the challenges in cancer treatment such as drug resistance and genomic heterogeneity of the tumors.[69,70]

3.3 PEVs as therapeutic agents

Cell-derived EVs are currently being investigated in many preclinical and clinical trials.[71] EVs can be isolated from different sources, such as mesenchymal stromal cells,[72] bacteria,[73] dendritic cells[74] for various applications including regenerative medicine,[72] vaccines[75] reducing adverse inflammatory responses,[76] reducing cancer growth,[77,78] etc., There are only a few reports concerning clinical application of PEVs.[49] Platelet concentrates are used for maintaining hemostasis post-traumatic injury such as musculoskeletal injury.[79] Customized platelet lysates preparations are being investigated for neuroprotection.[80]

The PEVs are expected to have many advantages over platelet products. Because PEVs have a high surface-to-volume ratio, they often demonstrate enhanced platelet hemostatic functions.[81] In ideal clinical applications, the PEVs have additional advantages such as biocompatibility, access to the platelet-derived growth factors, small size, and the ability to transmit through barriers. The PEVs should have a prolonged shelf life than platelets since PEVs could be frozen for storage.

The therapeutic potential of the PEVs may vary relative to the induction method of PEV generation and the source such as resting platelets or activated platelets. It can also vary because of the difference in the proportion of EV subpopulations. Small PEVs are found to be useful in treating wound healing[82] and platelet microparticles promote angiogenesis and neurogenesis after ischemic stroke in animal models.[83]

The inflammatory properties, cytokine cargo, lipid mediators, and damage-associated molecules such as high-mobility group box 1 suggest the potential activity of PEV-cargo mediated inflammation.[53] Conversely, PEVs also downregulate the inflammatory state of macrophages of dendritic cells upon incubation.[84] Such contradictive roles of PEVs in cancer

inhibition/promotion are also reported.[85] These observations could indicate that PEVs have different and diverse properties and roles depending on the mode of platelet stimulation. Such nature of PEVs underscores an important as well as the vital need for in-depth as well as reliable characterization methods for translating the potentials of PEVs into beneficial clinical applications for various harmful diseases.

3.4 PEVs as drug carriers

While PEVs themselves are studied for their healing properties, the efficacy of EVs based formulations could be enhanced by incorporating the PEVs with an additional therapeutic agent. Compared to a polymeric or a liposomal formulation, PEVs could offer improved biosafety and targeted drug delivery solutions. Several strategies of exogenous loading of a drug into the PEVs such as incubation, sonication treatment, electroporation, freeze-thaw cycles, and extrusion are found in the literature. Alternatively, the drug molecules could be loaded endogenously into the platelets, and the drug-loaded PEVs could also be generated.

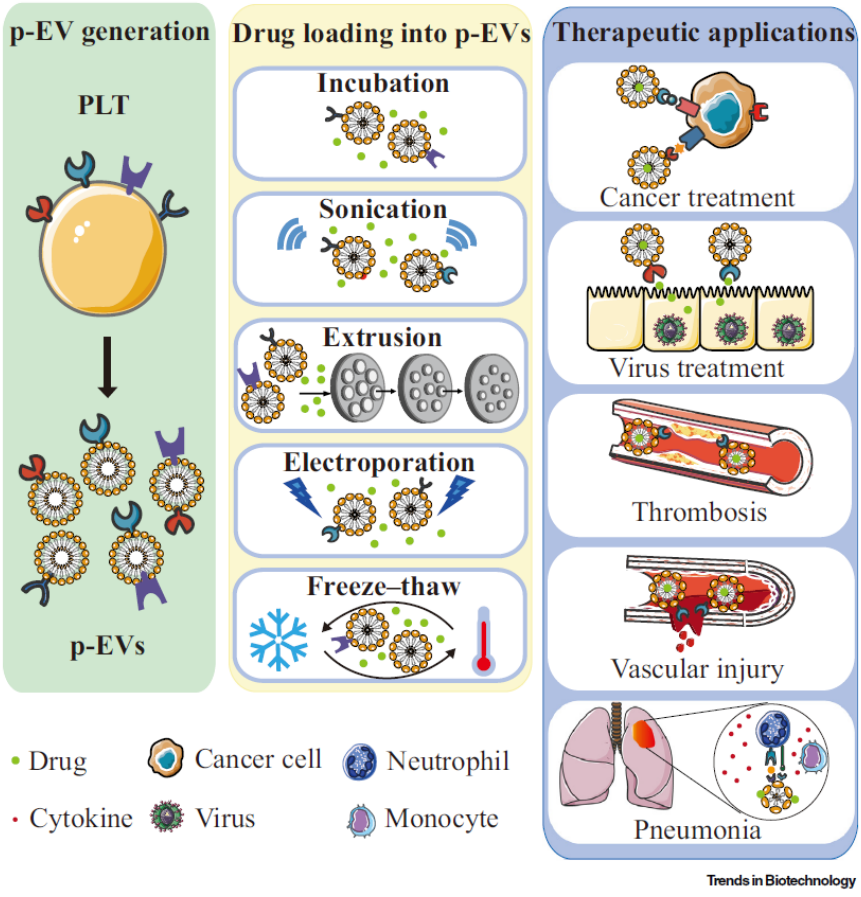

Figure 4 Picture depicting the PEVs drug loading methods together with drug-loaded EVs in action for various conditions. Picture from Johnson et al[49]

Wu et al investigated the endogenous loading of doxorubicin and eventual generation of PEVs during the tumor cell EVs and platelets interaction and the eventual tumor cell activation/ PEVs generation loop. The PEVs structures are locally destabilized in the tumor environment and facilitate the targeted release of cancer drugs.[86] This method offers a scalable, accessible process of efficient drug loading as well as anti-cancer application. Apart from PEVs, several trials are underway utilizing cell-derived EVs as targeted drug delivery systems (TDDS).[87]

The potential translation of PEVs as drug carriers warrants further studies so that the know-how of inducing PEVs that do not contribute to adverse responses could offer further axes of exploration of PEVs mediated drug delivery systems.

3.5 Isolation methods of EVs

EVs are isolated from a wide range of fluids such as blood/plasma/ serum, cell culture supernatants, urine, saliva, and other bodily fluids. Translating EVs science into potential clinical applications relies on efficient isolation, enrichment, and reliable characterization EVs. Parameters of EVs such as concentration, surface markers, and cargo contents are being investigated. However, there is a bottleneck since EV research lacks standardized methods and references for their efficient isolation.

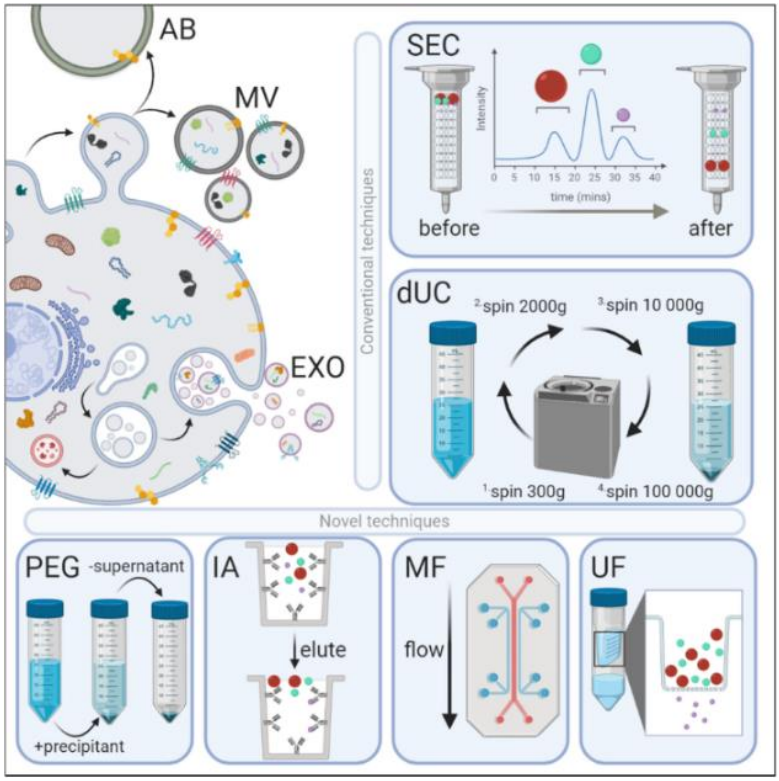

Figure 5 Description of different methods of EVs isolation techniques. SEC: Size exclusion chromatography, dUC: Differential ultracentrifugation, PEG: Polyethylene glycol-based polymer precipitation. IA: Immunoaffinity capture. MF: microfluidic assisted EVs sorting UF: Ultrafiltration technique. Picture credits Sidhom K et al.[94]

Conventionally, EVs are isolated by a differential centrifugation process. Although it remains the most used method, certain challenges still exist. The centrifugation process co-precipitates EVs with cellular debris, free molecules, and lipid fragments affecting the purity of the isolated vesicles. Strong centrifugal forces also induce aggregation of isolated EVs.[88]

Because of the difficulties associated with obtaining the pure EVs in centrifugation-based methods, various novel EVs isolation methods such as density gradient separation, and isolation methods independent of centrifugation such as size exclusion chromatography, filtration, affinity-based exclusion, precipitation using polymers, asymmetric flow fractionation, and microfluidic-based technologies are developed. All these methods differ in scale and result in different yields, and purity.

3.5.1 Centrifugation based isolation methods

3.5.1.1 Differential centrifugation

Differential centrifugation, also known as ultracentrifugation (UC), isolates the suspended materials based on their buoyancy. Step-wise centrifugation is used to precipitate materials of different buoyant gradients and various pellets are recovered and resuspended in a buffer. Pellets at a weak centrifugal force around 2000-3000x*g* are discarded as they contain mostly bacterial remains, cell debris, and apoptotic bodies. MVs are usually isolated by suspending 10,000-20,000x*g* pellets[89] and exosomes are isolated by resuspended 100,000-200,000x*g* pellets.[90,91]

3.5.1.2 Density gradient separation

To maximize the purity of the EVs separated by the UC process, a density gradient is used. This process is similar to that of UC. Although the UC process sediments the materials based on size, in a density gradient process, the particles are separated based on their size and additionally by density. During centrifugation, the suspended particle in a solution stabilizes at different distances from the axis of rotation based on its mass. The heavier objects reach the furthest away from the centre of rotation due to high inertia. This causes the denser objects to settle close to the edge of the rotor and low-density particles remain close to the centre. Sucrose or iodixanol are used to form a density gradient and EVs of different density gradient values are further purified.[92] While it results in purer EVs, this method is slower as low-density EVs take much time to reach their zone. This process also yields lower EVs amount than the UC process.

3.5.1.3 Size exclusion chromatography

Size exclusion chromatography (SEC) is developed for purer, gentler isolation of EVs than centrifugation-based processes.[93] The exclusion columns contain a stationary phase of porous polymeric resins. When the solution containing EVs is eluted through the exclusion column, large objects drain out faster as the smaller particles are locked in the pores thereby delaying their elution. Different fractions are collected and measured in a UV spectrometer at 280nm to evaluate the protein content. The fractions could also be characterized in particle concentration techniques such as dynamic light scattering (DLS), Nanoparticle tracking analysis (NTA), and resistive pulse sensing. The EVs are usually eluted at first and the contaminations and small proteins are trapped and eluted later. This method is faster and results in purer EVs compared to other isolation methods.[94–96] SEC also results in a slight dilution of EVs as a result of passage through a column containing elution buffer. Several commercial columns are available and claimed to have the smallest possible size of elution as low as 35nm.

3.5.1.4 Immuno-affinity based EVs isolation

Affinity-based EVs isolation uses antibody-antigen recognition of EVs expressing specific markers.[97–99] Since antibody-antigen reaction results in robust capture this method is faster and allows specific isolation of EVs subpopulation. Magnetic beads functionalized with specific targets are used to capture EVs plasma and separated using a magnet.[100,101] Magnetic bead coated antibody EVs conjugates can also be detected in a magnetic surface known as a hall sensor.[102] They are also being investigated in combination with microfluidic assisted EVs sorting.

Various bio sensing platforms such as plasmonic, interferometric, electrochemical, acoustic biosensors also offer a way to immobilize and thereby isolate EVs expressing a particular biomarker. However, as they are not designed for the isolation of EVs, these bio sensing-isolation methods have limited yields and are generally restricted to a small surface area.

3.5.2 Polymeric precipitation method

Hydrophilic polymers, such as polyethylene glycol (PEG), reduce solubility by lowering the hydration of EVs and lead to their precipitation.[103] The EV solution is added with polymeric precursors and forms a warp around the EVs, and such organic residue is pelleted using a weak centrifugal force. This process however is not specific to the EVs and the purity of the EVs is affected. Several commercial kits are available using this technology.

3.5.3 Asymmetric Flow Field-Flow Fractionation (AF4)

The AF4 works on the principle of field flow fractionation. The samples are introduced in an asymmetric fluidic chamber and the sample is carried to a stage by establishing laminar flow from the opposing directions. The cross-flow from the side of the fluidic chamber is then applied to push the particles towards the membrane-coated wall of the fluidic chamber. This helps all the particles suspended in the sample to align in a particular space. Because of the difference in the diffusion coefficient of the particles, small particles align on the top and the large particles align at the bottom. A parabolic laminar flow then carries the particles of different diffusion coefficients (thus size) at different flow rates and the sample is thus fractioned in various fractions where the small molecules are eluted first followed by the larger particles.

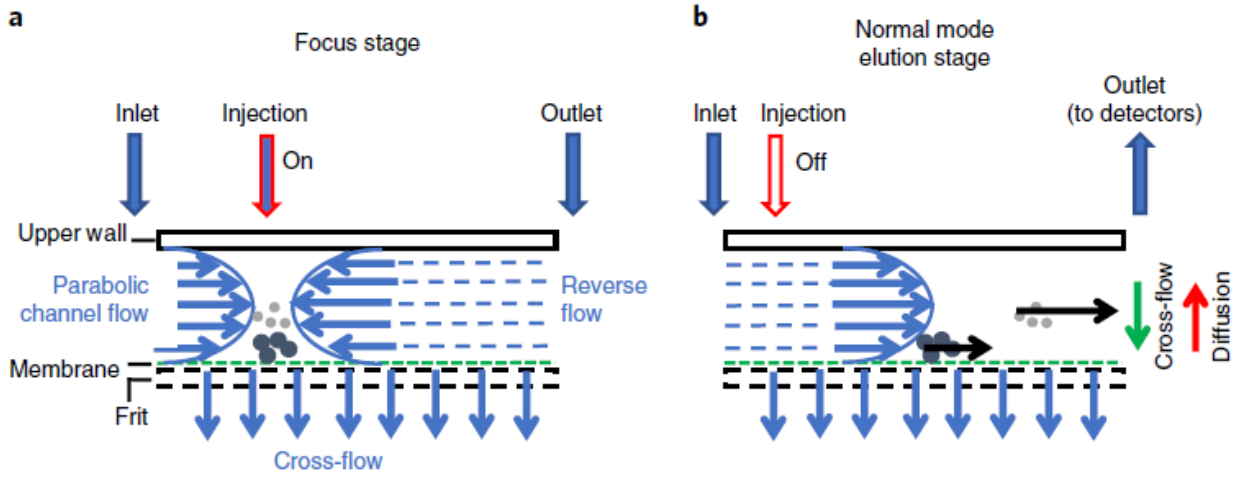

Figure 6 Working principle of AF4 technique. a) The sample is focused on a plane by opposing flows, b) In elution stage, the particles are carried by the parabolic flow to the detectors and fractionization. Picture credits Zhang et al[17]

The fractionated particles can also be detected by a dynamic light scattering system for characterizing the size subpopulations. The small exomeres were indeed discovered using AF4.[40] The AF4 technology could be combined with other isolation techniques such as centrifugation, size exclusion, or used with an applied external field such as electrical force to separate the sample based on their charge.

3.5.4 Ultrafiltration

In ultrafiltration, as a preparatory process, the medium containing EVs is sequentially filtered to eliminate debris and big objects. Ultrafiltration methods contain a nanomembrane and the solution is filtered through the nanomembrane for retention of particles bigger than the desired cut-off size. Several filters based on different molecular weight threshold are available and it is usually performed in a process combined with centrifugation or a cross-flow filtration. Consequently, this method is known as tangential flow filtration. Ultrafiltration can also be

used with a pressure device that acts as a squeezer. The material retained in the filter membrane is recovered and high purity EVs with different cut-off ranges are obtained.[104] The ultrafiltration method could be used in tandem with SEC.[105]

3.5.5 Microfluidic assisted methods

Microfluidic technologies are emerging applications for EVs enrichment. Several technologies are reported to use many EV enrichment methods.[106–109] The microfluidics sorting can be broadly classified into two groups. Active and passive separation. Active separation uses external force fields such as using acoustic waves (acoustophoresis)[110] or electrical field (dielectrophoresis),[111] immunocapture using specific antibody capture. Immunocapture is used with surface modified microstructures[112] and functionalized beads.[113] Passive microfluidic sorting involves manipulating EVs with the channel geometry and hydrodynamic flow.[114,115] Viscoelastic sorting,[116] nano porous membrane filtration[117] belongs to the passive microfluidic separation. Microfluidics offers many advantages such as be used as a diagnostic device, integrated EVs detection, and characterization, RNA profiling,[118] etc. Isolation of EVs using microfluidics is comparatively a rapid process. Processing time is reported from 4 minutes to less than 30 minutes[119] although they are limited in terms of sample volume. The maximum volume that can be processed using microfluidics is less than 500μL.[119,120] Different strategies of microfluidic enrichment are detailed in the recent article by Zhao et al.[107] Microfluidics are also being developed for point of care applications. Portable, highly integrated, user-friendly microfluidics show promising applications as point of care devices.[121]

3.5.6 EVs characterization methods

Characterizing the EVs is a crucial step in understanding the role of EVs in normal physiological processes and various disease conditions, it is also essential to compare different EVs preparations and for normalization. Reliable characterization of EVs is challenging because of the diversity, complexity, and heterogeneity of EVs. Currently, there are no established standards exist for consistent EVs characterization. Nevertheless, developments carried out in the past years made significant advancements in the reliable characterization of EVs.

EVs are characterized using various techniques and they can be broadly categorized such as imaging, physical, biochemical, biomolecular, and spectroscopic characterization techniques. Various features of EVs such as morphology, phenotype, biomolecular signature (presence of a particular marker, such as protein, or phospholipid, or nucleic acid) of a

biomolecule in the EV are used to obtain qualitative information., Measurements such as the size, total concentration, protein content, density, the mass of EVs, are quantitative information. Each method has its advantages and none of the single methods so far can characterize the EVs completely because of their challenging nature. Moreover, it is recommended to combine complementary techniques on the same sample to obtain a multifaceted characterization of EVs. The combined characterization is preferable on the same sample as emphasized in the ISEV guidelines.[1,2]

3.6 EVs Imaging

3.6.1 Optical imaging

As EVs are smaller than the diffraction limit, it is impossible to visualize them without a fluorescence biomarker in an optical microscope. EVs are either tagged with a bioluminescent or a fluorescence dye and excited with a light source to be detected in the optical detection system. The process is relatively straightforward. The isolated EVs are treated with a label of choice such as membranous or cytoplasmic label and washed for removing the excess dye. The solution is then applied in a glass coverslip and imaged in a microscope.[122] Confocal microscopy and super-resolution microscopy can visualize a broad range including small EVs.[123] For the potential EVs based clinical applications such as a drug delivery system, it is advantageous to be able to visualize EVs *in* vivo. The tagged EVs are administered intravenously and tracked using *in* vivo or *ex* vivo imaging techniques.[124–128] EVs imaging is used in EVs research for many applications such as monitoring the kinetics of the EVs, observing the metastatic property of a tumor, etc.[126–128] One study reported monitoring of EVs mediated delivery of RNA and translation by live-cell confocal imaging.[129] Usage of various fluorescence imaging for EVs phenotyping is summarized in a review article by Panagaopoulou et al.[130]

3.6.2 Electron microscopy imaging

Electron microscopy (EM) is considered as a standard method of EV imaging as they have excellent spatial resolution and could resolve the finer structural morphology of EVs. The biogenesis of exosomes and tubular platelet MVs are first revealed by EM.[16,41] EMs uses electron beams that have extremely smaller wavelengths (few picometers) than visible light in optical imaging (400-800nm) which results in increased resolution up to few nanometers. Scanning electron microscopy (SEM), Transmission electron microscopy (TEM), and cryo-TEM are used to image the EVs. In TEM, the dehydrated samples are sectioned into small

specimens and mounted in a carbon coating grid. The accelerated electrons transmit through the samples and scatter in many directions. The transmitted electrons are detected in a charge-coupled diode (CCD) and used to generate the brightfield images and the scattered electrons generate the contrast images.

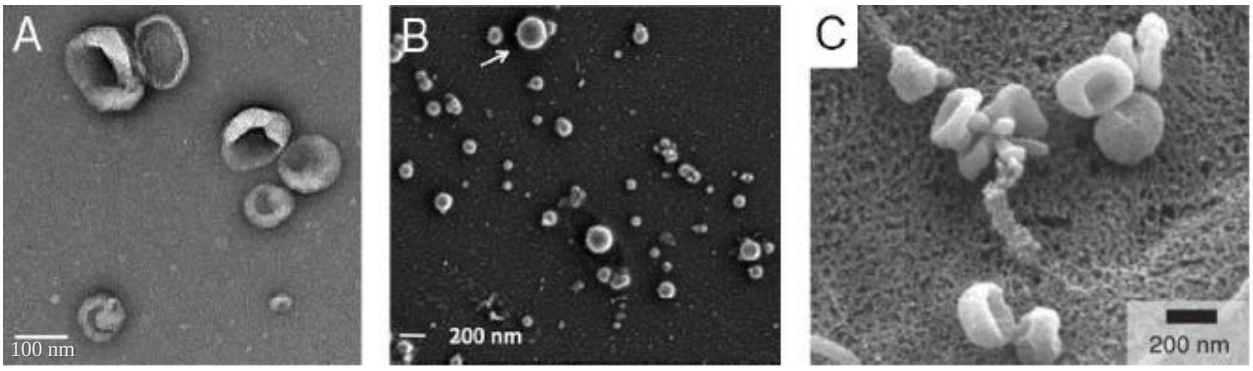

Figure 7 A) TEM images of EVs appear as a cup shaped morphology. (Scale bar100nm) B) SEM image of a EV showing intact spherical morphology.[44] *C) SEM image of EVs showing cup shaped features.*[130]

The destruction of EVs results in the cup-shaped morphology although many EM images could reveal perfect spherical geometry. Immunogold labeling is used to identify the subpopulation of EVs and to quantify them in the EM images.[41,131]

The SEM scans electron beams across a surface and the scattered electrons are captured in a detector and used to generate the SEM image. Samples can be immobilized in a specific surface expressing immunoaffinity or naïve EVs also could be deposited in a surface and dry-fixed. This does not involve slicing and relatively easier sample preparations. The surface is then treated in a sputtering chamber for deposition of a thin metal layer (titanium or gold) for facilitating the conduction of electrons and imaged in a Scanning electron microscope. Therefore, this technique is limited to relatively big EVs that are not buried under the metal layer of the surface.

Cryo-TEM involves fixation of the samples in low temperatures using liquid ethane to freeze the sample without ice crystal formation (-175°C). Thus, preventing structural damage by preserving the natural state. Then the normal TEM procedure is undertaken for high-quality EV imaging.[41,88,132]

3.6.3 Atomic force microscopy

The atomic force microscopy works on the principle of hook's law. A cantilever with a sharp tip is raster scanned across a surface. The atomic force interaction between the cantilever tip and the surface atoms causes the tip to deflect. When the cantilever tip is probed across a

surface, these deflections reveal the topography. The resolution of AFM is often attributed to the atomic scale. The AFM offers a multitude of information about the EVs such as their morphology, size, protein mapping by force spectroscopy,[133]and molecular spectroscopy. AFM can also be combined with EM in an approach known as correlative spectroscopy.[134,135] Specific EV populations could be analyzed in AFM by preparing the EVs in a bio interface specific to a biomarker.[89,135,136] Our team had developed a specific characterization method combining biosensor and AFM imaging techniques.[89,137,138]

3.7 Techniques for EVs concentration measurement

3.7.1 Flow cytometry

Flow cytometry (FC) was developed for cell counting and is a popular method for EV characterization because it is a high throughput and multiparametric single EV analysis technique. Conventional flow cytometers can resolve EVs larger than 300nm. Modern high-resolution FC is capable of detecting EVs of upto100 nm.[139] The FC system consists of a fluidic cell, an optical laser setup, and a detector. The EVs labeled with fluorescence markers are streamlined in the narrow channel and are made to intercept with a laser beam. The scattered light is detected in various angles such as forward to the flow cell (forward scattered light) and detected at the side of the flow cell (side scattered light). The wavelength of the scattered light is filtered depending on the fluorophore used. The amount of scattered light is used to derive the size of the particle. The forward scattering, as well as side scattering data, is used to differentiate the subpopulations. The different subpopulations can also be sorted based on their size in which case the technique is called fluorescence assisted cell (particle) sorting (FACS). In the advancements made in the detection and signal processing of the scattered light, a nano FCM is developed and is capable of detecting eventually sorting particles of size around 100-150nm.[139,140]Although promising, the FC results in the overestimation size and underestimation of concentration due to simultaneous counting of several particles known as “swarm detection”.

3.7.2 Nanoparticles Tracking Analysis

Nanoparticles tracking analysis (NTA) detects the scattered light to measure the Brownian motion of the particles in a suspension. Stokes-Einstein equation describes the relationship between the size and diffusivity of a particle and that is used to deduce the hydrodynamic diameter of the particles. The NTA provides size and concentration data and is simple to use. The measurement is performed rapidly without any additional preparations. Fluorescence labels could be used to discriminate subpopulations of EVs. NTA has a better

resolution than a flow cytometer and can detect small EVs around 50nm.[140] It is noteworthy that the raw concentration estimation from NTA may count particles other than the EV in the suspension as well.

3.7.3 Dynamic Light Scattering

Dynamic light scattering (DLS) is a technique that also uses the scattered light from the particles to define their size. In the DLS system, the sample is illuminated with laser light and the scattered light is detected at a particular angle called scatter angle. The variation in the intensity of the detected light is used to compute the size and index of dispersion of a given sample. Unlike NTA, DLS does not track the motion of the particle which is a key difference between both techniques. DLS has a lower limit of detection than the NTA.[141] Since DLS data is estimated based on mathematical linearization and assumed particle size distribution, the results are often containing a "false peak" at a low size range. It is also not suitable for heterogenous samples for the same reason as the different modal peaks are normalized and result in underestimation.

3.7.4 Resistive Pulse Sensing

Resistive pulse sensing (RPS) is an electrical characterization technique that is used to measure the size, concentration, and zeta potential of EVs. The change in the electrical resistance caused by the flow of a nanoparticle through a nanopore is measured as a signal pulse. The magnitude of the pulse is proportional to the volume of the particle. The change in the magnitude of the pulse, the frequency of the pulses, and electrical charge parameters of calibration beads compared to EVs are used to compute the size, concentration, and zeta potential of the EVs respectively.

The size of the nanopore is adjustable and thus, a tunable RPS system is developed (TRPS). This is a sensitive technique although the size resolution of the EVs is limited by the size of the nanopore. This method is susceptible to nanopore clogging, as well as contamination from the calibrants since the sample and the calibrants are measured in succession in the same measurement conditions.

3.7.5 Molecular and biomolecular characterization techniques

3.7.5.1 Vibrational Spectroscopy

The spectroscopic characterization of EVs recently attracted interest as it can provide molecular signatures of various biomolecules such as proteins, nucleic acids, peptides, etc.

Several spectroscopic techniques are available such as Infrared spectroscopy (IR), Surface Enhanced Raman spectroscopy (SERS), and Tip-Enhanced Raman Spectroscopy (TERS). Such spectroscopic characterizations are based on the interaction of molecules with electromagnetic radiation. Molecules vibrate at a certain frequency known as the resonance frequency. They absorb energies at a specific frequency based on their structure. The sample is deposited in an interferometer and the absorption spectra at different frequencies are obtained; these are then treated to obtain characteristic peaks or valleys associated with different molecular subunits such as amide bonds, sugars, lipids, etc.[142] Raman spectroscopy works on the principle of Raman scattering invented by Sir C. V. Raman, who was awarded Nobel prize in Physics in 1930. In Raman scattering when the light is excited on the sample, the vibrational state of the molecule is moved into a virtual energy state and the molecule returns to the (nearly) original state by losing the excess energy in form of a photon. However, the molecule after the excitation and reemission (scattering event) rests in a different vibrational state since the energy of the emitted photon is either higher or lower than the excitation energy. Thus, this can be used to characterize the molecular vibrational state of a molecule in the EVs. Although the technique is not specific to EVs, the fingerprint of many molecules in a spatial dimension can be studied to potentially discriminate EVs based on their surface molecules. In EV characterization a recent study indicated distinguishing EVs under autophagic conditions using the SERS technique.[143,144] Raman spectroscopy could be coupled with AFM inside new instrumentation called TERS although an interesting and deep investigation of EVs is yet to be reported. As the IR and vibrational spectroscopy are sensitive to molecular vibrations, this technique could potentially differentiate proteins, lipids, and other constituent biomolecules on the surface of the EVs.

3.7.5.2 Biosensors and immunoassays

Various biosensing techniques are used to detect EVs. Popular sensing techniques include transducing elements as optics (plasmonic, interferometry) Acoustic or Electrochemical sensors. These biosensors are based on ligand layer Biosensors immobilize an antibody or protein or a synthetic probe on a sensor surface, and the EVs are made to interact on the sensor surface. Upon specific interaction with the binding epitopes in the EVs, the signal is detected such as a change in the reflectivity, or acoustic frequency, or electrical properties are then used to monitor the binding activity. Using a standard curve or dynamic range data, these signals can be translated to the absolute quantity of the bound material. The biosensors can also detect multiple biomarker expressions when used in a sandwich assay format.

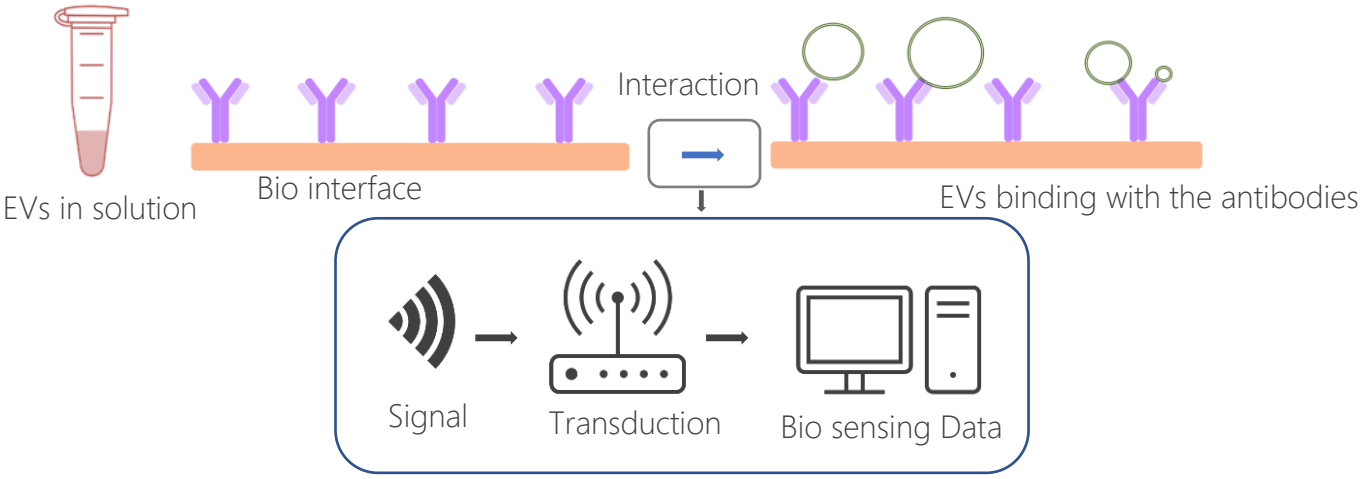

Figure 8 Schematic diagram of a EVs biosensor. Different signals could be detected such as optical, piezoelectric, or electrical upon interaction of EVs in the bio interface.

Plasmonic biosensors such as surface plasmon sensors monitor the change in reflectivity or change in the resonance angle to characterize the EV's biomolecular interaction.[145,146] The piezoelectric sensor such as a quartz crystal microbalance uses the change in frequency.[147,148] The electrochemical EVs biosensor uses the change in electrical resistance or current using a pair of electrodes for detecting the EVs.[149,150] EVs biosensors are often label-free but there are signal amplification strategies developed to enhance the signal at low concentrations. Biosensors are sensitive and are capable of specific sensing a few hundred to thousand EVs per mL.[150] Label-free biosensors also facilitate the captured EVs to be studied in one or more additional characterization methods such AFM or EM, on-chip proteomics, etc. The EVs contents could also be chemically digested for a targeted multi-omics study. Thus, the biosensing method offers a correlative multi characterization of EVs.

3.7.5.3 Immunoblotting

Immunoblotting is also known as qualitative western blotting. It is a technique developed to identify a single protein or its isoforms. It is a widely used technique in molecular biology and biochemistry. Although this technique is specific to single proteins, it is widely used in EVs research for the identification of a biomarker or a protein associated with a desired functional activity. In western blotting, the EVs are lysed, and the protein is separated based on its molecular weight or electric charge, or isoelectric point in gel electrophoresis. The separated protein is then transferred into a membrane to facilitate detection by a revealing

antibody. To prevent the antibody coating everywhere in the membrane, it is usually blocked with a non-relevant protein such as bovine serum albumin (BSA) and then incubated with the labeled antibodies and revealed in a photodetector. The immunoblotting yields qualitative information and can be quantified compared to normal positive control. The international society of EVs (ISEV) recommends characterizing EVs for their surface markers such as CD63, CD81, CD9, etc., as well as a protein other than commonly found in EVs such as albumin, lipoprotein to assess the purity of the EVs.[2]

3.7.5.4 ELISA

Characterization of EVs using Enzyme Linked Immunosorbent Assay (ELISA) was first described in 2009.[151] This method works on the principle of antigen-antibody interaction. The targeted antigens in EVs are captured in a substrate and the detection step involves an antibody tagged with an enzyme. The reaction between the enzyme and the chromatic substrate develops color change which can be measured in a spectrophotometer. The intensity of the color change is directly proportional to the level of expression of a protein depending on the configuration of the assay, it can be called as sandwich assay, double sandwich assay as well as biotinylated sandwich assays. ELISA technique offers direct quantification of a particular protein in the EVs although the specificity or the proportion of an EV marker versus freely available in the body fluid is difficult to be distinguished.[152]

3.7.5.5 EVs functional assay

EVs functional assays are emerging and being developed to assess the effect of EV in a dose-dependent manner for a desired functional activity. Such assays, intended to study target cells or organs, facilitate the comparison of different EV preparations. They can be used in microfluidic models, *in* vitro, or *in* vivo. Various EV detection methods particularly qualitative assays could also be considered as non-biological assays since they reveal a characteristic of the EVs in a reproducible, comparable manner. An exhaustive review article summarizes the state of the art of EVs based assays.[153]

3.7.5.6 Proteomics and Lipidomics:

Proteomic and lipidomic studies of EVs are interesting as they can reveal a wealth of information about the existence of various proteins and lipids in EVs. Mass spectrometry is the widely used technique to characterize the protein profile of EVs. The isolated EVs are digested in an electron evaporation chamber or by electrospray ionization. The ionized molecules are accelerated in a vacuum chamber and deflected using electromagnets. The lightest molecules

deflect more and are detected at different places in the mass detector. The mass spectrum is composed of charge to mass ratio. Each molecule has a characteristic charge-to-mass ratio which is used to identify the molecular weight of the detected molecule. The fragment of the peptide sequence is usually identified from mass spectrometry data. Mass spectrum libraries of proteins nucleic acids, lipids, etc. are available. The protein structure is predicted using these libraries. This technique can usefully provide large-scale information about different proteins in the EVs and may elucidate the difference in proteomic profile for a given pathophysiological condition. Proteins associated with different biological processes are mapped and a potential pathway of EVs mediation could be described. Proteomics is also useful to compare the protein profile between different EV preparations.

EVs isolated by UC are commonly processed in MS proteomics. Since these preparations are not pure, it is difficult to associate an identified protein with EVs. Several advances are made in mass spectrometry-based proteomics, and it can be combined with size exclusion columns to obtain purer EVs. As a targeted proteomics approach, EVs captured in a biosensor surface can be digested using an enzyme such as trypsin and the specific EV subsets can be further analyzed in MS for protein profiling.[154]

The EVs characterization involves diverse methods, tools, and techniques but currently, no standardized method of EVs characterization is available. However, there are many meaningful developments made in the previous years together with useful advancements in standardized isolation, detection, and data analysis techniques that could move the EVs research into diagnostic, clinical applications, and improved patients care.

4. nPEVs characterization and establishing the limits of NanoBioAnalytical (NBA) Platform

4.1 Context

The NanoBioAnalytical (NBA) platform is a label-free and multiplexed characterization method developed by Femto-ST Institute, France. This system combines complementary biodetection and Nano-Bio characterization tools on a common substrate.[89] It comprises Surface Plasmon Resonance-imaging (SPRi), Atomic Force Microscope (AFM), and Mass Spectrometry (MS).

On-chip bio-molecular characterization by SPRi, while providing valuable information such as interaction kinetics as well as the level of amount of capture, also allows the interacting partner to be enriched on the specific location of the surface. This does pave the way for the captured object to be further studied in any of another on-chip deep characterization technique such as AFM or MS. Thus, a label-free, NBA platform functions to provide the exploratory characterization of biological targets.

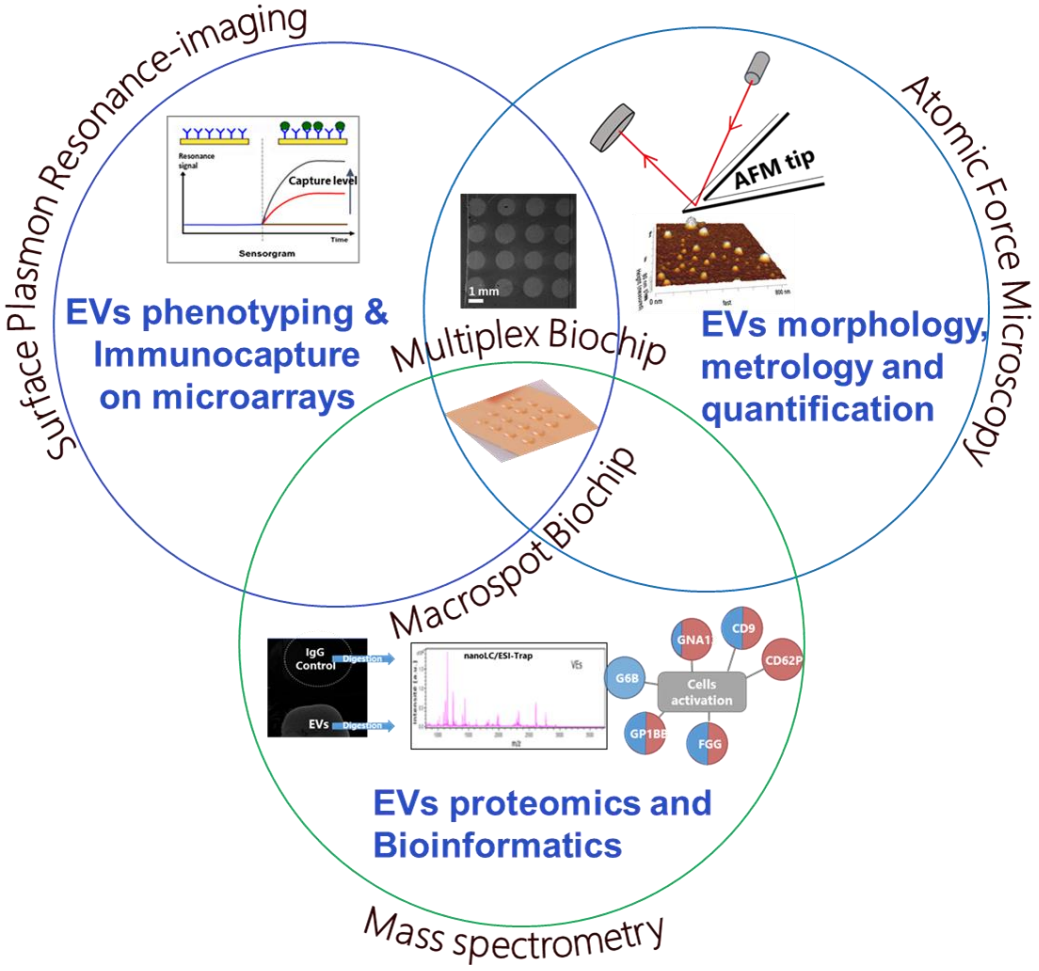

Figure 9 Description of different modalities of the NanoBioAnalytical platform. The NBA platform is based on unique gold biochip on which multiple characterization techniques are integrated.

EVs are interesting subjects to be explored in the NBA platform as they express several membrane proteins on the surface which can be captured using a complementary antibody or else a biological or synthetic receptor. This leads to the study of EVs with a particular phenotype and its quantification, their morphological and biophysical properties by AFM. As the physical and biochemical properties of EV subsets make them hard to be distinguished in a complex sample, the complementary nature of the NBA platform can provide reliable as well as realistic estimation about the biomarker expression, size parameters, and proteomic contents of the EVs.

The core constituent that makes these combinations possible is the biochip. For SPRi, a gold biochip, which is compatible with the available surface grafting chemistries. This provides plentiful potential options for customization of the ligands and thereby specific, deep characterization/exploratory research of EVs. Application of the NBA platform for EVs characterization is highlighted in the Information for Studies of EVs MISEV)[1] updated guidelines of the position statement the ISEV.

4.2 Modalities of the NBA platform

The EV characterization in the NBA platform can be used in two different modalities.

- "SPRi and AFM" mode:

In this configuration, a biochip is prepared with many ligands (up to 16, usually in 4*4 format) known as the multiplexed format, allowing to study the expression of specific biomarkers and further characterization in nanoscale metrology measurements.

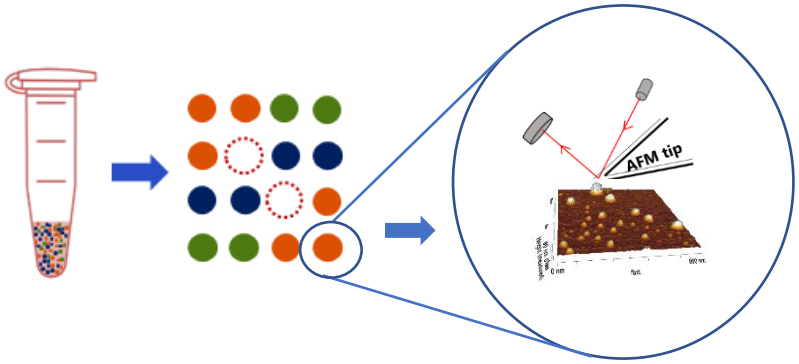

Figure 10 Capture of EVs expressing different biomarkers on a multiplexed surface and their further specific and deep investigations in AFM.

The EVs captured on a biochip can be scanned in one of two ways in AFM depending on the purpose of the investigation. EVs fixed with a cross-linking agent such as glutaraldehyde are imaged in dry condition and in-air. Alternatively, it is possible to scan the EVs in their

physiological condition preserving their native structure after the capture on specific ligands. This is carried out without fixation and by imaging in liquid.

- ❖ "SPRi and Mass Spectrometry" mode

This configuration consists of a macrochip format of antibodies that covers most of the surface. EVs are captured comparatively in large quantities to be compatible with the MS platform. (500ng of total material is recommended to achieve MS analysis). This approach also contains two analytical pathways. The main method consists of enzymatic digestion using trypsin and the collected solution is analyzed in a mass spectrometer to identify different proteins and biomolecules. In an alternative method, on-chip proteomics is carried out so that the protein fragments of EVs are ionized and desorbed directly from the surface to an ion detector[155]. The scheme of the SUPRA-MS (SUrface Plasmon Resonance imaging in Arrays coupled with Mass Spectrometry) model is presented in figure 11.

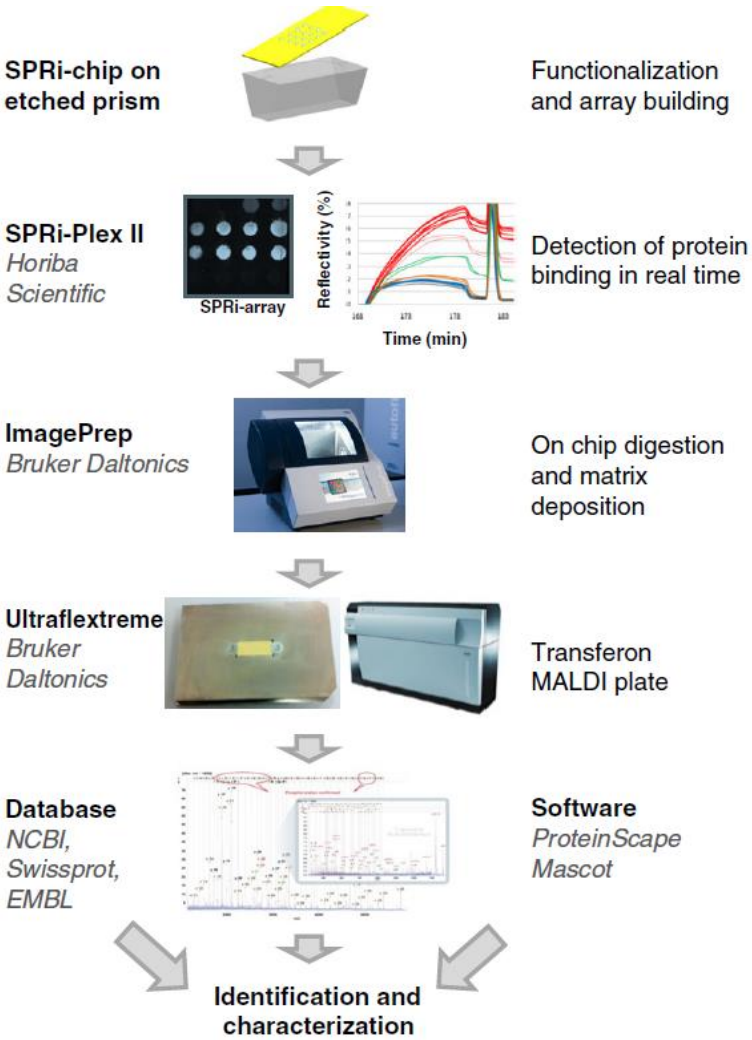

Figure 11 Schematic of combining SPRi and Mass-spectrometry demonstrated by Remy-Martin F et al[155]

4.3 Development and previous performances of the NBA system

The first approach of coupling SPRi sensing and MS is demonstrated in 2012 by Fabien Remy-Martin et al.[156] In this work, the authors have developed a methodology that enabled immunocapture of a human breast cancer biomarker in complex media. In a multiplexed surface, containing a-LAG3 (Lymphocyte-activation gene 3) ligand, its complementary target LAG3 protein, spiked in diluted human plasma, is specifically captured. This is followed by in-situ enzymatic digestion of the LAG3 and further analyzed in MS. The above methodology was further developed to link SPRi with a Matrix-Assisted Laser Desorption Ionization-Time of Flight (MALDI-ToF). This approach extended the sensitive detection of LAG3 spiked in human plasma in femtomole levels.[155] This work offered solutions to identify a biomarker in a complex sample without labeling, after validation of its specific capture of analytes on a homemade sensor surface.

The NBA platform was developed in 2017 by Sameh Obeid et al.[89] The AFM module in the platform allowed label-free detection and metrological investigations of natural-platelet derived microparticles (nPMPs). Before the application of biological EVs, the system is validated with calibration particles of two sizes of diameter 53 nm and 920 nm. (CP53 and CP920 respectively) to be compatible with the physical size range of the EVs. The CP53 are virus-like particles that express capsid protein VP1. The CP920 are microbeads functionalized with LAG3. By designing a biochip with ligands against VP1, LAG3, and control, the LOD of such configuration is established to be $1x10^{10}$ CP53 particles/mL and a dynamic range of $1x10^{10}$ to $2x10^{11}$ VLPs/mL is validated. For CP920, the LOD started at $3.25x10^{7}$ microbeads/mL, and the dynamic range was described from $3.25x10^{7}$ to $3.25x10^{8}$ microbeads/mL. The values are almost reproduced after spiking each analyte in native platelet microparticles (nPMPs). This suggested as a proof- of concept that the NBA platform is capable of detecting specific analytes in a complex sample. The validation of the NBA platform for the biological sample was performed in a study comparing the expression level of EVs in a multiplexed biochip. Basal EVs secreted by platelets and collagen-activated EVs are used in this work. Among the various ligands used, a-CD41 was found to have the maximum reactivity in both the analytes. The findings are validated by a flow-cytometry test. An attempt to detect the nPMPs at a low concentration (in the order of 10^{7}/mL, estimated by flow cytometry) on a surface of a-CD41 was made. This study resulted that the signal in a-CD41 was noisy. Although further AFM investigations revealed that a large proportion of small EVs present in a-CD41.

This work already highlighted the need to establish the standard ranges where the NBA platform is sensitive and useful for EVs characterization.

A comparative study of EVs from nPMPs and thrombin-activated PMPs (t-PMPs) between crude and 75nm-nanofiltered plasma was extensively characterized to assess the safety of the plasma for transfusion.[137] In this work, a multiplex of ligands is used to qualify EVs expressing different biomarkers to characterize the aforementioned samples. The study was able to identify a significant difference in the size of the EVs between crude and nanofiltered plasmas. This work was also successful in describing a qualitative differentiation of markers between various samples by the NBA platform.

4.4 Scope of the study and objectives

The NBA platform has been calibrated and is proved to be conceptually usable to study EVs from a complex biological source. The objective of this part of the project is to push the limit of the analytical platform for studying biological EVs. This implies establishing an optimized procedure to reach the best LOD and define the dynamic range of this analytical solution for real EVs. Native platelet-derived EVs (nPEVs) are used to investigate the analytical limits of the system for this sample. This, in principle, could allow the NBA platform to be used for deep characterization of EV samples from diverse origins and different functionalities while providing a comparable system of measurement. The well-characterized analytical system is also useful in determining the optimized sample quality for reliable as well as reproducible measurements.

The defined goals of the study are:

1. To test the nPEV samples in varying concentrations (rounded to the order of magnitude) to find out the LOD of the system without any signal amplification strategies. This was done on a specific ligand (a-CD41) but grafted at two different concentrations, in reference to negative control surface realized in the same way.
2. To establish the dynamic range of the analytical solution.
3. To find out the particle size distribution and to see the evolution of the particle size distribution at varying concentration ranges.
4. To recommend an adaptation of appropriate measurement parameters for the reliable characterization of EVs.

4.5 Materials and methods

4.5.1 Description of the samples

The samples used in the study were provided by Pr. T. Burnouf's team from the College of Biomedical Engineering (CBME), Taipei Medical University (TMU), Taiwan. The nPEV samples were received in a frozen condition in dry ice and stored at -80°C. The first assessment was usually performed to check the quality of the samples in Tunable Resistive Pulse Sensing (TRPS). After this test, the sample was fractioned into several small aliquots of 10 µL and stored at -80°C.

4.5.2 Sample preparation

The precursor for preparing the nPEVs are clinical grade Platelet concentrates (PC). They were obtained either from Platelet rich plasma (PRP) method or from the whole blood by apheresis method. They are obtained from healthy, volunteer donors at the Taipei blood centre. The approval for processing the platelet concentrates were obtained from the institutional review board of TMU.

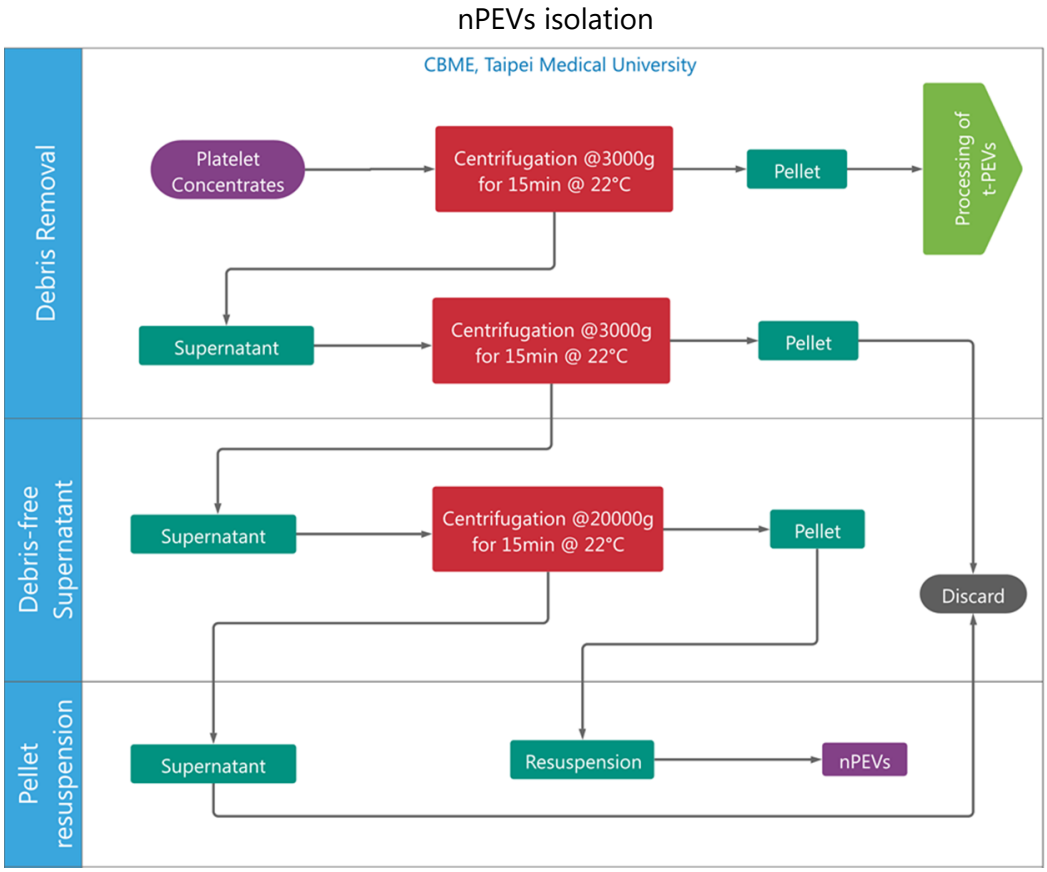

Figure 12 Preparation of nPEVs. They are also referred as naturally occurring platelet microparticles (nPMPs)

Apheresis PC was prepared using the licensed Haemonetics MCS+ cell separator (Haemonetics Corp., Braintree, MA, USA) and whole blood-derived PC by the "platelet-rich-plasma" method. PC was anti-coagulated using a licensed citrate phosphate dextrose solution. Obligatory tests for viral markers were carried out and found to be negative. The PCs were made available at the facilities of TMU from the blood collection centre within 3 days and stored in 22°±2°C on a platelet agitator. The native Platelet-derived Extracellular Vesicles (nPEVs) were prepared within 9 days of arrival at the facilities of CBME using the procedure reported previously.[157] Briefly, the EVs in the plasma of the platelet concentrates were pelleted at 20,000 *g* after removing the debris. The final 20k pellet was suspended in PBS buffer. The 1st pellet of the platelet concentrates was used in another parallel process for various preparations. The prepared nPEVs were tested by TRPS and NTA for measuring the concentrations and mean diameter of EVs and protein quantification using Bicinchoninic acid (BCA) assay.

4.5.3 EVs characterization in solution

4.5.3.1 Measurement of EVs concentration by TRPS

The TRPS system was developed by Izon science and is a useful tool for measuring the concentration of the particles in solution. Izon TRPS system works on the Coulter principle developed by Wallace Coulter.[158] When the voltage is applied in an electrolytic cell, a baseline current is established by the ionic transfer in the electrolyte. When a particle moved through a nanopore, this causes a drop in the baseline current in the form of a pulse also known as a blockade or an event. The magnitudes of the pulse, compared with that recorded with the controlled measurement conditions of calibration particles of known size and concentration and electric charge are used to deduce the size distribution, concentration estimation, and zeta potential measurement. Izon offers a wide range of nanopores with different pore sizes to be compatible with the size range of the objects being studied.

The nanopore is pierced in the centre of an elastic polyurethane membrane and the apparatus allows to tune the size of the nanopore with a four-jaw stretching mechanism.

The movement of the particle inside the nanopore is governed by three forces namely convection dependent, electrophoretic mobility, and electroosmotic forces. The convection-dependent force is exerted by the gravitational force which causes the particles from the upper fluidic cell to flow through the nanopore to the bottom fluidic cell. The device comprises a variable pressure module (VPM) that can exert additional force by compressing air through a

pressure hose connected to the top of the fluidic cell. The electrophoretic and electroosmotic forces are influenced by the electric charge of material and therefore have an impact on the velocity of the particles flow through the nanopore.

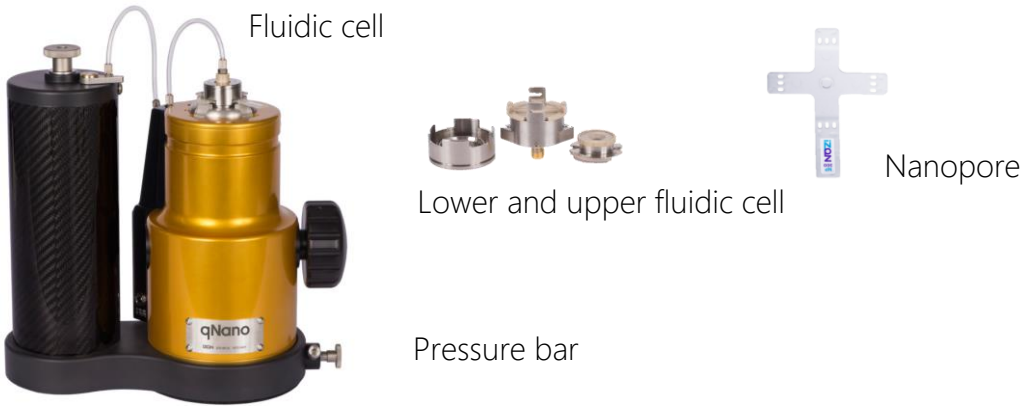

Figure 13 Photograph of a TRPS system attached with the VPM. Fluidic cell components and the nanopore is also shown.

The continuous, uninterrupted, and uniform flow of particles is thus controlled by stretching the pore size and optimizing the applied pressure to achieve smooth flow and avoid blocking of the nanopore. The signal-to-noise ratio is improved by selecting the appropriate setpoint voltage to have the baseline current between 120nA-140nA.

The assessment of the size and concentration of the analytes are projected from the measurements of carboxyl-coated polystyrene particles for calibration (CPC). The change in the blockade magnitude is proportional to the volume of the particles. Assuming the objects are spherical, the diameter can be deduced from the volume for a unit change in the blockade current. The concentration is derived from the so-called rate plot which is the cumulative count of the particles as a function of time. The gradient of the flow rate and the applied pressure are used to estimate the gradient of the function. The ratio of the gradient of the flow rate of the CPC particles and the analyte multiplied by the CPC concentration is the expected concentration of the analyte.

Since the TRPS system is sensitive, the measurement parameters for the calibration particles and nPEVs are to be rigorously applied for reproducible and reliable measurements. In particular, the uneven flow of particles affects the flow rate of the particles which directly impacts the estimated concentration. Therefore, particular attention is paid to all the TRPS measurements to achieve a linear flow rate.

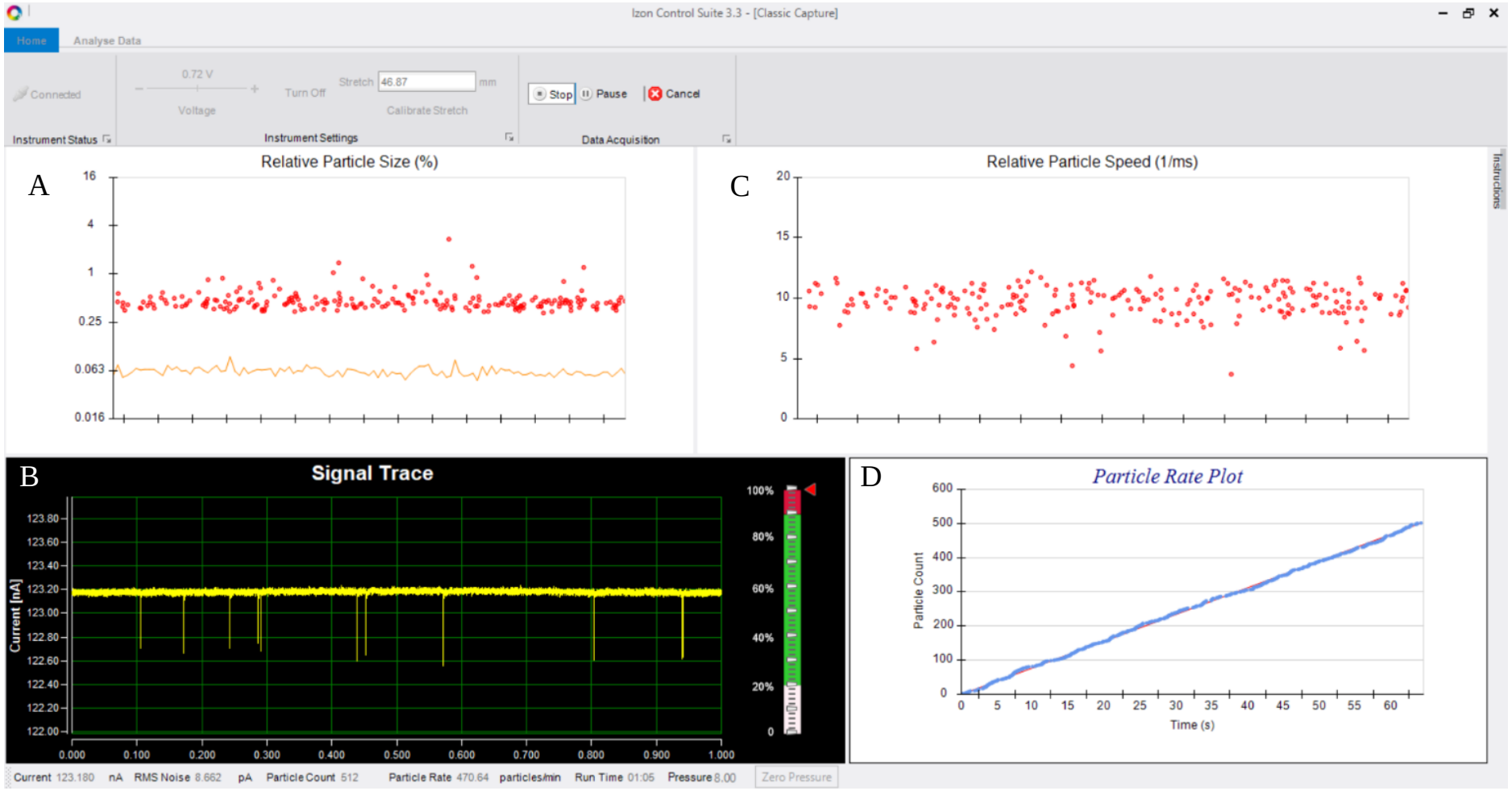

Figure 14 Screenshot of a measurement of a CPC 200 window of TRPS control suite software. B) Signal trace is monitored as a series of blockade events with each even represent a particle. Several blockade events indicate the flow through the nanopore. The relative size scatter plot(A) indicates homogenous size distribution of the CPC particles. C) This scatter plot describes the relative speed of transfer of particles through the nanopore. D) The line chart indicates the flow rate, and it is largely linear and un-interrupted

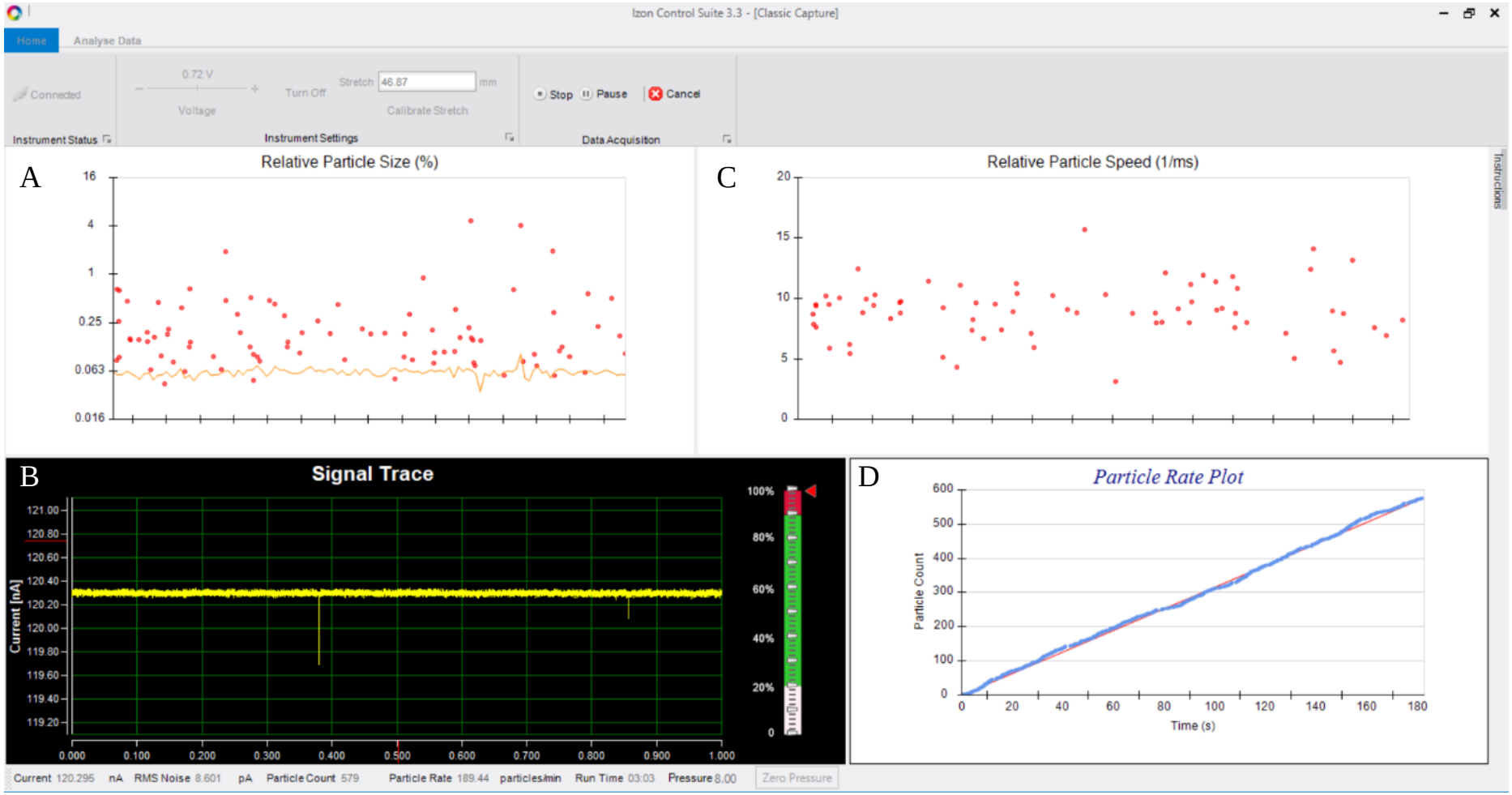

Figure 15 Screenshot of a measurement of nPEVs diluted by 100x. B) Signal trace is monitored as a series of blockade events with each even represent a particle. Fewer blockade events than the CPC indicates the concentration is relatively lower than the CPC concentration. The relative size scatter plot(A) indicates heterogenous size distribution of the nPEV particles. C) this scatter plot describes the relative speed of transfer of particles through the nanopore and it is varied with the size. D) The line chart indicates the flow rate, and it is largely linear and un-interrupted.

As the recording must be interrupted between calibration particles and the analyte, it is also essential to maintain the baseline current variation between the calibration particles and analytes within ± 5%. The root mean square (RMS) of the noise is maintained within 10pA. The dilution factor for measurement is adjusted to have a flow rate of at least 100 particles/minute.

4.5.3.2 Protein quantification by BCA assay

The concentration of total protein content in the nPEVs was estimated with a BCA assay.[159] The assay relies on the colorimetric change of an alkaline chemical solution when it is interacting with the protein molecules. The peptide bonds in protein reduce Cu^{++} ions to Cu+. The BCA chelates with the Cu^{+} ions and forms a purple color complex. The intensity of the color is proportional to the amount of protein, thus, by comparing the color resulting of an unknown quantity of protein against a known gradient of Bovine Serum Albumin (BSA) range is then measured in a spectrophotometer by quantifying the absorbance at 562nm. Several standard concentrations of BSA ranging from 200 μg/mL to 1000 μg/mL were prepared. The test sample was usually diluted 10-folds or 25-folds to be within the standard range. The exact dilution was adapted based on the expected protein content of the sample. The BCA solution and $CuSO_4$ were prepared at a ratio of 50:1. The BCA solution was mixed with the standard as well as the sample protein solution at a ratio of 8:1. The tubes were treated in an incubator at 37° C for 30 minutes. Then the tubes were cooled in ice and measured in the spectrometer. The standard curve was drawn, and the protein concentration of the unknown sample was estimated from the standard curve.

4.6 nPEVs characterization in NBA platform

The nPEVs were characterized in the "SPRi and AFM" mode also known as the Nanobiocharacterization mode of the NBA platform. As the first step of this multiphysical characterization, the SPRi enabled to follow the capture of EVs in real-time and in a label-free manner on a multiplexed sensor surface. Then this biochip was further studied by atomic force microscopy for qualitative and quantitative imaging. The working principle, as well as description of both the apparatus, are discussed in this chapter.

4.6.1 Surface Plasmon Resonance imaging (SPRi)

Surface plasmon resonance was first observed in the form of dark bands of the reflected light by Prof. Wood in 1902.[160] A theoretical explanation of this phenomenon was proposed by Fano as the difference in the intensity of the reflected light is linked to surface waves.[161] In 1968, Otto and Kretschmann independently developed a method to excite surface plasmon with light.[162,163] The initial application of this technique was mainly utilized in characterizing thin films. The first renowned application of this technique as a sensing device was reported in 1983.[164] This was the first demonstration of a biosensor with an adsorbed antibody layer and its binding with an a-IgG is monitored by studying the change in the plasmon angle.

HORIBA Scientific has acquired the optical configuration (originally developed by Genoptics SA, a French company) that allows an integrated imaging system. The light from the laser source is collimated and illuminated on a 2D matrix of the biochip. The reflected light from the prism-biochip interface is captured in a 2D Charge-Coupled Diode (CCD) camera array and each pixel is consistent with the location in the biochip surface. Thus, the SPR-imaging systems allow monitoring of the interaction across a spatial surface. By differentiating the Region of Interest (ROI), it is possible to examine the interaction in multiple spots at the same time. Because the system does not require a complex microfluidic circuit involving valves and capillaries, the SPR-imaging system permits to work with samples that are more complex than the SPR systems. In the SPR system, the analytes are required to be filtered with 0.22 μm to avoid the risk of blockage in the microfluidic cartridges.

The SPR sensors in biosensing are used since then for a wide variety of applications including pathogenic detection[165,166], biomarker discovery[155], DNA sensing[167], and many others including

biomedical analytes.[168] In summary, the SPRi sensor is a non-destructive, label-free analytical technique that can be used to monitor the specificity, kinetics as well as quantification of the analytes in solution in real-time.[165,169]

4.6.1.1 Principle of operation

The SPRi system works on the principle of surface plasmon waves. The surface plasmon wave is an evanescent wave that occurs at a metal-dielectric interface when the p-polarized light through a glass prism, and at a certain angle of incidence causes the momentum of the light to match with the plasmon of the surface atoms. The energy picked up by the free electrons of the metal film results in a sharp decrease in the intensity of the reflected light.[169] The angle at which the surface plasmon phenomena occur depends on the Refractive Index (RI) of the prism and the metal-dielectric interface. Therefore, by monitoring the change in the surface plasmon angle, the biomolecular interaction on the surface can be studied.

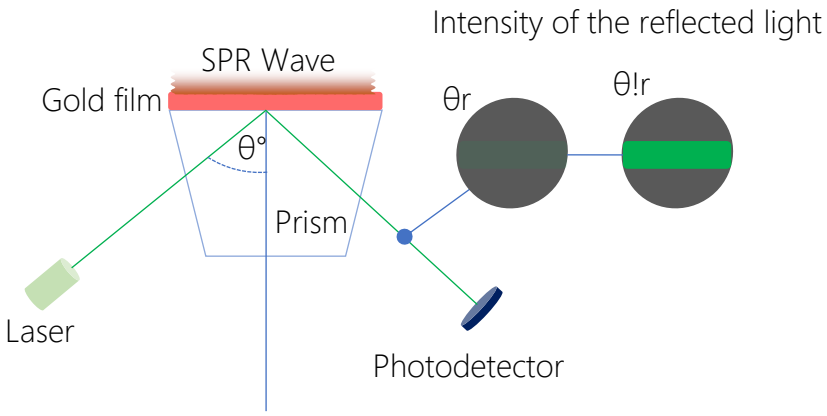

Figure 16 Principle of surface plasmon resonance. The resonance angle is described as θ_r and angle other than the resonance angle is mentioned as $\theta_{!r}$

Different configurations of SPR system area available and the two well-known implementations are Otto and Kretschmann-Raether configurations. In Otto configuration, the metal is not directly deposited on the prism rather it is placed in proximity so that the evanescent wave penetrates through the metal film and causes plasmonic excitation. The Kretschmann configuration has the metal film deposited directly on the glass block as shown in Figure 16 so that the electrical field of the total internal reflected light is absorbed by the free electrons in the surface and causes the plasmonic wave. The intensity of the surface plasmon waves decays

exponentially and it extends roughly one-quarter of the wavelength of the incident light. As the surface plasmon propagates along the metal surface, due to absorption, the energy loss manifests as decay in the intensity of SPR with the square of the electric field of the incident light.[170]

4.6.1.2 Signal acquisition in SPRi systems

Depending on the configuration of the SPRi apparatus, different deployments of signal monitoring are possible. E. Stenberg et al calculated the correlation of SPR angle shift to the absolute quantity of the protein that is adsorbed on the surface.[171] In this work, radiolabeled monoclonal antibodies and proteins are used as analytes and the change in SPR angle is recorded. The absolute quantity of these biomolecules is determined using a surface scintillation counter. Biacore systems by GE Healthcare measure shift in resonance angle.

However, it is also possible that without changing the angle of incidence, the kinetics of the interaction can be monitored by measuring the intensity of the reflected light. SPR imaging systems manufactured by Horiba scientific uses this as the mode of signal acquisition.

4.6.1.3 Horiba SPRi Plex II

The SPRi Plex II, Horiba France, was used in the experiments of this project. The SPRi Plex II consists of a plasmonic sensing setup composed of a light source, a polarizer, and a motorized mirror, and a CCD sensor. The system is configured as a Kretschmann setup. A fluidic system comprised of a running buffer loop, analyte injection system, waste disposal that is connected into a fluidic circuit. The modular construction allows the prism to be mounted and covers the fluidic chamber with a mechanical lever system. A rubber gasket seals and avoids fluid leakage during the operation of the system. A degassing system to avoid the introduction of bubbles in the medium and a temperature control system are also connected to the fluidic chamber.

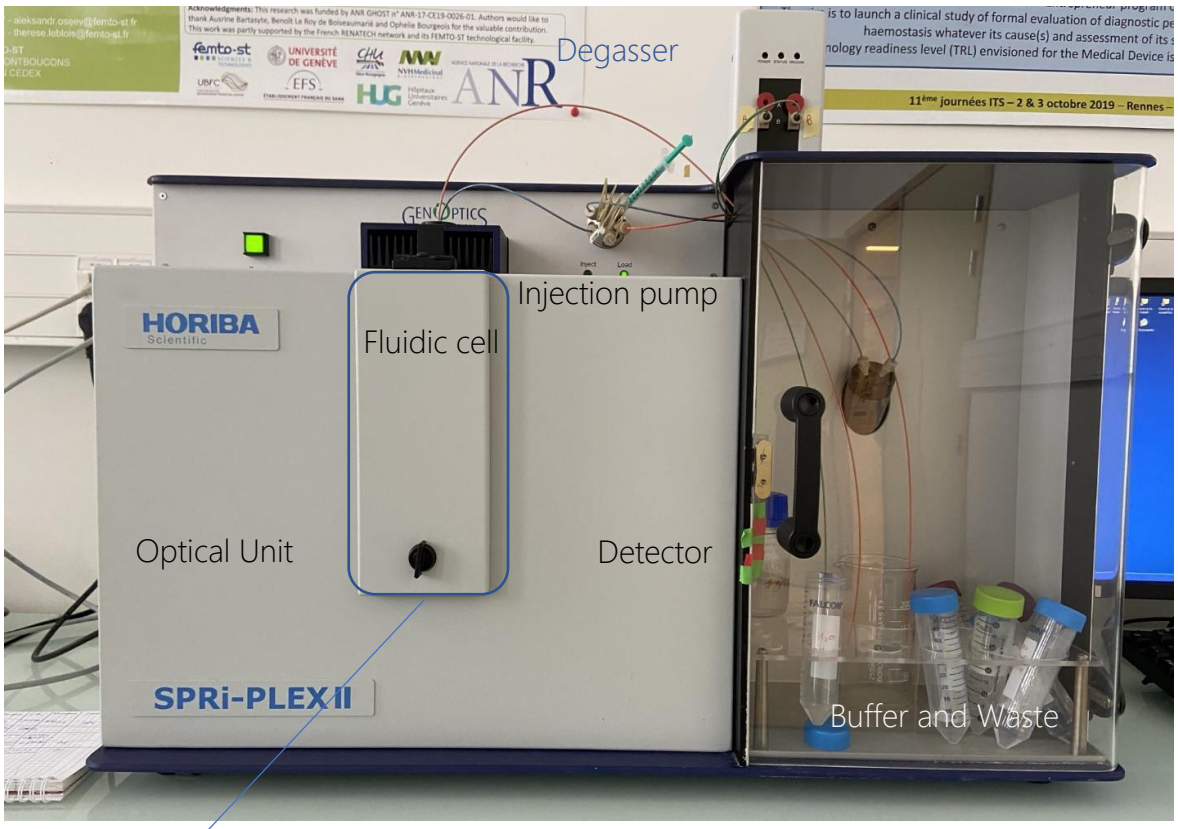

B) Prism holder

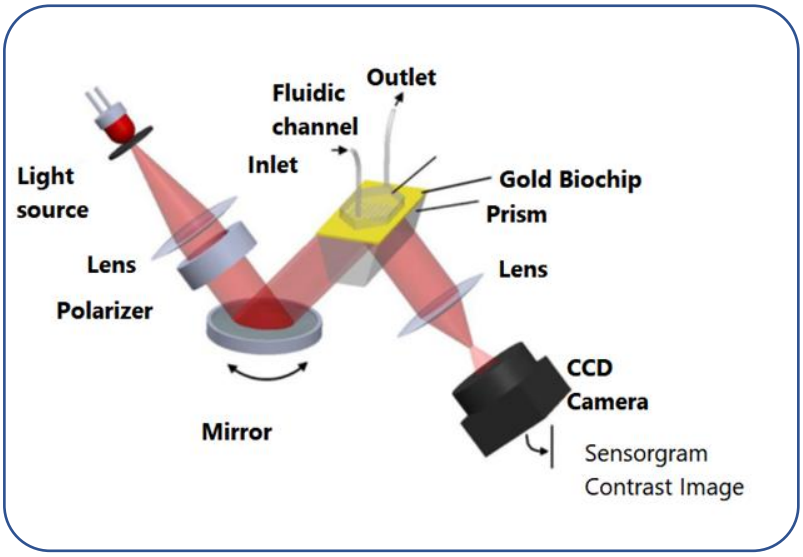

C) Working principle of SPRi Plex II

Figure 17 A) Photograph of SPRi-Plex II. It features an optics system which contains light source, polarizer and the lens, integrated fluidic system, portable prism holder and photodetector. A supply pump system and degassing unit is also shown. In the inset photo B), prism mounted in the fluidic cell can be seen. C) Working principle of the SPRi system. Picture adapted from the manuscript of S. Obeid. [226]

4.6.1.4 Controlling of the injections

The system was designed to allow the flow of media through a dedicated fluidic circuit. Normally, the system operates in the loading position where the running buffer is connected to the flow cell.

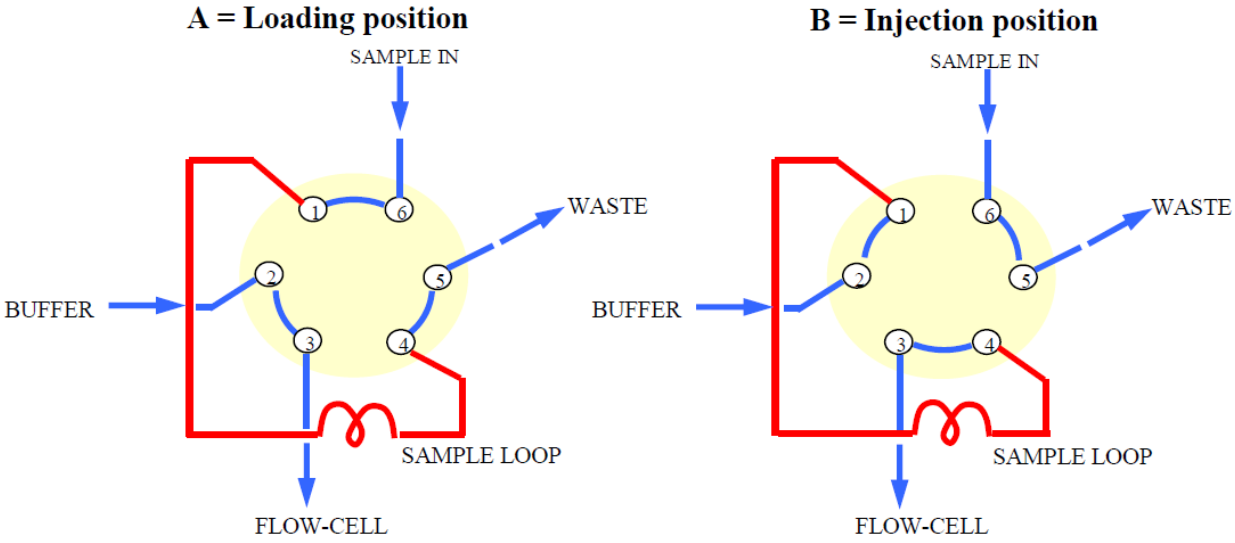

Figure 18 Valve connection diagram of the SPRi Plex II. Image reproduced from the instruction manual.

Sample injections can be performed with defined flow conditions such as flow rate and the duration of the injections. In the laboratory, the system is capable of injecting analytes up to 500 µL. This is performed by switching the flow circuit into injection mode. In this study, the sample is stored in a reservoir loop of a volume of 200 µL and is injected into the fluidic channel at the defined rate. During this time, the flow coming from the running buffer is connected to the waste disposal.

The SPRi Plex II system records the interaction of the analytes in a fixed angle known as working angle and the CCD camera detects the reflectivity of the measurements in real-time. The biochip can be functionalized with a multiplex of various ligands and the particle size suspended in the samples are generally compatible without filtrations. The system records 20 measurements of reflectivity in a minute and therefore the resolution is 3 seconds. It is possible to follow hundreds of region of interest (ROIs) simultaneously. It is also possible to record images of the flow-cell in two channels namely flow cell images and difference images.

The operation method of Biacore SPR is discussed in the next chapter. A table of comparative performance indicators is listed in the following table.

Parameters	**SPRi Plex II**	**Biacore 3000**
Manufacturer	Horiba Scientific	BIAcore, GE Healthcare (now Cytiva life sciences)
The wavelength of the light source	810nm	760nm
Detection system	Integrated 2D CCD camera matrix	Photodiode
Limit of Detection	5pg/ mm^2	1pg/mm^2
Fluidic cell	A single fluidic cell of 1cm^2 with a height of 80μm	4 channels of each 1mm^2 with a height of 20μm
Sample injections	Manual injection to a reservoir and automatic injection to the fluidic cell from the reservoir loop	Fully automated injection system
Signal acquisition	change in reflectivity	change in plasmon angle
Type of samples	Samples in complex media, whole cells, cell supernatants, lysates, EVs	Samples suspended in a buffer and filtered with 0.22μm to avoid blockage in the fluidic cartridge
Price	~120k€	~200k€

Table 2 Comparison of performance indicators of the different SPR systems available in the laboratory.

4.6.2 Atomic Force Microscopy (AFM)

The AFM was invented in the IBM research laboratory.[172] The inventors Gerd Binnig and Heinrich Rohrer shared the Nobel Prize in Physics in the year 1986 for the invention. With the inception of AFM, it was possible to resolve the structures into an atomic resolution which was previously limited to only conducting surfaces by scanning tunneling microscope[173] which was also developed by G. Binnig and H. Rohrer in the previous years.

The AFM is an imaging technique that reconstructs the topography of a surface by tracing the deflection of a sharp cantilever caused by atomic repulsion that arises from the tip and surface by scanning different form measurable forces such as electrical, magnetic, thermal, the scanning force microscopy can provide information of different forces across a spatial surface. The collective use of the technique is known as scanning probe microscopy.[174] Apart from the topographic imaging of biological objects, the AFM is also used to study the molecular mapping of biological objects[175], as well as nanoscale manipulation of objects in an emerging field known as nanorobotics.[176,177]

4.6.2.1 Operating principle of AFM

AFM is driven by natural interatomic forces. Different forces are dominant to the distance between the atoms in the cantilever tip and the surface. At a large distance, the interaction between the tip and the surface is essentially null. As the tip approaches the surface, at closer distances, the interaction is governed by two kinds of forces. The attractive force arises because of oppositely charged subatomic particles. The negatively charged electron cloud of the tip is attracted by the positively charged nucleus of the surface and vice versa. This attractive force balances each other when the distance is brought closer. At further close distances, starting from Van der Waals contact distance, the electrons start to repel each other. This repulsive force causes the tip to be deflected. By measuring the deflection of a probe across a surface, the profile of the surface is then reconstructed up to atomic resolution.

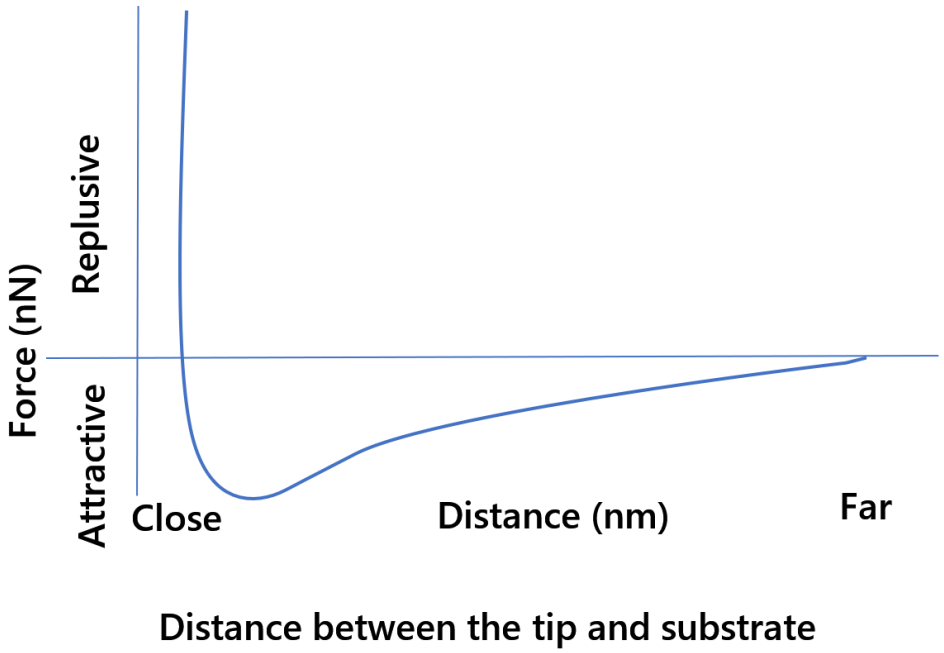

Figure 19 Force-distance curve of two atoms. As the distance between the tip and the surface is closer, the mutual attraction causes the tip to deflect towards the surface. At certain point, the electron repulsion causes the tip to push back the tip.

4.6.2.2 Components of an AFM

In its simplest configuration, the AFM system is essentially constructed with the cantilever probe to scan the surface, a deflection recognition system, a piezo controller driven by the feedback from the deflection signal.

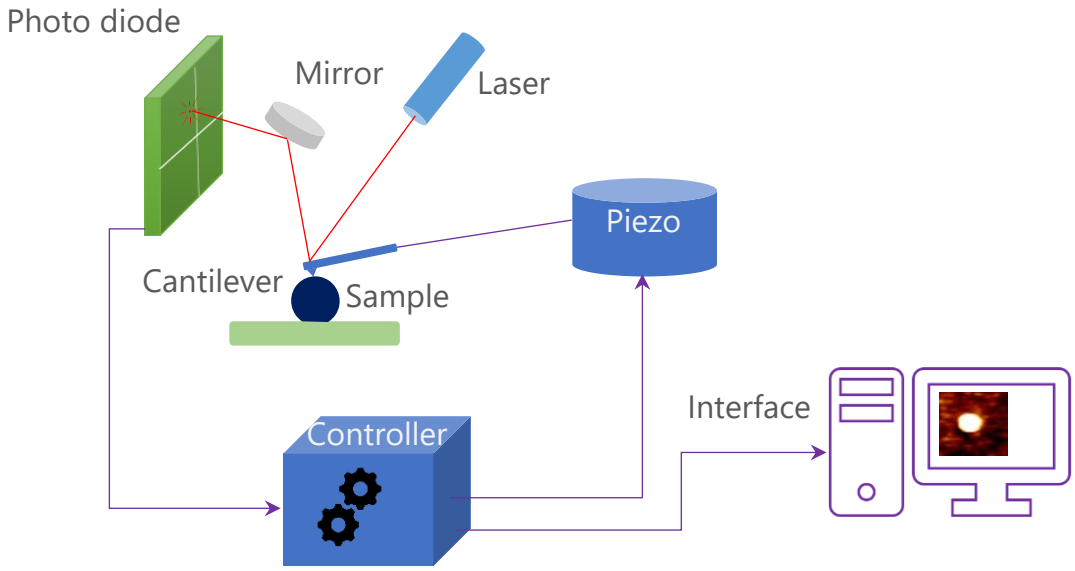

Figure 20 Schematic of an AFM. The piezo drive is used to displace the scanning head up or down to keep the force / distance between the tip and sample constant.

The AFM works in different modes such as contact, non-contact, and tapping modes. In contact mode, the topography is generated by detecting the deflection of the tip of the cantilever. A laser is positioned on the reflective surface of the tip and the reflected light is detected in a four-quadrant photodiode and the position of the laser spot in the photodiode is used to trace the topography of the surface being scanned.

In the non-contact mode of operation, the cantilever tip is not brought close to the surface it is kept at a distance where the atomic interaction between the tip and the surface does not cause deflection of the tip, but it influences the resonant frequency of the cantilever. By adjusting the height of the piezo to achieve a set frequency value, the topography of the image is generated. This mode is particularly useful for sticky samples.

In tapping mode, the cantilever tip oscillates at a frequency close to its resonant frequency and when the tip is interacting with the surface, the Van der Waals force and electrostatic forces cause the amplitude of the cantilever tip to change. To compensate for this change, the piezo drive the scanning head on the z-axis. Thus, a distribution of z values across an x, y coordinates produce the structure of the surface being scanned.

In this project, the AFM scans were imaged using a Bruker-JPK NanoWizard® 3 Bioscience AFM. The AFM system was comprised of the following parts.

- A scanning head with a modular ceramic block to hold the cantilever.
- A stage to hold the sample as well as the scanning head. Both sample and scanning head are maneuverable in x and y-direction.
- A top view optical microscope for locating the cantilever tip. The laser spot can also be seen in the camera of the microscope.
- An active vibration isolation table upon which stage is placed.
- A controller to regulate the scanning operation and to communicate with the user interface.
- A software interface to control and record the scanning and to process the image.

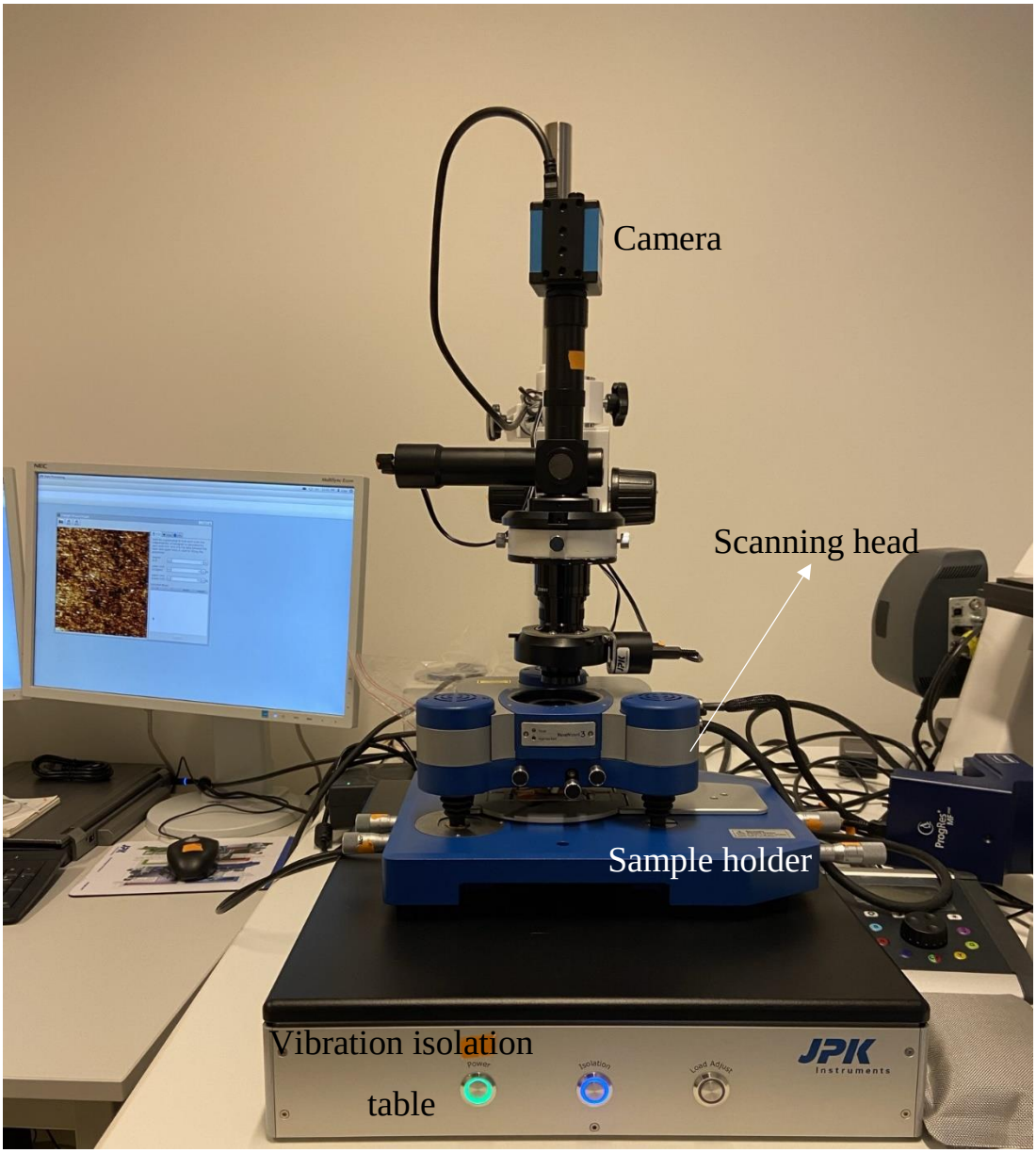

Figure 21 Photograph of JPK NanoWizard III AFM. Vibration isolation table, stage, scanning head and top view optics are seen.

4.6.2.3 Scanning head

The scanning head is equipped with 3 stepping motors and can be controlled independently. In its center, there is a holder mechanism to clutch the ceramic block which is fixed with the cantilever. The scanning head also features knobs to navigate the laser to the tip of the cantilever.

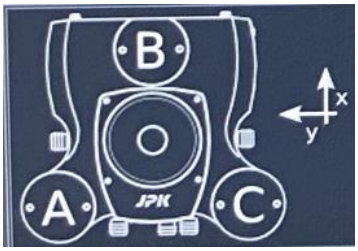

Figure 22 Schema of a scanning head. A, B C are stepper motors. Knobs for laser positioning is also present.

An additional knob is used to adjust the mirror so that the reflected laser light is projected to the photodiode as well as a separate set of knobs to position the laser to the center of the photodiode.

The cantilever is mounted on a ceramic block with a flat spring holder which can be tightened with the adjusting screw.

4.6.2.4 Stage

The stage has 3 supporting points to rest the stepping motors A, B and C and is movable in 2 directions. The movement in the z-axis is controlled by the stepping motor and piezo. The stage also has a flat spring-loaded sample holder. The sample stage is also independently movable. The stage is movable with a screw mechanism like that of a micrometer. The distance of the movement can be adjusted with the graduations on the sleeve and thimble of the screws.

4.6.2.5 A top view optics (Camera)

The tip and sample substrate can be seen through a JPK top view optics™. There are 3 optical light sources. The light is exposed from the bottom through the substrate and is detected on the CCD camera at the top. The focus and magnification are adjustable with the two separate adjusting wheels. Two auxiliary LED light sources are provided above the scanning head and are inverted so that they face the ceramic holder. The intensity of the light is adjustable and the

exposure time, shutter speed of the camera is controllable with the integrated software module in the JPK SPM controller.

4.6.2.6 Active vibration isolation table

An active vibration isolation table is essential to mask the noise caused by the vibrations in the environment. The table provides a suspension by acting as a damper.

4.6.2.7 Control and image processing

JPK SPM software is used to control the scanning operation. The software features a control panel to set the feedback control parameters such as Setpoint voltage, Proportional gain, and integral gain. The setpoint value signifies the level of force applied to the cantilever tip. The difference between the set values and the actual deflection measurement is known as error signal and the limits defined by p-gain and i-gain are used to stabilize, improve the signal/noise ratio of the measurement. Scanning parameters such as scan size, resolution, and scan speed can be defined. It is also possible to displace the scanning head within a limited window. The image window has several tools to interrogate the image such as measuring the distance between the objects, finding the cross-section of a feature, and zoom control. A dedicated software system is available for image processing and is discussed in section 4.10.3. The parameters of movement such as the rate of tip approach, are also controllable in the panel. The laser position, photodetector signal, deflection in the x and y direction can be monitored in the dedicated tab. There is a separate tab for the optical microscope image.

4.7 Experimental design: Adapting the NBA platform for studying nPEVs

4.7.1 Schema of ligands grafting

The biochip was prepared in 4 by 4 multiplexed format. Two different concentrations of a-CD41 antibody at 200 µg/mL and 100 µg/mL were used with the corresponding negative control with irrelevant IgG grafted at the same concentrations.

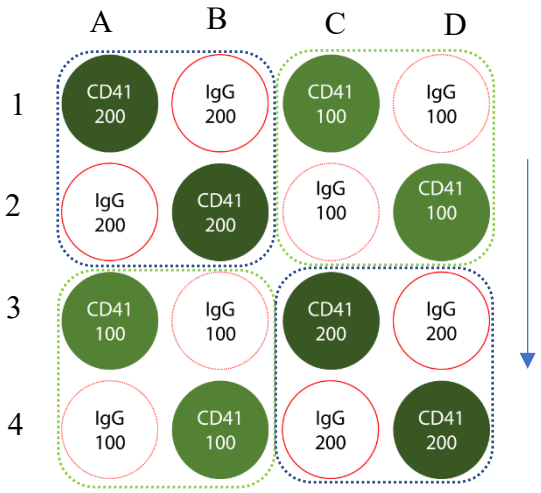

Figure 23: Scheme of the ligands grafting in an SPRi biochip. The number inside the spots indicates the concentration of the ligands grafted. The arrow shows the direction of the flow inside the fluidic cell. The repeating pattern of antibody and negative control (motif) is classified in the dotted line.

The biochip is designed by repeating a motif of four spots. It consists of duplicates of a-CD41 spots and IgG negative controls. For each concentration of ligands, two motifs are placed diagonally of each other to have homogeneous interaction across the surface.

For identification, the rows are named numerically, and columns are named alphabetically. A particular spot of a ligand is identified with an alphanumeric indicator such as the top-left spot of a-CD41 200 antibody spot is described as A1 and so on. We decided to associate a negative control within the vicinity of an a-CD41 spot is necessary to measure the noise in the surrounding. This also helps in estimating more precise variations of the control conditions at different places on the biochip. This procedure aims to avoid possible variations due to heterogeneity in the surface chemistry, variation in the ligand grafting, flow conditions inside the fluidic chamber, etc. This will also be used to determine the amount of specific capture that is occurring in the a-CD41 spot alone.

4.7.2 Biochip Preparation

4.7.2.1 Manufacturing of the biochip

The biochip is operated by FEMTO Engineering based on the facilities of the MIMENTO technology platform. For SPRi experiments, the biochip has a length of 28mm, a width of 12.5mm, and a thickness of 0.5mm. The biochip is realized in two steps. The fabrication step involves depositing a thin layer of metal film on the glass substrate.

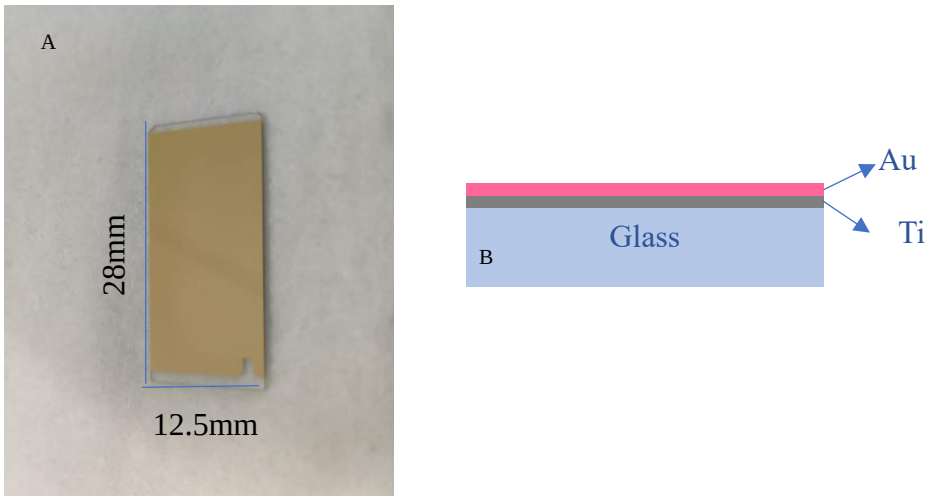

Figure 24 A) Image of a functionalized SPRi Biochip. The mark on the bottom -right is used to identify the face (gold coated) and back (glass) of the biochip. B) Schema of the biochip with different metal layers

The biochip is fabricated by electron beam evaporation. It is a thin film deposition technique that works on the principle of the Physical Vapor Deposition (PVD) process. The deposition is carried out in a vacuum evaporation machine EVA450, made by alliance concept, France. The deposition machine contains an electron source, a crucible to place the metal source, a sample holder, and a quartz crystal microbalance (QCM) to monitor the thickness of the coating. Under high vacuum conditions, an intense electron beam directed at the metal source causes it to evaporate and adsorb on the surface of the glass slides mounted on the holder at the top. For homogenous deposition, the glass-slide holder is rotated so that the deposition layer is uniformly covered.

Initially, 2 nm of titanium is deposited as an adhesion layer, and over that, about 48nm of gold of purity 99.99% is deposited. The method of fabrication is described elsewhere.[178] A small portion

is masked out on the bottom right side of the face of the biochip to identify the face and back of the biochip. After the fabrication process, the biochip is stored in a container and sealed in an aluminum pouch until use.

4.7.2.2 Functionalizing the biochip

The biochip was functionalized with a self-assembled monolayer of organic molecules containing sulfur head groups and a terminal group composed of alcohol or carboxylic acid. The molecular self-assembly is formed by the chemisorption of the sulfhydryl group on the gold surface. A mixture of HS-$(CH_2)_{16}$-COOH and HS-$(CH_2)_{11}$-OH (10%/90% mol/mol) is sonicated and the gold surface is immersed in this solution overnight. Then the biochip is washed with ethanol and ultra-pure water and dried. The process is described in the paper by Remy-Martin F et al.[156]

The resulting monolayer cushion is stable because of the strong chemical bond created by S-R and gold.

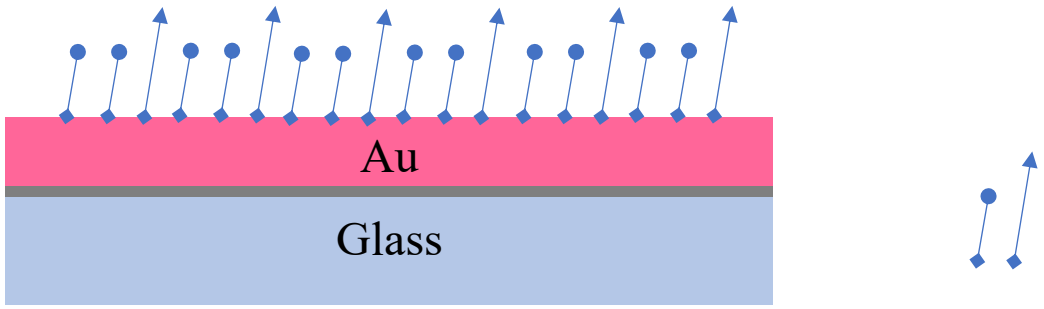

Figure 25 Formation of molecular self-assembly of alkyl chains with Sulfhydryl groups on the gold surface. Two different types of molecules with different length and terminal groups are used. C11-OH (round terminal) and C16-COOH (arrow terminal)

4.7.2.3 Mechanism of ligands immobilization on the biochip

The antibodies were immobilized covalently onto the biochip through the amine coupling reaction. The reaction yields amide bonding of the antibody with the carboxylic group in the self-assembled monolayer (SAM). The reaction mechanism is described below.

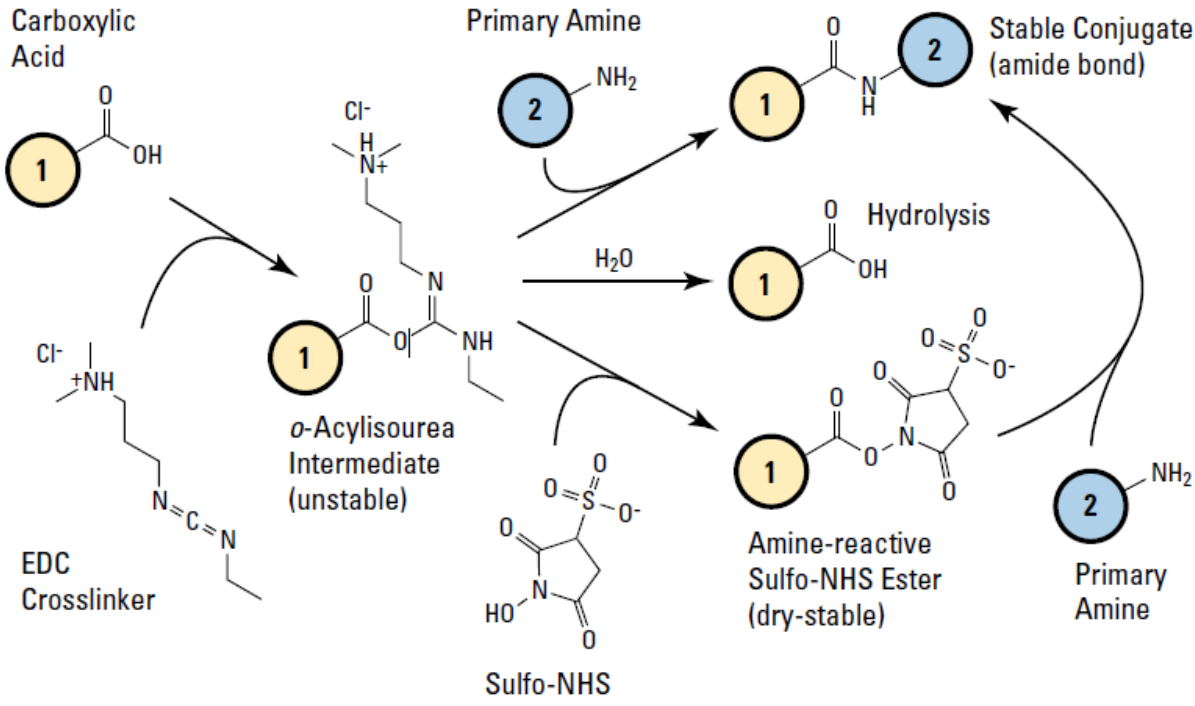

Figure 26 Description of the amine -carboxylic chemical bonding. Picture ref. Thermo Fischer handbook

The process begins with the activation of carboxylic moieties in the SAM of alkanethiols on the biochip by EDC (1-ethyl-3-(3-dimethyl aminopropyl) carbodiimide hydrochloride). The Nitrogen in the carbodiimide is basic and has lone pair of electrons that leads to reacting with the proton in the carboxylic acid and it creates carboxylate ions. The nucleophilic carboxylate ions then react with the carbon in the carbodiimide resulting in the electron transfer to the positively charged nitrogen (by breaking the carbon-carbon double bond to a single bond). This intermediate product is unstable and active. The primary amine which has lone pair of electrons reacts with the electrophilic carbon and thus antibody is bound with the carboxyl resulting in the dissociation of the urea derivative. The addition of sulfo-NHS (n-Hydroxysulfosuccinimide) forms an efficient grafting by forming carboxylic-NHS esters which are stable as well as reactive to the primary amines in the antibodies.

4.7.2.4 Determining the best pH for grafting the antibodies

The best pH for grafting was determined in a pre-concentration experiment done in SPR-Biacore with varying pH. The antibodies were prepared at a concentration of 20 µg/mL in an acetate buffer of pH 4.0 to 6.0. It was established in the pre-concentration experiment that the best pH for grafting a-CD41 is 4.0 and IgG negative control is 6.0. A similar experiment for another ligand (a-CD61) was performed in another project and will be discussed in the next chapter.

4.7.2.5 Grafting the ligands on the biochip

The biochip was activated using a 1:1 (v/v) mixture of sulfo-NHS (100mM) and EDC (400mM) for about 30 minutes inside a black box to avoid disturbance due to the UV light exposure. The biochip was then washed and dried and the spotting of the ligands as per the schema is performed in a manual spotter.

The spotting device was designed and developed by F. Remy-Martin [178] which has a compartment for storing the biochip which is held by a pair of flat springs. The cover of the spotter has been drilled with micropores of 550 ± 2 µm. The 2 µL micropipette was used to spot the ligands in a specific format. 300nL of the antibodies were deposited in non-contact mode on the surface of the activated biochip by placing the tip in proximity so that the droplet was deposited on the sensor chip. On either side of the spotter, there was a chamber to place small wet tissue to maintain the humidity and avoid the evaporation of the droplets during the subsequent ultrasonic step.

Once the ligands on all the 16 spots were spotted, the micropore on the top of the spotter was sealed and the spotter treated in an ultrasonic bath at a frequency of 37 kHz and 30% power setting, and the water in the ultrasonic bath was connected to a cooler to offset the heat generated by acoustic vibration. The ultrasonic treatment resulted in homogenous grafting of the ligands as seen in the image below.

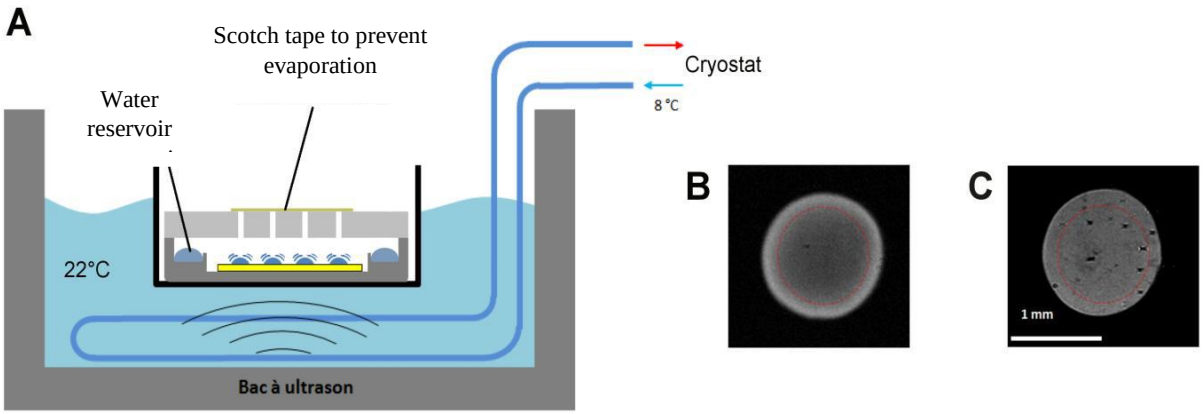

Figure 27 A) Ultrasonic treatment of the grafted biochip. The incubation was performed at ambient temperature. B) The effect of and absence of the ultrasonic treatment results in non-homogenous grafting of the ligand as seen in the difference image that dense grafting of the antibodies on the periphery of the spots than in the center. C) Spots with ultrasonic treatment and more homogenous grafting. (Results of F.R. Martin)[178]

After the grafting and ultrasonic treatment, the biochip was cleaned by flushing ultra-pure water rapidly so that the antibody spreading was minimized. A thin layer of water was left on the biochip to avoid biochip drying. The biochip was replaced on a prism with a thin layer of oil which had the same RI as the prism. This was necessary to act as an optimal optical path to the chip on the prism. It was now possible to observe the spots in the difference image window of the apparatus. (Figure 28)

4.8 SPRi experiments

4.8.1 Measurement parameters

Once the biochip was mounted on the SPRi plex, there were certain important settings to be chosen. The Region of Interest (ROIs) for each spot was defined. A circular ROI with a diameter of 800 µm was chosen for the assay and negative control spots. Together with these spots, a few ROIs in the areas where there was no antibody grafted were also chosen. These are called “surface spots” and they were chosen with a diameter of 500µm. The function of the surface spot was to monitor the level of grafting of Rat Serum Albumin (RSA) in the passivation step. Albumin is one of the blocking agents that is widely used to block the surface to avoid non-specific reactions in bioassays. RSA was used because of its conveniences, and it is used in various applications. Finally, the passivation step consisted of the injection of ethanolamine to avoid non-specific adsorption of the sample and to deactivate the surface.

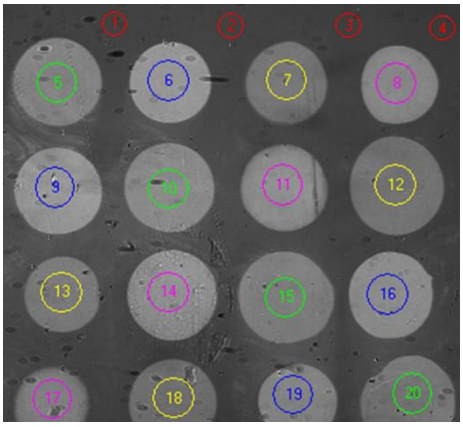

Figure 28 Difference image of the biochip after grafting the ligands. The ligands are grafted as per the scheme from Figure 23. The ROIs are labeled numerically. ROIs of red circles are of 500µm size and those at the ligand spots are of 800µm diameter.

Once the ROIs were defined, plasmon acquisition was performed by registering reflectivity between 53.5 degrees to 63.5 degrees. In total, 100 acquisitions (also known as graduations) of reflectivity were performed between the above-mentioned angles. The function of reflectivity with the angle is known as plasmon curves and the plasmon angle is characterized by the least reflectivity value as the light energy is transformed as an evanescent wave at plasmon angle. The sensitivity plot was constructed by calculating the change % of reflectivity per graduation in the plasmon angle compared to the previous graduation. The high sensitivity means, at a particular angle, that the reflectivity change is greater for a given amount of interaction compared to any graduation in the plasmon slope. The plasmon sensitivity graph was available for each ROI. The angle at which the highest sensitivity for the ROI of interest of the study was usually chosen as the working angle.

The selection of working angle was made where it had the highest sensitivity for surface ROIs in the passivation step. As the apparatus allowed only one working angle, the selection was done according to the function of the experimental design. At each important step of the experimental part, it was possible to restart a plasmonic acquisition to enable the choice of the best working angle appropriate to the objective of the investigation.

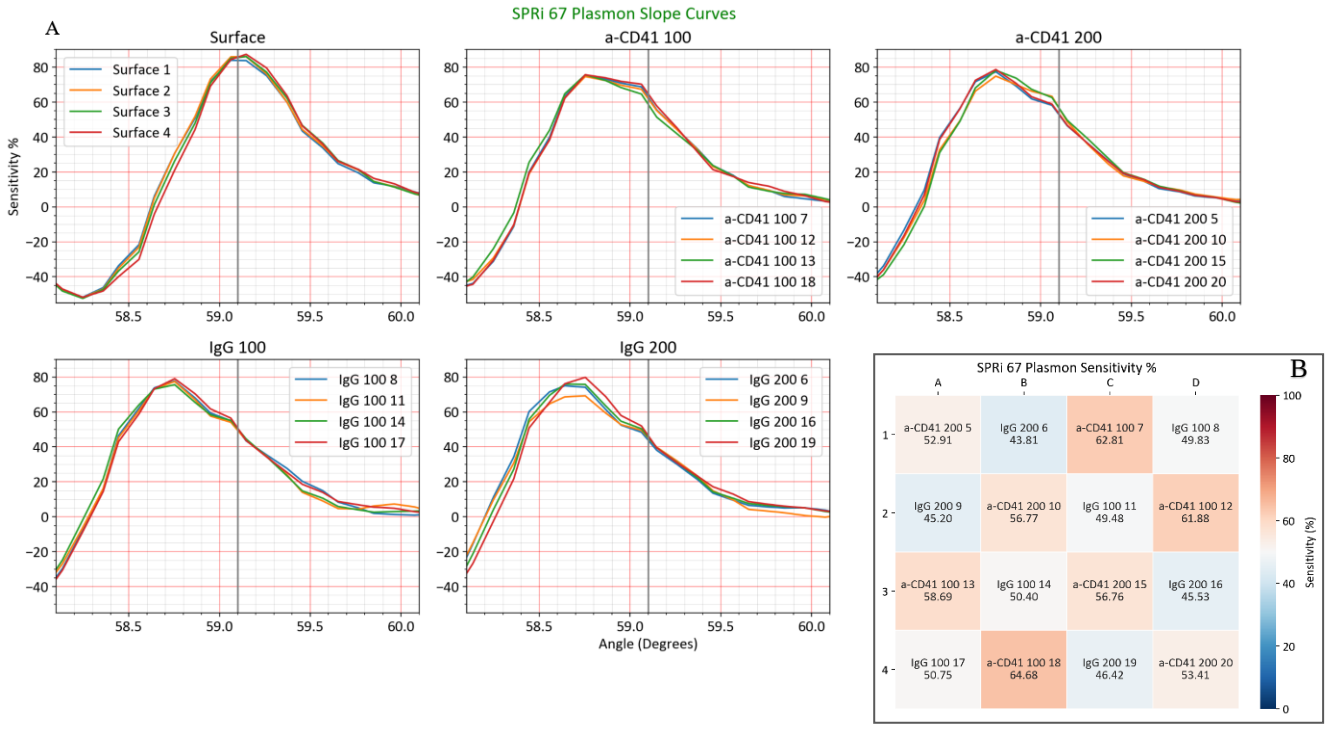

Figure 29 A) Plasmon slope curves of different ROIs mentioned in Figure 28. In this matrix plot, the ROIs are grouped as family to visualize the homogeneity of the grafting between ligands. The chosen working angle is denoted as a gray vertical line. B) a heat map is also shown to describe the sensitivity of ligands across the biochip. The ROI number is mentioned both in the legend as well as in the heat map labels.

4.8.2 Passivation of the biochip

Blocking the biochip by a passivation method is necessary to avoid non-specific adsorption of the EVs on the biochip. This step involved adsorbing the biochip with RSA then ethanolamine. The RSA blocks the surface by binding on the active COOH esters and the ethanolamine, in large excess, deactivates the free ester groups. This step began by injecting 40mM of octyl glucoside (OG) in PBS buffer for 3 minutes at a flow rate of 20 µL/min. After this cleaning step, injection of RSA at a concentration of 200 µg/mL at pH 4.5 was performed for 10 minutes at 20 µL/min. The RSA injection was followed by an injection of OG 40 mM in PBS and a second RSA injection. The passivation step was completed by injecting ethanolamine 1M at pH 8.0 at 20 µL/min for 10 minutes for passivating the surface and deactivate the surface.[155] At the end of the passivation step, the net change in the SPRi signal was calculated as the difference between the starting baseline and the baseline after ethanolamine injection.

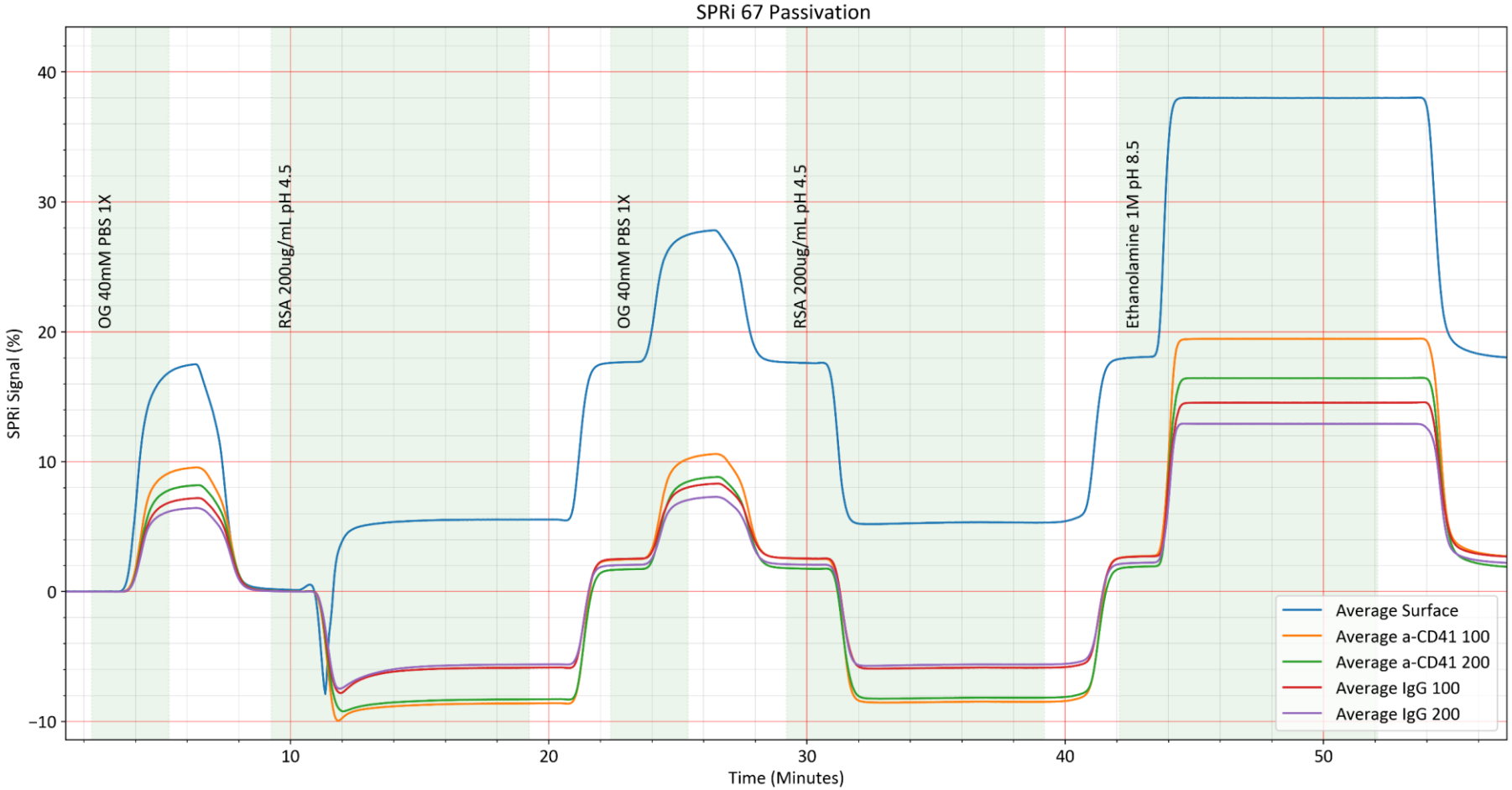

Figure 30 Sensorgram of passivation step. This chart shows the average of each family. Duration of each injection starting, and ending is highlighted by green color. As seen in the sensorgram, the RSA had bound mostly on the surface. The RSA grafting was low where ligands are grafted.

The net change in the reflectivity was calculated using the formula (ΔR%),

$$DR\ \% = Final\ signal\ \% - Start\ signal\ \%$$

With $DR\ \%$, it was possible to estimate the quantity of material adsorbed on the surface using the derivation established by Remy-Martin et al.[178] For the efficient grafting of RSA, based on internal observations, the expected grafting of RSA in the range of 24-28 fmol/mm^2.

The signal in the ligand, as well as the negative control spots, were also examined and expected to be minimum. The more amount of RSA in a ligand spot mean that there were not a lot of antibodies present in the spot. A maximum of 4% signal difference was considered to represent a good grafting quality. This would translate to around 6fmole/mm^2. Any values more than this in the ligand spots were discarded.

4.8.3 Injection of analyte and specific capture of EVs on the biochip

After the passivation and deactivation of the surface, the biochip was ready for Bio-molecular Interaction Assay (BIA) of the EVs. The plasmon acquisition was repeated for the second time as now the kinetic monitoring had to be focused on the a-CD41 spots. This was done by choosing the working angle providing the maximum sensitivity for a-CD41 spots.

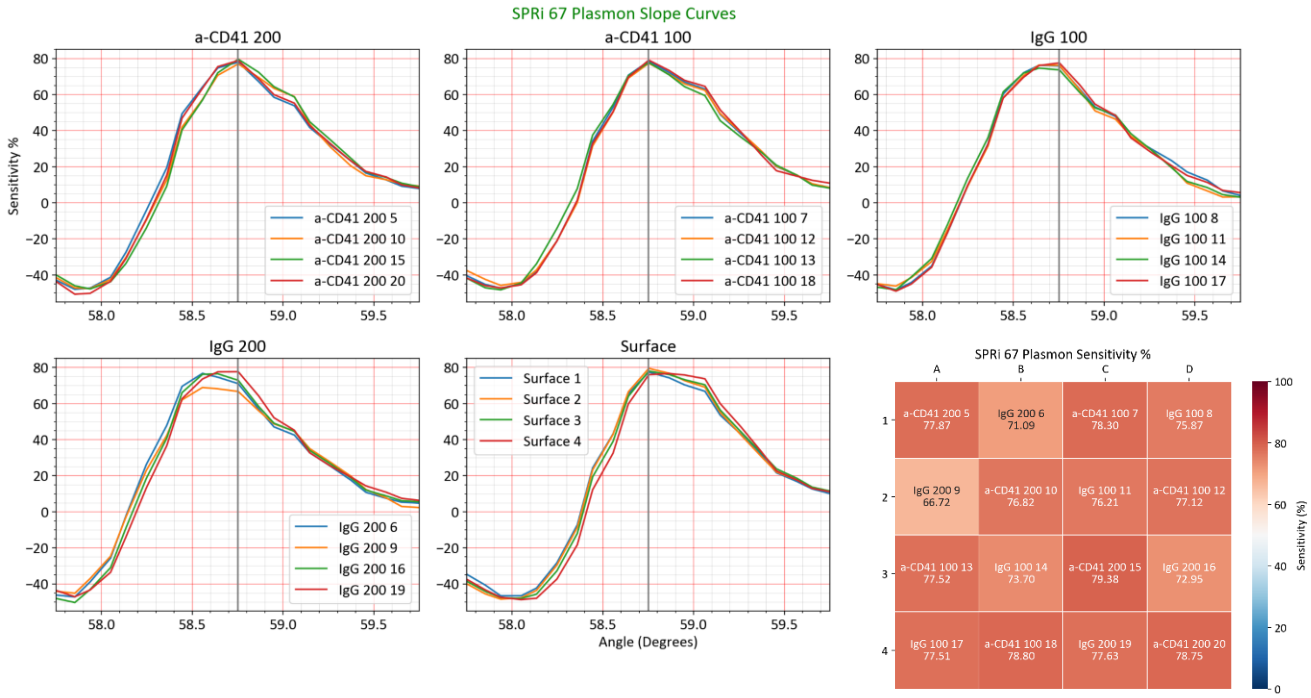

Figure 31 Plasmon slope curves after passivation of the biochip. Working angle is chosen to have maximum sensitivity for the assay spots. As seen in the heat map on the bottom right side at the chosen working angle, the sensitivity is quite homogenous between a-CD41 spots as well as IgG negative control.

After choosing the proper working angle in the second step, the nPEV was diluted in PBS. The raw concentration was obtained from TRPS results. Afterward, the serial dilution method was adopted in all experiments to achieve the target concentration. Series of dilutions of 100x was made and the final dilution factor was determined based on the target concentration of a particular experiment. For example, if a 1000x dilution was needed, the first solution was made with 100x, and the final dilution was made with 10x of the first solution. The dilution of EVs was performed in the same running buffer to avoid the difference in refractive index (RI). The injection was carried out for 9 minutes at a flow rate of 20 µL/min. After the end of the injection, the system was left for several minutes to observe the dissociation phase and estimate the response without any disturbance due to the samples.

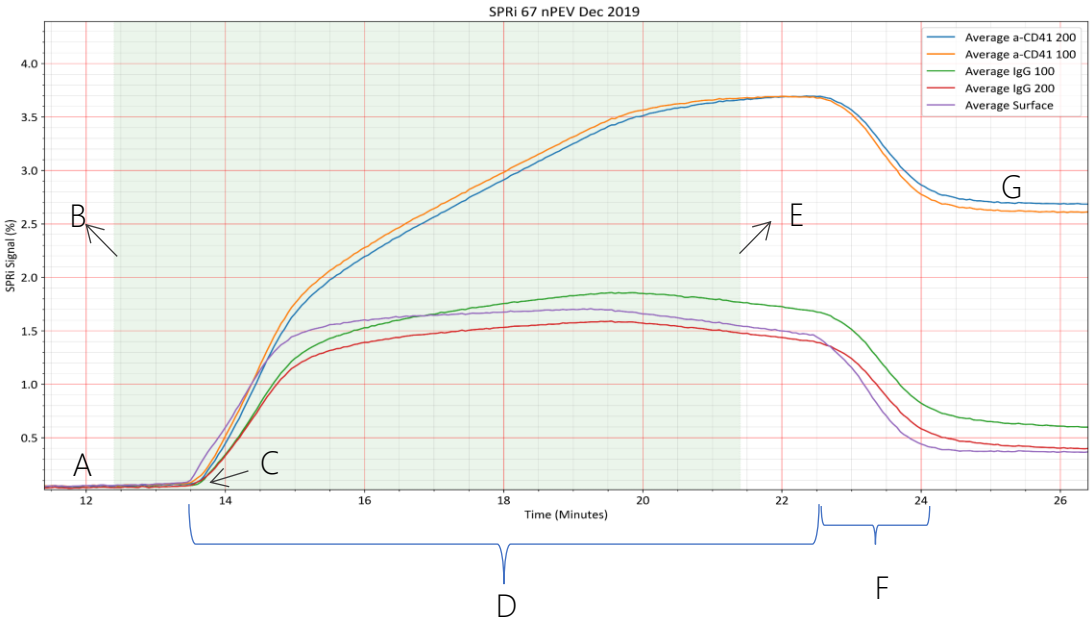

Figure 32 Sensorgram of nPEVs injection. The average signal of each ligand family is plotted in function of time. The duration between injection starting and ending is highlighted in green. Different elements of the sensorgram are explained below

A) Base line of the sensorgram. B) Start of the injection, switching of the valve to injection position thereby allowing the nPEVs in the loop to the flow circuit. C) The nPEV enters into the fluidic chamber and binding with the antibodies on the biochip. D) Association phase of the kinetic interaction. E) end of injection, the valve switches to the loading position. F) The running buffer arrives at the fluidic chamber. The contrast of RI between nPEV and running buffer results in a progressive dip in the sensorgram This can be attributed to either the contrast of the RI or

dissociation of the captured EVs. In the above sensorgram it is due to the difference in RI of the running buffer and the sample. G. New baseline after nPEV capture. The stability of the new baseline indicates the EVs are captured in the ligand spots as a result of avidity.

Finally, 0.5% glutaraldehyde in water was injected to fix the interacting materials with the biochip and after the end of the injection, the kinetic monitoring was stopped, and the biochip was removed and washed gently with water and then dried and stored for further studies in the AFM.

4.8.4 SPRi Data processing and validation

4.8.4.1 Matrix plot of the sensorgram

The data processing steps are performed using a custom-written python software code and multiple data visualizations are performed to validate the result. The sensorgram of the passivation step is studied for the quality of the biochip preparation. Like the plasmon plot, a family-wise matrix plot was made to qualify the grafting within and between ligand families.

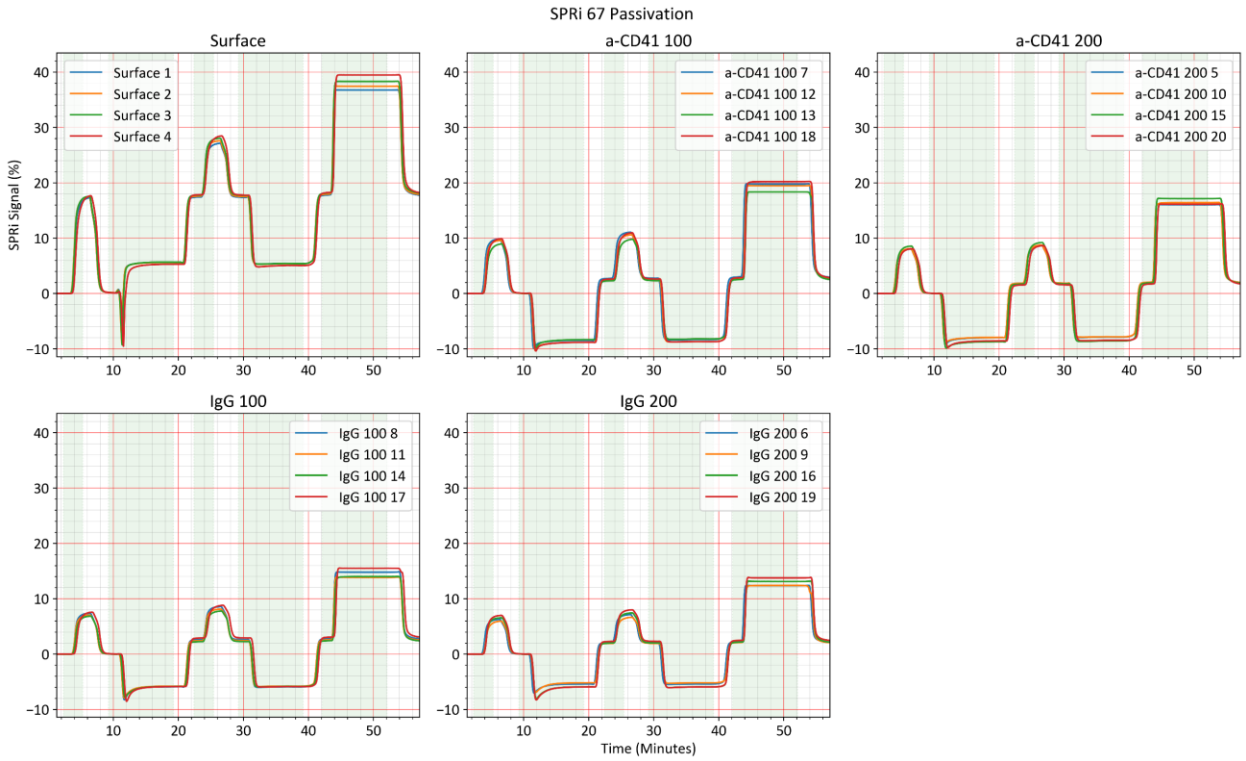

Figure 33 Matrix plot sensorgram of passivation step. Each subplot has the sensorgram of the respective family mentioned in the subtitle. The number in legends refer to the ROI (ref. Figure 28). The subplots are sorted with the level of final signal.

The matrix format of the sensorgram was useful in determining the uniformity of the ligands grafted in different spots. To appreciate the variation of interaction between ligands of the same species, it was important to ensure that the level of ligands availability was roughly the same. The low levels of ligand grafting usually resulted in high grafting of RSA. Such poor grafting would also be seen in the change in terms of usually higher plasmonic sensitivity % or close to that of the surface. Such ligands were not considered for computing the family average and estimating the EVs capture.

A similar matrix plot type sensorgram was also realized for the second part of the SPRi measurements, to visualize the level of capture in ligands compared between ligands as well as within different ROIs of the same family.

4.8.4.2 Heat map

The heat map of the response was useful to visualize the interaction across the biochip. The signal from different ROIs was plotted in a heat-density map. Heat map together with the recorded difference image at the same time (x-axis of sensorgram) of the signal acquisition (this is denoted as *t* in the following figure) was used to appreciate the capture level and the signal quantification.

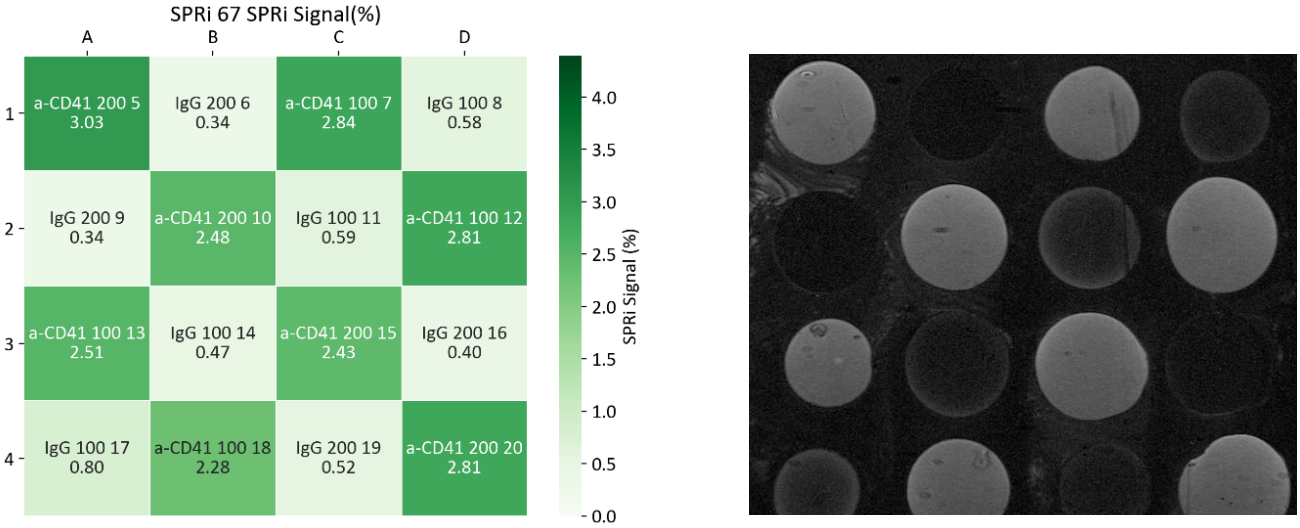

Figure 34 Heat map SPRi signal at time t=26 minutes (left). Difference image at t= 26 minutes(right).

4.8.4.3 Validating a result

The quality of measurement is critical in determining the sensitivity of the NBA platform for reproducible results as well as for accurate estimation. The replicate of the experiment was considered only if at least two of the ligands produced a positive response. Measurements for each concentration range were tested at least in triplicates and the average and standard deviation were reported in the function of increasing concentration range.

4.8.5 Negative control subtraction

4.8.5.1 Defining an injection.

The SPRi interaction signal from different biochips was aligned in such a way that the interaction starts at t=5 minutes and the 9 minutes of interaction will go on until t=14 minutes. The sensorgram was plotted until t=20 minutes.

4.8.5.2 Reference subtraction

When testing in the low concentration regime, it was very difficult to distinguish the signal captured in a-CD41 spots as well as negative control spots. One way to distinguish the interaction was to subtract the reference signal that was measured in an irrelevant spot.

As the negative control was irrelevant to CD41 protein or related proteins expressed on EVs, this was considered a good candidate for reference subtraction.

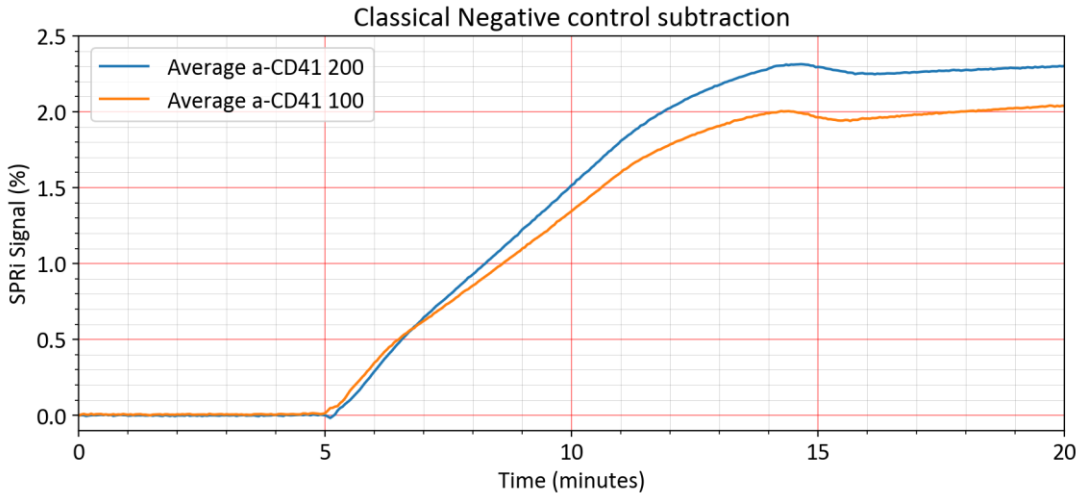

Figure 35 Negative control subtracted sensorgram of a-CD41 families. Family Average signal (of 4 ROIs) of negative control is subtracted from the family average signal (of 4 ROIs) of the assay spots for respective ligand concentrations.

The above reference subtraction method was useful in extracting the specific signal arising from the a-CD41 families, nevertheless, it was important to choose appropriate negative control for each ROIs as the signal and noise are possibly heterogeneous across the spatial dimensions of the biochip for the reasons on page 66. Thus, the reference subtraction was evolved into a more accurate method by considering the reference subtraction spot by spot (instead of few control spots randomized inside the spot pattern). Thus, each assay spot was surrounded by 2 negative controls, one in parallel and one in perpendicular. Hence, each assay spot was capable to be subtracted by both these signals. This would result in two reference-subtracted sensorgrams per spot. Such data for all the assay spots are presented in figure 36. Since the flow conditions were more uniform in the perpendicular direction than the parallel direction, the definitive signal for a given spot was considered to have the reference in the same direction as the flow of the analyte. The chosen spot for each ligand family is listed in the table below.

Ligand	Assay Spots – negative control
a-CD41 200	A1-A2, B2-B1, C3-C4, D4-D3
a-CD41 100	C1-C2, D2-D1, B4-B3, A3-A4

Table 3 List of spots for negative control subtraction for each family of ligands. Ref Fig 23 for the location of each spot.

4.8.5.3 Estimation of change in reflectivity before and after passivation

The level of RSA immobilization was estimated in terms of change in SPRi signal (ΔR%) before and after the passivation step. The ΔR% was calculated as per the following formula.

$$\mathrm{D}R\ \% = Final\ signal\ \% - Start\ signal\ \%$$

To reduce the influence of drift in the estimation of ΔR %, the start signal % was estimated as an average of all the signals of 3 minutes before a particular injection. Similarly, the final signal was computed as the average of all the signals of 3 minutes after the injection ends.

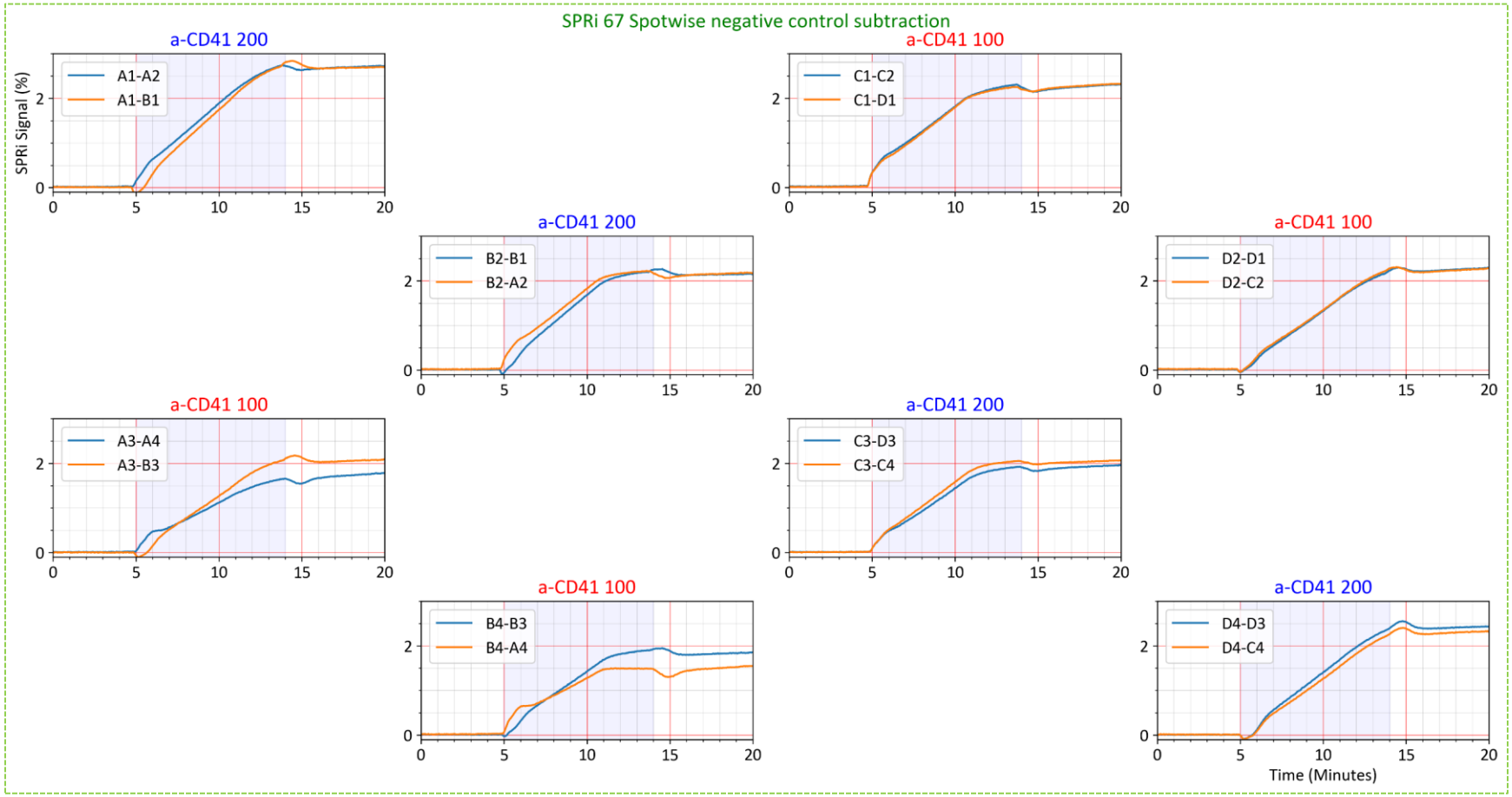

Figure 36 Reference subtraction sensorgram. Signal from negative control spot is subtracted from the nearby assay spot of same ligand concentration. The subplots are arranged in the same manner as the ligand grafting in the biochip.

4.9 Imaging EVs in AFM

4.9.1 Contact mode scanning of the biochip

All the images in AFM in this project were acquired in contact mode in air, after fixation of captured material with glutaraldehyde. To identify the location of various spots, a transparent mask was used. The tip of the biochip was aligned with the reference notch at the top of the mask and the biochip was fixed using scotch tape.

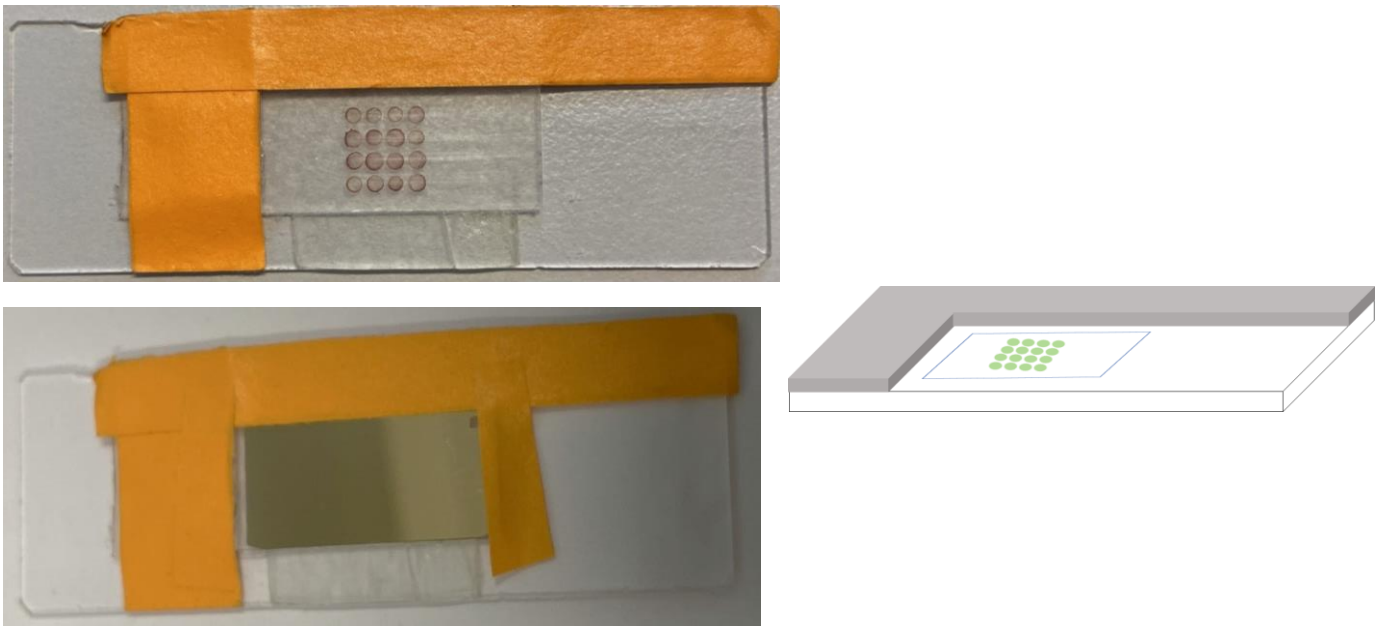

Figure 37 Photograph of a mask with marked location of a multiplex of ligands position. On the bottom, a biochip is installed over the mask. A schematic of a mask is described on the right.

The biochip with the mask was then mounted on the stage of the AFM. An upright camera was used to locate the spots as well as the cantilever tips. All the scans were performed using Pyrex-Nitride (NanoAndMore) probes. They are pyramid-type cantilever tips with 200 µm length, 28 µm width, and a spring constant of 0.08 N/m. Scans were realized with a resolution of 256px and for most of the scans, the scan area was chosen between 2.5x2.5 µm and 5x5 µm to be included for the quantification analysis. Few big scan area scans with a size of 10x10 µm with a resolution of 512px were imaged to visualize and confirm the homogeneity of the capture level in the spots. At least 40 images were acquired for each ligand families and at least 160 images for each concentration range were used to compute the size distributions as well as EVs density.

4.9.2 AFM Image treatment

The AFM image was treated in JPK Data processing software. Height channel was exclusively used in the analysis as well as grain extraction for quantification. To align the raster, a polynomial fit was subtracted from each line so that the scan lines were straightened.

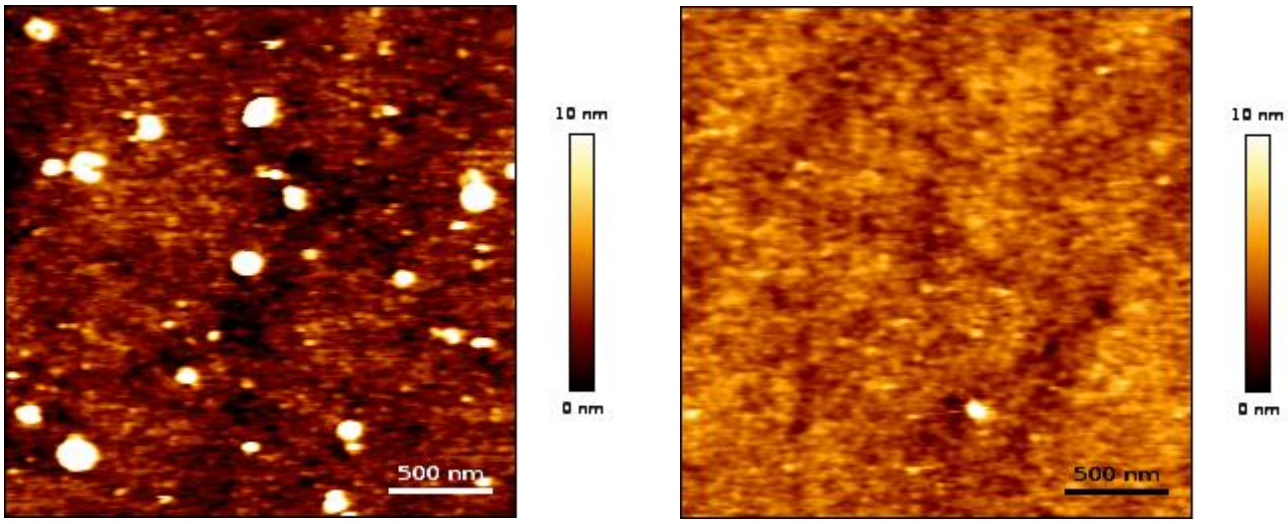

*Figure 38 A) Processed AFM image of EVs in a-CD41 200 spots. The injection was performed at a concentration of 1.52*10^9/mL. (TRPS estimation) B) Processed AFM image of nearby negative control spot (IgG 200) of the same biochip.*

4.9.2.1 Grain extraction and EVs quantification

One advantage of AFM compared to other imaging techniques is that AFM can resolve structures of nano-objects in three dimensions. The metrological analysis of particles was useful to estimate the size and areal density of EVs. Gwyddion SPM data processing and analysis software was used to extract the dimensions of the grains based on the height threshold. Different height threshold was applied for obtaining a reliable estimation of grain properties such as height, grain diameter, The extracted data was then exported and further analyzed.

4.9.3 AFM Data analysis and visualization

4.9.3.1 Metrological analysis

The configuration of the biochip allowed long-term storage and detailed studies of the EVs were possible since the EVs were fixed by glutaraldehyde. However, this contributed to extend the flattening of the captured EVs, therefore the direct measurement of the objects in the biochip may not necessarily be accurate for EVs. The tip convolution effect also contributes to the

overestimation of the size parameters.[179] For these reasons, an approach of estimating the effective diameter based on the calculation of the effective volume of the object is adopted as reported in the literature.[180] The "effective diameter" was calculated in two steps. In Gwyddion software, with the grain extraction module, the grains were marked by a height threshold value. Then several properties of the marked grains such as height, diameter were extracted. In the second step, with these values, the volume of the grains was estimated. Then an estimated "effective diameter" equivalent to a sphere of the same volume was derived. This is referred to as "effective diameter" in this manuscript. The surface density of EVs was directly computed from the number of objects and the scan area.

4.9.3.2 Quantitative analysis

Different data analysis methods were used in this project for the study of EV quantification. Descriptive statistics of the EVs size distribution were calculated for each concentration range. The distribution of metrological distribution of EVs was investigated for three different parameters namely grain diameter, effective diameter, and height.

4.9.3.3 Data visualization

Quantitative data from AFM images were visualized in a scatter plot to envisage the relationship between these measures. A heat map of the areal spread of EVs of each image was also composed to visualize the EVs chip surface coverage within and across spots. As the number of objects for each concentration range was statistically significant (more than 500), the probability density distribution was estimated and compared between each concentration range, and a comparative study was made on how the size distribution evolved between concentration ranges.

4.9.3.4 Scatter plot

The scatter plot is a type of data visualization that is used to envision quantitative data, to see the distribution of a quantifiable metric. Each object is labeled with a serial number and this identification number is plotted against the measure being studied, in this case, EVs effective diameter. It was possible to have multiple channels of the same data such as grain diameter, effective diameter, and height to see the relationship of each measure for specific EVs as they shared the same label in the x-axis.

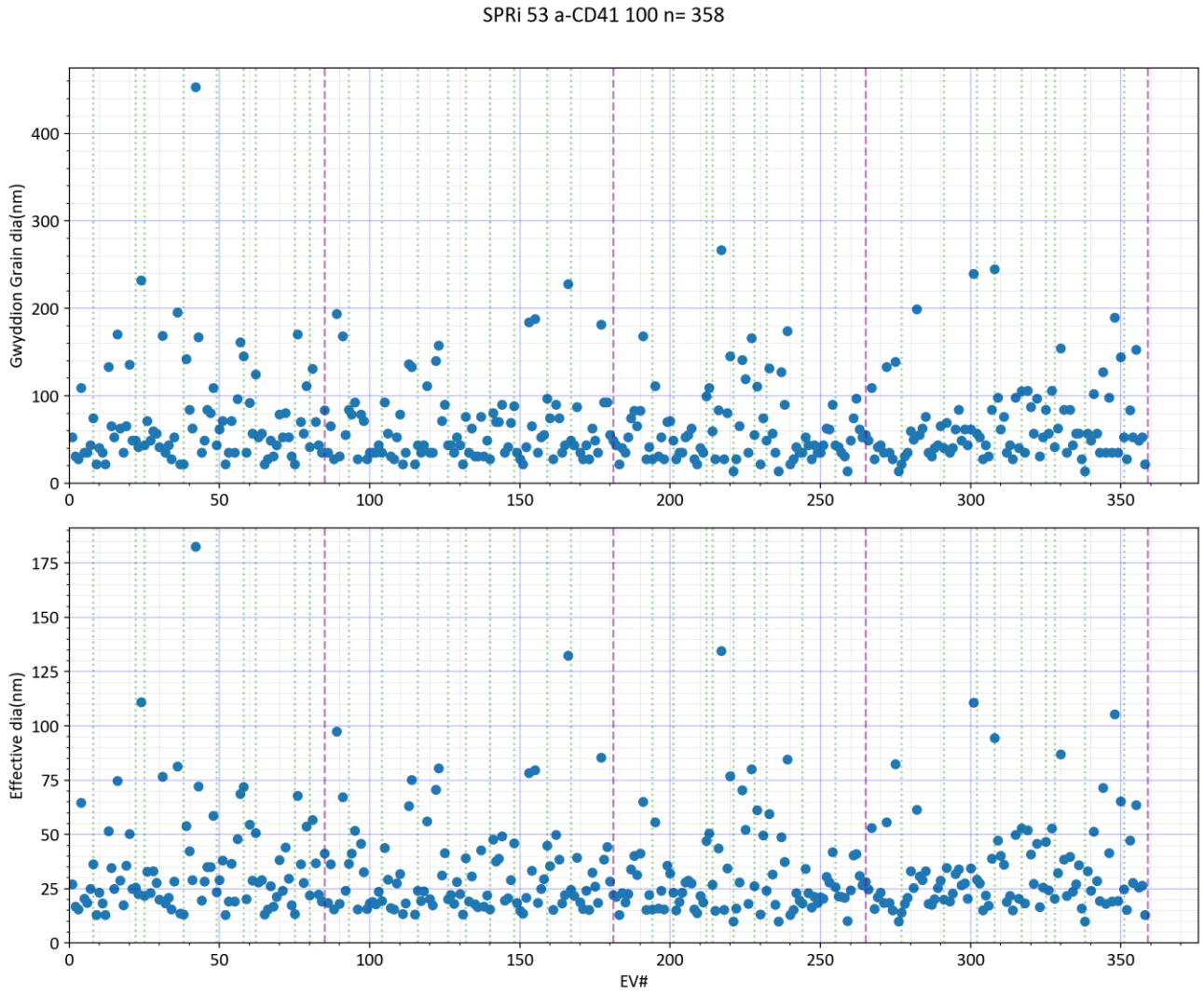

Figure 39 Scatter plot of objects in the AFM image in a-CD41 100 spots. This biochip is injected with nPEVs with a concentration range of 10^8/mL. The top scatter plot is the grain diameter extracted after filtering the background surface. On the bottom, the same grains are converted into effective diameter. Objects from each spot are enclosed between purple dashed lines. Object from each image is represented with green dotted lines. The total count of particles is mentioned in the title of the scatter plot.

As several scans were realized, the scatterplot offered a unique view of particle size distribution across several images. This was useful to visually compare the distribution of the size of objects between different images, within and between different spots and families. Since the EVs were labeled, it was possible to investigate or track up to a single particle level well as identifying clusters of the specific size range.

4.9.3.5 Heat map of EVs density

As the scatter plot describes the count of particles in an AFM image, comparisons between images and families are only visual. To measure and facilitate the comparison of the EVs captured in a specific ligand, the number of EVs per unit area was estimated by dividing the count of EVs

by the scan area of the specific image. This data was plotted in a heat map with a color gradient scale to indicate the level of EVs density. This helped to visually appreciate the EVs surface density across the biochip particularly to distinguish the specific signal from the control.

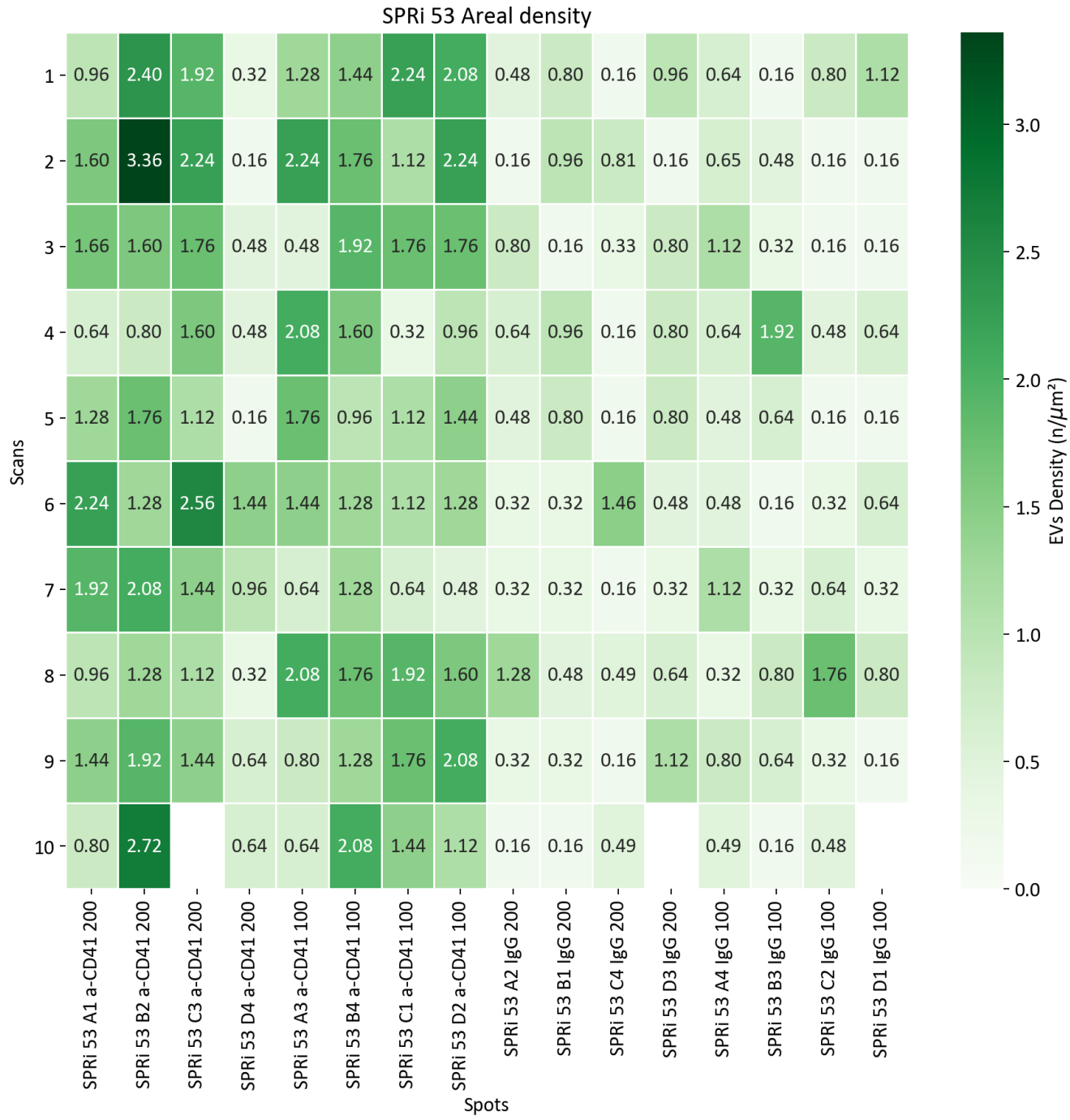

Figure 40 Heat map of EVs density in all the spots of a biochip. The number inside the cell refers to the density of EVs (n/μm) 2 in that scan.

4.10 Results: Establishing the Limit of Detection (LOD) and Dynamic Range (DR) of NBA platform for studying nPEVs

4.10.1 nPEV characterization in solution

As a first step, the nPEVs were characterized in TRPS and NTA for quantifying the concentration. The protein concentration was measured using a BCA assay.

4.10.1.1 TRPS results

The nPEV sample was tested in a qNano TRPS system with an NP200 nanopore. The measurements were calibrated with CPC200. The calibration particles were usually diluted at 1000x before measurement.

PBS 1x with Tween 20 0.02% (v/v) was used as the electrolyte as per the manufacturer's recommendation. Tween 20, which is a non-ionic surfactant helps in smooth particles flow by binding with the polar group of the phospholipids and makes them mix well in the solution. Without the use of such surface-active agents, the phospholipid vesicles are simply floating in the solution because of the hydrophobic head groups. Excessive use of surfactant could also lead them to disrupt the vesicular organization. The optimized use of a surfactant in the electrolyte for smooth measurement in TRPS for the concentration of EVs and liposomes is highlighted in the literature.[181–183]

Two batches of nPEVs were used in this study. The first batch of nPEVs was prepared in Feb - 2019 and another batch in Dec-2019.

The measurement parameters were kept identical in each measurement for comparability. The nanopore was stretched at an average of 46.65mm ± 0.29mm to achieve a baseline current between 120-140nA. RMS noise of each measurement was maintained not exceeding 15pA. The flow rate was maintained as at least 100 particles/minute. The dilution of nPEVs for TRPS measurement was kept 101x for the nPEV Feb-2019 batch and between 101x and 20x for the nPEV Dec-2019 batch. The dilution factor was adapted to have smooth as well as reliable measurement quality in the TRPS. The description of measurement parameters is reported in Annex 1. The average and standard deviation are reported here.

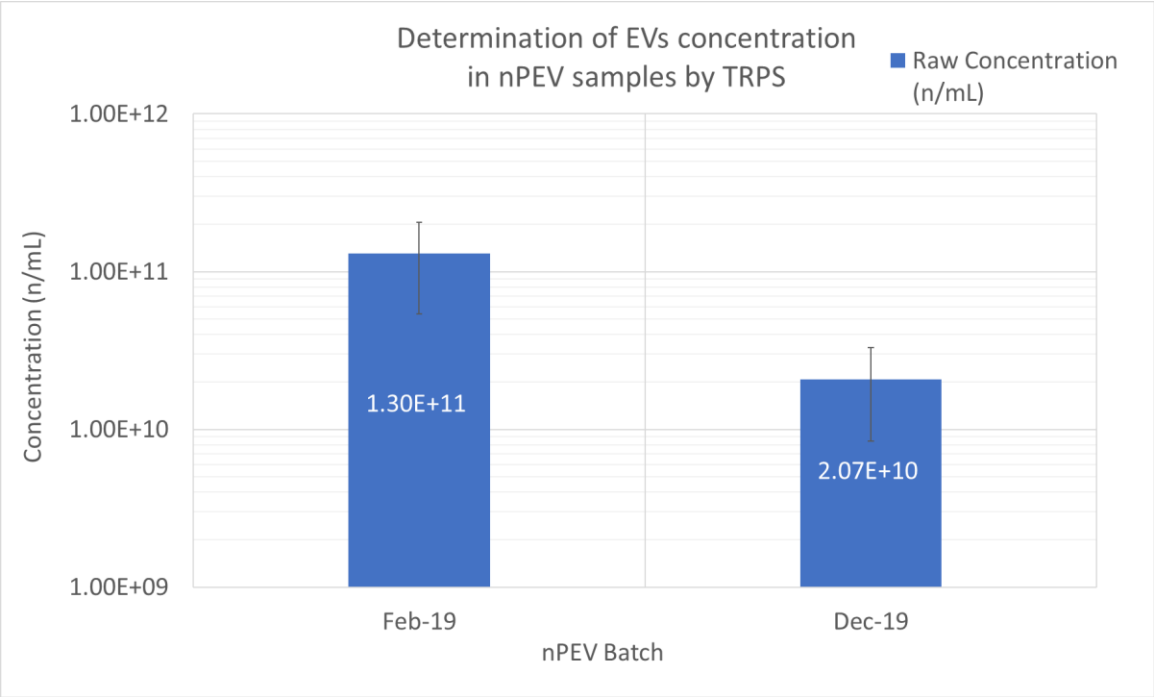

Figure 41 Average concentration of nPEVs measured in TRPS. The measured concentration is adjusted with the dilution factor used for measurement in TRPS to obtain the raw concentration. The average value is mentioned in the label of the bar chart. The error bar represents the standard deviation of the measurement in a particular batch.

From the TRPS observations, the concentration for nPEVs Feb-19 batch was found to be $1.30x10^{11}$/mL± $7.59x10^{10}$/mL and $2.07x10^{10}$±$1.23x10^{10}$/mL for Feb-19 batch. The data is reported as the average± SD from 12 measurements for Feb-19 batch and from 5 measurements for Dec-19 batch.

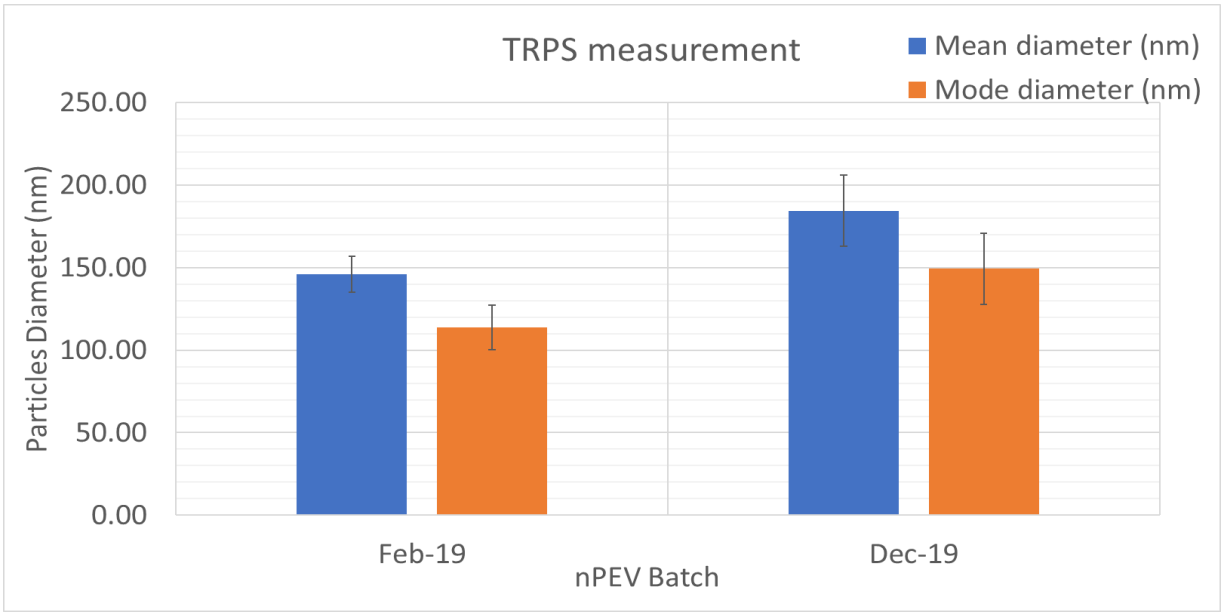

Figure 42 Size parameters of the nPEVs of different batches measured in TRPS. Error bar represents standard deviation.

The nPEVs from the Feb-19 batch had an average diameter of 145.83±10.85nm and 113.83±13.58nm for the Dec-19 batch. The mode diameter was noted to be 113.83±13.58nm for the Feb-19 batch and 149.40±21.55nm for the Dec-19 batch. The average diameter is the weighted average of all the measured objects whereas the mode diameter is the most frequently appearing size in the distribution. The data is reported as the average ± SD. The mean diameter with the increased standard deviation describes the heterogeneity of the distribution.

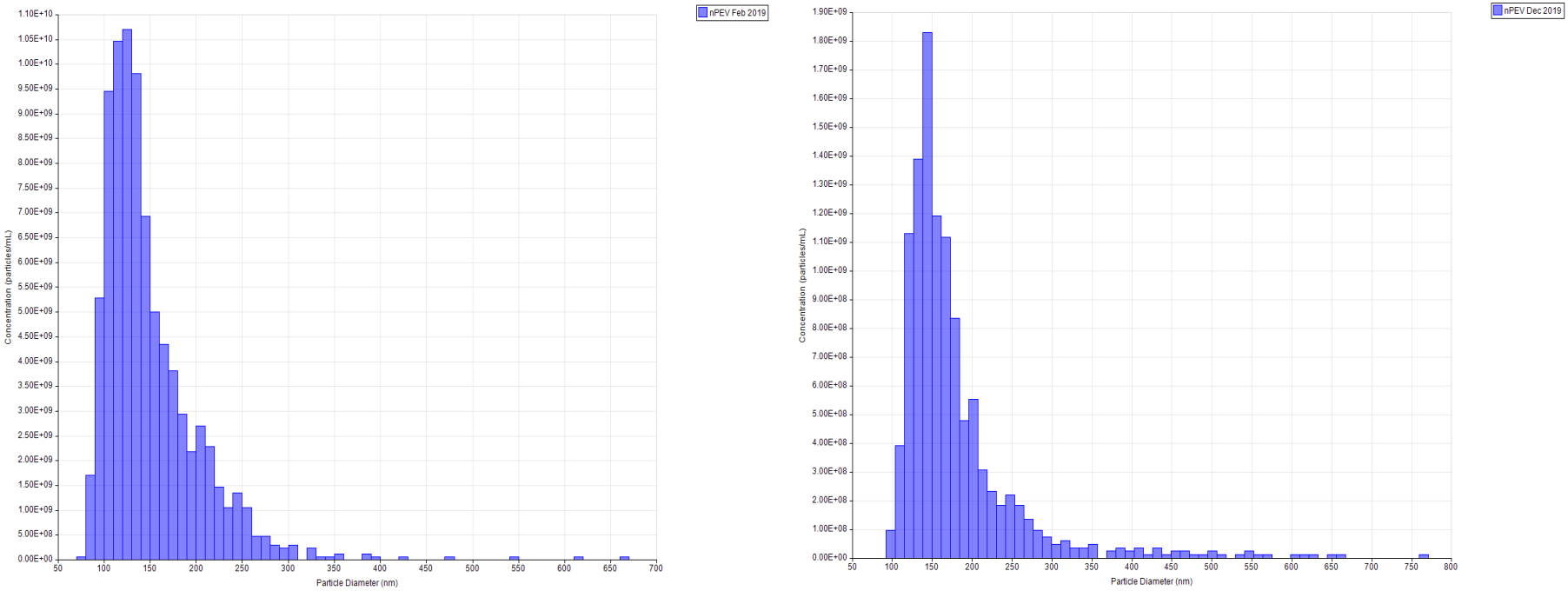

Figure 43 Histogram of particles analysis obtained in TRPS. nPEV from Feb-2019 in the left and from Dec-19 in the right side.

In summary, from the TRPS observations, it can be noted that the nPEVs from February 2019 batch is slightly more concentrated and present a smaller diameter compared to that of the December 2019 batch.

4.10.1.2 NTA Results

- As a confirmation test, EVs concentration from the Dec-2019 batch was tested in the Nanoparticle Tracking Analysis (NTA) and the results are presented here. The nPEVs were diluted 250x in PBS buffer and measurements are recorded in triplicates.

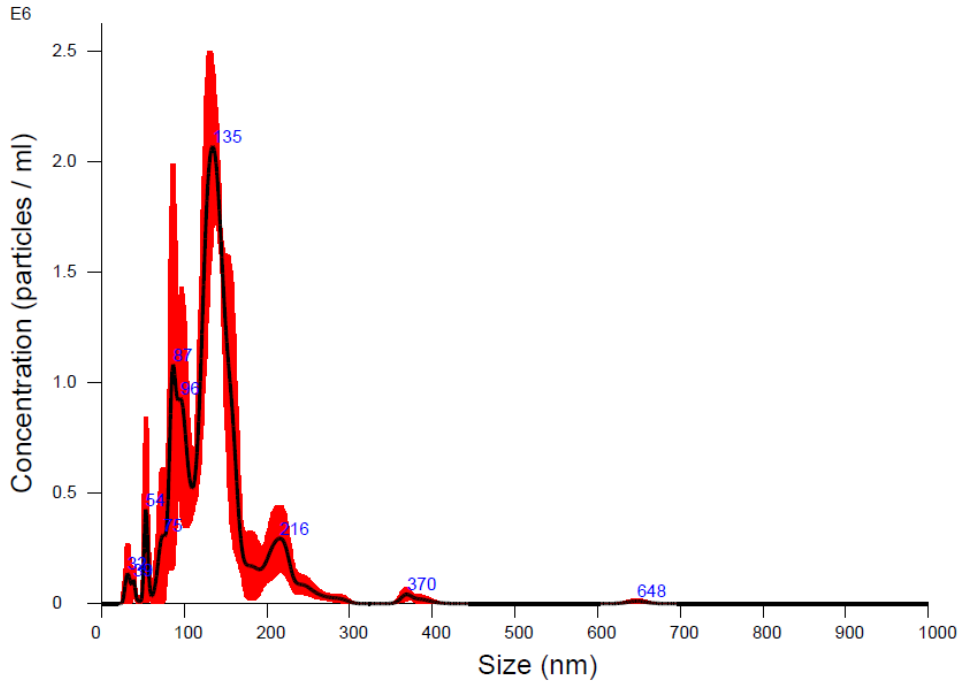

Figure 44 Particle size distribution of n-PEVs sample, obtained from NTA data; the estimation is an average of triplicates measured at a dilution of 250x.

Parameters	**NTA Results**	**TRPS results**
Adjusted average concentration with the dilution factor	$3.10x10^{10} \pm 1.40x10^{09}$/mL	$2.07x10^{10} \pm 1.23x10^{10}$/mL
Mean diameter	137.5 ± 1.3 nm	184.40 ± 21.56 nm
Mode diameter	104.9 ± 13.3 nm	149.40 ± 21.55 nm

Table 4 Comparison of concentration estimation from two techniques. nPEV from the Dec-19 batch is used in the study in both the observations.

This result confirmed the concentration range that was observed in TRPS. However, the size estimation is smaller in NTA for both the mean and mode diameters. This may be attributed to the fact that NTA is more sensitive in the smaller size regime.

4.10.2 SPRi Results

The nPEVs were tested in SPRi at least in triplicates for each nPEV concentration range. Each replicate contains 4 spots of ligands for each (ligand) concentration. Each ligand of a-CD41 species had a dedicated neighboring negative control spot (Ref Figure 23). Injections from both batches were performed for all the nPEV concentration range. A single injection of the respective concentration range is performed in each biochip. Three such biochips were prepared for each concentration range. The concentration of nPEV injection was performed by diluting the raw nPEVs to the required order of magnitude. This was done to minimize:

(i) the measurement bias caused by the TRPS since the sensitivity is limited only to a certain size range.

(ii) The exact proportion of nPEVs in the solution was unknown. Thus, normalizing by absolute concentration values often resulted in high variation in the SPRi results. (Data not shown)

	Dilution factor for the target concentration range (/mL)			
nPEV Batch	10^6	10^7	10^8	10^9
Feb-19	100,000	10,000	1,000	100
Dec-19	10,000	1,000	100	10

Table 5 Table of dilution factor for the injection of nPEVs in a different range of concentrations in the SPRi. The target concentration is highlighted in purple and the dilution factor for the respective nPEV batch is highlighted in green.

Each injection sensorgram is considered in a 20 minutes window with the following components.

- Baseline: from 0-5 minutes. This visualizes the noise as well as the drift of the biosensor signal.
- Injection: from 5 minutes to 14 minutes. This follows the interaction of the nPEVs on the ligand spots.
- Post injection: from 14 minutes to 20 minutes. This allows observing whether the bound EVs dissociate after the injection and to characterize the stability of the interaction.

The sensorgram of negative control subtraction was considered for analysis and establishing the LOD and dynamic range of the NBA platform. The process of calculating the negative control subtraction is described in the previous section 4.8.5.

4.10.2.1 Establishing the limit of blank

The Limit of Blank (LOB) is defined as the expected signal when a blank material with no analyte is injected. It is usually reported with a standard deviation.[184] By keeping all the measurement conditions identical, this LOB measurement was performed by injection of PBS 1X for 9 minutes. After negative control subtraction, the sensorgram was obtained.

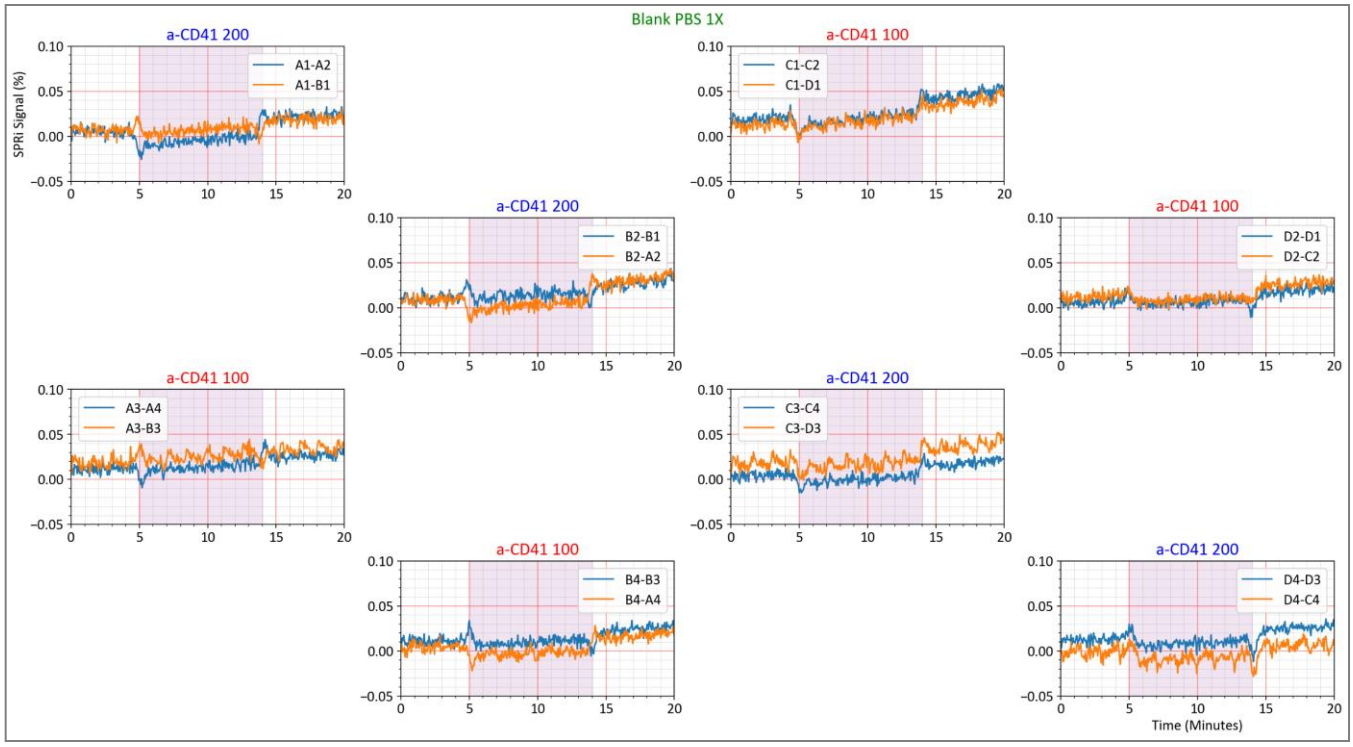

Figure 45 Sensorgram from multiplex spots. Each subplot of the a-CD41 is located according to its place in the biochip. Subtraction is performed with the two neighboring negative control. For computing the average, only the sensorgram from the same column is considered. (All those with blue color). The duration of injection is highlighted in purple color. The spot name is referred previously. Ref. figure 23

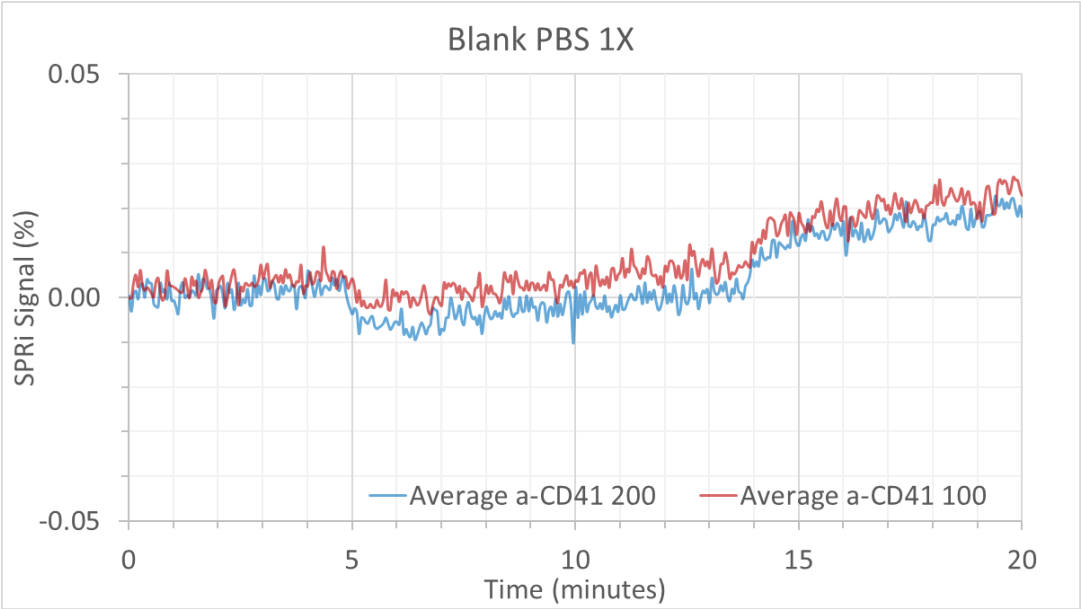

Figure 46 Average sensorgram of a blank injection (PBS 1X) at a flow rate of 20 µL/min.

4.10.2.2 Computation of net capture level (ΔR %) for blank

Using the formula mentioned in the section 4.8.5.3., the net capture level and the average for each ligand was estimated and tabulated here.

a-CD41 200		**a-CD41 100**	
A1-A2	0.017	C1-C2	0.029
B2-B1	0.017	D2-D1	0.014
C3-C4	0.014	A3-A4	0.016
D4-D3	0.014	B4-B3	0.014
Average	**0.016**		**0.018**
SD	**0.002**		**0.007**

Table 6 Net capture level in each ligand concentration for a blank injection.

Establishing the LOB is useful in distinguishing the noise and the signal of the interaction. It is also used to define the LOD of the NBA platform. D A Ambruster et al described a procedure to calculate the LOD of a biological assay. [184] As per this description, the LOD is equal to the LOB +1.645 SD of the LOB. In this study, the average signal of 4 spots in the blank experiment was 0.016% and 0.018%, and the SD was 0.002% and 0.007% for a-CD41 200 and a-CD41 100, respectively. Therefore, any signal in a-CD41 200 spots that were less than 0.020%, and signal less than 0.030% in a-CD41 100 spots were considered noise.

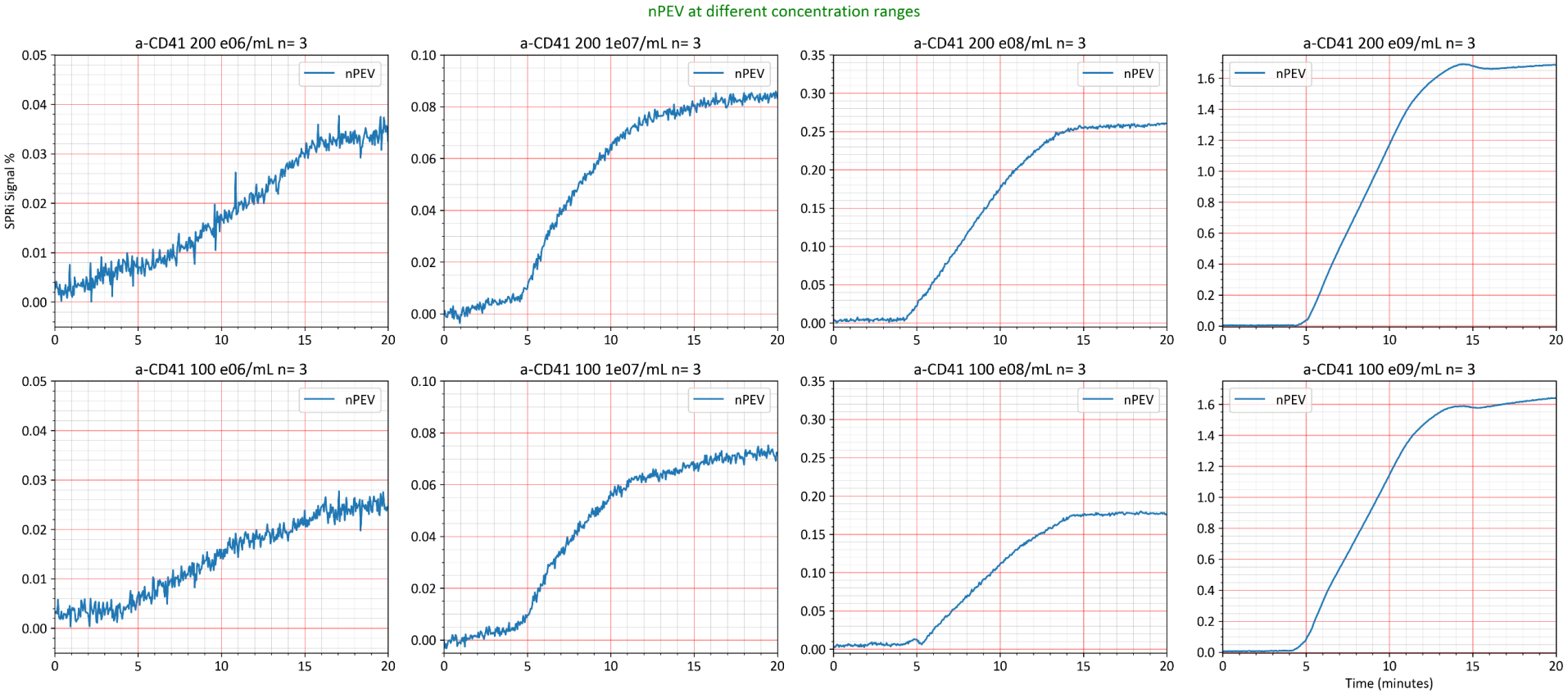

Figure 47 Sensorgram of nPEVs of various concentration range for a-CD41 200 and a-CD41 100 sorted by increase in the order of magnitude of the concentration of the EVs. The number of replicates is mentioned in the subplot title. Each replicate is the average of quadruplicate of the specific ligand family in the biochip.

4.10.2.3 Establishing the Dynamic range for nPEVs

The dynamic range of the SPRi was established by the capture level of nPEVs in function of concentration. The concentration for each order of magnitude was calculated by the average batch concentrations in the specific replicate. The standard deviation is reported as error bars.

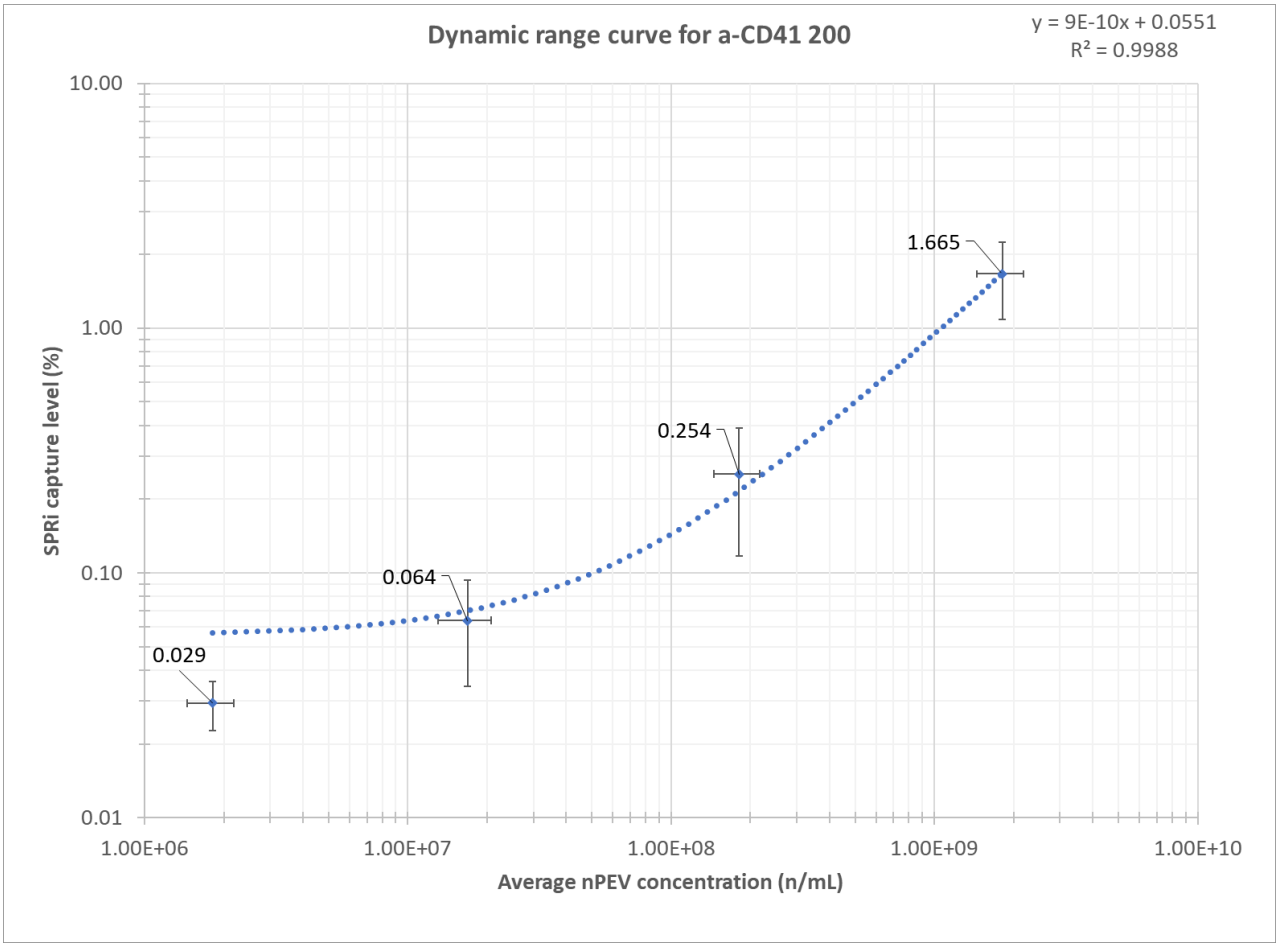

Figure 48 Dynamic range of SPRi for nPEVs in a-CD41 200 spots. The injections were performed for 9minutes at 20 µL/minute. The concentration and SPRi capture are plotted in logarithmic scale. The relationship between concentration and SPRi capture level are fitted with linear function. Error bars in x-scale and y-scale are standard deviation of concentration and SPRi capture level, respectively.

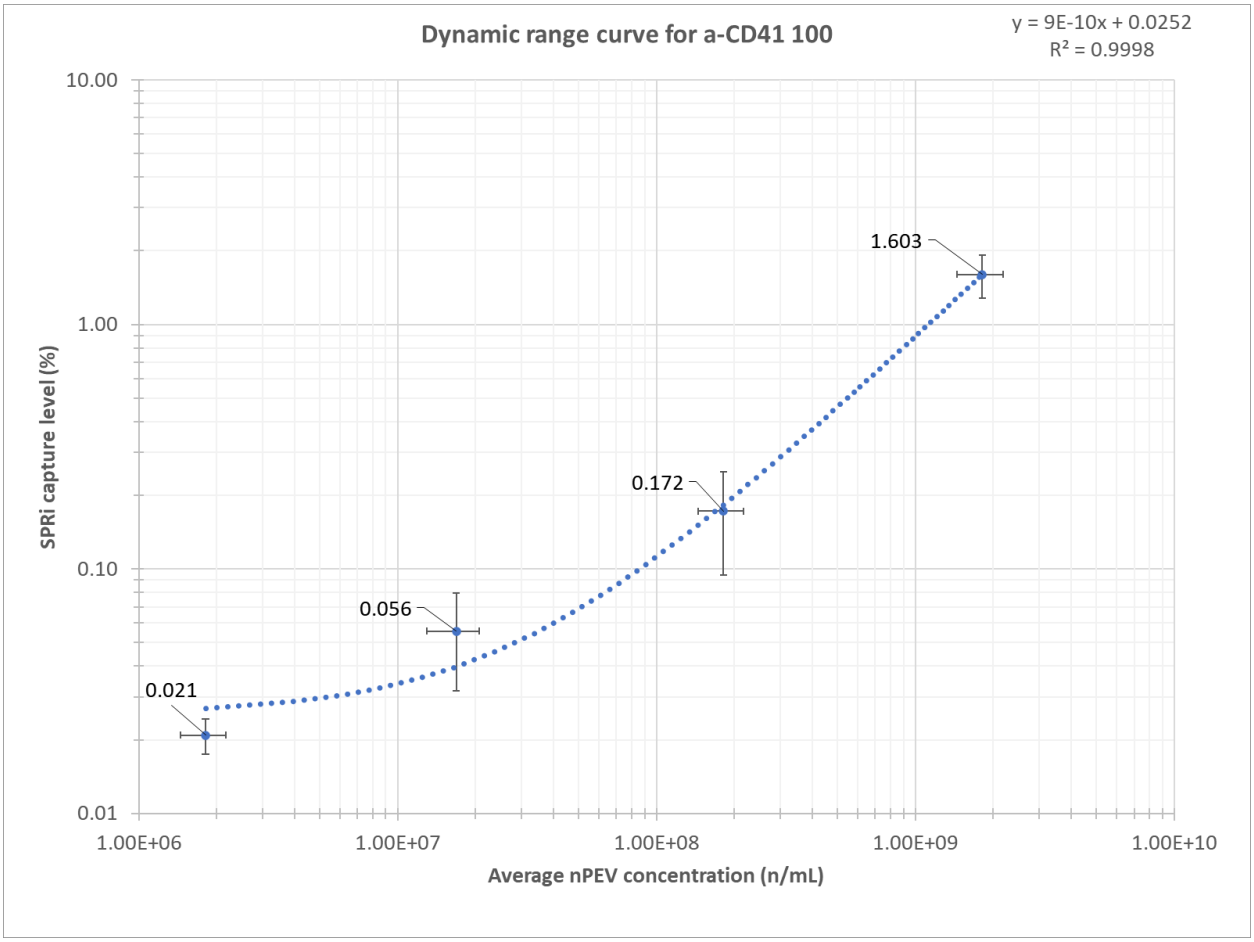

Figure 49 Dynamic range of SPRi for nPEVs in a-CD41 100 spots. The injections were performed for 9minutes at 20 µL/minute. The concentration and SPRi capture are plotted in logarithmic scale. The relationship between concentration and SPRi capture level are fitted with linear function. Error bars in x-scale and y-scale are standard deviation of concentration and SPRi capture level, respectively.

For both ligand concentration ranges, the relationship between the concentration and the capture level appeared to be linear and the slope of the curve had a regression coefficient of 0.998. The observation for the lowest concentration in a-CD41 200 was 0.029 which was well above 0.019 which was the limit of blank $+1.645SD_{LOB}$. However, for a-CD41 100, the capture level appeared to be 0.021 which was lower than the LOB+1.645 SD_{LOB}. This suggested that the Limit of Detection (LOD) was in the order of 10^6/mL for a-CD41 200, and between 10^6 and 10^7/mL for a-CD41 100. It is also observed that the plasmon sensitivity for a-CD41 100 was slightly higher than that of a-CD41 200 which may have resulted in higher LOB for a-CD41 100. This data is detailed in the discussion section 4.11.1.

4.10.2.4 Confirmation test for the LOD

To emphasize the estimation of the LOD, a set of experiments were performed with an order of magnitude less than the LOD previously seen. nPEVs with an average concentration of $1.30*10^5$/mL $\pm 3.33*10^4$ /mL were injected and the average sensorgram is presented below.

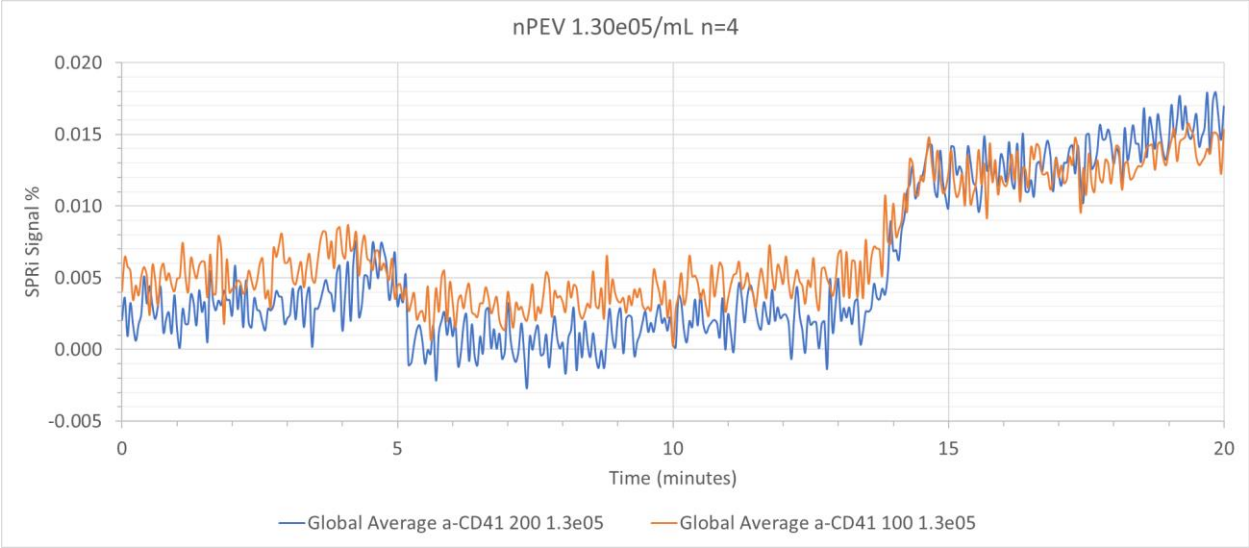

Figure 51 Sensorgram of nPEVs injected in the order of 10^5/mL. The sensorgram is obtained after subtracting the negative control.

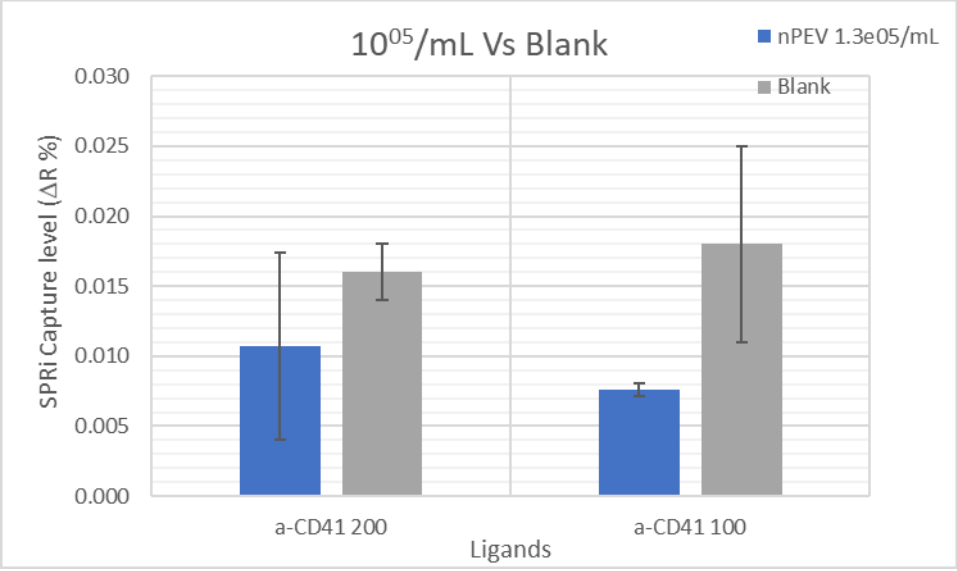

Figure 52 Comparison of capture level in the SPRi between nPEVs $1.30*10^5$/mL and blank test. The relative low signal of nPEVs suggest that the LOD starts above this concentration range.

The average capture level was calculated for both the ligand groups and was found to be 0.016 ± 0.002 and 0.018 ± 0.007 for a-CD41 200 and a-CD41 100 respectively. Since both values were in the same range as the limit of blank, this confirmed that the LOD was indeed above this concentration range. In blank tests as well as in this low concentration range, the resulting capture level may arise because the plasmon working angle was selected to be more sensitive for a-CD41 spots. This choice is limited in the apparatus to only one selection, thus the small difference in the sensitivity between a-CD41 spots and IgG control spots could result in a small underestimation of signal in the IgG spots.

4.10.3 Study of EVs in AFM

Biochips from various concentration ranges were scanned in the AFM in contact mode in air. Scans from several spots resulted in the accumulation of many images for each condition. Many images need to be acquired to survey the capture in the spots which were in the mm^2 range. While an image with a big scan area could give an idea about the spread of EVs, accurate estimation of number and size parameters required the scan to be in good resolution with a small scan area.

The scanned images were processed in Gwyddion software for grain extraction and then the effective diameter was calculated. The total EVs count was normalized with the scan area between each measurement and the areal density of EVs was estimated. The images obtained in the AFM were leveled in JPK Data processing software. A polynomial fit from each scan line was subtracted to obtain the leveled image. Height trace channel of the jpk format is chosen for analysis in Gwyddion. In Gwyddion, using the mark grains tool, a height threshold of 5.5 nm was set to extract grains. The marked grains were treated with an additional filter to screen based on the surface area of around $4x10^{-15}$ m^2. The properties such as grain diameter, zero-base volume and height are saved in a text file. Using a method proposed by Yuana et al,[136] the effective diameter is calculated and used in further analysis.

4.10.3.1 AFM Images

a-CD41 200

10^6/mL 10^7/mL 10^8/mL 10^9/mL

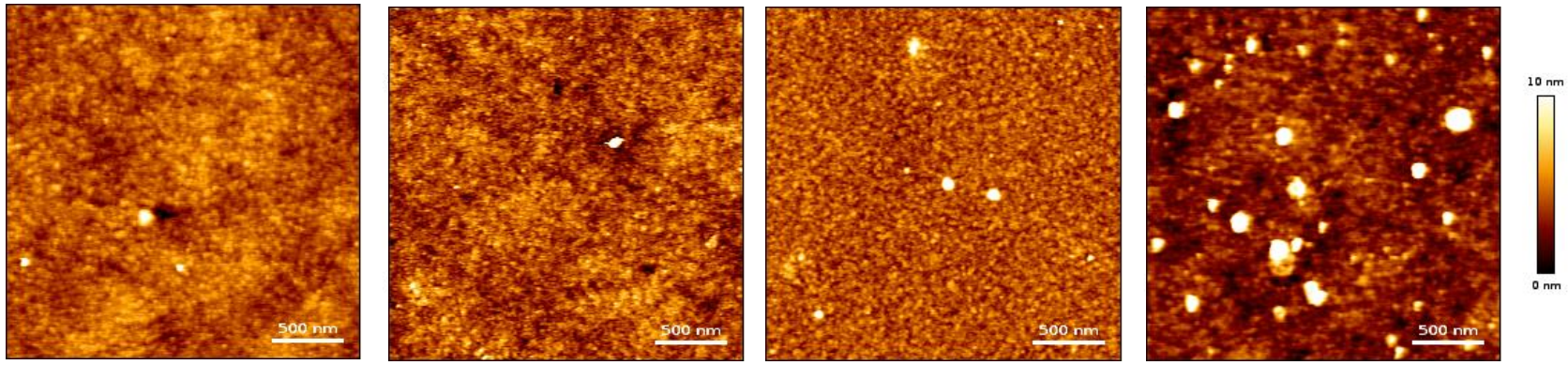

IgG 200

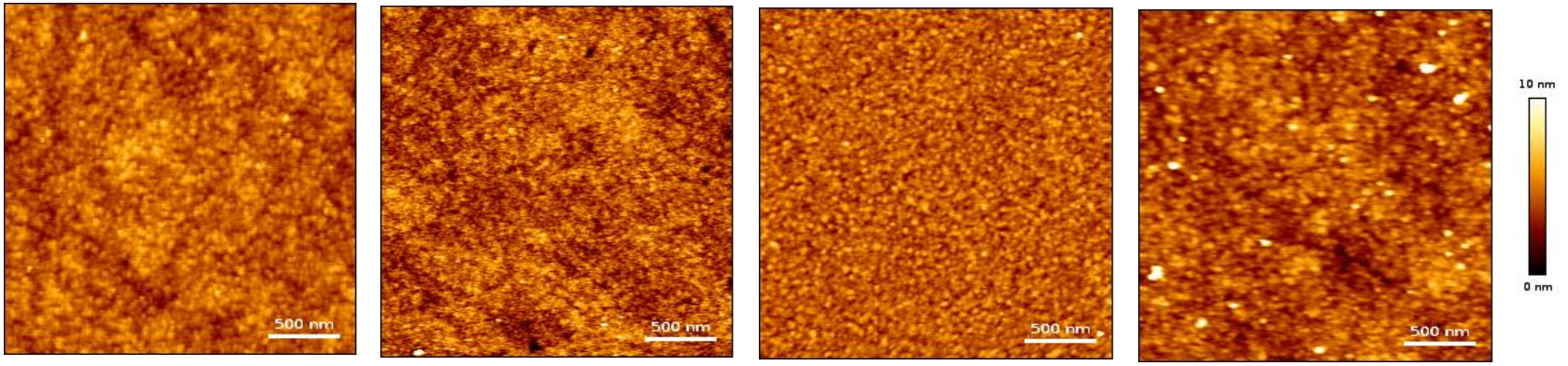

*Figure 53 Representative AFM images of nPEVs in a-CD41 200 (top row) and IgG 200 (bottom row) from the biochips of different concentration range. All images are same size 2.5 * 2.5 μm, at resolution 256px, and has the same z-axis scale.*

a-CD41 100

10^6/mL 10^7/mL 10^8/mL 10^9/mL

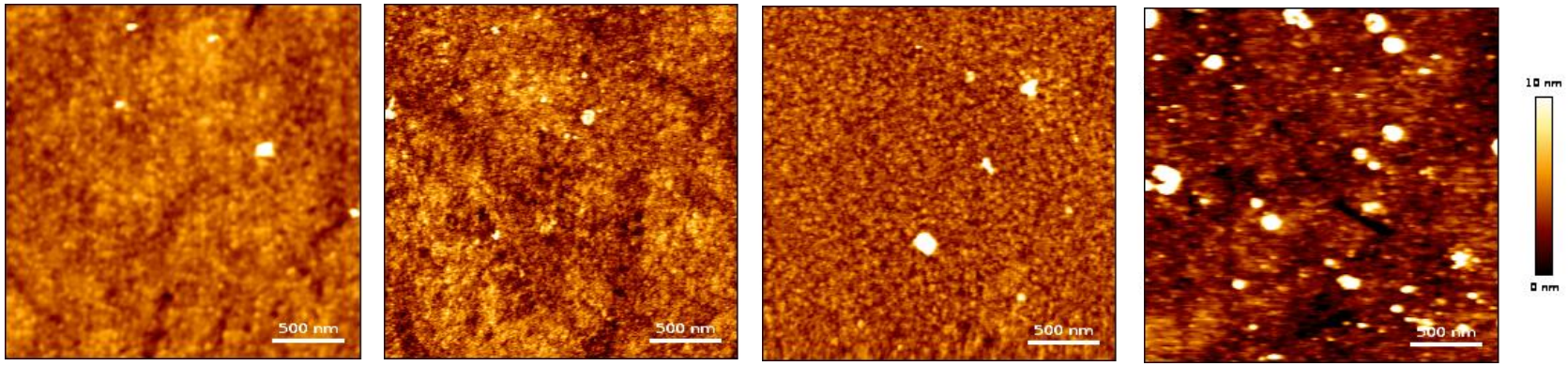

IgG 100

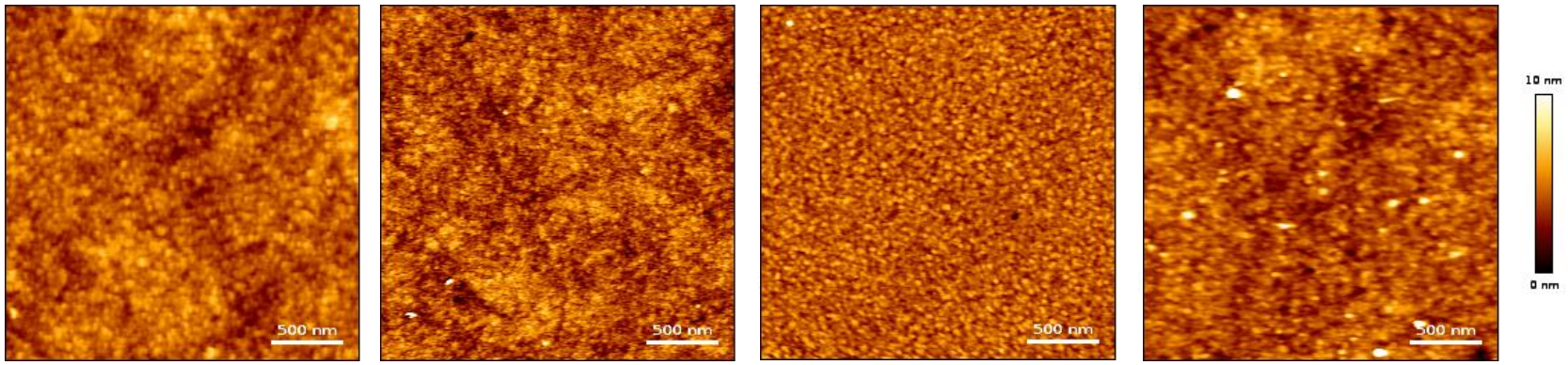

*Figure 54 Representative AFM images of nPEVs in a-CD41 100 (top row) and IgG 100 (bottom row) from the biochips of different concentration range. All images are same size 2.5 * 2.5 μm, at resolution 256px, and has the same z-axis scale.*

4.10.3.2 Estimation of EVs density

Initial estimation of EVs density was done for all the concentrations by dividing the count of EVs by the total scan area.

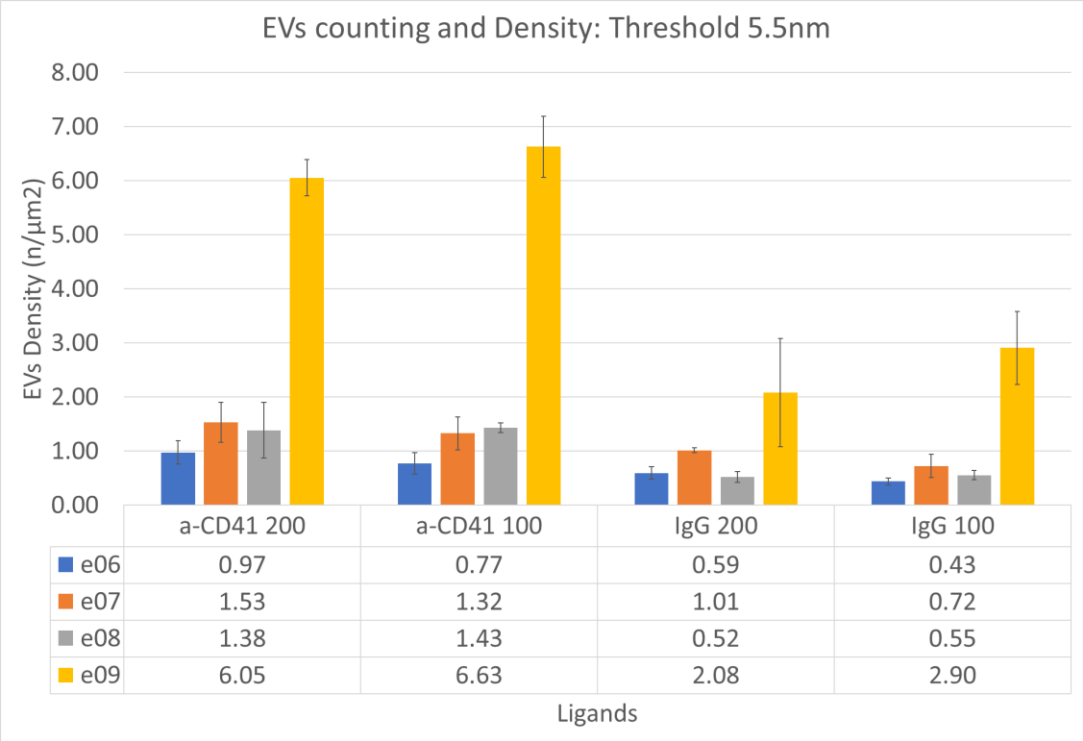

	a-CD41 200	a-CD41 100	IgG 200	IgG 100
e06	0.97	0.77	0.59	0.43
e07	1.53	1.32	1.01	0.72
e08	1.38	1.43	0.52	0.55
e09	6.05	6.63	2.08	2.90

Figure 55 EVs density estimated from the AFM images for different concentration ranges in various ligands.

As can be noted from the bar chart above for a-CD41 100, the EVs density for 10^7/mL was smaller than that of 10^6/mL. However, one can note from SPRi dynamic range curve, that the signal was getting more and more intense with increasing concentrations. One explanation could be that, unlike SPRi, AFM is not specific. This means that the particles present in a spot are counted no matter whether they originated from a specific capture of EVs or adsorption of a contaminant. One way to offset this effect was to adjust the threshold for all the images to fix a threshold at which the AFM density estimation resembled the SPRi dynamic range. The specific data obtained in the SPRi complemented such exploration. As an additional method of improving the quantification analysis, the images with scan areas between 6.25µm^2 and 25µm^2 were selected uniquely. While the bigger scans provide an overview of the surface coverage by objects in the biochip, counting of EVs and sizing from such large scans may have influenced the results as the EVs were not resolved in the same way between scan areas.

4.10.3.3 Scatterplot of EVs

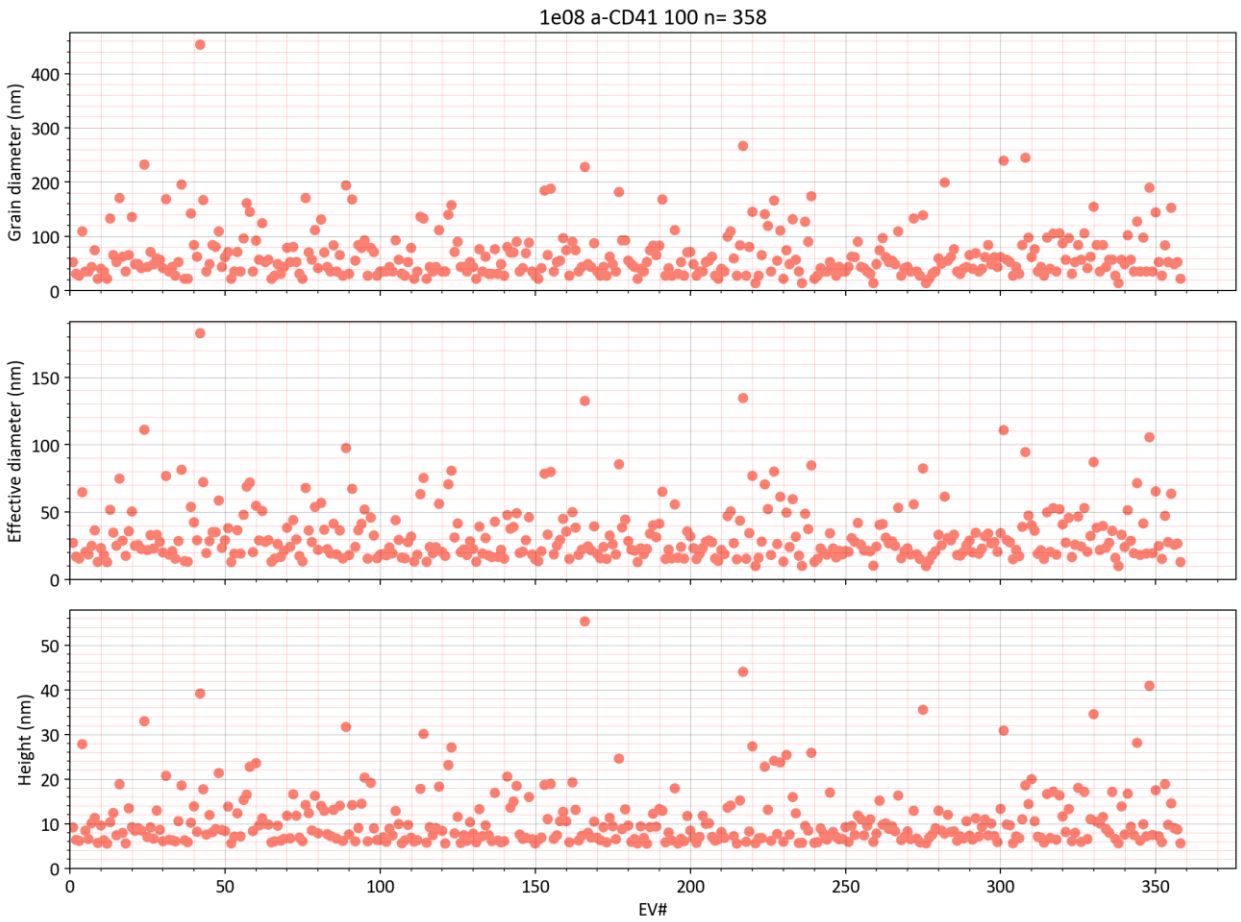

Figure 56 Scatter plot of EVs at a threshold 5.5 nm. The scatterplot visualization is useful to visualize the distribution and to identify clusters. Scatterplot of EVs is constructed for its various parameters such as grain diameter, effective diameter and height.

The grains data were obtained with a threshold of 5.5nm from Gwyddion. The scatterplot was constructed using a python program. Each grain was labeled with an id number (EV#) and plotted on the x-axis. Various parameters such as grain diameter, effective diameter, and height of the EVs were plotted in the y-axis. This correlative scatterplot is useful to compare the distribution of all three parameters. The above data corresponds to the a-CD41 100 family of the biochip injected with 10^8/mL. The EVs grain data consists of 4 spots of a-CD41 100, from a total of 40 images.

4.10.3.4 Dynamic Threshold selection

The scatterplot as well as the density data in the previous step was obtained with a height threshold value of 5.5nm. To be sure not to count gold grains and other background features as EVs, various height thresholds were selected in the quantification data obtained by Gwyddion. This time only the images of the scan area mentioned above were chosen for the analysis.

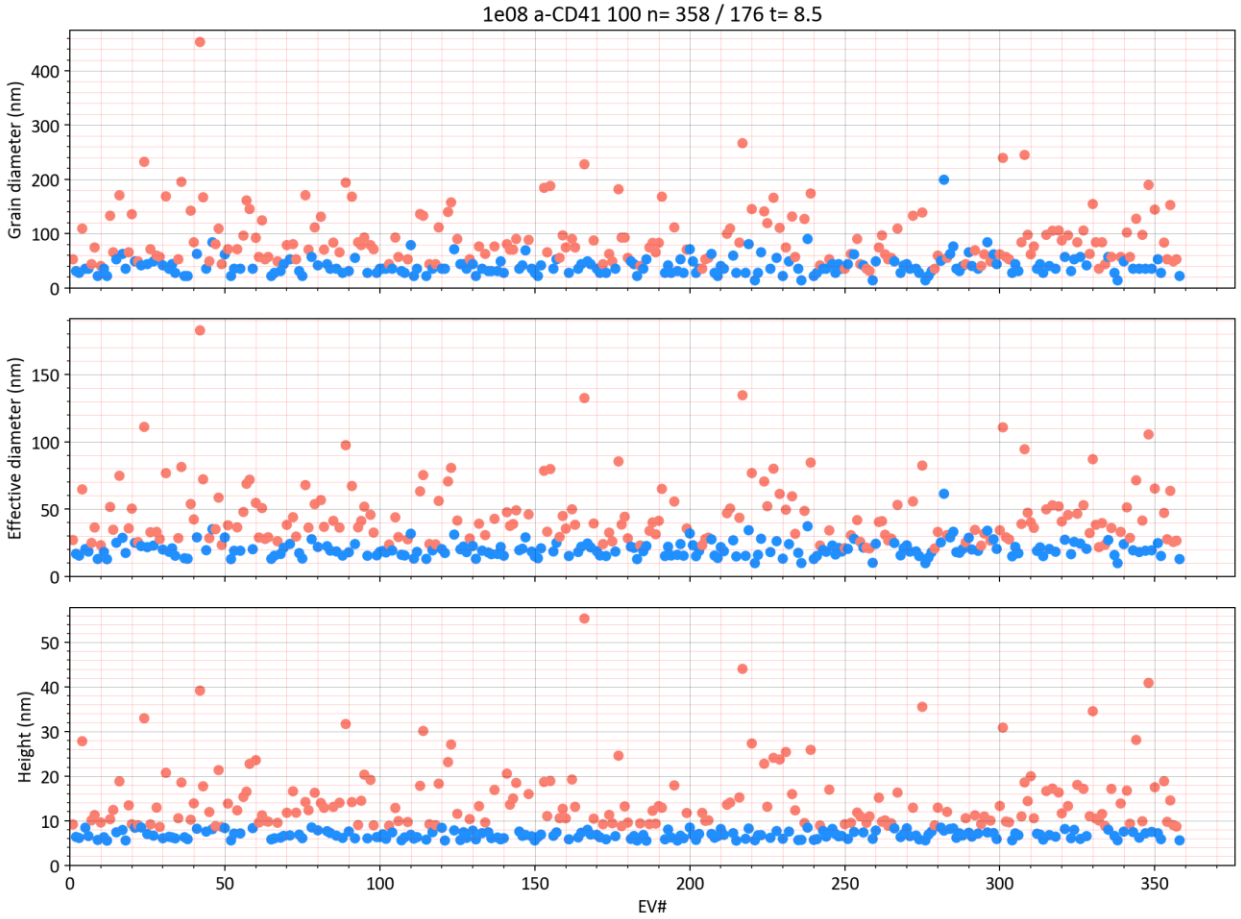

Figure 57 Scatter plot of differential threshold selection at 8.5 nm. Particles of height more than 8.5 nm, the corresponding grain diameter and effective diameter is highlighted in light orange color. Particles in blue represent objects of height up to 8.5nm and are considered as background. The count of total particles and particles above selected threshold is mentioned in the title. "t" refers the threshold. The biochip corresponds to 10^8 /mL in a-CD41 100 ligands.

Various thresholds ranging from 6.0 nm to 10nm in the interval of 0.5 nm were investigated and the area density was individually estimated for each threshold and all the concentration ranges. Data are presented in Annex 2.

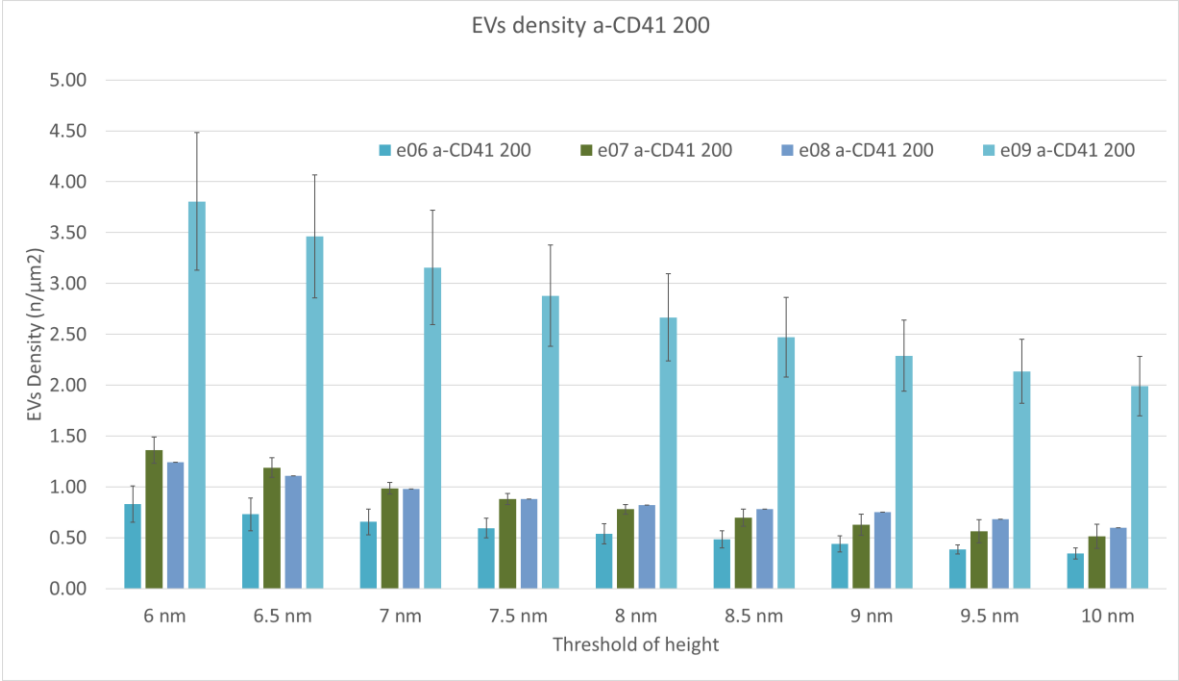

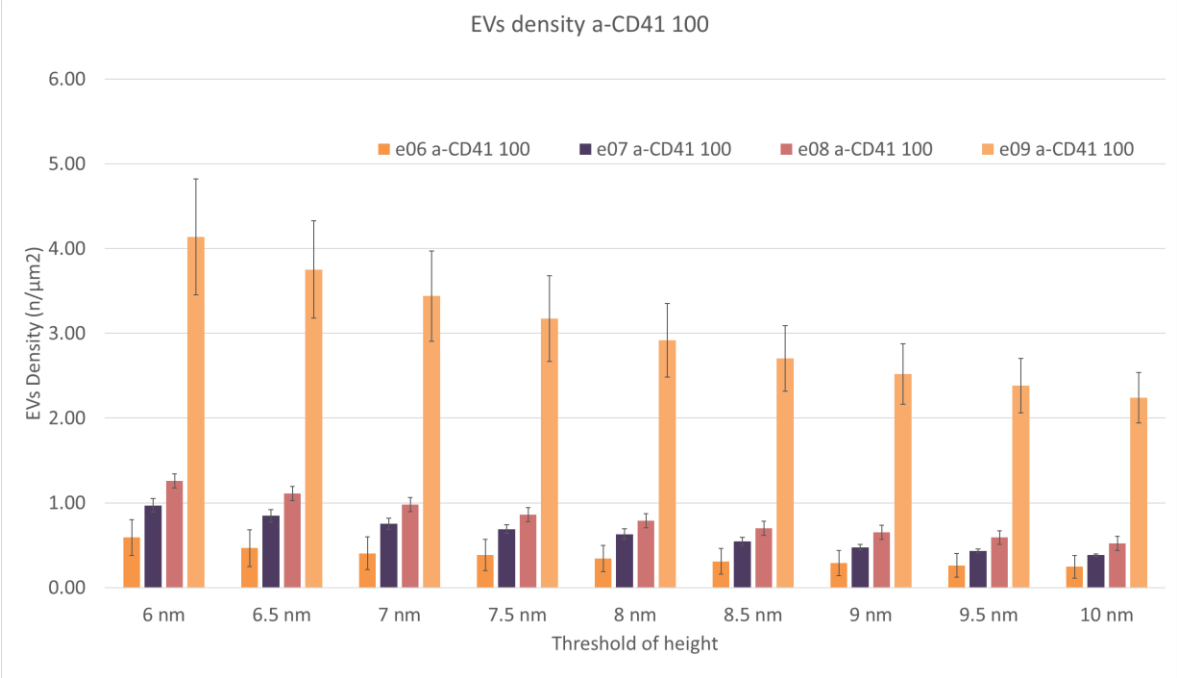

Figure 58 Density of EVs with Dynamic threshold for a-CD41 200 (top) and for a-CD41 100 (bottom). After limiting the scan size and from threshold 8nm, the trend of EVs density is at par with the SPRi capture level.

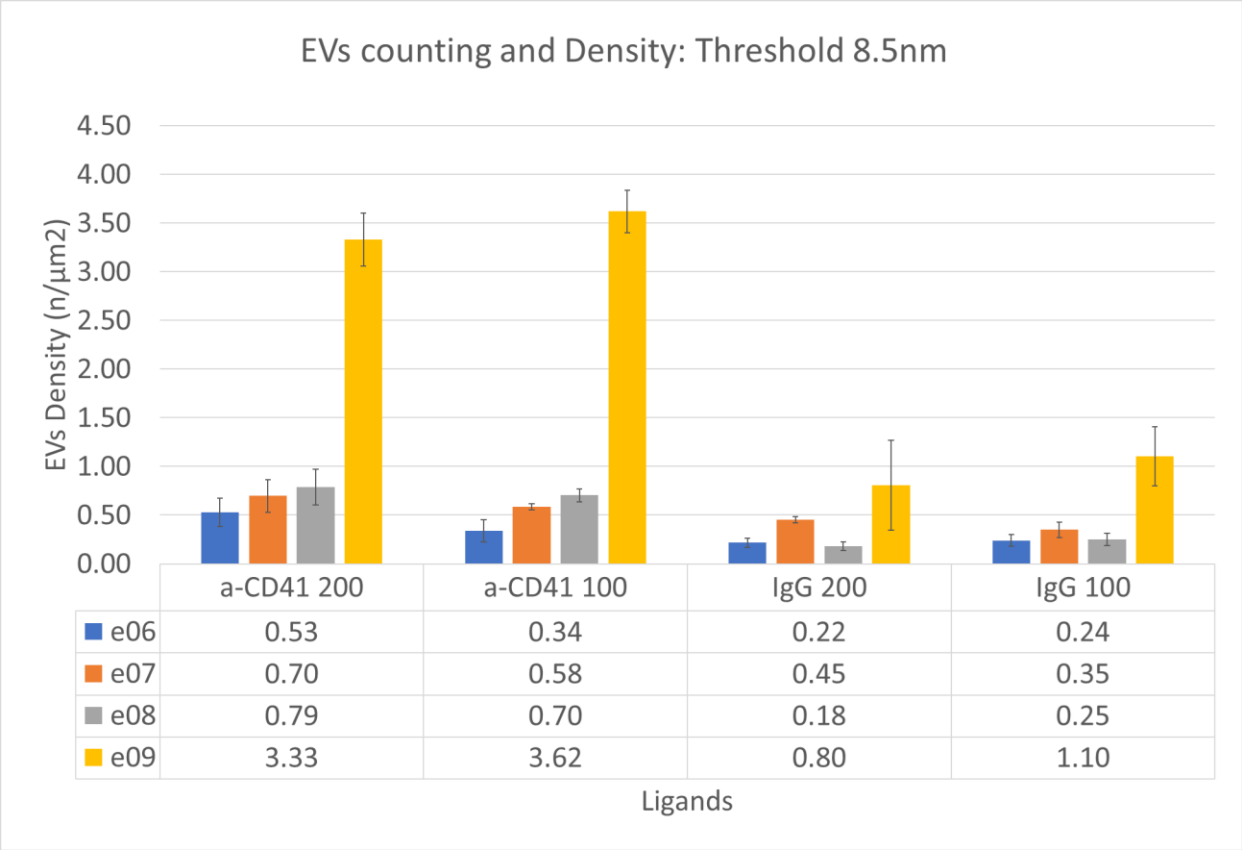

Figure 59 EVs density at Threshold 8.5nm It can be noted that at this concentration a more accurate estimation of EVs is established in function of SPRi signal.

As can be noted from the bar chart (figure 59), the EVs density was increased corresponding to the concentration range analogous to SPRi data. This complementary approach provided more accurate estimates of EVs quantification. This was useful to remove the background noise, choosing a threshold of 8.5 nm in order to avoid counting other components on the biochip than the EVs.

4.10.3.5 Metrological analysis

After the dynamic thresholding, the estimation of central tendencies of the distribution of effective diameter for all the concentration range was calculated, as presented below.

Effective diameter of EVs	**e06**				**e07**				**e08**				**e09**			
Parameters	**a-CD41 200**	**IgG 200**	**a-CD41 100**	**IgG 100**	**a-CD41 200**	**IgG 200**	**a-CD41 100**	**IgG 100**	**a-CD41 200**	**IgG 200**	**a-CD41 100**	**IgG 100**	**CD41 200**	**IgG 200**	**CD41 100**	**IgG 100**
Total count (n)	255	134	129	78	303	141	289	150	191	44	176	60	1137	107	1060	105
Average diameter (nm)	62.16	68.57	53.15	71.31	54.63	62.92	50.74	60.29	43.37	55.30	46.34	42.73	54.08	46.03	55.17	47.72
SD	39.47	48.08	32.63	35.57	38.36	40.91	23.79	38.67	20.98	50.17	23.76	20.82	23.72	17.37	28.07	18.62
Minimum (nm)	13.98	22.75	24.55	24.20	18.88	20.05	16.54	20.61	13.66	19.83	20.83	20.42	23.12	27.59	15.65	18.87
Maximum (nm)	297.90	305.96	288.74	177.50	262.75	309.18	170.21	371.40	145.32	331.50	182.61	102.04	213.93	143.98	357.52	143.34
Scan Area (μm^2)	449.25	350.00	493.75	362.50	505.65	234.80	334.30	579.65	242.93	250.00	242.75	243.55	350.00	300.00	156.25	93.75

Table 7 Descriptive statistics of EVs from different concentration ranges in AFM

As can be noted from the above table, the total EV count was lower than at least 500 for most of the concentration ranges to compute the size distribution comparison with statistical significance. A low density of EVs posed a challenge to accumulate many images to reach the desired number of EVs (around 500) to decipher its size parameters. Therefore, the quantitative comparison was performed only for the 10^9/mL concentration range. However, the density data should serve as a qualitative indication of the difference in the density of EVs in the low concentration ranges.

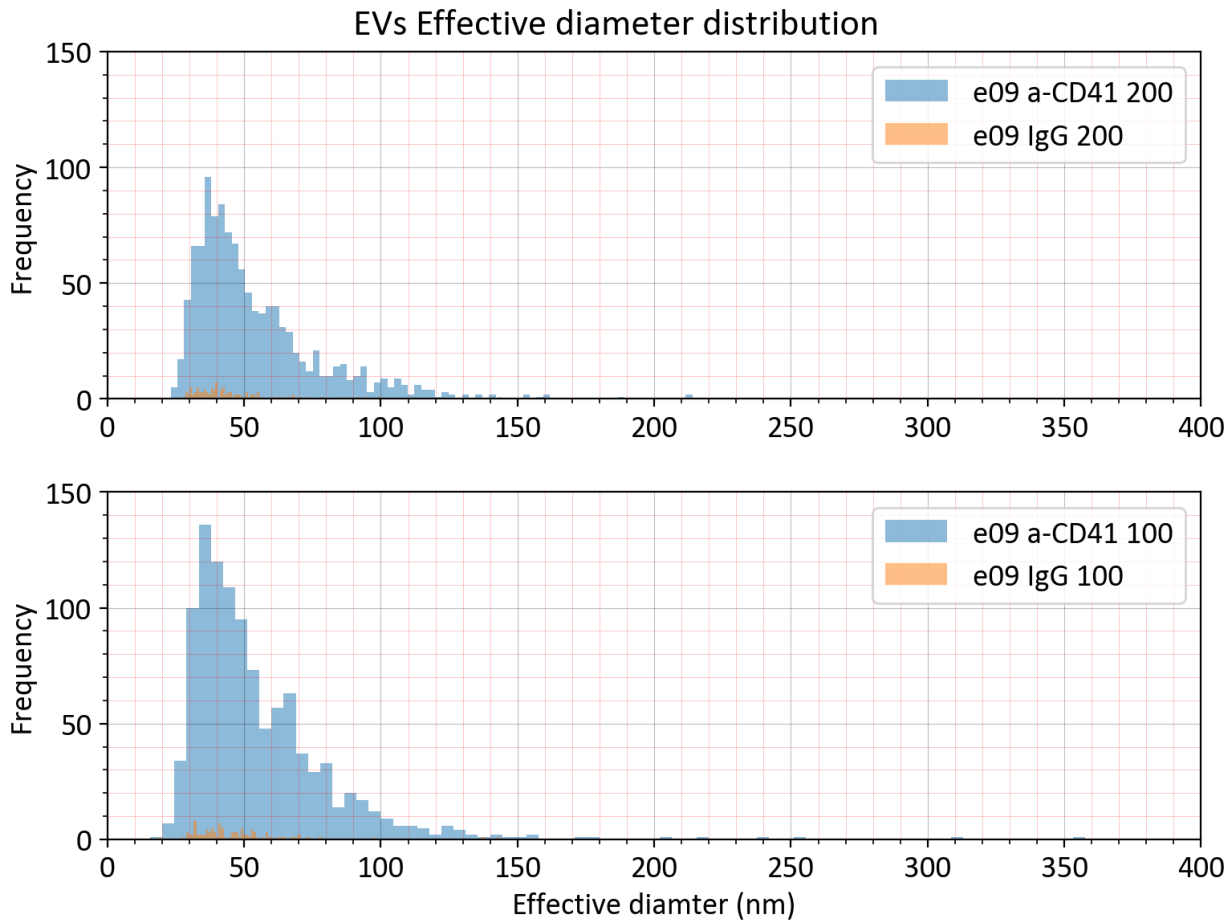

Figure 60 Size distribution of CD41+ nPEVs at 10^9/mL concentration range.

Both a-CD41 200 and a-CD41 100 had similar size distribution profiles. a-CD41 200 contained EVs of the average effective diameter of 54 ± 23 nm whereas a-CD41 100 ligands have an average effective diameter of 55 ± 28 nm. There is a clear contrast of the magnitude of EVs number between a-CD41 and respective IgG spots despite comparable scan area.

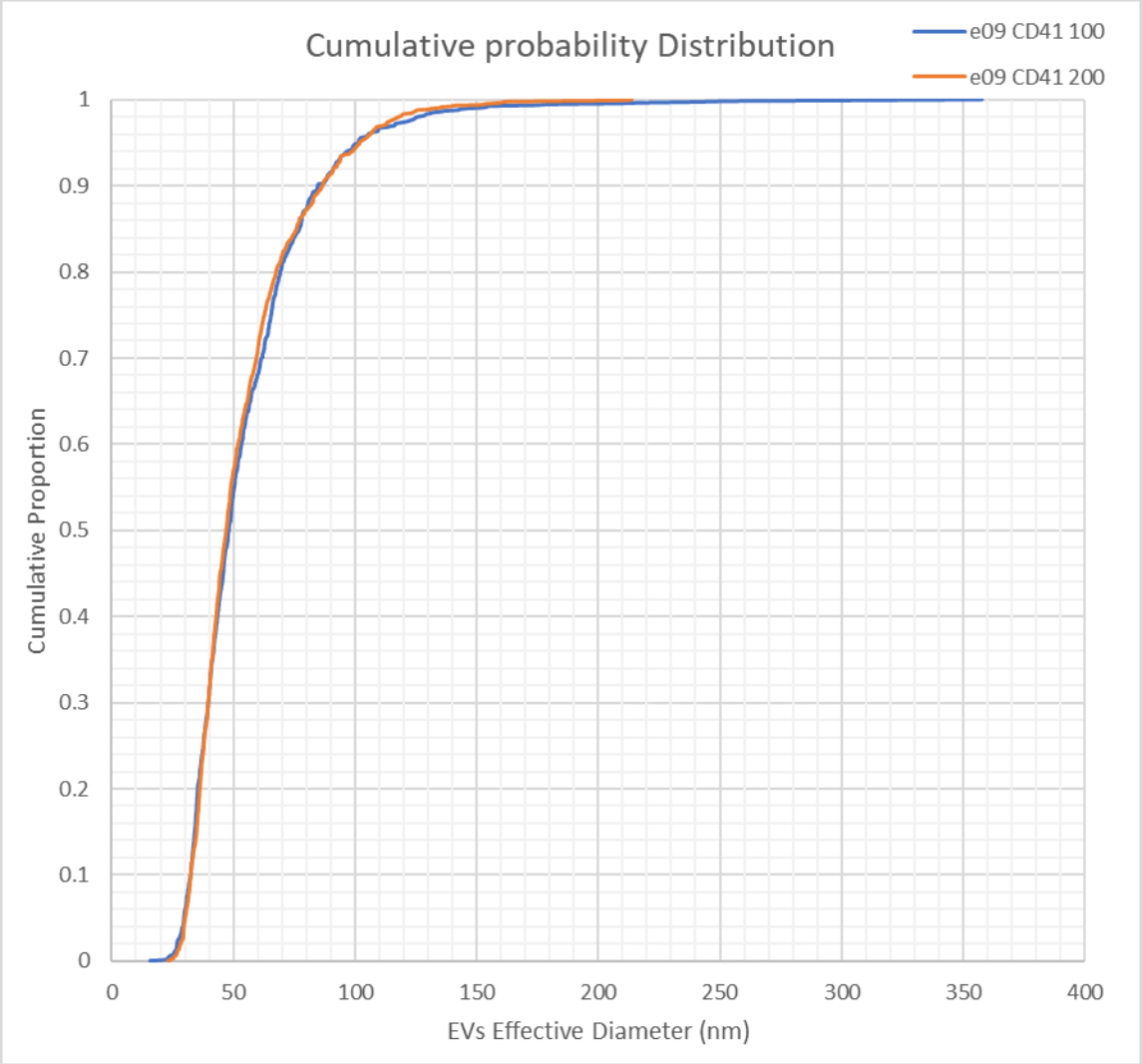

Figure 61 Cumulative probability distribution of EVs effective diameter. The probability proportion of each effective diameter is calculated and accumulated with the previous value. This plot is the normalized distribution and statistical inferences can be made from this type of visualization given that the sample is selected randomly from the distribution and enough samples.

As seen in the cumulative probability distribution, there was no difference in the EVs distribution between a-CD41 200 and 100 for EVs injected with 10^9/mL concentration which confirms the specificity of the objects observed in the CD41 spots.

4.11 Conclusion and Outlook

The analytical sensitivity and the dynamic range of the NBA platform for characterizing platelet-derived EVs were established in this study.

- The LOD is determined to be in the order of 10^6/mL for a-CD41 ligands at 20μL/min for 9 minutes of injection in a multiplexed format.
- The Dynamic Range of the NBA platform is defined for at least three orders of magnitude.
- The AFM data revealed spherical morphology of EVs validating the presence of EVs at all concentration ranges
- AFM data at 10^9/mL could recreate the size distribution profile of EVs expressing CD41.
- The complementary approach of SPRi detection and AFM quantification combined with dynamic thresholding strategy offers a unique perspective on EVs characterization without labeling or signal amplification approach.

4.11.1 Limit of Detection

The limit of sensitivity of the SPRi system was determined based on the LOB and the LOD was found to be 0.020% and 0.030% for a-CD41 200 and a-CD41 100, respectively. It can be noted that the lowest detected signal for 10^6/mL concentration range in a-CD41 100 spots was not significantly greater than that of the LOB, therefore the LOD for a-CD41 100 was determined to be between 10^6/mL and 10^7/mL range. In the plasmonic sensitivity of the LOB experiment, it can be noted that one of the ROIs of a-CD41 100 (spot C1), had higher sensitivity than the rest of a-CDC41 100 ROIs.

This might influence the final signal as, as can be noted from Table 4, the signal corresponding to this spot was higher than that of all other three ROIs. This resulted in a higher average and standard deviation of LOB for a-CD41 100 spots. This highlights the importance of plasmonic sensitivity in signal acquisition.

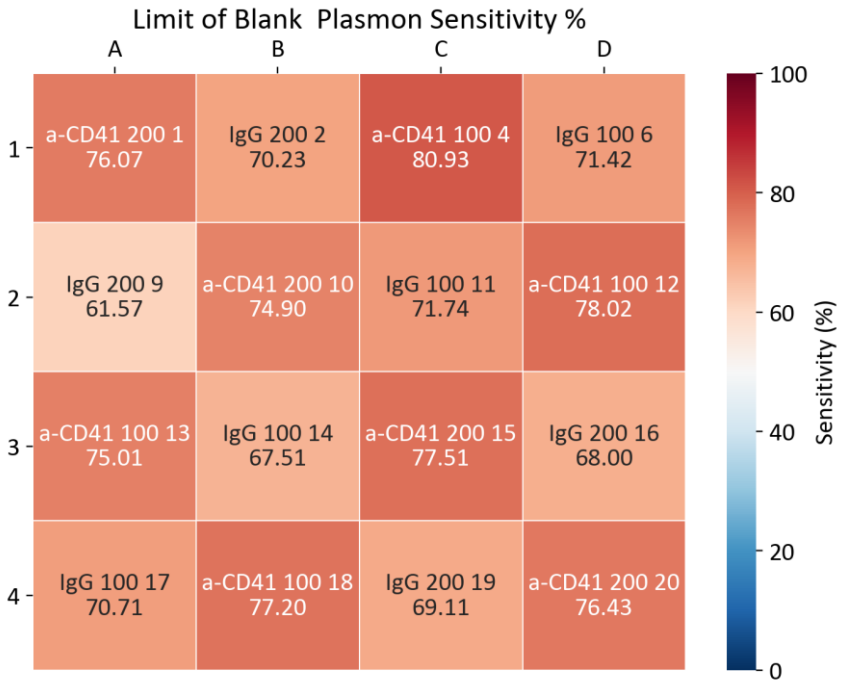

Figure 62 Plasmonic sensitivity heatmap for Limit of blank experiment.

4.11.2 Comparison of NBA platform Vs Label-free EVs detection

Numerous references in the literature address label-free EVs biodetection, using a wide range of detection methodologies such as electrochemical[185], optical sensing, and electrical sensing,[150] and acoustic sensing[147,186]. Among the available label-free sensing techniques, electrochemical sensing seems to have the lowest detection limit. Kilic et al claimed that their approach using electrochemical biosensing for cancer cell-derived EVs can detect EVs as low as in the range of 10^2/mL,[185] although it is noteworthy that the control experiments had to be done separately due to the limitations in the electrochemical cell. Also, it is not possible to visualize the EVs as the detection was based on antibody-antigen interaction. However, a recent study reported a sensitivity limit of 10^3/mL using electrochemical sensing and confirmation of EVs structure captured in the nano interdigitated electrodes by imaging in AFM.[149] EVs detection using a Quartz Crystal Microbalance (QCM) with dissipation monitoring is another approach for EVs detection.[147] In this work, the QCM-D sensor could detect exosomes bearing CD63 at $1.4x10^8$/mL in complex media containing human serum up to 75% (v/v). The complementary information about the EV structure and morphology was obtained in AFM. SPR and SPRi are the leading optical label-free biosensing technologies. SPR-based techniques offer sensitive, selective detection of EVs while providing improvement using gold nanoparticle probes to enhance the signal. The localized surface plasmon resonance (LSPR) generated by a modified geometry of the photonic crystal was able to detect EVs at a concentration of 10^4/mL.[187] The SPR sensing of EVs without signal amplification approach

was studied by Sina et al.[188] They used a sandwich assay on a surface of EVs captured with a-CD9 and a-CD63 ligands and used a-HER (human epidermal growth factor receptor-2) to reveal subpopulations of exosomes expressing HER biomarker. Considering the detection of spiked exosomes bearing HER biomarker, sensed on the a-CD9 antibody, the paper indicates a detection limit of $3.3x10^7$/mL. S. Piccolini et al detected brain-derived exosomes in an SPRi biochip made of a multiplex of antibodies.[189] Although the concentration of EVs is not reported, the detection limit was 1μg total proteins/mL. This result is not directly comparable with the result of this study as the paper reports qEV isolation in a size exclusion column (SEC) resulting in most of the soluble proteins being removed. Thus, the protein content they estimate is that of proteins present in the EVs.

Thus, the sensitivity of the LOD of the NBA platform for EVs characterization could be positioned as the lowest LOD comparable to the available label-free optical detection technologies without amplification.

5. Characterization of EVs from platelet lysates preparations and their role in neuroprotection

5.1 Human Platelet lysates

Platelets contain various growth factors including Platelet-derived growth factor, (PDGF), fibroblast growth factor (FGF), insulin-like growth factor-1 (IGF1), epidermal growth factor (EGF), and vascular endothelial growth factor (VEGF) which have multiple functions in wound healing and injury recovery.[190] Human platelet concentrates (HPC), or platelet-rich plasma (PRP) is used in clinics as a growth factor delivery preparation to sites that require regeneration.[191] Human platelet lysates (HPLs) obtained by lysis or activation of the platelets are developed as an alternate to fetal calf serum (FCS) as a cell-expansion medium supplement for regenerative therapies. In 2005, Christelle Doucet et al proposed HPLs as an effective substitute to FCS for mesenchymal stem cell (MSC) expansion[192]. The authors found that growth factors-rich HPLs provided an increased efficiency for MSC expansion, a faster rate of cell growth while maintaining the MSC's ability to differentiate compared to FCS. It is recommended that the whole cultivation process be conducted under xeno-free conditions for clinical applications.[193] Thus, providing evidence that the HPLs are a viable alternative to the supplements such as FCS and underscore the potential use of HPLs for cellular and tissue regeneration.

HPLs are produced by lysing the platelets by freeze-thaw cycles[192], direct activation[194] by treating with $CaC1_2$, sonication,[195] or by solvent-detergent (S/D) treatment.[196,197] The freeze-thaw cycle destructs the structure of the platelets, thereby releasing the growth factors. Treating platelets suspended in plasma with $CaC1_2$ induce endogenous thrombin generation and fibrin formation, as well as platelet degranulation, and likely EV release. Recently, direct treatment of platelets with thrombin is also developed for HPL production.[198] Sonication is another simple method for manufacturing HPL. This method is also used in combination with the freeze-thaw cycle. Briefly, the platelets are sonicated at 20 kHz for 30 minutes for the release of growth factors. S/D method was developed to inactivate lipid-embedded pathogens. The viral lipid structures are dissolved by solvents such as tri(n-butyl) phosphate (TNBP). To make solvents dispersible in aqueous solutions, detergents like Tween 80 (polysorbate 80), Triton X-100 (octoxynol), or Na-cholate are additionally required.[199]

5.1.1 HPLs in regenerative medicine and tissue engineering

5.1.1.1 Use for human cell propagation

Although promising for *in vitro* applications of HPL to provide a xeno-free alternative to animal serum, clotting occurring in the culture medium represents a technical problem that is usually addressed by adding an optimized quantity of porcine heparin.[200] One can also perform a fibrinogen-depletion process to convert it into insoluble fibrin by treating it with calcium or thrombin and precipitating the clotting associated factors. This serum conversion process results in a product called "serum-converted platelet lysates" (SCPL) which do not need heparin addition and is used as a real xeno-free cell culture medium.[201] However, it is also noteworthy that depletion of fibrinogen-associated factors by serum conversion process could result in depletion of growth factors that are functionally important for cell growth. [201] Discovering the risk-benefit ratio for safe and effective use of HPLs is crucial to take advantage of the successful application of HPL for regenerative medicine and tissue engineering.

5.1.1.2 Novel applications in neurological diseases

Neurodegenerative disorders such as Parkinson's disease (PD), Alzheimer's disease (AD), or amyotrophic lateral sclerosis (ALS) are chronic disorders caused by progressive loss of neurons. In the central nervous system, the damaged or lost neuron cells are not repaired or replaced as the neuronal cells are amitotic. Therefore, novel neuroprotective strategies based on advanced biomaterials are developed. These advanced therapy products are intended to delay neurodegeneration and improve clinical outcomes. Various HPL preparations are being investigated for their neuroprotective activity.[202]

HPLs typically contain 50-60 mg/mL of total protein[203] and long-term administration of HPL for neuronal regeneration could saturate the cerebrospinal fluid (CSF). In addition, the presence of coagulation factors in the traditional HPL poses the risk of neuroinflammation and thrombogenesis in the brain which could lead to further complications. Therefore, like the serum conversion process, depletion of the potential toxic agents that otherwise may cause adverse effects is extremely beneficial for the safe application of HPLs for neuronal regeneration.

Chou et al, in the TMU laboratory, designed various preparations of HPL products intended for brain administration that have low protein content and are fibrinogen-, proteolytic and thrombogenic factors- depleted, as well as heat-inactivated for further inactivation of proteolytic enzymes. These preparations are also enriched in neurotrophic factors. Their safety

and neuroprotective activity are evaluated using dopaminergic Lund human mesencephalic (LUHMES) cell model and, *in* vivo in a mice Parkinson's disease model.[80]

The freeze-thaw operation disrupts the pellet of the platelet concentrates. After depleting the debris, it yields a product termed "Platelet Pellet Lysate (PPL)". The PPL then undergoes heat inactivation process at 56°C for 30 min and produces a modified lysate termed "Heat-treated Platelet Pellet Lysates (HPPL)". The detailed process steps are described in the materials and methods section 5.3.2. In their observation, Chou et al found the HPPL biomaterial, rich in neurotrophins, and depleted of neurotoxic and thrombogenic factors, to induce strong neuroprotection of dopaminergic neurons in a cellular model of PD and through intranasal delivery in a mouse model of PD.[80] The same material was found to be neuroprotective in two animal models of traumatic brain injury.[204]

5.2 Objectives of the project

Platelets, upon activation, degranulate and release a plethora of biomolecules which in turn induce activation of additional platelets. These bioactive molecules are functionally potent for the recruitment, growth, and morphogenesis of cells.[205] Platelets release various growth factors as free molecules but also in form of secretory vesicles[206] likely belonging to the group of EVs. Extensive characterization of the different preparations of HPLs are performed by Delila et al. In this work, they have identified substantial functional and biochemical differences in biochemical and functional properties depending on the mode of production.[207] In summary, the main findings indicated PPL and HPPL are enriched of growth factors such as BDNF, PDGF-AB, EGF, VEGF, and TGF-β (Transforming Growth Factor β). Comparing the heat-treated platelet lysates with their non-heat-treated counterparts, revealed a relative depletion in BDNF, PGDF-AB, EGF, and an increased level of IGF-1. Furthermore, the thrombin generation capacity of SCPL was higher than PPL while it is not detectable in HPPL. Tests carried out to detect the pro-coagulant activity of Tissue Factor (TF) and Phosphatidylserine (PS) expressing EVs showed higher PS exposure in PPL compared to HPPL whereas it is not detected in SCPL. There was no TF activity found in any of the HPLs. Therefore, the mode of preparation and implementation of a heat treatment influence the potency of HPLs. In addition, HPLs are likely to contain EVs. Thus, profiling EVs in these preparations and identifying their functional significance in future clinical applications is an interesting subject worth to be explored. Such a study could not only reveal any contribution

of EVs to the therapeutic outcomes but might also pave the way to extend the application of EV-based therapeutics for a wider spectrum of diseases.

This builds the bases for performing a differential characterization of EVs in these platelet lysate preparations HPPL, PPL, and SCPL using the NBA platform. The goal of the project is to

- Identify the EVs that are present in HPPL, PPL, and SCPL
- Reveal the differential expression of surface markers in these preparations
- Quantify the EVs by AFM and compare their morphology in different HPL preparations.

Upon confirming the presence of EVs in HPLs, future studies could move towards deep characterization of these preparations in the NBA platform for differential proteomics and potentially EVs mediated RNA contents to elucidate the functional activity of EVs in particular for neuroprotection.

5.3 Materials and methods

5.3.1 Preparation of different types of platelet lysates

As mentioned in section 5.2, three different types of platelet lysate preparations were used in this project to characterize their EV content. These samples were prepared in the facilities of Pr. T. Burnouf's laboratory in the College of Biomedical Engineering (CBME), Taipei Medical University (TMU), Taiwan. They were sent under frozen conditions with dry ice and stored upon reception at -80°C. The sample was defrosted for the first assessment in TRPS, protein concentration test, and NBA platform. Several aliquots were made in smaller volumes and stored at -80°C. For replicates, aliquots from this second cycle were used. The method of preparation of each type of platelet lysates used in this project is discussed below.

5.3.2 Preparation of PPL and HPPL

PPL, HPPL, and SCPL were obtained from PC. All necessary permissions for the human PC which was the precursor for preparing the platelet lysates containing EVs were obtained from the institutional review board of TMU. HPPL and PPL were manufactured using a similar process as HPPL is derived from PPL. The PC was centrifuged at 3000x*g* for 30 minutes at 22°C to obtain the pellet of the platelet concentrates. It was then resuspended in $1/10^{th}$ of its initial volume and lysed using a freeze-thaw cycle method. The PC was frozen at -80°C and thawed at 30°C and the cycle was repeated three times in total. The lysed platelet pellet was centrifuged at 4500x*g* for 30 minutes at 22°C to precipitate the cellular and protein debris and the supernatant was collected as PPL. For heat inactivation, PPL was put in a dry bath at 56°C for 30 minutes and then cooled in ice for 5 minutes. This product underwent additional centrifugation at 10000x*g* for 15 minutes at 4°C for clarification and removal of insoluble proteins. The resulting supernatant was collected as HPPL. These preparations were frozen till use.

The SCPL was obtained in a dedicated process from the whole PC without prior isolation of the platelets. As the PC contains anti-coagulants, $CaC1_2$ was added to initiate the coagulation cascade, generate endogenous thrombin, convert fibrinogen into a fibrin clot, and activate and degranulate the platelets. These clots were removed by centrifugation at 6000x*g* for 30 minutes at 22°C and the resulting supernatant was collected as SCPL and aliquoted and stored frozen.

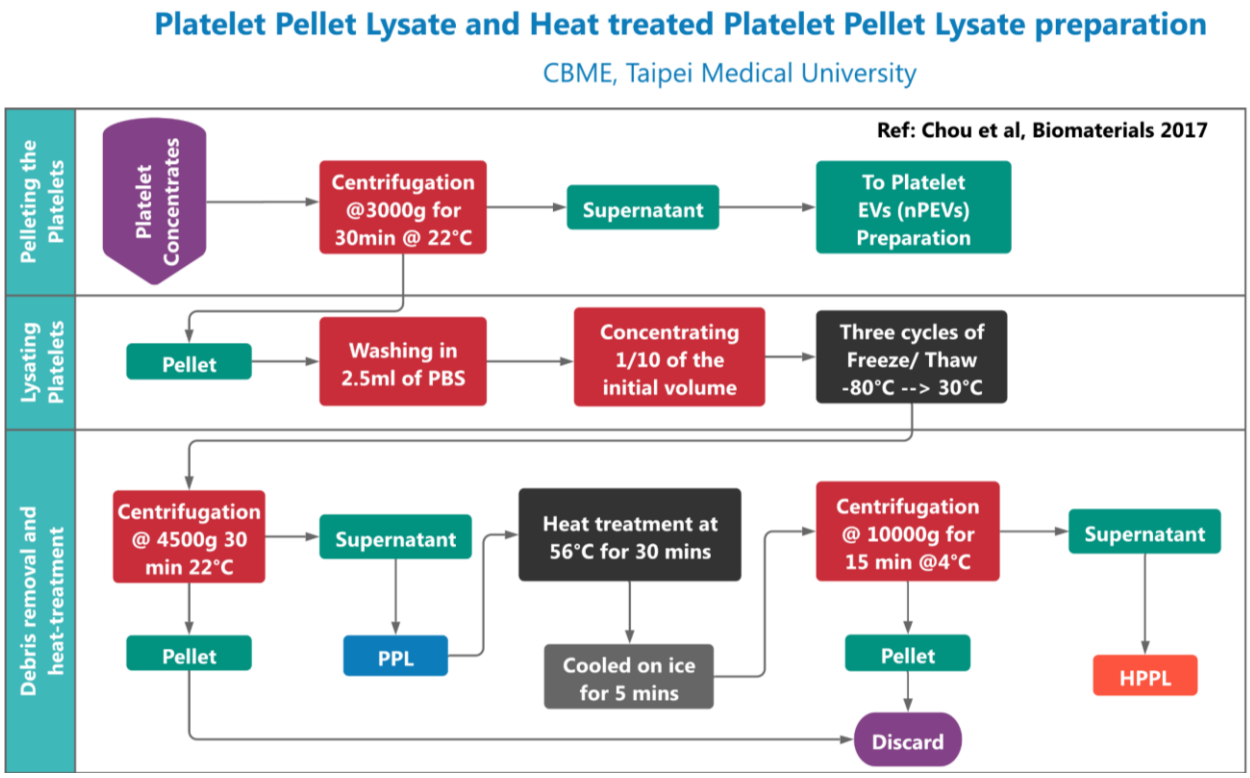

Figure 63 Manufacturing of Platelet Pellet Lysates and heat-treatment step to obtain Heat-treated PPL (HPPL)

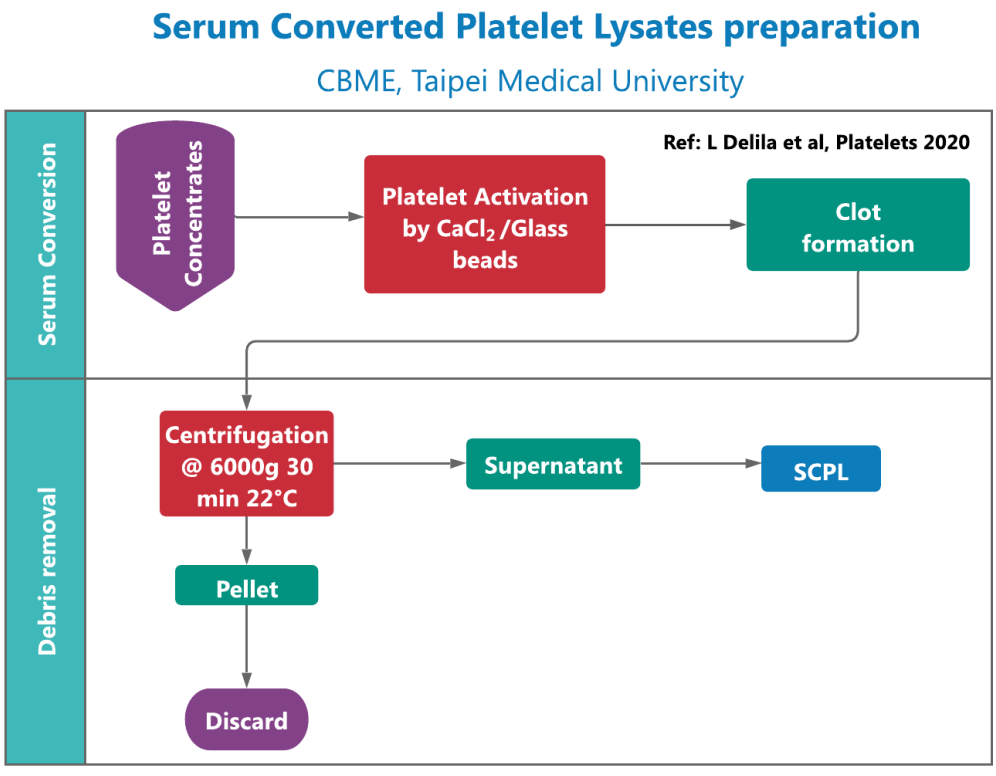

Figure 64 Manufacturing of Serum Converted Platelet Lysates.

5.4 Experimental Design

For characterizing EVs from these platelet lysates in the NBA platform, the biochip was designed with the following ligands: a-CD41, a-CD62p, Annexin V, a-TF, a-CD61, a-CD81, a-CD9, and IgG negative control. Since phosphatidylserine (PS) exposing vesicles and Annexin V interaction is calcium dependant,[208,209] the running buffer contained $CaCl_2$ and was composed of HEPES 10mM NaCl 150mM and $CaCl_2$ 5mM.

5.4.1 Biochip Design

The 4x4 ligand grafting format was chosen thanks to the spotter available for this purpose. Each ligand and negative control were grafted in duplicate in a biochip for reproducibility. Three replicates of such biochips for each type of platelet lysates were performed.

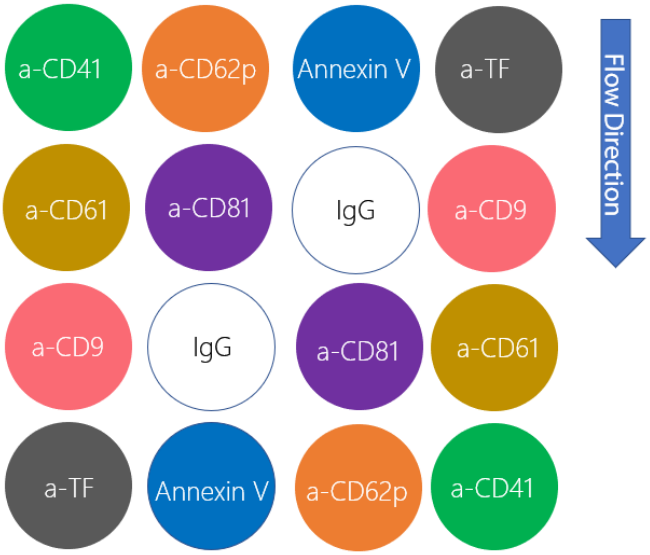

Figure 65 Schema of ligands grafted on the chip, for a HPL investigation in NBA platform

5.4.2 Choice of ligands

The differential expression of EVs in different preparations of HPLs was studied in the NBA to find out the level of EVs expressing different markers. Therefore, the choice of markers was done to reflect EVs from two forms of platelets activated or not. EV markers indicating platelet activation are chosen along with representative markers for small EVs.

5.4.2.1 a-CD41 and a-CD61

Platelet membrane glycoprotein (GP) acts as a mediator of platelet adhesion to the subendothelial matrix and platelet-platelet cohesion. CD41, a protein also known as GPIIb, is

mostly responsible for fibrinogen-dependant platelet aggregation.[210] CD41 also interacts with CD61 (GPIIIa) to form a complex GPIIb/IIIa which acts as a substrate where fibrinogen, fibronectin, and von Willebrand Factor can bind and mediate platelet adherence. The conformational change of these GPs leading to complex formation is mediated by Adenosine diphosphate (ADP) and Thromboxane A2. Therefore, using antibodies against these GPs could indicate platelet activation. Although the GPIIb/IIIa has different conformations such as active, inactive and ligand-bound, the choice of monoclonal antibody clone was employed in the context of demonstrating the technical capability of the NBA platform rather than targeting a particular configuration of the protein.

5.4.2.2 a-CD62p

CD62p is a transmembrane protein which is also called P-selectin. Platelets contain many compartments such as α-granules, dense granules, and lysosomes. CD62p is found in α-granules. It plays important role in platelet recruitment and aggregation. Platelet activation by thrombin, ADP, or Type II collagen could result in the release of CD62p.[211,212] Thus, this marker is essential to identify platelet activation.

5.4.2.3 a-TF

Tissue Factor (TF) also called CD142 has a central role in hemostasis and thrombosis. TF becomes exposed by the vascular endothelium to the blood upon injury and binds to plasma factor VIIa, and the resulting complex initiates a series of enzymatic reactions leading to thrombin generation, clot formation, and vascular sealing.[213] TF-dependent assembly of coagulation proteases on vascular cells activate protease-activated receptors, which contributes to inflammation, angiogenesis, and metastasis.[214] TF could therefore serve as a marker of activation and thrombosis.

5.4.2.4 a-CD81 and a-CD9

CD81 and CD9 belong to the tetraspanins superfamily and are known as integrins. They are classically considered markers of small EVs of endocytic origin.[215] They are used in this study as a measure to qualify small EVs in the HPLs.

5.4.2.5 Annexin V

Annexin V is a protein that has a high affinity to PS in presence of Ca^{++}. Several apoptosis assays use annexin V to detect PS exposure.[216,217] The PS is predominantly present in the inner leaflet of the plasma membrane, and it is translocated to the outer membrane by

enzymes such as floppase and scramblase. This plays a vital role in the biogenesis of the microvesicles as the phospholipid asymmetry leads to blebbing of the plasma membrane (PM) and eventual separation from the PM as a structurally unique microvesicle[32] which was also defined as microparticles. It is therefore utilized to detect platelet-derived microvesicles in the HPLs.

5.5 Determining the experimental parameters

Since a-CD61 had been used for the first time in the laboratory, the grafting pH was tested in a preconcentration experiment in Biacore 3000 SPR system. The working principle of Biacore and the method of preconcentration is discussed here.

5.5.1 SPR Biacore 3000

The Biacore™ SPR system (GE Healthcare) monitors the change in plasmon angle upon biomolecular interaction. The apparatus consists of the following components.

- Two fluid delivery pumps. One for handling the flow of analytes in the fluidic channel and the other for managing the injections from the autosampler.
- An autosampler. This module is an automated injection system programmable in the computer such as the location of the analyte and the flow conditions.
- An integrated microfluidic cartridge consisting of delivery channels, loops, and valves to control the flow in a different channel. This part forms four different channels against the gold surface. The biochip is placed in a cartridge, and it is automatically docked/undocked using a controller.
- An optical system and detector for monitoring the surface plasmon angle.

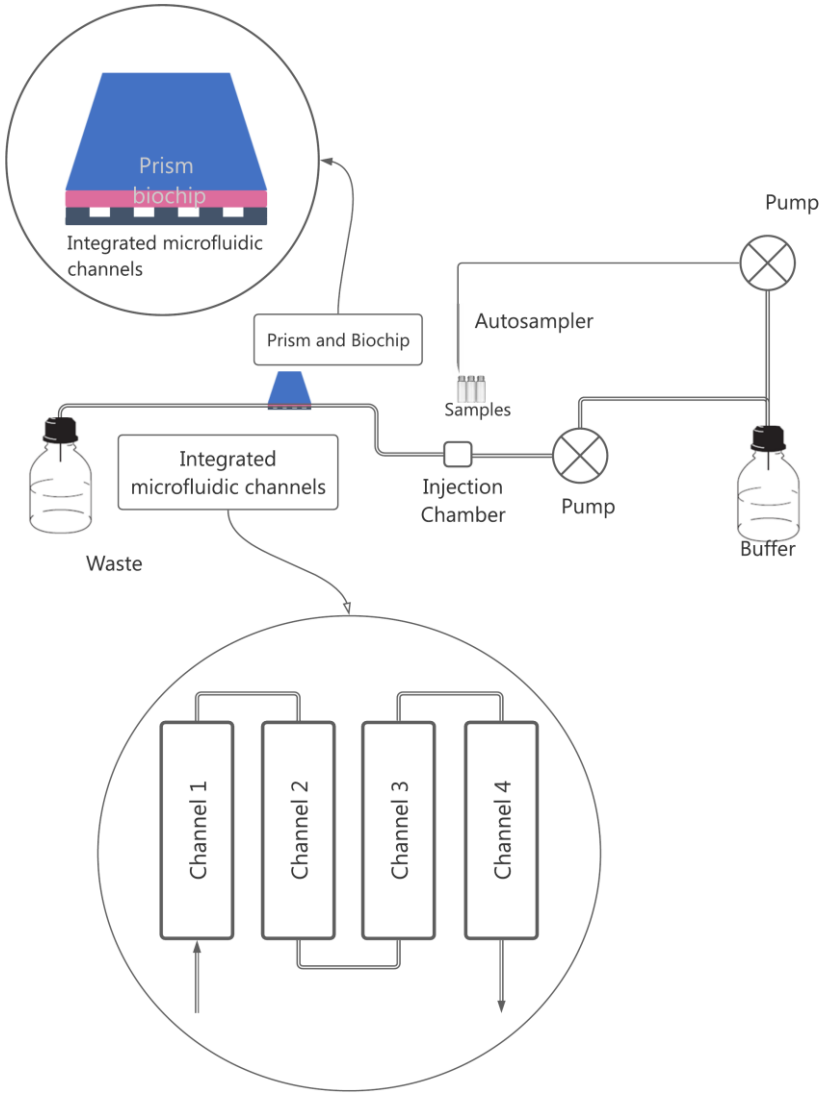

Figure 66 Schema and passage of sample and buffer in the Biacore 3000. This scheme describes the plasmonic sensor setup and the fluidic cartridge, and the layout of flow channels.

The Biacore™ system has an autosampler setup that is controlled by a microprocessor which also handles the fluidic supply and signal processing. The autosampler can dispense samples or reagents from the vials in the supply rack and is connected to the connector block of integrated microfluidic channels (IFC). The fluid cartridge forms four channels of approximately $1mm^2$ each, the IFC has control valves that can operate the channels so that one can either work exclusively in one channel or collectively in 2, 3, or 4 channel formats. The channels have a height of 20 μm. The optical setup has a Light Emitting Diode (LED) source of a wavelength of 760 nm and the reflected light from the prism is detected on a photodiode.

As the system detects the angle of minimum reflectivity during the interaction, the result is reported in Response Units (RU). The change in angle ($\Delta\theta°$) is measured in degrees

and 1000 RU corresponds to 0.1 ° of Δθ °. The quantification of plasmonic angle shift is established as 0.1 ° shift corresponding to 1 ng/mm^2 by Stenberg et al.[171] The measurements in the Biacore system have a resolution of 1 RU. Thus, in principle, the SPR system has a LOD of approximately 1 pg/mm^2. The SPR angle is determined at a frequency of 160 Hz (measurements/s), and then averaged and transmitted to the control software at rates up to 10Hz.

The stream of fluids is managed by a set of pumps. The continuous flow pump handles the running buffer circuit whereas the autosampler pump is used to distribute samples to the IFC. The injection syringe draws samples or reagents from the vials. The autosampler pump has a stroke capacity of 500 µL and can operate at a flow rate from 1µL/minute up to 500 µL/minute. The flow conditions such as flow duration and volume, as well as the location from where the sample has to be drawn, can be programmed in the controller. The mix-up of different reagents in a sequential injection is prevented by a small bubble after each dispense of fluids which is maintained in the tubing. The operation of the apparatus is controlled by a control software interface.

5.5.2 Biacore Biochips

The biochips for the SPR system are manufactured the same way as that of SPRi biochips. The biochip is fixed on a plastic support frame in a protective cassette. The docking of the cassette is controlled by software. During docking, the cassette is loaded in the dedicated port from where the cassette is delivered by a conveyor mechanism. This process presses the sensor chip in place between the glass prism and Opto-interface unit on one side and the IFC flow cell block on the other. Thus, the cavities of the IFC enclosed by the biochip form the flow channels.

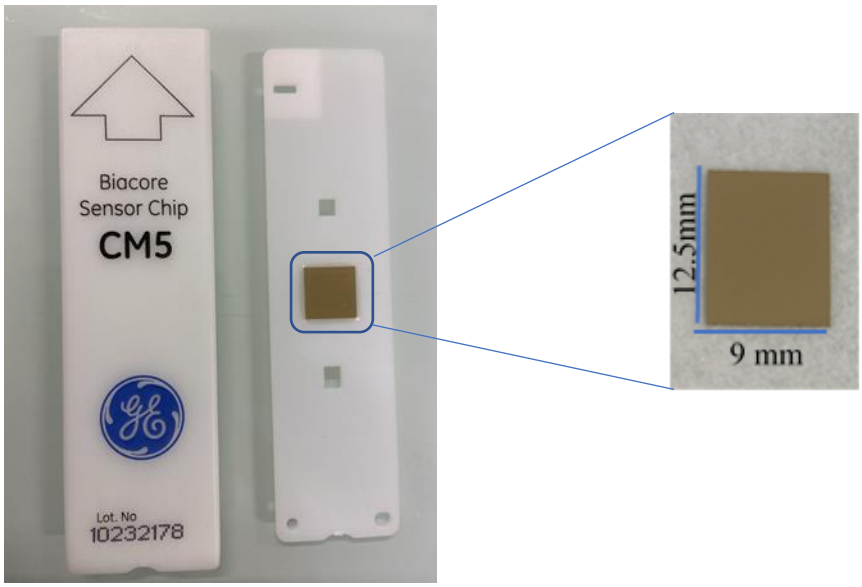

Figure 67 A Biochip cassette and frame that holds the biochip. Inset, a closeup view of the biochip

5.5.3 Optimization of ligand grafting pH

The best pH for immobilizing the antibody was determined in a preconcentration experiment in Biacore. The a-CD61 antibody was tested for the best grafting pH. The SPR biochip was 12.5 mm in length and 9 mm in width and 0.5mm in thickness. The biochip was prepared in a vapor deposition process and functionalized with a mixture of HS-$(CH_2)_{16}$-COOH and HS-$(CH_2)_{11}$-OH (10%/90% mol/mol). The method of biochip fabrication and functionalization is discussed in section 4.7.2.2. The biochip was activated by injecting a 1:1(v/v) mix of s-NHS: EDC at a flow rate of 2 µL/min for 20minutes. The antibodies were prepared at a concentration of 20 µg/mL in acetate buffer pH 4.0 to 6.0. The antibody solutions were injected at a flow rate of 20 µL/min for 30 seconds.

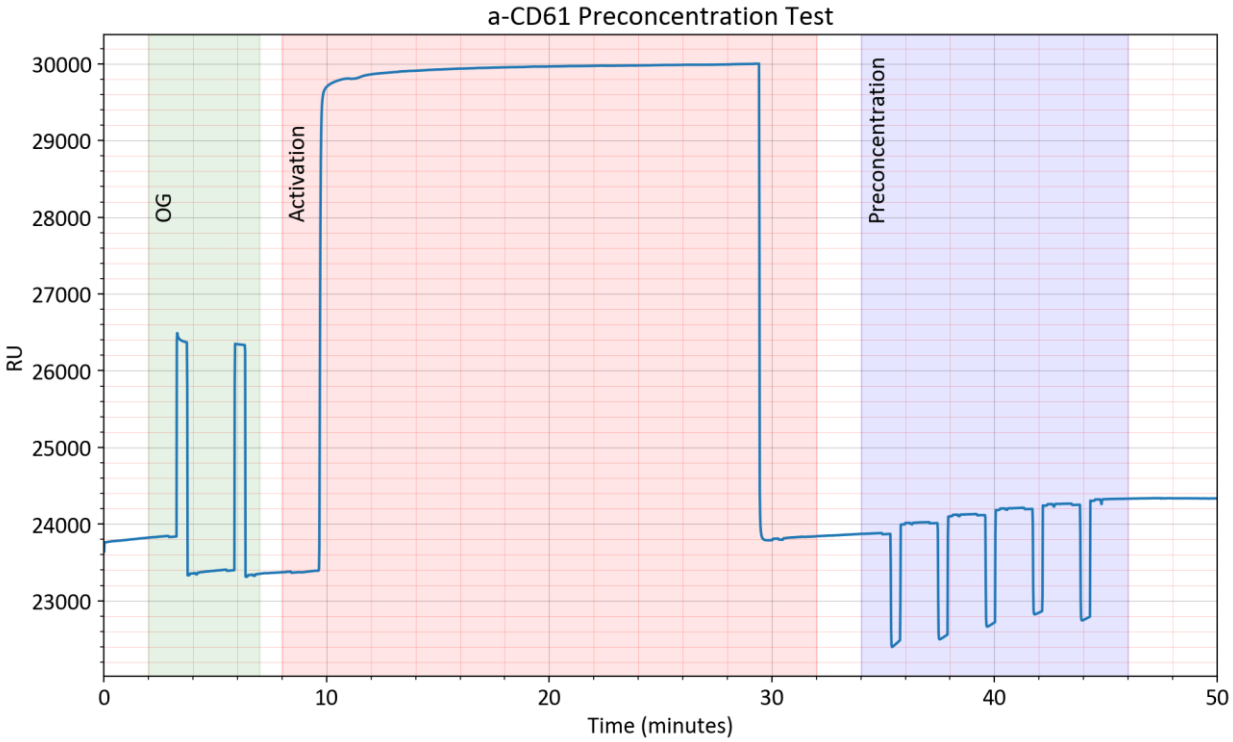

Figure 68 Global sensorgram of a preconcentration experiment in Biacore 3000

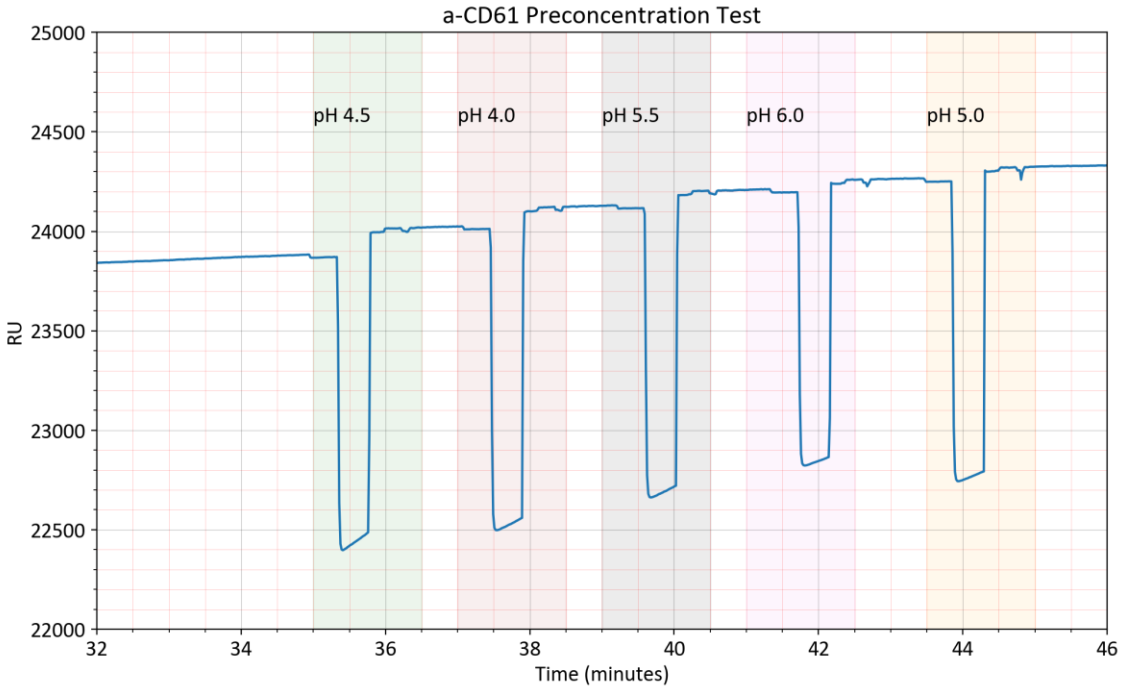

Figure 69 Sensorgram of a-CD61 grafting at different pH

The injections were performed in a random order to avoid interferences from the previous injections and residual effects. For each pH, the net RU was determined by the difference in the RU before and after injection of ligands.

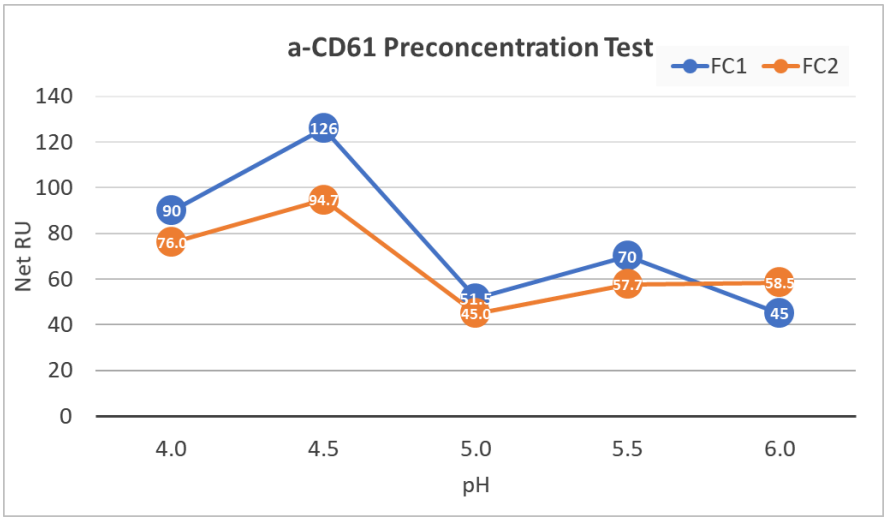

Figure 70 Line chart describing the SPR response in function of the pH for a-CD61 grafting. pH 4.5 shows better response compared with other pH ranges. FC in the legend means flow cell

The measurement was repeated in another flow cell and the best performing pH was confirmed. As can be seen in the chart above, the pH 4.5 condition gave better responses than all other pH ranges. Thus, pH 4.5 was selected as the optimum pH for grafting a-CD61 ligand.

5.6 Differential characterization of HPL

5.6.1 Particle concentrations measurements

Particle concentrations were measured by TRPS. Protein concentrations were also tested using a BCA assay. The methodology of all these techniques is described in section 4.5.3.

5.6.2 SPRi Biochip preparation

The biochip was prepared as per the method described in the previous chapter. a-CD41, a-CD61, a-CD62p were grafted at pH 4.0, Annexin and a-TF were grafted at pH 4.5, a-CD81, a-CD9, and IgG negative control were grafted at pH 6.0. All the ligands were grafted at 200µg/mL for 30 min and under an ultrasonic bath at 37 kHZ and 30 % power.

5.6.3 SPRi Experiments

The biochip was passivated in the same manner as described in the previous chapter. Initially, two injections of RSA at 200 µg/mL at pH 4.5, and an ethanolamine injection to passivate and deactivate the biochip. All the HPL used in this project were from the same batch of PC (batch number 12). In the EVs capture step, the working angle was chosen to be sensitive for a-CD61 in all the experiments. The HPLs was injected for 10 minutes at a flow rate of

20µL/minute. The samples were diluted by 1000-fold in running buffer and injected once. The SPRi experiment was carried out at 25 °C. The biochip was fixed with glutaraldehyde 0.5% (v/v) and stored at 4 °C in a sealed container until AFM imaging. The SPRi measurements were carried out at 25 °C

5.6.4 AFM Experiments

AFM images were acquired in contact mode in the air. Several images were acquired at 256 px resolution. Only the images with scan sizes between 6.25 μm^2 and 25 μm^2 were considered for AFM quantification. The location of the spot in the biochip was identified using the mask. At least 50 images/family for each PPL and SCPL. At least 10 images/family for HPPL were performed to have enough EVs for counting and measure their size. EVs were identified in the AFM images by their morphology and their spread. EVs quantification was performed in Gwyddion software with a threshold setting of 8.5 nm for grains extraction. The extracted grains are analyzed using a python program to estimate the size parameters such as height, grains diameter, and effective diameter.

5.7 Results of differential characterization of EVs

5.7.1 HPL characterization in solution

5.7.1.1 TRPS Results

All the HPL preparations were tested in a TRPS system with an NP200 membrane. The CPC 200 calibration particles were used to validate the measurements. PBS 1X with 0.02% Tween was used as the electrolyte in TRPS. Five replicates of HPPL and PPL samples were measured. SCPL was tested in duplicate. All the measurement parameters are depicted in Annex 3. The average concentration, average diameter, and mode diameter are reported. The error bars represent the standard deviation.

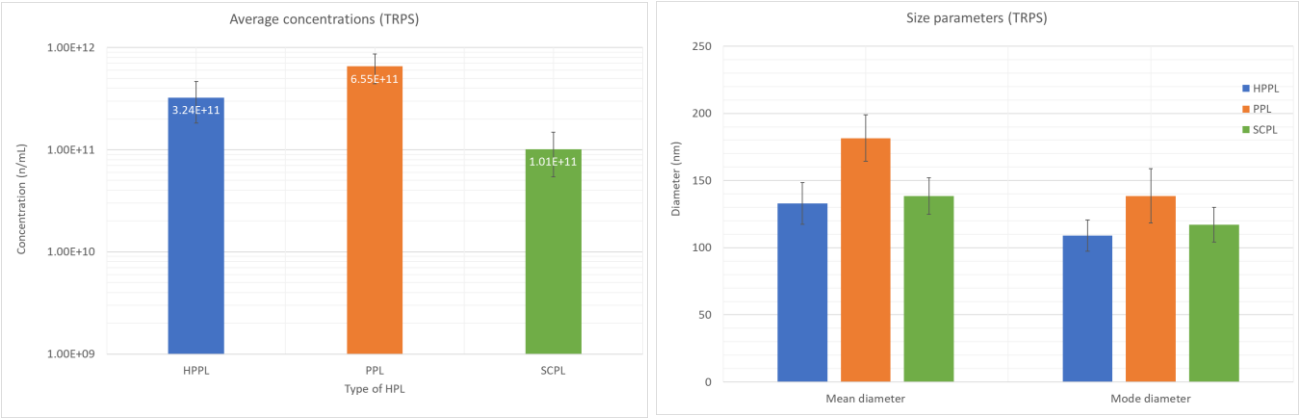

Figure 71 Comparison of concentration and size parameters of different HPL samples. The y -axis scale of concentration data is constructed in a log scale.

As can be noted in the data above, PPL appeared to have nearly double the concentration of EVs than HPPL and six-fold higher than SCPL. As indicated with the bigger mean diameter values, PPL has a high proportion of large objects as well. The histogram of all the HPL looks like a positively skewed distribution. It is noteworthy that these observations are performed in a single nanopore, which is sensitive only to a particular size range. Therefore, the full-size distribution cannot be appreciated with the TRPS results; we can note that PPL has a relatively higher proportion of big objects compared to HPPL and to some extent to SCPL as well. As the different sizes of the EVs are asymmetrically distributed between the different HPLs, it was necessary to adopt the same dilution factor in SPRi measurements for all the HPLs rather than adjusting the dilution factor to have the same absolute concentration levels.

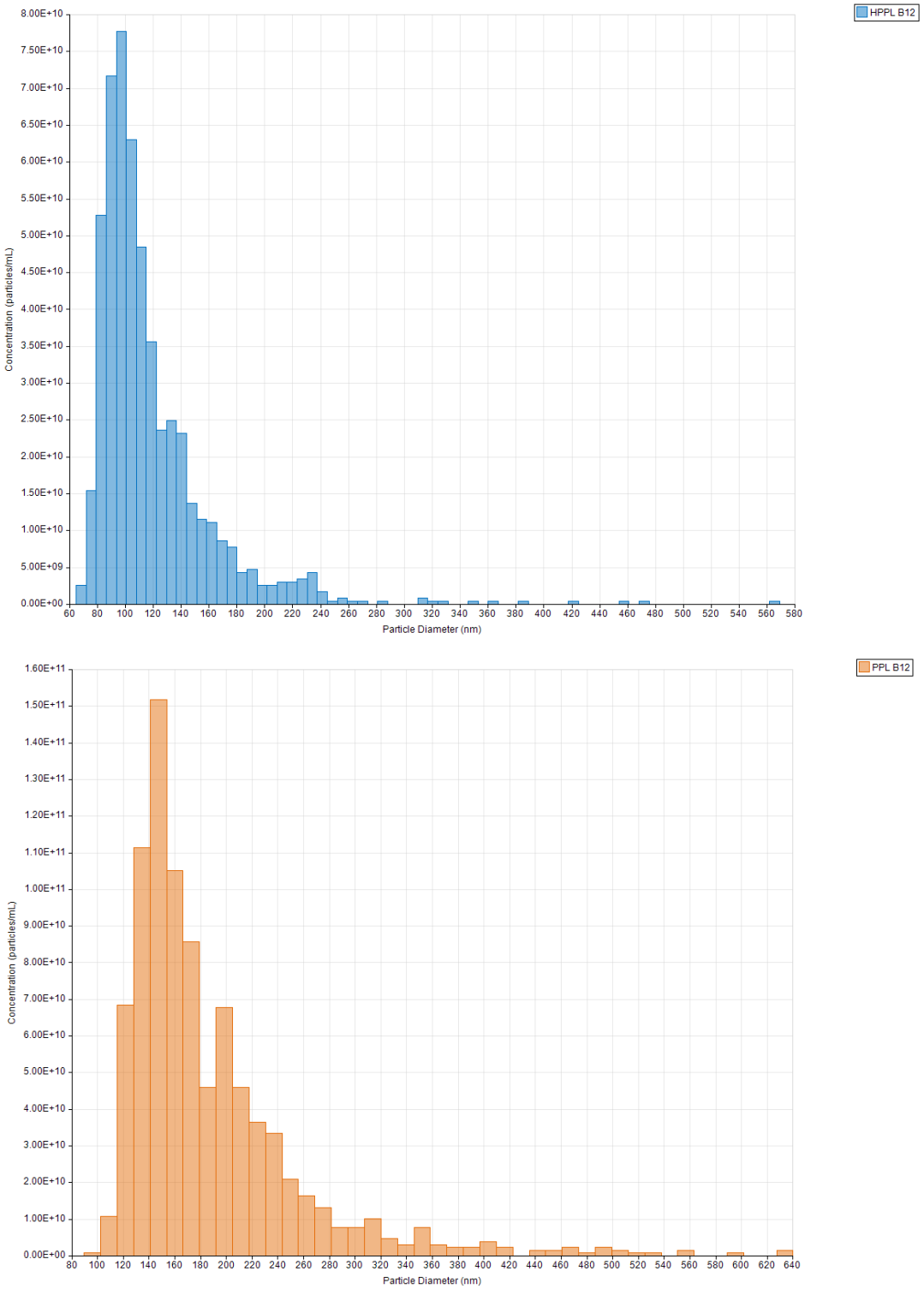

Figure 72 Histogram of size distribution of HPPL and PPL

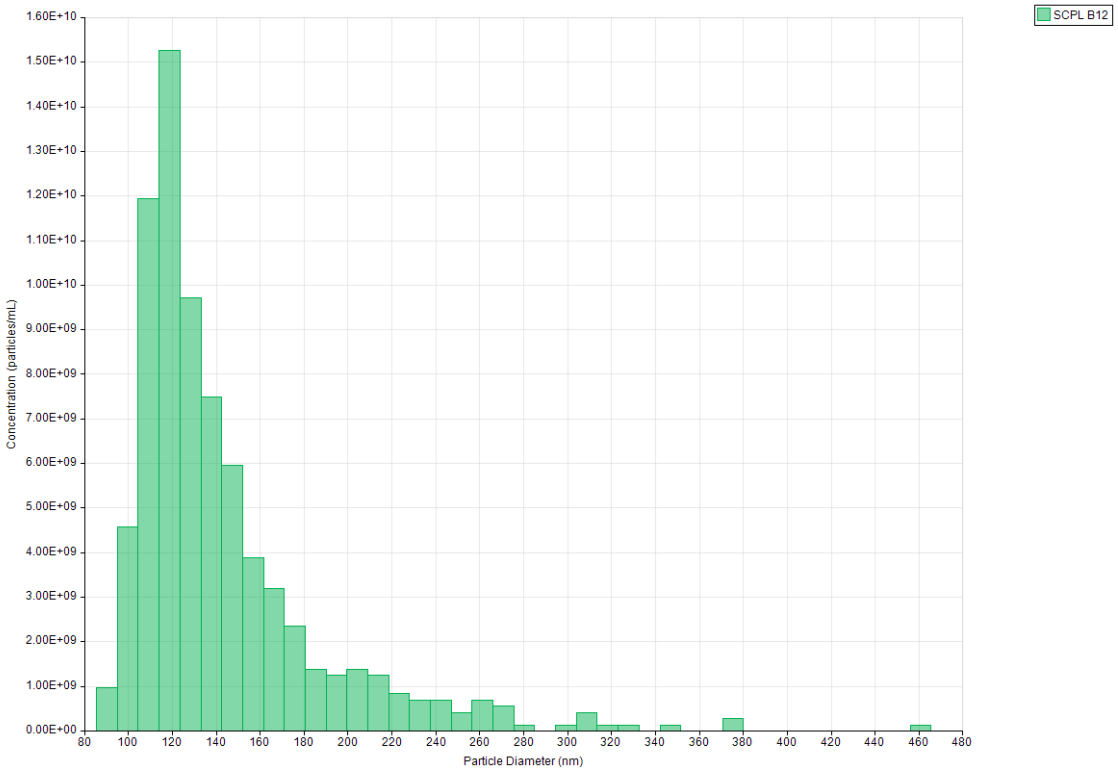

Figure 73 Histogram of size distribution of SCPL

5.7.2 Protein assay results

The BCA protein assay was used to measure the total protein content of the HPLs, using various dilutions of BSA ranging from 200 μg/mL to 2 mg/mL as standard. The optical density at 562 nm was recorded for all the standard samples in a spectrophotometer. The test samples were then measured, and the relative concentration was obtained from the standard curve. Each HPL sample was tested in duplicate. SCPL had the highest protein content. The average total protein of SCPL was 45.69 ± 2.5 mg/mL and PPL contained 16.6 ± 3.1 mg/mL. HPPL had the lowest protein content among the three with 10.25 ± 3.7 mg/mL. Since SCPL contains plasma, this resulted in a higher protein amount. PPL was obtained by the physical rupture of the platelets, still, the secretory granules are not activated, thus resulting in a relatively lower protein amount than SCPL. The heat treatment process should have denatured some protein which further reduces the total protein in HPPL.

5.7.3 SPRi results

In SPRi, the HPL was injected for 10 minutes at a flow rate of 20 µL/min and further investigated in AFM. The total injection was defined in a 20-minute window. The system is started with the running buffer for the baseline. This gave an indication of the drift as well as the noise level of the blank signal. The injection of HPLs is then performed. The binding of EVs started from 5 minutes until 15 minutes the valve was switched to running buffer from 15 - 20 minutes and the injection was completed. At the end of the injection, the biochip was fixed with 0.5% (v/v) of glutaraldehyde fixing the EVs and observation in AFM. The SPRi sensorgram of each experiment was plotted with the average of the duplicate of each ligand. Average values of the triplicates of such experiment values were reported as the representative sensorgram of a particular HPL type. The net change in capture (ΔR %) was calculated as follows. The starting value was taken from the average of 0 to 3 minutes and the final value from the average of 16 to 19 minutes. The ΔR % (figure 79) was obtained by subtracting the final and starting values. Average and SD of triplicates are reported for comparability between different HPL types in various ligands.

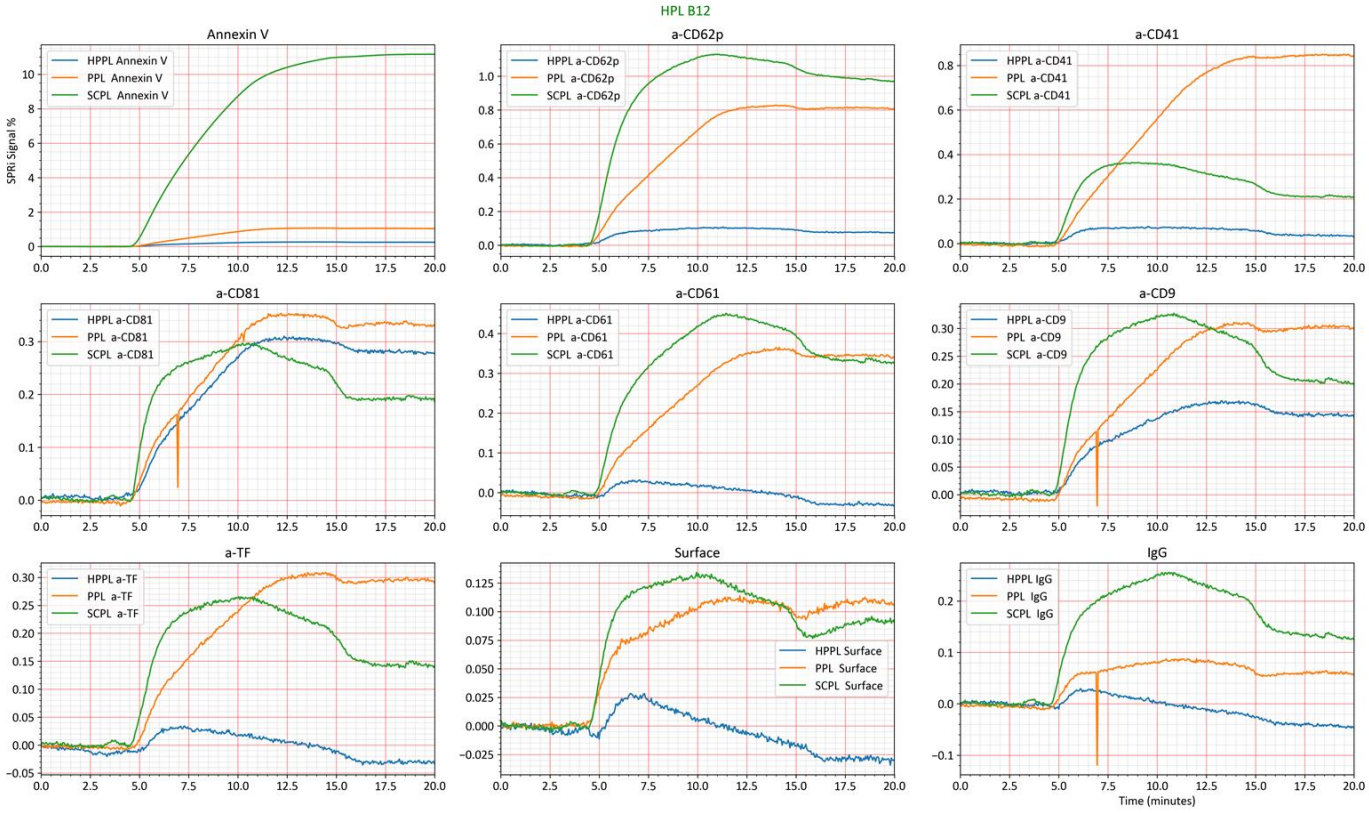

Figure 74 Sensorgram of differential capture of EVs in SPRi. Each block corresponds to a particular ligand. The y-axis scale is not uniform for all the blocks since huge difference in signal between ligands. Samples diluted at 1000x, in a buffer composed of HEPES 10 mM NaCl 150 mM and $CaCl_2$ 5mM.

5.7.3.1 *SPRi Sensorgram for each HPL type*

The following graphs show the average from triplicate experiments in all ligands. Each ligand data was obtained by taking the average of 2 spots of the ligand family. Injections were performed at a dilution factor of 1000x in a buffer composed of HEPES 10mM NaCl 150mM and $CaCl_2$ 5mM. Sensorgrams are presented in the increasing order of complexity. (HPPL, PPL, and SCPL)

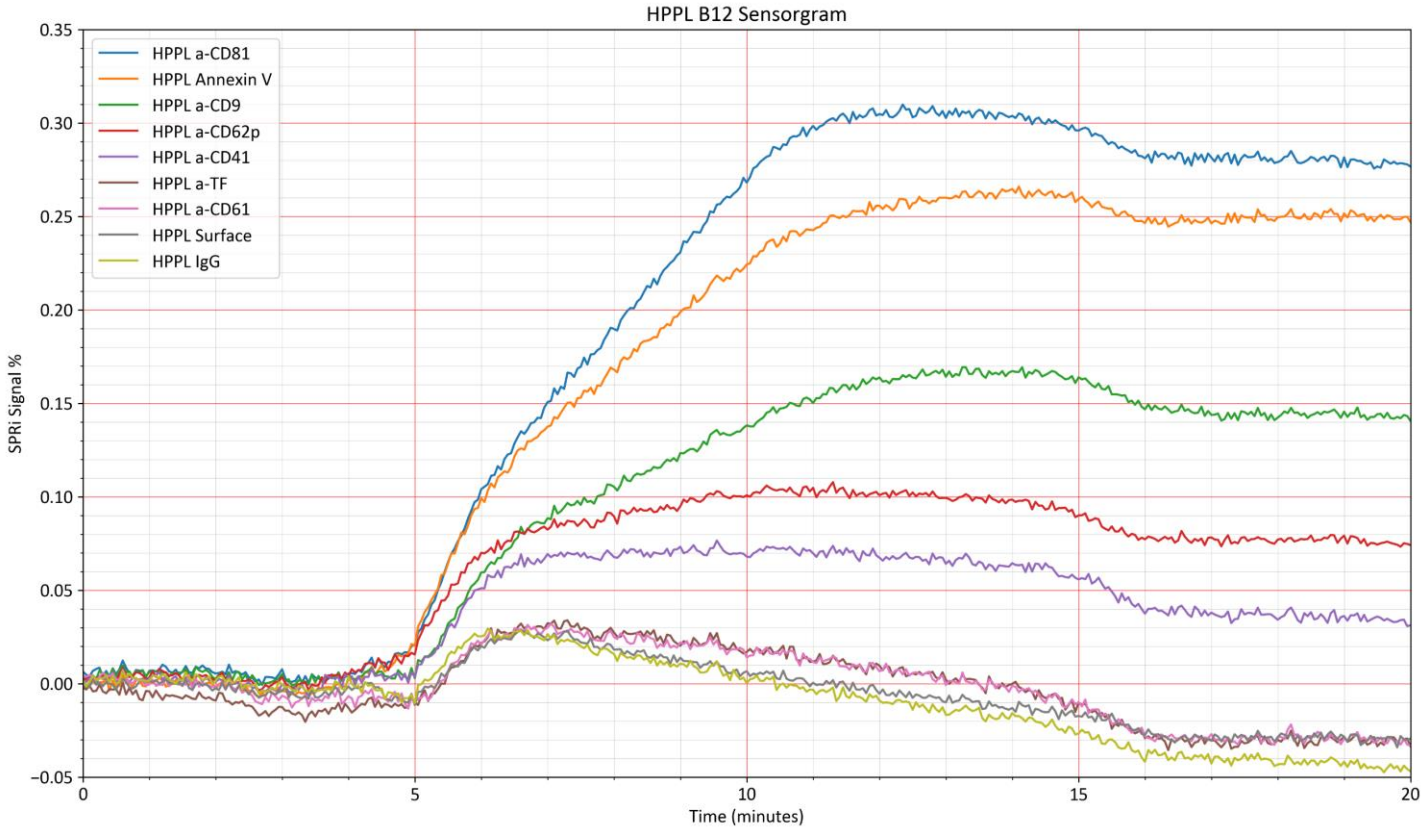

Figure 75 Sensorgram of HPPL in various ligands. This sensorgram is useful in comparing the differential marker expression within the sample itself. The sensorgram is the result of average of three replicates. Each replicate is the average of 2 spots in the biochip. Samples diluted at 1000x, in a buffer composed of HEPES 10 mM NaCl 150 mM and $CaCl_2$ 5mM.

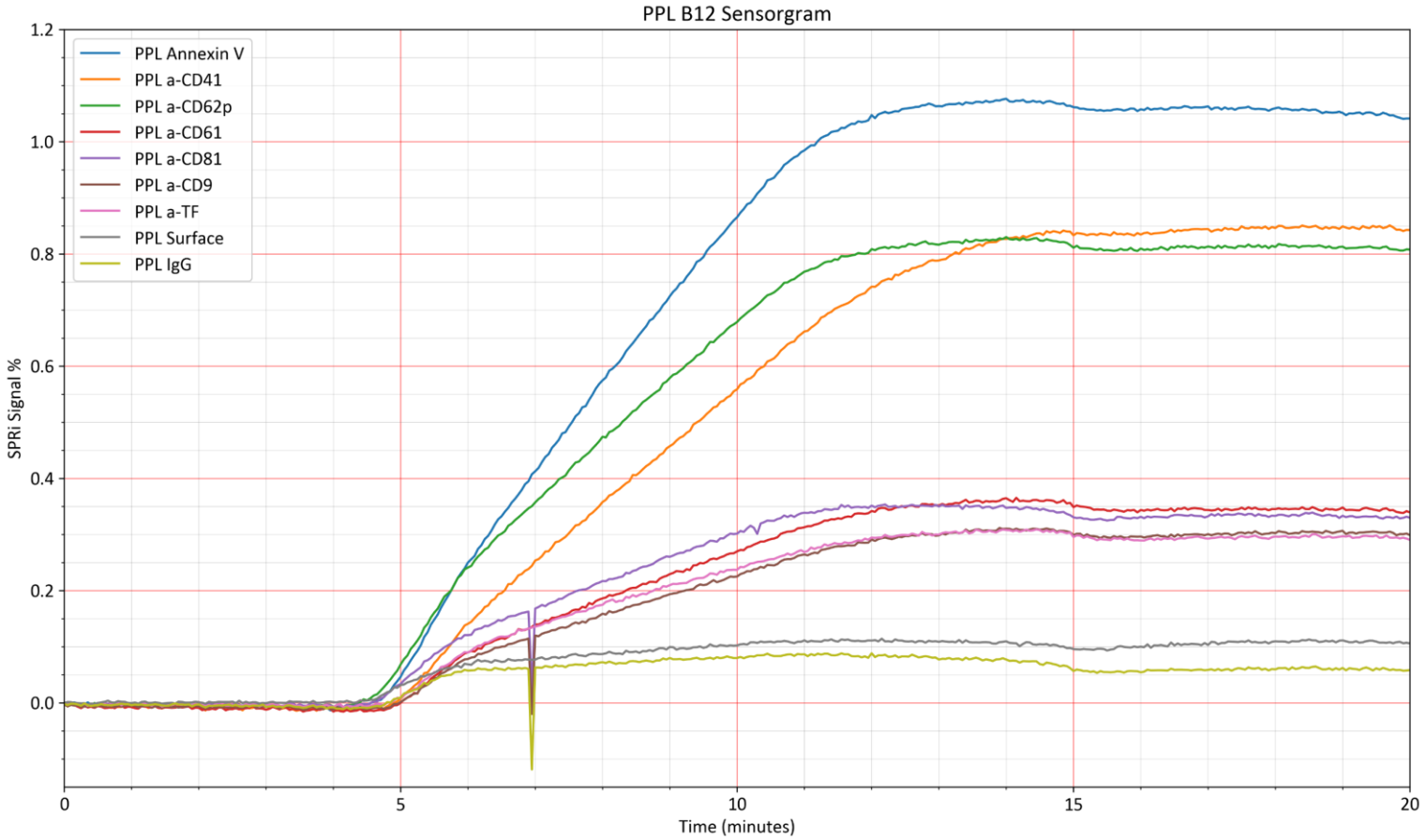

Figure 76 Sensorgram of PPL in various ligands. This sensorgram is useful in comparing the differential marker expression within the sample itself. The sensorgram is the result of average of three replicates. Each replicate is the average of 2 spots in the biochip. Samples diluted at 1000x.

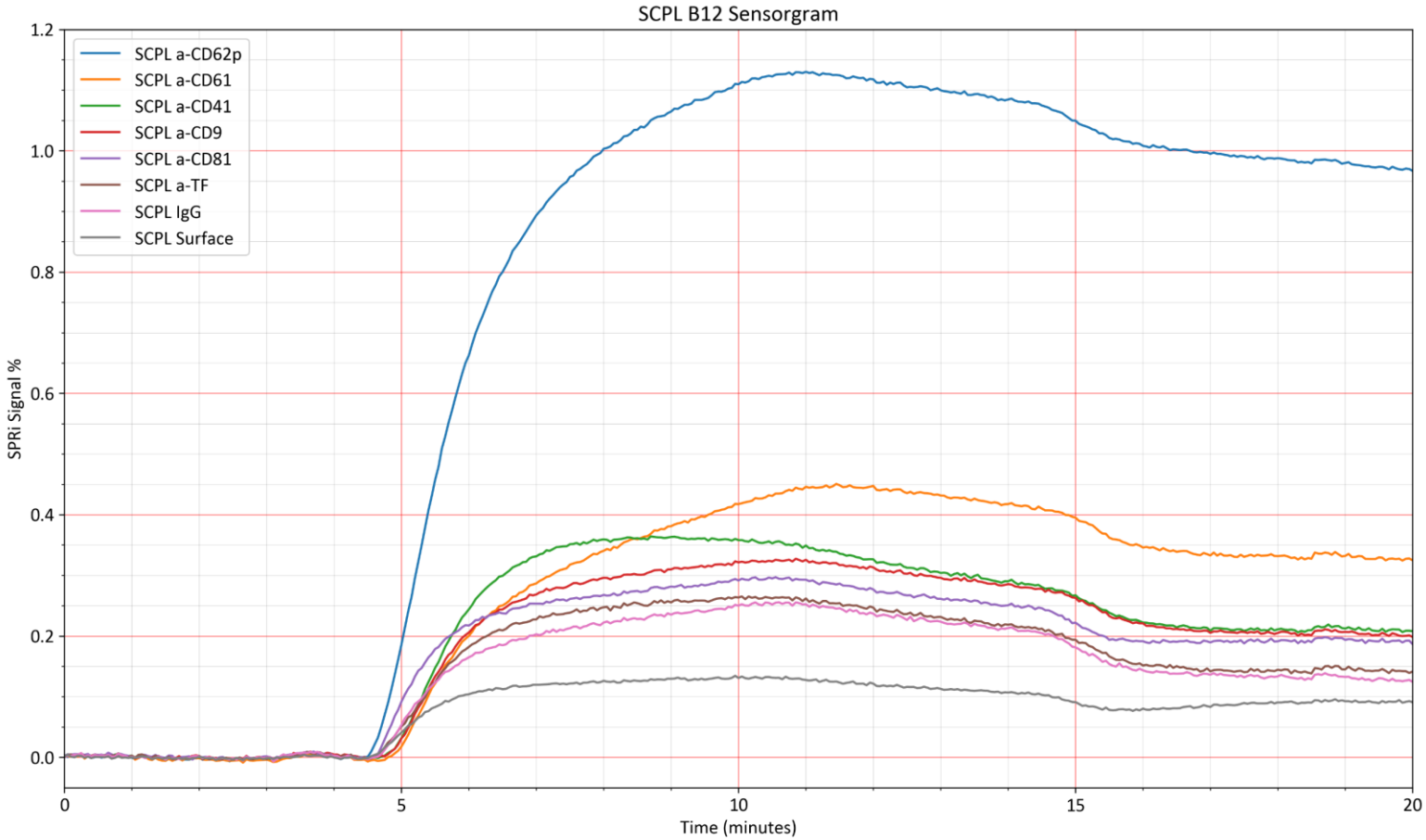

Figure 77 Sensorgram of SCPL in various ligands. This sensorgram is useful in comparing the differential marker expression within the sample itself. The sensorgram is the result of the average of three replicates. Each replicate is the average of 2 spots in the biochip. Samples diluted at 1000x.

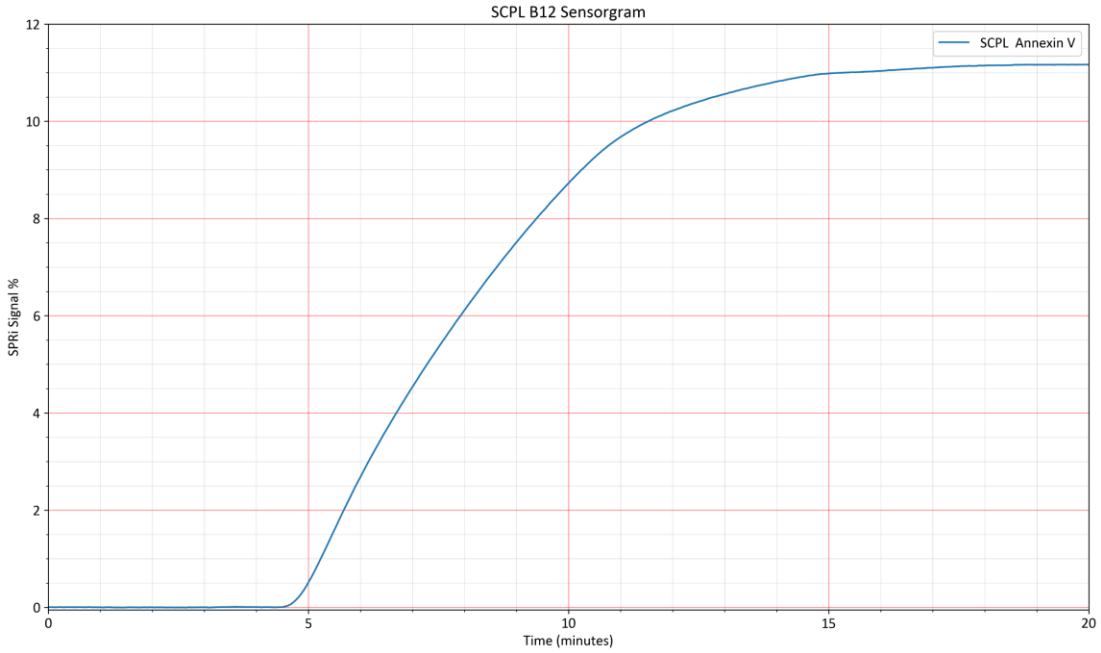

Figure 78 Response on Annexin spots for SCPL sample. This sample showed binding with Annexin V. The injection is performed at a dilution factor of 1000x.

5.7.3.2 Capture level on different ligands between HPPL, PPL, and SCPL

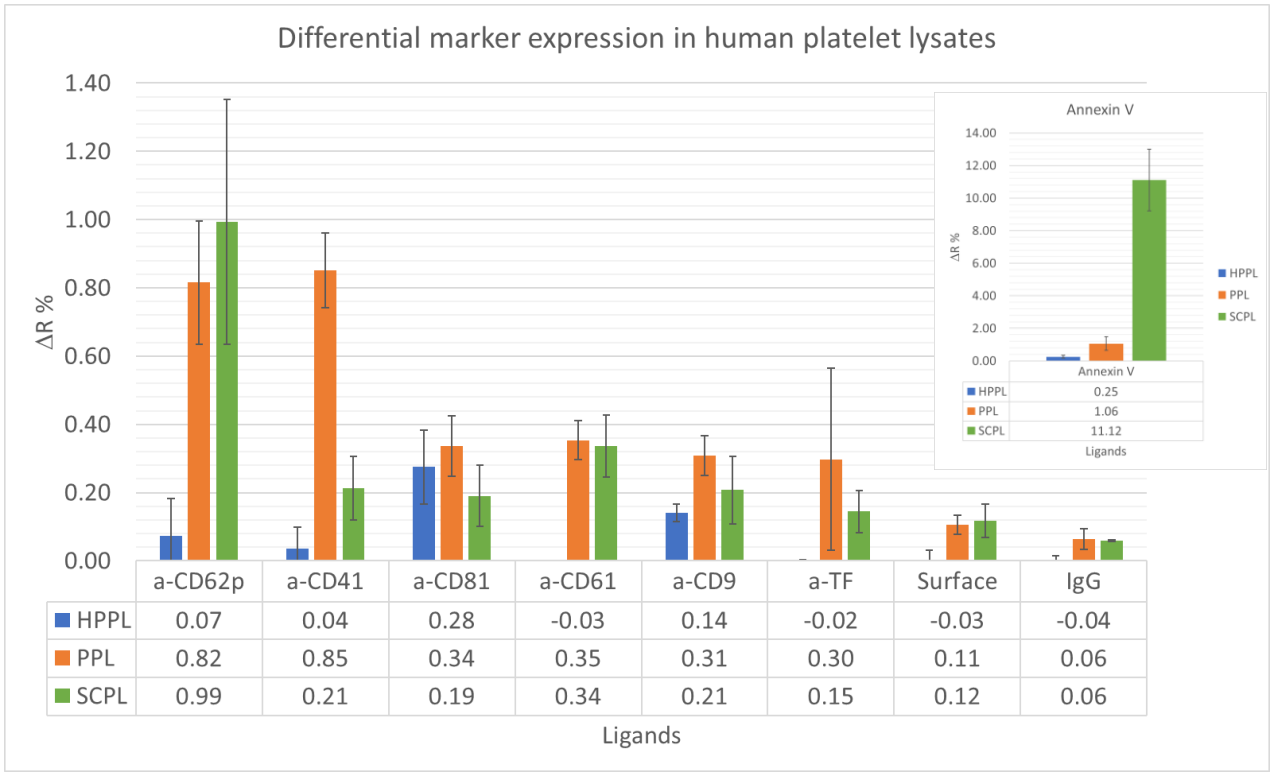

	a-CD62p	a-CD41	a-CD81	a-CD61	a-CD9	a-TF	Surface	IgG
HPPL	0.07	0.04	0.28	-0.03	0.14	-0.02	-0.03	-0.04
PPL	0.82	0.85	0.34	0.35	0.31	0.30	0.11	0.06
SCPL	0.99	0.21	0.19	0.34	0.21	0.15	0.12	0.06

Figure 79 Net capture level in different ligands of various HPL preparations. The bar chart is represented as the average of 3 measurements (also the value in the data table) and the error bar is the SD between measurements. Inset picture shows Annexin V ligand for better comparability of other ligands.

5.7.4 Interpreting the SPRi results

Each ligand in each HPL type showed different affinity and capture levels. Accordingly, the sensorgram was arranged from higher to lower capture levels for each HPL family. The positive expression of a particular marker was characterized if it had at least 2 times more net capture level than the IgG negative control. From the data above (the bar chart in figure 83 and all the sensorgram), it can be seen that HPPL showed weak capture compared to PPL and SCPL for all ligands. PPL showed a positive response in all the markers studied. SCPL had a small non-specific interaction compared to PPL and HPPL.

5.7.5 Differential marker expression in HPL

The differential marker expression in HPL samples could be determined considering the SPRi data alone and it can be classified into two groups.

- The first group was a group of markers that were expressed in all the three types of HPLs tested. Annexin V, a-CD62p, a-CD81, and a-CD9 are positive in HPPL, PPL, and SCPL.
- The second group ligands such as a-CD41 and a-CD61, and a-TF were present only in non-heat-treated samples. They were found in PPL and SCPL but not in HPPL.

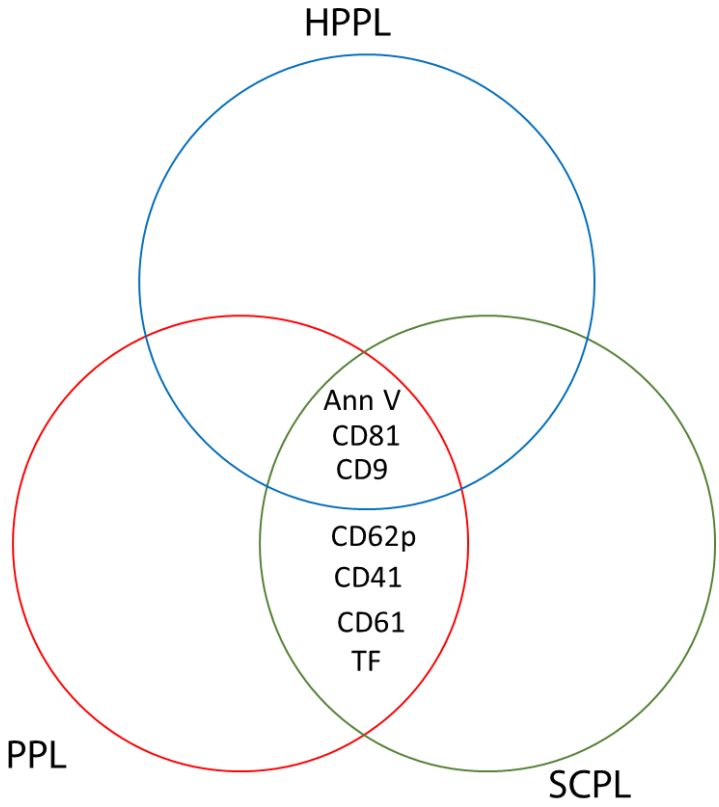

Figure 80 Differential marker expression enabling capture in different type of HPL preparations from SPRi data

5.7.6 AFM Measurements

Since HPPL has resulted in weak capture in SPRi, two additional injections at a dilution factor100x were performed to have enough materials available to be investigated in AFM. The AFM images of HPPL were therefore considered only for a qualitative evaluation and the quantification data from HPPL was not compared with PPL and SCPL. PPL and SCPL biochips were prepared with only one injection at a dilution of 1000x. The injection was carried out at a dilution factor of 1000x and fixed with 0.5% (v/v) of glutaraldehyde. The biochips were stored at 4°C until AFM image acquisition.

5.7.6.1 *AFM images of HPPL*

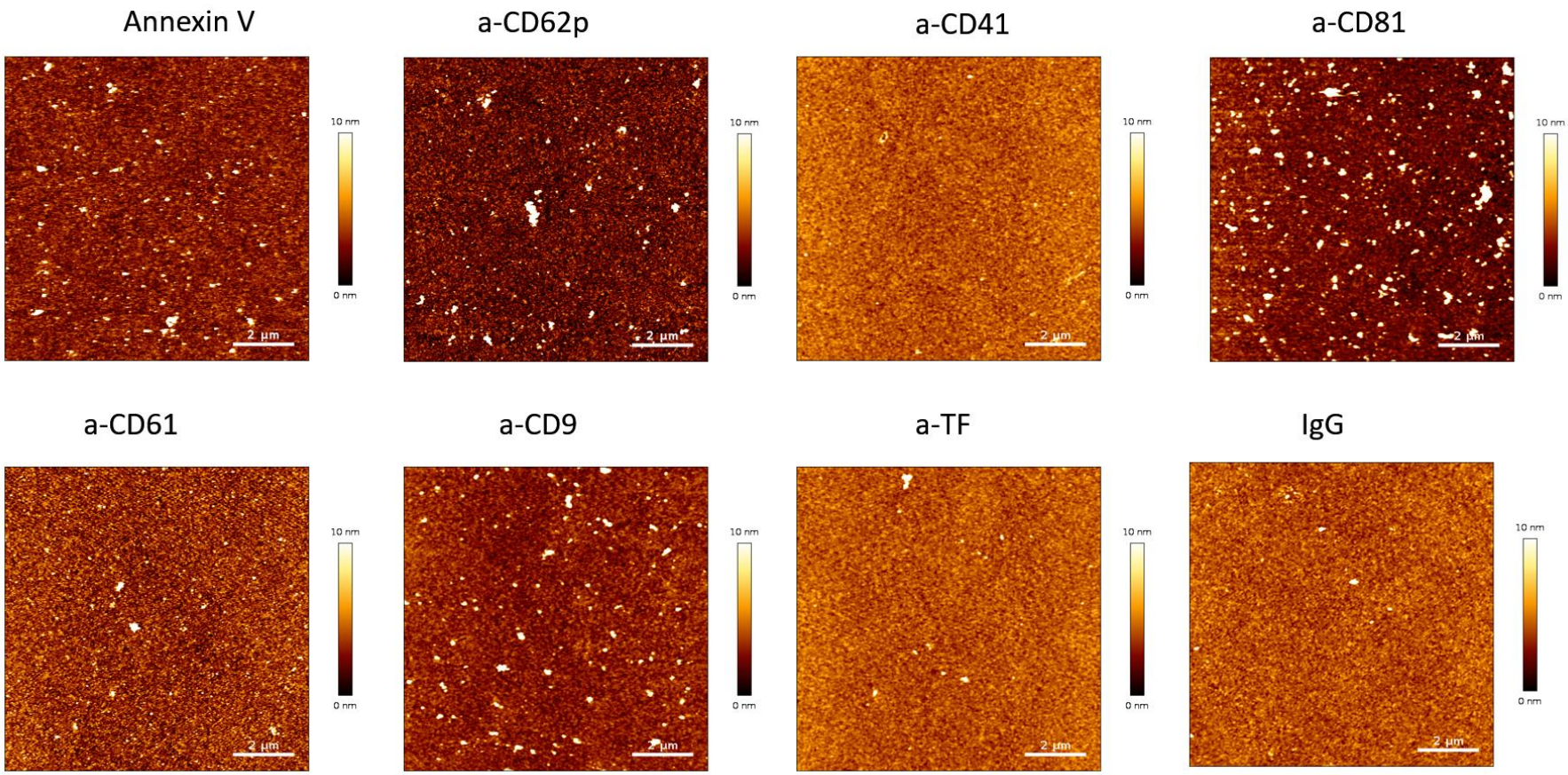

Figure 81 representative AFM images on different ligands after 3 injections of HPPL sample. Since HPPL showed weak capture, The biochip was prepared with 3 injections. The first injection was performed with a dilution factor of 1000x and 2 additional injections at a dilution factor of 100x are performed to facilitate more capture. (Not shown in SPRi data)

5.7.6.2 *AFM images of PPL*

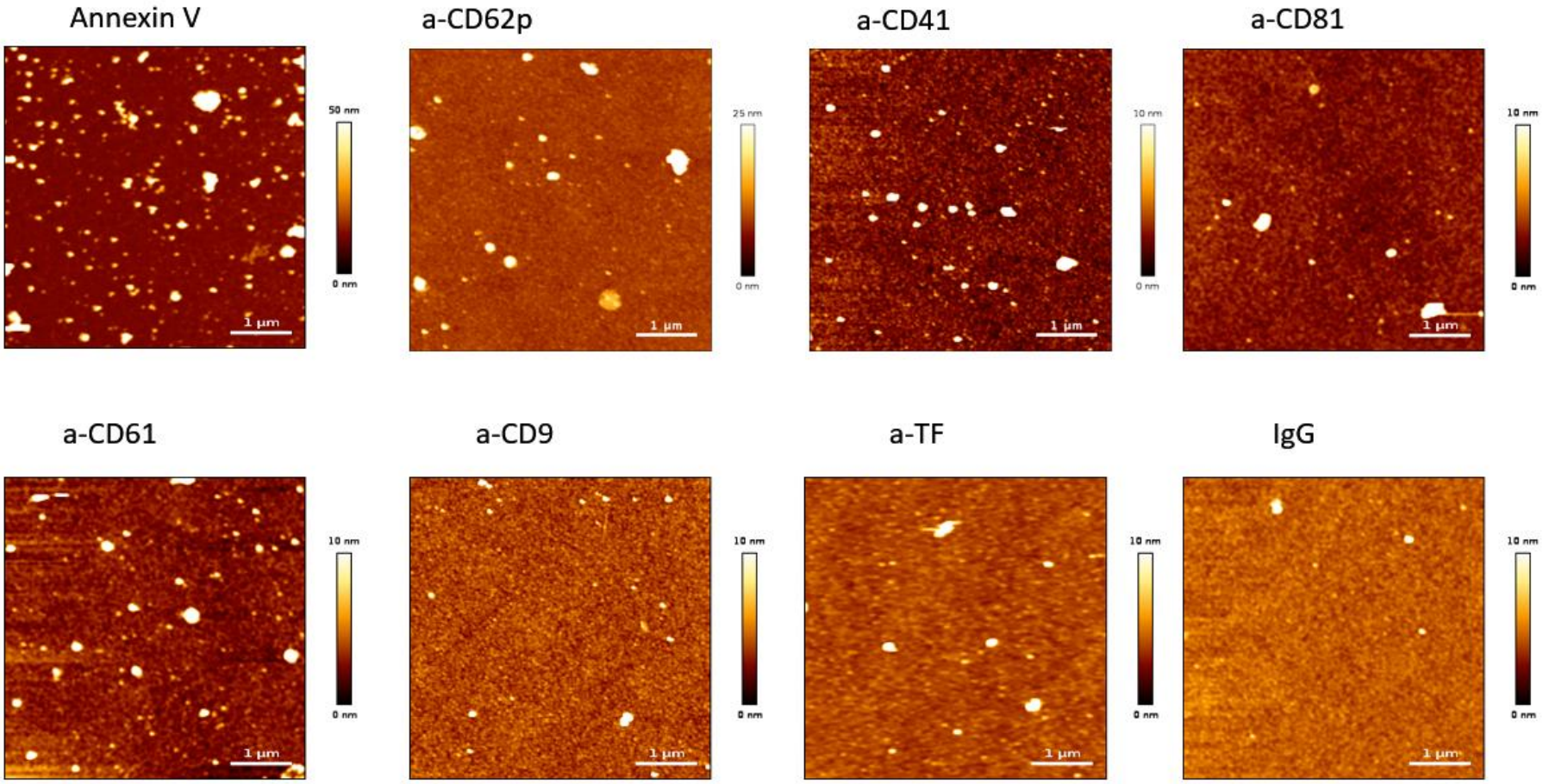

Figure 82 AFM scans of PPL sample captured in different ligands. PPL sample is injected with a dilution of 1000x

5.7.6.3 AFM images of SCPL

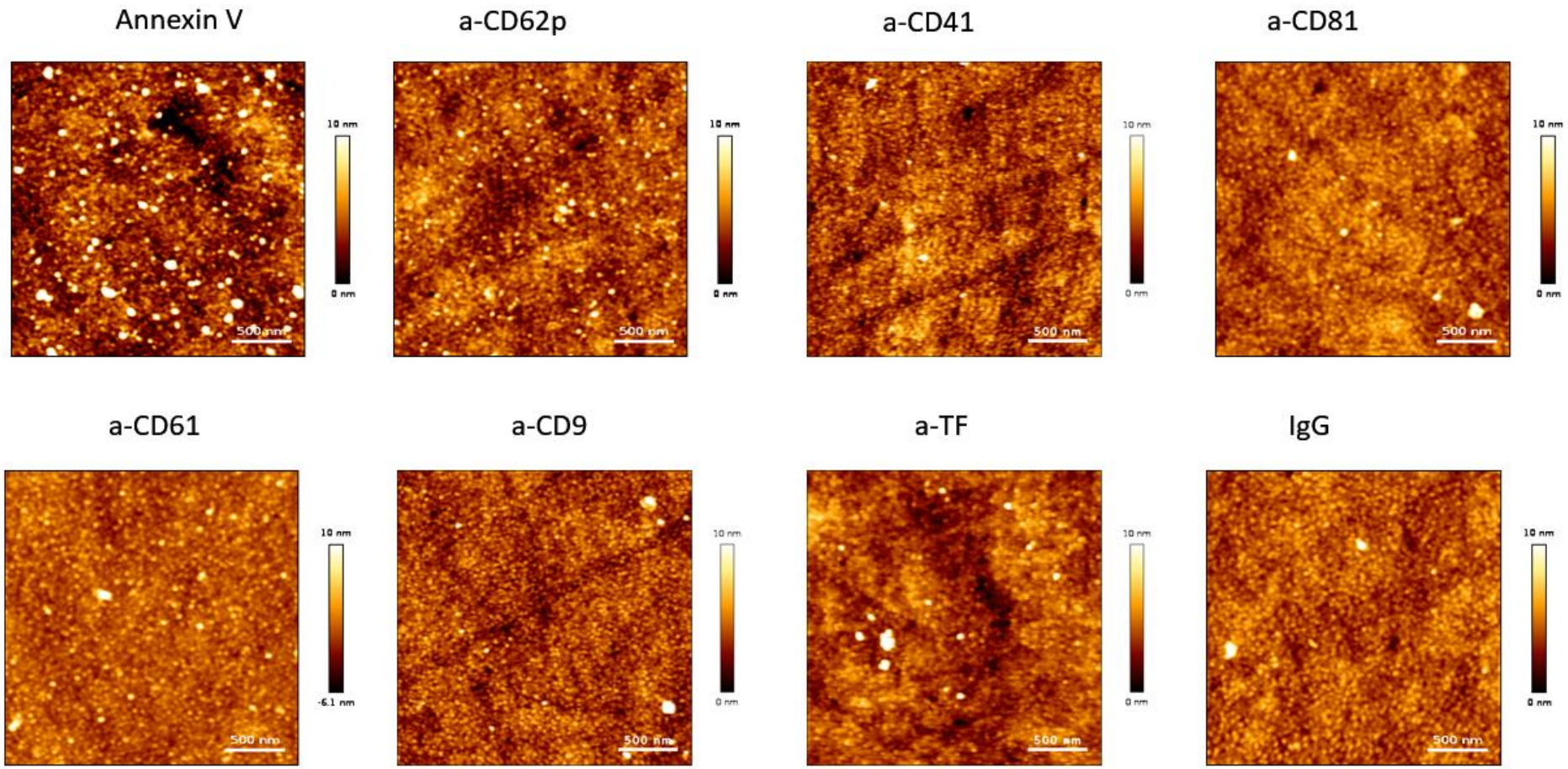

Figure 83 AFM images of EVs captured from SCPL sample. The biochip was prepared by injecting SCPL with a dilution of 1000x.

5.7.7 Qualification of EVs in AFM images

EVs in AFM images were characterized by their morphology and their size. As can be seen in the AFM images, the HPPL sample showed EVs morphology only in a few of the ligands. Some small spherical aggregated objects were found in a-CD81 and a-CD9 images. However, given that they showed weak signal in the SPRi, it is likely that the HPPL contains very little to no EVs. It can be argued that the heat treatment might have denatured the structure of the EVs.

In PPL, EV structures were observed in Annexin V, a-CD62p, a-CD41, a-CD81, a-CD61, a-CD9, and a-TF ligands with varying density. In Annexin V and a-CD61 spots together with large EVs were also observed. In Annexin spots, the big EVs were observed around 300-400nm with a height ranging from 80-120nm. The small objects were found with a diameter around 150nm and a height around 35nm.

The AFM images in Annexin V, a-CD62p, and a-CD61 spots in SCPL were seen with debris-like structures together with the EVs. These small objects are less prevalent in other ligands e.g., and a-CD41, a-CD81, and a-TF spots. Interestingly, these ligands also had capture levels close to that of IgG control spots in SPRi. This suggests the small objects were indeed specific to the sample and Annexin V, a-CD62p, and a-CD61. However, this observation needs to be confirmed in a dedicated study using a complementary approach.

5.7.8 Quantification of EVs in AFM

The EV quantification was performed using Gwyddion. The background was filtered with a threshold of 8.5 nm to extract the grains other than the bio-interface. The density of EVs was calculated for PPL and SCPL and the comparison is given below.

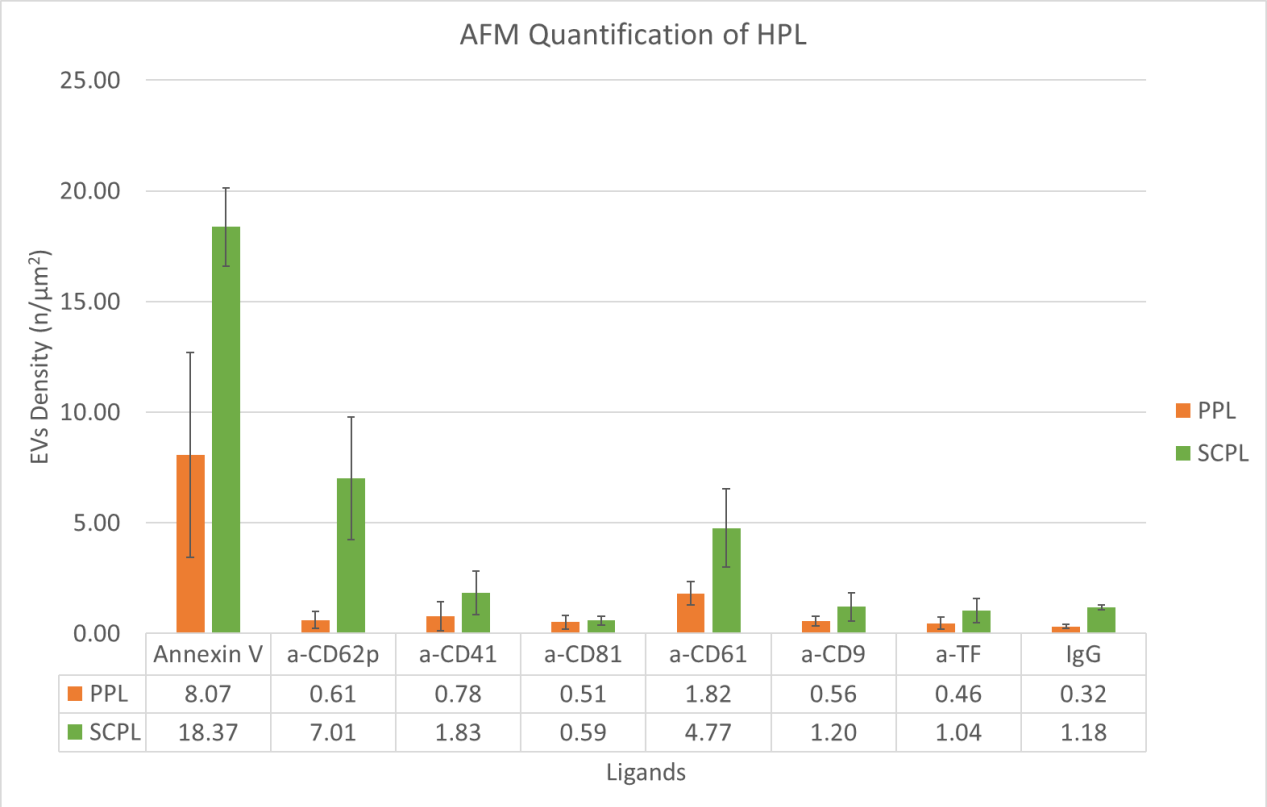

	Annexin V	a-CD62p	a-CD41	a-CD81	a-CD61	a-CD9	a-TF	IgG
PPL	8.07	0.61	0.78	0.51	1.82	0.56	0.46	0.32
SCPL	18.37	7.01	1.83	0.59	4.77	1.20	1.04	1.18

Figure 84 AFM quantification data of PPL and HPPL injected at a dilution factor of 1000x. The data reported here is the average of density data from 3 biochips for each ligand. The standard deviation is reported as the error bars.

5.7.9 Differential EVs expression in HPL

In the "SPRi-AFM" mode of the NBA, both the identification of the EV markers in SPRi and the existence of spherical morphology in corresponding AFM images are needed to be considered that EVs containing a particular marker are present.

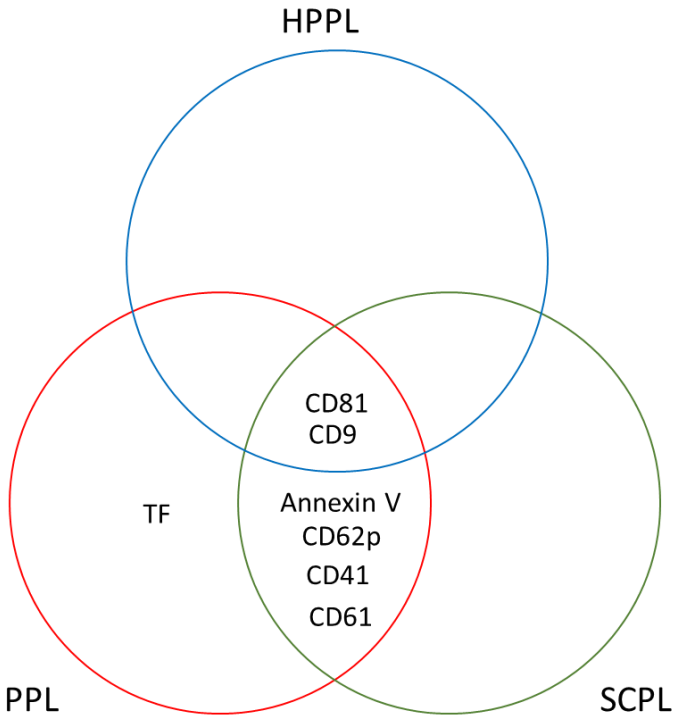

Figure 85 Differential EVs expression in different types of HPLs.

In HPPL, small EVs are present in a-CD81 and a-CD9 spots. Annexin V, a-CD62p are positive in SPRi. However, in AFM they show some objects that do not resemble the EVs morphology. a-CD61 was negative in SPRi, and this spot is seen with objects that do not look like EVs as well. a-CD41 and a-TF were neither positive in SPRi nor contain EVs. Notably, HPPL had undergone several folds of injections compared to PPL and SCPL, which suggests HPPL EVs containing CD81 and CD9 are of less abundance.

PPL showed EV structures for all the ligands. This sample had a positive response in SPRi as well. Therefore, EVs containing biomarkers of CD62p, CD41, CD61, CD81, CD9, and TF as well as EVs expressing PS were present in PPL. Their abundance could be in varying amounts.

Annexin V, a-CD62p, a-CD41, and a-CD61 spots were seen with a clear difference in EVs density than the negative control IgG. Although a-CD81, a-CD9, and a-TF spots show clear EVs morphology, their density (number of EVs per μm^2) was not considerably different from that of IgG. This suggests that there was some degree of non-specificity due to the complexity of the sample.

SCPL showed EV structures on Annexin V, a-CD62p, a-CD41, a-CD61 spots. Particularly, Annexin V, a-CD62p, and a-CD61 spots are seen with a high density of EVs with a lot of small particles. EVs are seen in a-CD81 and a-CD9, and a-TF but at density levels close to IgG. Thus, the data in this study suggest that among the ligands investigated:

- HPPL might contain EVs bearing a-CD81 and a-CD9 in low levels.
- EVs containing TF were present only in PPL at low levels and not in SCPL.
- PPL and SCPL contained EVs expressing PS, CD62p, CD41, and CD61.
- SCPL contained EVs expressing PS, CD62p, and CD61 together with small objects.

6. Conclusion and Prospects

6.1 Establishing analytical performance of the NBA platform

The first project of this thesis aimed at determining the LOD and analytical performances of the NBA platform in the "SPRi-AFM" mode for platelet-derived EVs. With the successful optimization of the sensing properties and then of the performances of the NBA platform, the results should help to determine the best analytical parameters for EVs.

The Ph.D. research project produced useful strategies for reliable EVs characterization:

1. Maintaining various checkpoints throughout the analytical workflow to ensure the measurement quality is reliable and relevant to the object of the study. In the sensing part, this included
    a. Optimized method for defining the ROI,
    b. Selection of plasmonic sensitivity in a uniform manner,
    c. Assessing the quality of ligands grafting,
    d. Qualifying the specificity of the signal,
    e. Ensuring the sample quality before injection by a test in TRPS,
    f. Standardized pre-analytical steps and variables such as the grafting pH, dilution method.
2. Signal processing techniques: To filter out the noise in the experiments with a low concentration of EVs, the negative control subtraction strategy proved to be a valid method to isolate the noise surrounding the weak capture.
3. Organization of measurement data: Since the experimental design involved many variables such as ligands concentration, a simultaneous measurement from multiplex spots in a single experiment, AFM images, and quantification data were organized systematically. Each experiment had a unique reference number. Spot level data was maintained for all the SPRi experiments, and single EVs level data was maintained for AFM quantification data. Such activity is critical to explore and exploit the full potential of the measurement data obtained from the precious EV preparations.

6.2 NBA platform to study the functional contribution of EVs for neuroprotection in HPL samples

This project helped to make progress in applying the NBA platform as a multiplexed bioassay for a set of complex samples. The presence of EVs, the relative abundance, and purity in HPPL, PPL, and SCPL samples were identified. Such a differential study is useful to study the role of EV in a functional context. It could also be used as a monitoring tool in various steps of developing an advanced therapy product. Further studies in the NBA platform could be envisioned comparing the differential marker and EVs expression with the nPEVs. As HPPL exerted an enhanced neuroprotective activity, a proteomic study could be engaged to compare the difference in proteomic profiles to better understand the way these HPL provides neuroprotection.

6.3 Advancements in EVs quantification from AFM imaging

This project also facilitated an accurate detection and quantification of EVs in AFM images. Although AFM is used as a qualification tool to visualize the EVs, owing to the complexity of the sample, other components in the EVs suspensions such as protein aggregates, salts crystals in the buffer, and sometimes the fixating agents could contribute as small structures. This is because of the complexity of the samples and the analytical procedure. Some artifact can occur on the surface. Owing to the specificity of the interaction as well as the evaluation of the capture level in SPRi combined with exploratory data analysis such as dynamic thresholding in the scatter plots, heatmap plot permits with high confidence to effectively choose the threshold required to filter out those objects that may not be EVs.

This work further attempted to reconstruct the size distribution profile of the subpopulation of EVs containing CD41 in a mix of PEVs and proteins. Such reconstruction of size distribution could be helpful to find a significant difference in the size of EVs bearing different markers as well as different biological conditions.

6.4 Developments in data processing and analytics

Combining multiple (bio) physical characterization techniques for a comprehensive EVs study offered a unique opportunity in processing, analyzing, and making use of insights from the data generated on various fronts. Data analysis and visualization are carried out using custom-written software code using python language. Some of the data processing and visualization

techniques that are developed specifically for NBA and used first time in the laboratory are briefly discussed here.

The code is automated in such a way that all the input data such as kinetics data, slope curve data, working angle, injection start, end time are directly read from the instrument data folder.

6.4.1 Matrix plot

In SPRi, when working with multiplex biochip consisting of different ligands, it is crucial to monitor the signal of interest (e.g., plasmon slope curve, sensorgram) from all the ROIs. However, this produces a complex overlap of line plots, making it difficult to extract meaningful information. While computing the average of each family is a strategy often used, data from all the ROI could be easily validated by constructing a matrix of subplots. In matrix plots, dedicated family-wise subplots enabled easier comparison of the signal of interest between, and within ligand families. It was also then possible to track the performance of a particular ROI throughout the experiment.

It is worth mentioning that in SPRi, only one working angle could be chosen. When working with a multiplexed format, this limits the kinetics of the measurement to be not measured in uniform sensitivity across all ligands. New development in the SPRi instrumentation (Horiba Xelplex) with multiple working angles could be more useful in acquiring accurate data in all the ligands simultaneously.

6.4.2 Heat map

Heat map offers a unique view of a variety of measures such as SPRi signal or plasmonic sensitivity across 2 dimensions. Visualizing data in such spatial coordinates gives insights into the uniformity of interaction across the surface. While it helps to validate the density data at a glance for many images, the heat map also helps in improving the rigor in AFM data acquisition and quantification. Correlative heat maps such as heat map of measurement parameters (such as scan size, scan rate) and the heat map of results (density) could be potentially useful in optimizing the acquisition parameters. With the development of the motorized sample stage, it will be possible to correlate the heatmap of AFM results to the coordinates in the biochip itself. This could help in making true replicates of an image and quantitation.

6.4.3 Visualizing AFM quantification data

Visualizing grains or EVs size parameters in a scatterplot proved to be useful as it offered a way to compare the distribution of EVs for a family. It also permits the visualization of the EVs from an assay spot and even down to individual images (Ref Figure 39). This was possible by placing a small vertical axis for EVs from each image and spot differentiated with a color code. While histogram and box plot are the popular method to visualize the size distribution, scatter plot is a method even more useful with the single particle resolution of NBA data specifically.

6.5 Challenges in EV characterization and the way forward

6.5.1 Revisiting the challenges in EVs science

Despite promising role in the physiology and pathophysiology, liquid biopsy, utilization as an advanced therapy product, significant challenges remain which hinder their ability in translational clinical applications. The main bottlenecks in the EVs research can be broadly categorized into two categories.

(i) The first and foremost challenge in the EVs study is the nature of EVs themselves. Since EVs are components of complex biofluids, they are very vulnerable to interferences by the contents of the media such as lipid-enclosed fats, lipoproteins, and membrane aggregates.[1,2] This also requires determining whether the desired functional role is borne by the EVs and not by the other components of the biological matrix, or both. One way to address this obstacle is to measure the purity of the samples. It can be obtained by normalizing the protein content of the EVs solution and the concentration of the EVs. Weber et al, proposed to a method to obtain the purity of EVs,[218] the investigators described a ratio of 3×10^{10} particles per µg of total protein, or greater as high purity. This method is one of the key performance indicators in describing the purity of EVs used in a biological assay.

(ii) The next challenge in EVs science is the limitations that arise from the measurement techniques. A wide range of analytical techniques are available to characterize the EVs, but as a stand-alone module, they provide only partial information about the EVs. Notably, so far there is no single technique allowing to analyze the EVs since EVs are physically and functionally diverse and thus, this analyte deserves to be studied by a combination of techniques. The NBA platform offers one such unique combination and

multifaceted information on qualitative and quantitative fronts. Like the NBA platform, many complementary techniques may be developed. In the coming section, some recommendations are proposed for the effective characterization of EVs for a given research question using the NBA platform and EVs characterization in general.

6.6 Revisions and proposals for improved EVs characterization using the NBA platform

For the effective utilization of the NBA platform as a modular EVs assay, the research can be performed in different modalities based on the questions to be addressed. This is useful in adapting the experimental method more tailored to the objective of the study.

6.6.1 Different modalities of the NBA platform

6.6.1.1 EVs phenotype screening

In biomarker screening mode, the primary objective is to qualify EVs expressing different biomarkers. Several biomarkers could be engaged as the system is capable of immobilizing few hundreds of different ligand spots, thanks to an automatic spotter. This makes the NBA platform a perfectly flexible tool for screening EVs based on the expressed biomarkers. Biacore could assist optimize the ligand grafting parameters whereas SPRi could evaluate the biomarkers in EVs in substantial amounts in parallel. This method in principle would provide qualitative expression of a particular biomarker. EVs markers positively expressed could be selected in the next step for more in-depth characterization.

It is also possible to reveal more surface markers using SPRi. After a specific capture of the EVs, free or labelled antibodies against other markers could be injected in the system to study the co-localization of the EVs marker.

6.6.1.2 SPRi- AFM mode or deep characterization mode

The “SPRi-AFM” mode, also known as deep characterizing mode, is intended to study the EVs for multi-physical parameters. AFM could bring a range of additional information such as structural, morphological, morpho-mechanical, and spectroscopic features of EVs. The EVs could be prepared in a biochip for two different concentrations (preferably at higher orders of magnitude). Such duplication in different concentration ranges or different capture levels is necessary to determine the optimum threshold for EVs. This can be done by dynamic threshold

selection in the AFM images in complement with SPRi signal. Stringent control measures in quantification analysis could be adopted to obtain and validate the following EVs specific data.

- The normalized EVs size distribution of EVs bearing a particular biomarker
- The relationship between SPRi signal, EVs density in AFM.
- Potential sub-populations identification using AFM with different morphological features such as spherical or tubular EVs.

All the above information will be useful in discovering and discriminating EVs from components of the media other than EVs. This will also help in developing a strategy for applied/translational EVs research.

6.6.1.3 EVs multi-omics

This modality is aimed to discover the proteomic, transcriptomic, and genomic contents of the EVs. Ideally, this mode should be engaged after confirmation of EV structures in the deep characterization mode. On-chip targeted proteomics could be envisioned in the experimental research design specific to the research objective. The biochip after enzymatic processing of the EVs could be further analyzed in AFM to quantify and to ensure the level of EVs removed from the surface for multi-omics analysis.

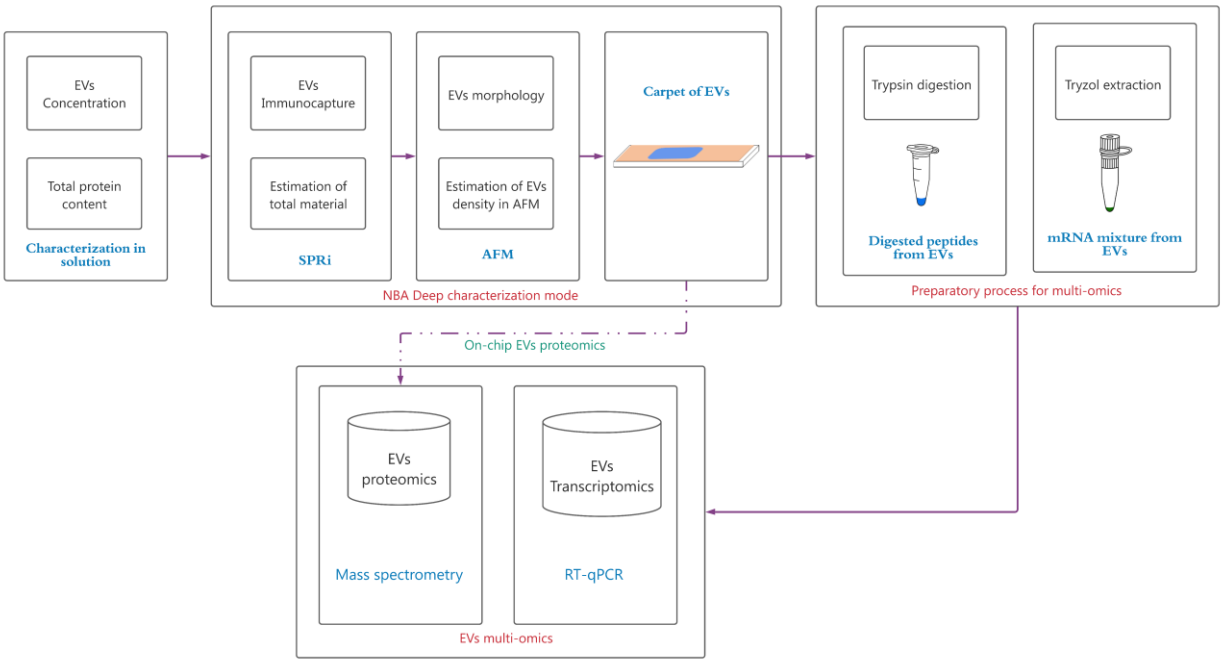

Figure 86 Schema of different modalities of NBA platform in multi-omics

By this way, the consistency of EVs-omics could be maximized. The relative identification of various functional proteins should give supporting information about EVs involvement in a functional study. Comparing different samples of EVs in the above three modes of the NBA platform could reveal potent and reliable information about EVs, their functional significance, and potentially the associated pathway. Thus, the NBA platform could serve the EVs research community for meaningful contributions.

6.6.2 Envisioning an Index that better describe the EVs

6.6.2.1 Need of standardization methods in EVs characterization for reproducible measurements

The outcome of each technique is governed by either the ability of a biomolecule in EV to interact with another partner, which we shall call power, or the abundance of the EVs, or by both. In general, the power should impact the qualitative results and the abundance should aggregate the quantitative information. Some techniques offer both qualitative and quantitative information therefore they are sensitive to both the abundance and power of EVs. Normalization methods for measurements need careful consideration in light of these two properties of the EVs. An imbalance in one of the pans of the balance could lead to a bias and as a consequence, inaccurate estimation of EVs in a functional assay. It is for these very reasons that the dilution factor was preferred over normalizing in terms of absolute EVs number in both the projects.

Improving the standardization in EVs measurements is needed. Several scientific standardization committees are set up and guidelines are published.[219,220] These guidelines provide many useful recommendations for careful consideration by the researchers. They further recommend adopting important preanalytical variables in the sample for each measurement technique.[220] Reference materials mimicking EVs structures,[221] biological materials that could be used as reference materials are also recommended. [222] A useful metric called EV-metric was also developed for the transparent reporting of experimental parameters. EV metric is a value in percentage units of satisfied components from a list of nine, which were proposed by the EV-TRACK consortium.[223] Such metric facilitates easier comparison of different studies with a single number. A similar metric for EVs characteristics which may be called as “EVs consistency index” (EVCI), which could be immensely useful. The first challenge of establishing EVCI is to build a method to compare results from different characterization techniques. This will be followed by

determining the weightage of each property in the proposed EVCI. The purer EVs of the same concentration should have a different EVCI compared to impure EVs.

While each characterization techniques are developed for a very specific purpose and have their advantages and disadvantages, the utilization potential of such technique could be extended to many folds when many techniques are used in a combined manner. For example, western blotting is used to identify a specific protein in a sample, this is also the same information that is obtained in qualitative SPRi and other biosensors provided, the particular protein is not part of the macromolecular cargo. Thus, establishing the relationship between such techniques should facilitate translating the results from one technique to the other with appreciable confidence levels. This has beneficial implications since the advantages of each technique could merge and help the investigator to better standardize EVs and make informed decisions for a prospective study.

One such application would be to augment the purity metric proposed by Weber et al[218] to a new metric that expresses the purity of EVs containing the specific marker. Such specific purity would normalize the amount of specific protein and the concentration. Selecting the dilution factor in SPRi based on the specific purity of the EVs would help to discriminate the EVs and co-eluents because AFM could clarify the morphological properties of the EVs and size distribution. Considering a hypothetical set of two samples normalized in such a way that they closely have the same signal in SPRi but have a significant difference in AFM density (and size distribution) could help conclude about the nature of EVs. There is a large potential to be explored in future research surrounding the thematic of EVs standardization and developing EVCI that more or less describes both the abundance and power of the EVs.

Annex 1: TRPS measurement parameters

Batch	Number of observations (n)		Stretch (mm)	Pressure (mbar)	Voltage (V)	Average Baseline current (nA)	Average Noise (pA)	Particles count (n)	Flow rate (n/min)	Raw Concentration (n/mL)	Mean diameter (nm)	Mode diameter (nm)
		Average	46.65	8.00	0.59	128.88	10.41	1249.92	625.28	1.30E+11	145.83	113.83
Feb-19	12	SD	0.29	0.00	0.12	3.42	0.71	188.56	169.00	7.59E+10	10.85	13.58
		Average	46.55	8.20	0.48	130.07	9.55	950.00	305.40	2.07E+10	184.40	149.40
Dec-19	5	SD	0.03	0.24	0.08	6.97	0.98	216.98	170.48	1.23E+10	21.56	21.55

Table 8 Details of measurements parameters of nPEV in TRPS

Annex 2: Dynamic Threshold data of AFM quantification of nPEVs

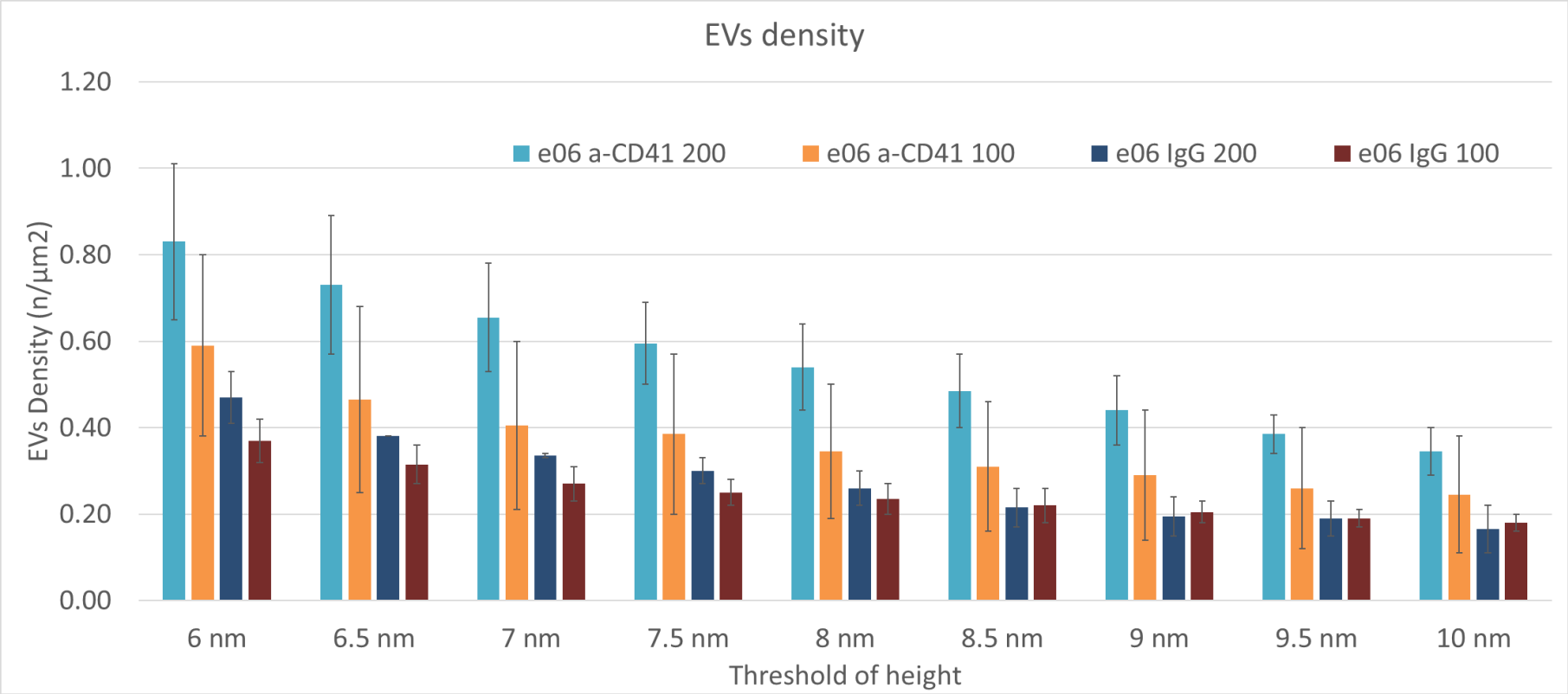

Figure 87 Dynamic threshold data for finding the best threshold for the nPEVs at 10^6/mL concentration from AFM images.

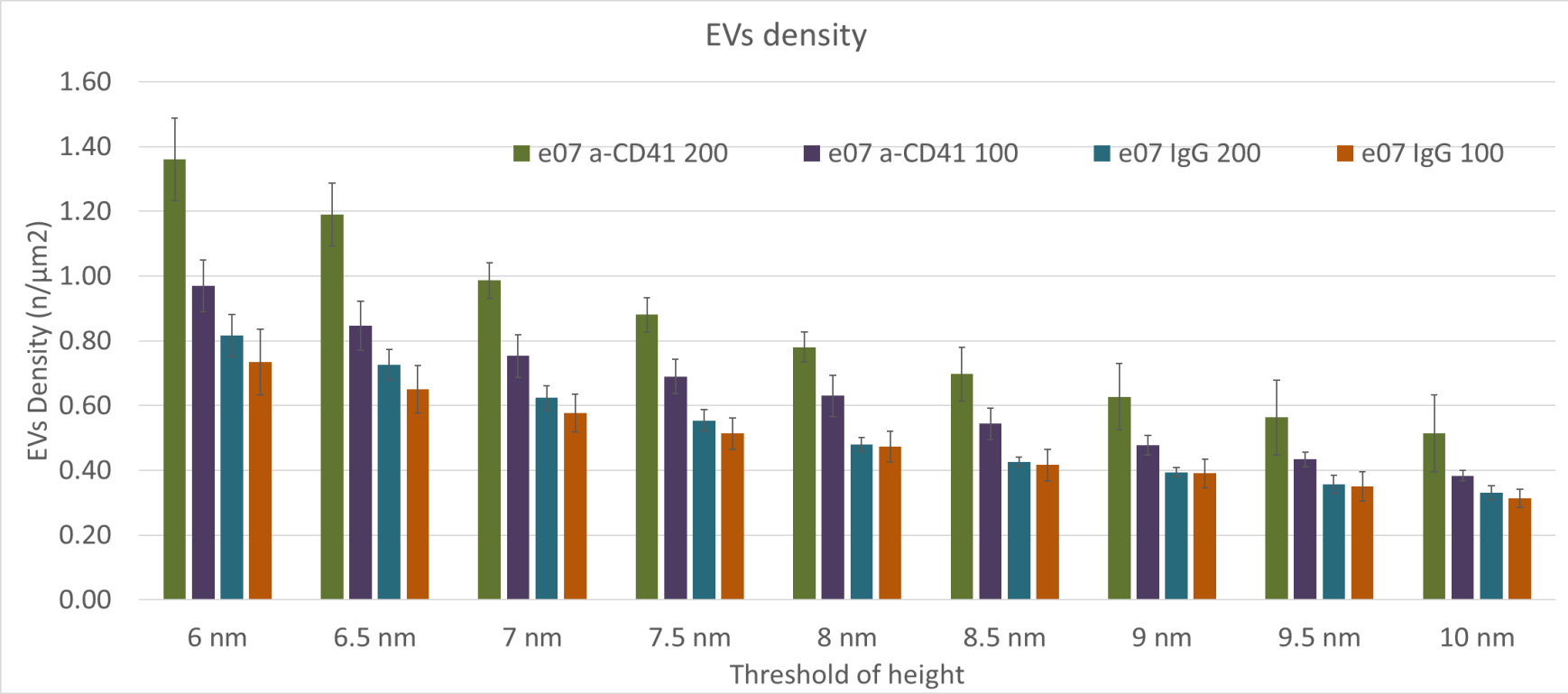

Figure 88 Dynamic threshold data for finding the best threshold for the nPEVs at 10^7/mL concentration from AFM images.

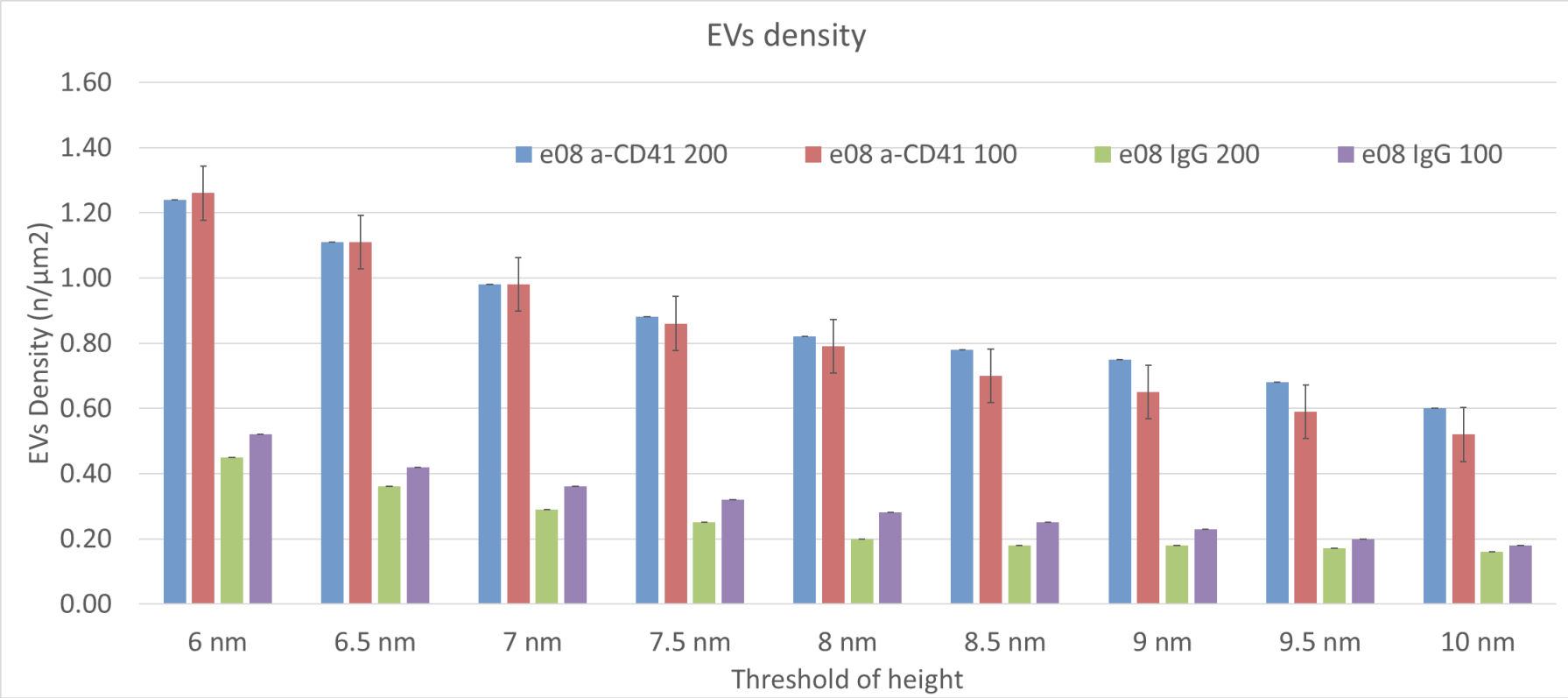

Figure 89 Dynamic threshold data for finding the best threshold for the nPEVs at 10^8/mL concentration from AFM images.

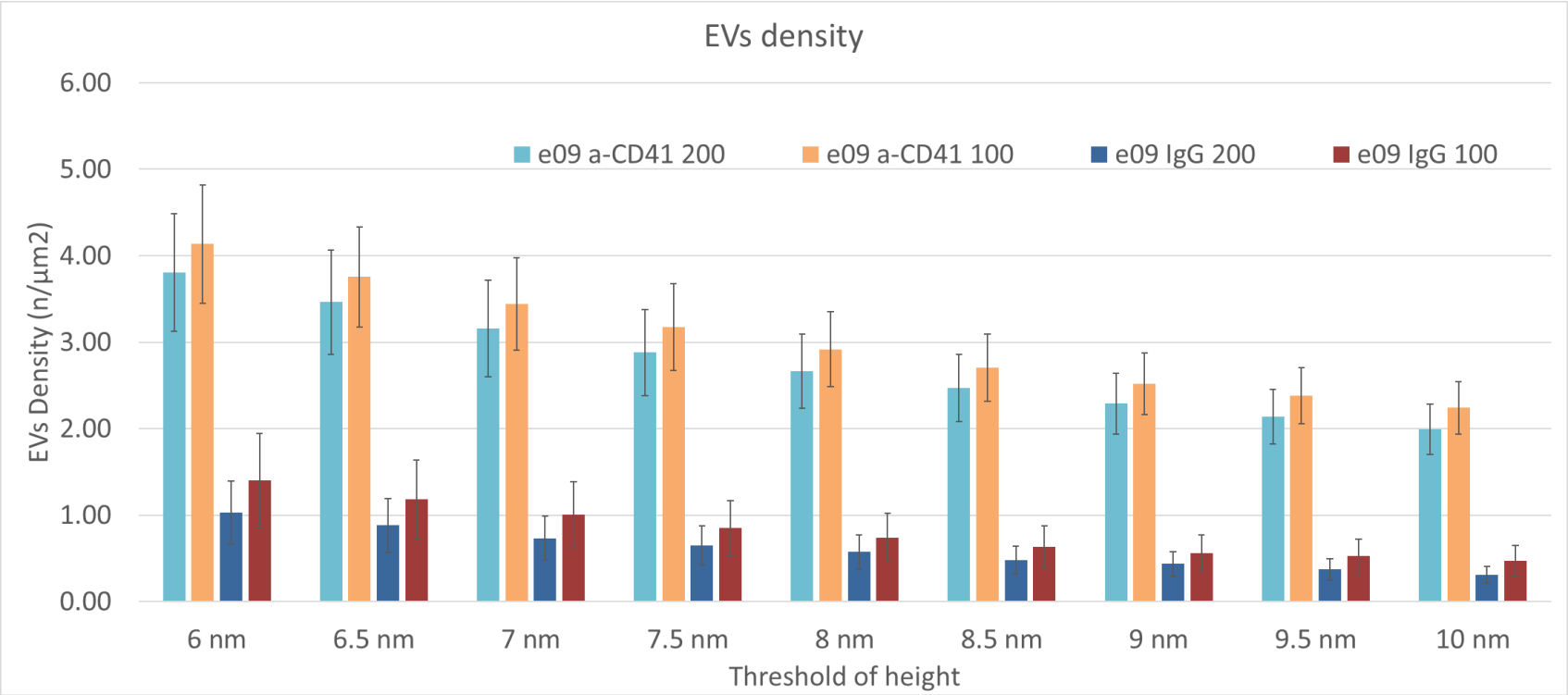

Figure 90 Dynamic threshold data for finding the best threshold for the nPEVs at 10^9/mL concentration from AFM images.

Annex 3 TRPS measurement data for the concentration tests.

HPL Type	Number of observations (n)		Stretch (mm)	Pressure (mbar)	Voltage (V)	Average Baseline current (nA)	Average Noise (pA)	Particles count (n)	Flow rate (n/min)	Raw Concentration (n/mL)	Mean diameter (nm)	Mode diameter (nm)
HPPL	5	Average	47.21	8.00	0.59	126.53	12.60	1383.40	1135.26	3.24E+11	133.00	109.00
		SD	0.49	0.00	0.12	4.58	0.31	135.62	106.16	1.42E+11	15.48	11.51
PPL	5	Average	46.54	8.00	0.48	129.41	10.25	1019.80	449.78	6.55E+11	181.60	138.60
		SD	0.02	0.00	0.05	6.91	0.64	138.22	45.53	2.14E+11	17.44	20.24
SCPL	2	Average	46.92	8.00	0.64	134.38	11.36	542.50	296.25	1.01E+11	138.50	117.00
		SD	0.00	0.00	0.00	2.63	0.87	0.50	125.35	4.69E+10	13.50	13.00

Table 9 TRPS measurement parameters of different HPLs. All tests are carried with a nanopore of size 200 nm (NP200)

Annex 4 Catalogue of products

Product	Reference	Supplier
PBS	P5368	Sigma
HEPES	H3375	Sigma
NaCl	S3014	Sigma
CaCl2	C1016	Sigma
s-NHS	56845	Sigma
EDC	03450	Sigma
a-CD41	853.223.020	Diaclone
a-CD62p	ab54427	Abcam
Annexin V	1005-100	BioVision
a-TF	ab17375	Abcam
a-CD61	27094	Signalway
a-CD81	GTX43505	GeneTex
a-CD9	ab2215	Abcam
IgG	A9H12 (clone)	Immutep
RSA	A6272	Sigma
Ethanolamine	T1502	Sigma
Glutaraldehyde	5882	Sigma
Octyl glucoside	O8001	Sigma

Table 10 Reference number of materials mentioned in this manuscript.

References

1. Théry C, Witwer KW, Aikawa E, et al. Minimal information for studies of extracellular vesicles 2018 (MISEV2018): a position statement of the International Society for Extracellular Vesicles and update of the MISEV2014 guidelines. *Journal of Extracellular Vesicles*. 2018;7(1):1535750. doi:10.1080/20013078.2018.1535750

2. Witwer KW, Soekmadji C, Hill AF, et al. Updating the MISEV minimal requirements for extracellular vesicle studies : building bridges to reproducibility. *Journal of Extracellular Vesicles*. 2017;6(1). doi:10.1080/20013078.2017.1396823

3. Tissot JD, Canellini G, Rubin O, et al. Blood microvesicles: From proteomics to physiology. *Translational Proteomics*. 2013;1(1):38-52. doi:10.1016/j.trprot.2013.04.004

4. Aqrawi LA, Galtung HK, Vestad B, et al. Identification of potential saliva and tear biomarkers in primary Sjögren ' s syndrome , utilising the extraction of extracellular vesicles and proteomics analysis. *Arthritis Research & Therapy*. Published online 2017:1-15. doi:10.1186/s13075-017-1228-x

5. Welton JL, Loveless S, Stone T, von Ruhland C, Robertson NP, Clayton A. Cerebrospinal fluid extracellular vesicle enrichment for protein biomarker discovery in neurological disease; multiple sclerosis. *Journal of Extracellular Vesicles*. 2017;6(1). doi:10.1080/20013078.2017.1369805

6. Admyre C, Johansson SM, Rahman K, et al. Exosomes with Immune Modulatory Features Are Present in Human Breast Milk. Published online 2019. doi:10.4049/jimmunol.179.3.1969

7. Street JM, Koritzinsky EH, Glispie DM, Star RA, Yuen PST. Urine Exosomes: An Emerging Trove of Biomarkers. *Advances in Clinical Chemistry*. 2017;78:103-122. doi:10.1016/bs.acc.2016.07.003

8. Ho JL, Lo J. Diversity of extracellular vesicles in human ejaculates revealed by cryo-electron microscopy. 2015;1:1-11.

9. Hargett LA, Bauer NN. On the origin of microparticles: From "platelet dust" to mediators of intercellular communication. *Pulmonary Circulation*. 2013;3(2):329-340. doi:10.4103/2045-8932.114760

10. Mathieu M, Martin-jaular L, Lavieu G, Théry C. communication. *Nature Cell Biology*. 2019;21(January). doi:10.1038/s41556-018-0250-9

11. Théry C, Zitvogel L, Amigorena S. Exosomes: composition, biogenesis and function. *Nature reviews Immunology*. 2002;2(8):569-579. doi:10.1038/nri855

12. Armstrong JPK, Stevens MM. Strategic design of extracellular vesicle drug delivery systems. *Advanced Drug Delivery Reviews*. 2018;130:12-16. doi:10.1016/j.addr.2018.06.017

13. Randolph WE, Service M. The Biological Significance of the Thromboplastic Protein of Blood. 1946;(7).

14. Anderson HC. Vesicles associated with calcification in the matrix of epiphyseal cartilage. 1969;(6).

15. Harding C V, Heuser JE, Stahl PD. Exosomes : Looking back three decades and into the future. 2013;200(4):367-371. doi:10.1083/jcb.201212113

16. Harding C, Heuser J, Stahl P. 363. exosome discovery 2- Receptor-mediated Endocytosis of Transferrin and of the Transferrin Receptor in Rat Reticulocytes Recycling. *J Cell Biol*. 1983;97:329-339. doi:10.1038/nrm973

17. Zhang H, Lyden D. Asymmetric-flow field-flow fractionation technology for exomere and small extracellular vesicle separation and characterization. *Nature Protocols*. 2019;14(4):1027-1053. doi:10.1038/s41596-019-0126-x

18. Anand S, Samuel M, Mathivanan S. Exomeres: A New Member of Extracellular Vesicles Family. In: *Subcellular Biochemistry*. Vol 97. Springer Science and Business Media B.V.; 2021:89-97. doi:10.1007/978-3-030-67171-6_5

19. Distler JHW, Pisetsky DS, Huber LC, Kalden JR, Gay S, Distler O. Microparticles as regulators of inflammation: Novel players of cellular crosstalk in the rheumatic diseases. *Arthritis and Rheumatism*. 2005;52(11):3337-3348. doi:10.1002/art.21350

20. Janowska-Wieczorek A, Majka M, Kijowski J, et al. Platelet-derived microparticles bind to hematopoietic stem/progenitor cells and enhance their engraftment. *Blood*. 2001;98(10):3143-3149. doi:10.1182/blood.V98.10.3143

21. Janowska-Wieczorek A, Wysoczynski M, Kijowski J, et al. Microvesicles derived from activated platelets induce metastasis and angiogenesis in lung cancer. *International Journal of Cancer*. 2005;113(5):752-760. doi:10.1002/ijc.20657

22. Ratajczak J, Miekus K, Kucia M, et al. Embryonic stem cell-derived microvesicles reprogram hematopoietic progenitors: Evidence for horizontal transfer of mRNA and protein delivery. *Leukemia*. 2006;20(5):847-856. doi:10.1038/sj.leu.2404132

23. Mack M, Kleinschmidt A, Brühl H, et al. Transfer of the chemokine receptor CCR5 between cells by membrane- derived microparticles: A mechanism for cellular human immunodeficiency virus 1 infection. *Nature Medicine*. 2000;6(7):769-775. doi:10.1038/77498

24. Simák J, Holada K, D'Agnillo F, Janota J, Vostal JG. Cellular prion protein is expressed on endothelial cells and is released during apoptosis on membrane microparticles found in human plasma. *Transfusion*. 2002;42(3):334-342. doi:10.1046/j.1537-2995.2002.00072.x

25. Ratajczak J, Wysoczynski M, Hayek F, Janowska-Wieczorek A, Ratajczak MZ. Membrane-derived microvesicles: Important and underappreciated mediators of cell-to-cell communication. *Leukemia*. 2006;20(9):1487-1495. doi:10.1038/sj.leu.2404296

26. Spees JL, Olson SD, Whitney MJ, Prockop DJ. Mitochondrial transfer between cells can rescue aerobic respiration. *Proceedings of the National Academy of Sciences of the United States of America*. 2006;103(5):1283-1288. doi:10.1073/pnas.0510511103

27. B Lymphocytes Secrete Antigen-presentingVesicles. 1996;183(March).

28. Stahl PD. Exosomes and extracellular vesicles : the path forward. 2018;(May):119-124.

29. Valadi H, Ekström K, Bossios A, Sjöstrand M, Lee JJ, Lötvall JO. Exosome-mediated transfer of mRNAs and microRNAs is a novel mechanism of genetic exchange between cells. 2007;9(6). doi:10.1038/ncb1596

30. Nabhan JF, Hu R, Oh RS, Cohen SN, Lu Q. Formation and release of arrestin domain-containing protein 1-mediated microvesicles (ARMMs) at plasma membrane by recruitment of TSG101 protein. *Proceedings of the National Academy of Sciences of the United States of America*. 2012;109(11):4146-4151. doi.10.1073/pnas.1200448109

31. Stachowiak JC, Schmid EM, Ryan CJ, et al. Membrane bending by protein – protein crowding. *Nature Cell Biology*. 2012;14(9):944-949. doi:10.1038/ncb2561

32. Hugel B, Martínez MC, Kunzelmann C, Freyssinet JM. Membrane microparticles: Two sides of the coin. *Physiology*. 2005;20(1):22-27. doi:10.1152/physiol.00029.2004

33. Colombo M. Biogenesis , Secretion , and Intercellular Interactions of Exosomes and Other Extracellular Vesicles. Published online 2014:255-292. doi:10.1146/annurev-cellbio-101512-122326

34. Jadli AS, Ballasy N, Edalat P, Patel VB. Inside(sight) of tiny communicator: exosome biogenesis, secretion, and uptake. *Molecular and Cellular Biochemistry*. 2020;467(1-2):77-94. doi:10.1007/s11010-020-03703-z

35. Tzeng H, Wang Y. Rab-mediated vesicle trafficking in cancer. *Journal of Biomedical Science*. Published online 2016:1-7. doi:10.1186/s12929-016-0287-7

36. Szabo G, Momen-heravi F. Extracellular vesicles in liver disease. doi:10.1038/nrgastro.2017.71

37. Heijnen HFG, Schiel AE, Fijnheer R, Geuze HJ, Sixma JJ. Activated platelets release two types of membrane vesicles: Microvesicles by surface shedding and exosomes derived from exocytosis of multivesicular bodies and α-granules. *Blood*. 1999;94(11):3791-3799. doi:10.1182/blood.v94.11.3791

38. Kalra H, Simpson RJ, Ji H, et al. Vesiclepedia: A Compendium for Extracellular Vesicles with Continuous Community Annotation. *PLoS Biology*. 2012;10(12). doi:10.1371/journal.pbio.1001450

39. van der Pol E, Böing AN, Harrison P, Sturk A, Nieuwland R. Classification, functions, and clinical relevance of extracellular vesicles. *Pharmacological Reviews*. 2012;64(3):676-705. doi:10.1124/pr.112.005983

40. Zhang H, Freitas D, Kim HS, et al. Identification of distinct nanoparticles and subsets of extracellular vesicles by asymmetric flow field-flow fractionation. *Nature Cell Biology*. 2018;20(3):332-343. doi:10.1038/s41556-018-0040-4

41. Brisson AR, Tan S, Linares R, Gounou C, Arraud N. Extracellular vesicles from activated platelets: a semiquantitative cryo-electron microscopy and immuno-gold labeling study. *Platelets*. 2017;28(3):263-271. doi:10.1080/09537104.2016.1268255

42. Arraud N, Linares R, Tan S, et al. Extracellular vesicles from blood plasma: Determination of their morphology, size, phenotype and concentration. *Journal of Thrombosis and Haemostasis*. 2014;12(5):614-627. doi:10.1111/jth.12554

43. Marzesco AM, Janich P, Wilsch-Bräuninger M, et al. Release of extracellular membrane particles carrying the stem cell marker prominin-1 (CD133) from neural progenitors and other epithelial cells. *Journal of Cell Science*. 2005;118(13):2849-2858. doi:10.1242/jcs.02439

44. Shao H, Chung J, Balaj L, et al. Protein typing of circulating microvesicles allows real-time monitoring of glioblastoma therapy. *Nature Medicine*. 2012;18(12):1835-1840. doi:10.1038/nm.2994

45. Atkin-Smith GK, Poon IKH. Disassembly of the Dying: Mechanisms and Functions. *Trends in Cell Biology*. 2017;27(2):151-162. doi:10.1016/j.tcb.2016.08.011

46. García-Romero N, Carrión-Navarro J, Esteban-Rubio S, et al. DNA sequences within glioma-derived extracellular vesicles can cross the intact blood-brain barrier and be detected in peripheral blood of patients. *Oncotarget*. 2017;8(1):1416-1428. doi:10.18632/oncotarget.13635

47. Żmigrodzka M, Guzera M, Miśkiewicz A, Jagielski D, Winnicka A. The biology of extracellular vesicles with focus on platelet microparticles and their role in cancer development and progression. *Tumor Biology*. 2016;37(11):14391-14401. doi:10.1007/s13277-016-5358-6

48. Antunes-Ferreira M, Koppers-Lalic D, Würdinger T. Circulating platelets as liquid biopsy sources for cancer detection. *Molecular Oncology*. 2020;15(6):1727-1743. doi:10.1002/1878-0261.12859

49. Johnson J, Wu YW, Blyth C, Lichtfuss G, Goubran H, Burnouf T. Prospective Therapeutic Applications of Platelet Extracellular Vesicles. *Trends in Biotechnology*. 2020;39(6):598-612. doi:10.1016/j.tibtech.2020.10.004

50. Kao CY, Papoutsakis ET. Extracellular vesicles: exosomes, microparticles, their parts, and their targets to enable their biomanufacturing and clinical applications. *Current Opinion in Biotechnology*. 2019;60:89-98. doi:10.1016/J.COPBIO.2019.01.005

51. Boilard E, Duchez AC, Brisson A. The diversity of platelet microparticles. *Current Opinion in Hematology*. 2015;22(5):437-444. doi:10.1097/MOH.0000000000000166

52. Berckmans RJ, Lacroix R, Hau CM, Sturk A, Nieuwland R. Extracellular vesicles and coagulation in blood from healthy humans revisited. *https://doi.org/101080/200130782019168893*6. 2019;8(1). doi:10.1080/20013078.2019.1688936

53. Puhm F, Boilard E, MacHlus KR. Platelet Extracellular Vesicles: Beyond the Blood. *Arteriosclerosis, Thrombosis, and Vascular Biology*. Published online 2020:87-96. doi:10.1161/ATVBAHA.120.314644

54. Gasecka A, Nieuwland R, Siljander PRM. Platelet-derived extracellular vesicles. In: *Platelets*. Elsevier; 2019:401-416. doi:10.1016/B978-0-12-813456-6.00022-9

55. Nomura S, Tandon NN, Nakamura T, Cone J, Fukuhara S, Kambayashi J. High-shear-stress-induced activation of platelets and microparticles enhances expression of cell adhesion molecules in THP-1 and endothelial cells. *Atherosclerosis*. 2001;158(2):277-287. doi:10.1016/S0021-9150(01)00433-6

56. Barry OP, Praticò D, Savani RC, FitzGerald GA. Modulation of monocyte-endothelial cell interactions by platelet microparticles. *Journal of Clinical Investigation*. 1998;102(1):136-144. doi:10.1172/JCI2592

57. Nomura S. Extracellular vesicles and blood diseases. *International Journal of Hematology*. 2017;105(4):392-405. doi:10.1007/s12185-017-2180-x

58. Liu W, Lin H, He X, et al. Neurogranin as a cognitive biomarker in cerebrospinal fluid and blood exosomes for Alzheimer's disease and mild cognitive impairment. *Translational Psychiatry*. 2020;10(1):1-9. doi:10.1038/s41398-020-0801-2

59. Vingtdeux V, Sergeant N, Buée L. Potential contribution of exosomes to the prion-like propagation of lesions in Alzheimer's disease. *Frontiers in Physiology*. 2012;3 JUL. doi:10.3389/fphys.2012.00229

60. Wang L, Zhang L. Circulating Exosomal miRNA as Diagnostic Biomarkers of Neurodegenerative Diseases. *Frontiers in Molecular Neuroscience*. 2020;13:53. doi:10.3389/fnmol.2020.00053

61. Sáenz-Cuesta M, Irizar H, Castillo-Triviño T, et al. Circulating microparticles reflect treatment effects and clinical status in multiple sclerosis. *Biomarkers in Medicine*. 2014;8(5):653-661. doi:10.2217/bmm.14.9

62. Sáenz-Cuesta M, Osorio-Querejeta I, Otaegui D. Extracellular vesicles in multiple sclerosis: What are they telling us? *Frontiers in Cellular Neuroscience*. 2014;8(MAR). doi:10.3389/fncel.2014.00100

63. Robbins PD, Dorronsoro A, Booker CN. Regulation of chronic inflammatory and immune processes by extracellular vesicles. *Journal of Clinical Investigation*. 2016;126(4):1173-1180. doi:10.1172/JCI81131

64. Corrales-Medina VF, Simkins J, Chirinos JA, et al. Increased levels of platelet microparticles in HIV-infected patients with good response to highly active antiretroviral therapy. *Journal of Acquired Immune Deficiency Syndromes*. 2010;54(2):217-219. doi:10.1097/QAI.0b013e3181c8f4c9

65. Cappellano G, Raineri D, Rolla R, et al. Circulating Platelet-Derived Extracellular Vesicles Are a Hallmark of Sars-Cov-2 Infection. *Cells*. 2021;10(1). doi:10.3390/cells10010085

66. Żmigrodzka M, Witkowska-Piłaszewicz O, Winnicka A. Platelets extracellular vesicles as regulators of cancer progression—an updated perspective. *International Journal of Molecular Sciences*. 2020;21(15):1-18. doi:10.3390/ijms21155195

67. Castaman G, Yu-Feng L, Rodeghiero F. A bleeding disorder characterised by isolated deficiency of platelet microvesicle generation [25]. *Lancet*. 1996;347(9002):700-701. doi:10.1016/S0140-6736(96)91259-3

68. Liu J, Chen Y, Pei F, et al. Extracellular Vesicles in Liquid Biopsies: Potential for Disease Diagnosis. *BioMed Research International*. 2021;2021. doi:10.1155/2021/6611244

69. Mathai R, Vidya R, Reddy B, et al. Potential Utility of Liquid Biopsy as a Diagnostic and Prognostic Tool for the Assessment of Solid Tumors: Implications in the Precision Oncology. *Journal of Clinical Medicine*. 2019;8(3):373. doi:10.3390/jcm8030373

70. Collins FS, Varmus H. A New Initiative on Precision Medicine. *New England Journal of Medicine*. 2015;372(9):793-795. doi:10.1056/nejmp1500523

71. Wiklander OPB, Brennan M, Lötvall J, Breakefield XO, Andaloussi SEL. Advances in therapeutic applications of extracellular vesicles. *Science Translational Medicine*. 2019;11(492). doi:10.1126/scitranslmed.aav8521

72. Arslan F, Lai RC, Smeets MB, et al. Mesenchymal stem cell-derived exosomes increase ATP levels, decrease oxidative stress and activate PI3K/Akt pathway to enhance myocardial viability and prevent adverse remodeling after myocardial ischemia/reperfusion injury. *Stem Cell Research*. 2013;10(3):301-312. doi:10.1016/j.scr.2013.01.002

73. Shen Y, Torchia MLG, Lawson GW, Karp CL, Ashwell JD, Mazmanian SK. Outer membrane vesicles of a human commensal mediate immune regulation and disease protection. *Cell Host and Microbe*. 2012;12(4):509-520. doi:10.1016/j.chom.2012.08.004

74. Deng Z-B, Zhuang X, Ju S, et al. Exosome-like Nanoparticles from Intestinal Mucosal Cells Carry Prostaglandin E 2 and Suppress Activation of Liver NKT Cells . *The Journal of Immunology*. 2013;190(7):3579-3589. doi:10.4049/jimmunol.1203170

75. Sandbu S, Feiring B, Oster P, et al. Immunogenicity and safety of a combination of two serogroup B meningococcal outer membrane vesicle vaccines. *Clinical and Vaccine Immunology*. 2007;14(9):1062-1069. doi:10.1128/CVI.00094-07

76. Lee C, Mitsialis SA, Aslam M, et al. Exosomes mediate the cytoprotective action of mesenchymal stromal cells on hypoxia-induced pulmonary hypertension. *Circulation*. 2012;126(22):2601-2611. doi:10.1161/CIRCULATIONAHA.112.114173

77. Gehrmann U, Hiltbrunner S, Georgoudaki AM, Karlsson MC, Näslund TI, Gabrielsson S. Synergistic induction of adaptive antitumor immunity by codelivery of antigen with α-galactosylceramide on exosomes. *Cancer Research*. 2013;73(13):3865-3876. doi:10.1158/0008-5472.CAN-12-3918

78. Ohno SI, Takanashi M, Sudo K, et al. Systemically injected exosomes targeted to EGFR deliver antitumor microrna to breast cancer cells. *Molecular Therapy*. 2013;21(1):185-191. doi:10.1038/mt.2012.180

79. Yung YL, Fu SC, Cheuk YC, et al. Optimisation of platelet concentrates therapy: Composition, localisation, and duration of action. *Asia-Pacific Journal of Sports Medicine, Arthroscopy, Rehabilitation and Technology*. 2017;7:27-36. doi:10.1016/j.asmart.2016.11.003

80. Chou ML, Wu JW, Gouel F, et al. Tailor-made purified human platelet lysate concentrated in neurotrophins for treatment of Parkinson's disease. *Biomaterials*. 2017;142:77-89. doi:10.1016/j.biomaterials.2017.07.018

81. Sinauridze EI, Kireev DA, Popenko NY, et al. Platelet microparticle membranes have 50- to 100-fold higher specific procoagulant activity than activated platelets. *Thrombosis and Haemostasis*. 2007;97(3):425-434. doi:10.1160/TH06-06-0313

82. Guo SC, Tao SC, Yin WJ, Qi X, Yuan T, Zhang CQ. Exosomes derived from platelet-rich plasma promote the re-epithelization of chronic cutaneous wounds via activation of YAP in a diabetic rat model. *Theranostics*. 2017;7(1):81-96. doi:10.7150/thno.16803

83. Hayon Y, Dashevsky O, Shai E, Brill A, Varon D, R. Leker R. Platelet Microparticles Induce Angiogenesis and Neurogenesis after Cerebral Ischemia. *Current Neurovascular Research*. 2012;9(3):185-192. doi:10.2174/156720212801619018

84. Sadallah S, Eken C, Martin PJ, Schifferli JA. Microparticles (Ectosomes) Shed by Stored Human Platelets Downregulate Macrophages and Modify the Development of Dendritic

Cells. *The Journal of Immunology*. 2011;186(11):6543-6552. doi:10.4049/jimmunol.1002788

85. Nazari M, Javandoost E, Talebi M, Movassaghpour A, Soleimani M. Platelet microparticle controversial role in cancer. *Advanced Pharmaceutical Bulletin*. 2021;11(1):39-55. doi:10.34172/apb.2021.005

86. Wu YW, Huang CC, Changou CA, Lu LS, Goubran H, Burnouf T. Clinical-grade cryopreserved doxorubicin-loaded platelets: Role of cancer cells and platelet extracellular vesicles activation loop. *Journal of Biomedical Science*. 2020;27(1):1-16. doi:10.1186/s12929-020-00633-2

87. Antimisiaris SG, Mourtas S, Marazioti A. Exosomes and exosome-inspired vesicles for targeted drug delivery. *Pharmaceutics*. 2018;10(4). doi:10.3390/pharmaceutics10040218

88. Linares R, Tan S, Gounou C, Arraud N, Brisson AR. High-speed centrifugation induces aggregation of extracellular vesicles. *Journal of Extracellular Vesicles*. 2015;4(1). doi:10.3402/jev.v4.29509

89. Obeid S, Ceroi A, Mourey G, Saas P, Elie-Caille C, Boireau W. Development of a NanoBioAnalytical platform for “on-chip” qualification and quantification of platelet-derived microparticles. *Biosensors and Bioelectronics*. 2017;93:250-259. doi:10.1016/j.bios.2016.08.100

90. Théry C, Amigorena S, Raposo G, Clayton A. Isolation and Characterization of Exosomes from Cell Culture Supernatants and Biological Fluids. *Current Protocols in Cell Biology*. 2006;30(1). doi:10.1002/0471143030.cb0322s30

91. Musante L, Tataruch D, Gu D, et al. A simplified method to recover urinary vesicles for clinical applications, and sample banking. *Scientific Reports*. 2014;4. doi:10.1038/srep07532

92. Zhang Z, Wang C, Li T, Liu Z, Li L. Comparison of ultracentrifugation and density gradient separation methods for isolating Tca8113 human tongue cancer cell line-derived exosomes. *Oncology Letters*. 2014;8(4):1701-1706. doi:10.3892/ol.2014.2373

93. Liangsupree T, Multia E, Riekkola ML. Modern isolation and separation techniques for extracellular vesicles. *Journal of Chromatography A*. 2021;1636:461773. doi:10.1016/j.chroma.2020.461773

94. Sidhom K, Obi PO, Saleem A. Molecular Sciences A Review of Exosomal Isolation Methods: Is Size Exclusion Chromatography the Best Option? doi:10.3390/ijms21186466

95. Gandham S, Su X, Wood J, et al. Technologies and Standardization in Research on Extracellular Vesicles. *Trends in Biotechnology*. 2020;38(10):1066-1098. doi:10.1016/j.tibtech.2020.05.012

96. Zhang M, Jin K, Gao L, et al. Methods and Technologies for Exosome Isolation and Characterization. *Small Methods*. 2018;1800021:1800021. doi:10.1002/smtd.201800021

97. du Cheyron D, Daubin C, Poggioli J, et al. Urinary measurement of Na+/H+ exchanger isoform 3 (NHE3) protein as new marker of tubule injury in critically ill patients with ARF. *American Journal of Kidney Diseases*. 2003;42(3):497-506. doi:10.1016/S0272-6386(03)00744-3

98. Clayton A, Court J, Navabi H, et al. Analysis of antigen presenting cell derived exosomes, based on immuno-magnetic isolation and flow cytometry. *Journal of Immunological Methods*. 2001;247(1-2):163-174. doi:10.1016/S0022-1759(00)00321-5

99. Ueda K, Ishikawa N, Tatsuguchi A, Saichi N, Fujii R, Nakagawa H. Antibody-coupled monolithic silica microtips for highthroughput molecular profiling of circulating exosomes. *Scientific Reports*. 2014;4(1):1-9. doi:10.1038/srep06232

100. Chen S, Shiesh SC, Lee G bin, Chen C. Two-step magnetic bead-based (2MBB) techniques for immunocapture of extracellular vesicles and quantification of microRNAs for cardiovascular diseases: A pilot study. *PLoS ONE*. 2020;15(2):e0229610. doi:10.1371/journal.pone.0229610

101. Pedersen KW, Kierulf B, Neurauter A. Specific and Generic Isolation of Extracellular Vesicles with Magnetic Beads. *Methods in molecular biology (Clifton, NJ)*. 2017;1660:65-87. doi:10.1007/978-1-4939-7253-1_7

102. Momen-Heravi F, Balaj L, Alian S, et al. Current methods for the isolation of extracellular vesicles. *Biological Chemistry*. 2013;394(10):1253-1262. doi:10.1515/hsz-2013-0141

103. Weng Y, Sui Z, Shan Y, et al. Effective isolation of exosomes with polyethylene glycol from cell culture supernatant for in-depth proteome profiling. *Analyst*. 2016;141(15):4640-4646. doi:10.1039/c6an00892e

104. Lamparski HG, Metha-Damani A, Yao JY, et al. Production and characterization of clinical grade exosomes derived from dendritic cells. *Journal of Immunological Methods*. 2002;270(2):211-226. doi:10.1016/S0022-1759(02)00330-7

105. Benedikter BJ, Bouwman FG, Vajen T, et al. Ultrafiltration combined with size exclusion chromatography efficiently isolates extracellular vesicles from cell culture media for compositional and functional studies. *Scientific Reports*. 2017;7(1):1-13. doi:10.1038/s41598-017-15717-7

106. Chen C, Skog J, Hsu CH, et al. Microfluidic isolation and transcriptome analysis of serum microvesicles. *Lab on a Chip*. 2010;10(4):505-511. doi:10.1039/b916199f

107. Zhao Z, Wijerathne H, Godwin AK, Soper SA. Isolation and analysis methods of extracellular vesicles (EVs). *Extracellular Vesicles and Circulating Nucleic Acids*. 2021;2(1):80-103. doi:10.20517/evcna.2021.07

108. Ko J, Carpenter E, Issadore D. Detection and isolation of circulating exosomes and microvesicles for cancer monitoring and diagnostics using micro-/nano-based devices. *The Analyst*. 2016;141(2):450-460. doi:10.1039/C5AN01610J

109. Meng Y, Asghari M, Aslan MK, et al. Microfluidics for extracellular vesicle separation and mimetic synthesis: Recent advances and future perspectives. *Chemical Engineering Journal*. 2021;404:126110. doi:10.1016/j.cej.2020.126110

110. Lee K, Shao H, Weissleder R, Lee H. Acoustic purification of extracellular microvesicles. *ACS Nano*. 2015;9(3):2321-2327. doi:10.1021/nn506538f

111. Lewis JM, Vyas AD, Qiu Y, Messer KS, White R, Heller MJ. Integrated Analysis of Exosomal Protein Biomarkers on Alternating Current Electrokinetic Chips Enables Rapid Detection of Pancreatic Cancer in Patient Blood. *ACS Nano*. 2018;12(4):3311-3320. doi:10.1021/acsnano.7b08199

112. Chen C, Skog J, Hsu CH, et al. Microfluidic isolation and transcriptome analysis of serum microvesicles. *Lab on a Chip*. 2010;10(4):505-511. doi:10.1039/b916199f

113. He M, Crow J, Roth M, Zeng Y, Godwin AK. Integrated immunoisolation and protein analysis of circulating exosomes using microfluidic technology. *Lab on a Chip*. 2014;14(19):3773-3780. doi:10.1039/c4lc00662c

114. Pillemont L, Guneysu D, Elie-Caille C, Boireau W, Marie Gué A, Marie Gué AA. *A Generic Microfluidic Approach for Deciphering Nanoscale BiovesiclES PropertieS*.; 2018. Accessed June 7, 2021. https://hal.laas.fr/hal-02473108

115. Pillemont L, Guneysu D, Elie-Caille C, Boireau W, Gué AM. Towards on-chip EVs separation: a lab-on-chip approach. Published online April 24, 2019:PS04.10. Accessed June 7, 2021. https://hal.archives-ouvertes.fr/hal-02421493

116. Liu C, Guo J, Tian F, et al. Field-Free Isolation of Exosomes from Extracellular Vesicles by Microfluidic Viscoelastic Flows. *ACS Nano*. 2017;11(7):6968-6976. doi:10.1021/acsnano.7b02277

117. Davies RT, Kim J, Jang SC, Choi EJ, Gho YS, Park J. Microfluidic filtration system to isolate extracellular vesicles from blood. *Lab on a Chip*. 2012;12(24):5202-5210. doi:10.1039/c2lc41006k

118. Reátegui E, van der Vos KE, Lai CP, et al. Engineered nanointerfaces for microfluidic isolation and molecular profiling of tumor-specific extracellular vesicles. *Nature Communications*. 2018;9(1). doi:10.1038/s41467-017-02261-1

119. Talebjedi B, Tasnim N, Hoorfar M, Mastromonaco GF, de Almeida Monteiro Melo Ferraz M. Exploiting Microfluidics for Extracellular Vesicle Isolation and Characterization: Potential Use for Standardized Embryo Quality Assessment. *Frontiers in Veterinary Science*. 2021;7:620809. doi:10.3389/fvets.2020.620809

120. Wunsch BH, Smith JT, Gifford SM, et al. Nanoscale lateral displacement arrays for the separation of exosomes and colloids down to 20nm. *Nature Nanotechnology*. 2016;11(11):936-940. doi:10.1038/nnano.2016.134

121. Guo SC, Tao SC, Dawn H. Microfluidics-based on-a-chip systems for isolating and analysing extracellular vesicles. *Journal of Extracellular Vesicles*. 2018;7(1). doi:10.1080/20013078.2018.1508271

122. Ter-Ovanesyan D, Kowal EJK, Regev A, Church GM, Cocucci E. Imaging of Isolated Extracellular Vesicles Using Fluorescence Microscopy. *Methods in molecular biology (Clifton, NJ)*. 2017;1660:233-241. doi:10.1007/978-1-4939-7253-1_19

123. Mondal A, Ashiq KA, Phulpagar P, Singh DK, Shiras A. Effective Visualization and Easy Tracking of Extracellular Vesicles in Glioma Cells. *Biological Procedures Online*. 2019;21(1). doi:10.1186/s12575-019-0092-2

124. Kalimuthu S, Oh JM, Gangadaran P, et al. *in* Vivo Tracking of Chemokine Receptor CXCR4-Engineered Mesenchymal Stem Cell Migration by Optical Molecular Imaging. *Stem Cells International*. 2017;2017. doi:10.1155/2017/8085637

125. Takahashi Y, Nishikawa M, Shinotsuka H, et al. Visualization and *in* vivo tracking of the exosomes of murine melanoma B16-BL6 cells in mice after intravenous injection. *Journal of Biotechnology*. 2013;165(2):77-84. doi:10.1016/j.jbiotec.2013.03.013

126. Androuin A, Verweij FJ, van Niel G. Zebrafish as a preclinical model for Extracellular Vesicle-based therapeutic development. *Advanced Drug Delivery Reviews*. Published online May 2021. doi:10.1016/j.addr.2021.05.025

127. Hyenne V, Ghoroghi S, Collot M, et al. Studying the Fate of Tumor Extracellular Vesicles at High Spatiotemporal Resolution Using the Zebrafish Embryo. *Developmental Cell*. 2019;48(4):554-572.e7. doi:10.1016/j.devcel.2019.01.014

128. Verweij FJ, Hyenne V, van Niel G, Goetz JG. Extracellular Vesicles: Catching the Light in Zebrafish. *Trends in Cell Biology*. 2019;29(10):770-776. doi:10.1016/j.tcb.2019.07.007

129. Lai CP, Kim EY, Badr CE, et al. Visualization and tracking of tumour extracellular vesicle delivery and RNA translation using multiplexed reporters. *Nature Communications*. 2015;6(1):1-12. doi:10.1038/ncomms8029

130. Panagopoulou MS, Wark AW, Birch DJS, Gregory CD. Phenotypic analysis of extracellular vesicles: a review on the applications of fluorescence. *Journal of Extracellular Vesicles*. 2020;9(1). doi:10.1080/20013078.2019.1710020

131. Park YH, Shin HW, Jung AR, et al. Prostate-specific extracellular vesicles as a novel biomarker in human prostate cancer. *Scientific Reports*. 2016;6. doi:10.1038/srep30386

132. Höög JL, Lötvall J. Diversity of extracellular vesicles in human ejaculates revealed by cryo-electron microscopy. *Journal of Extracellular Vesicles*. 2015;4(1). doi:10.3402/jev.v4.28680

133. Sharma S, Gillespie BM, Palanisamy V, Gimzewski JK. Quantitative nanostructural and single-molecule force spectroscopy biomolecular analysis of human-saliva-derived exosomes. *Langmuir*. 2011;27(23):14394-14400. doi:10.1021/la2038763

134. Sharma S, Rasool HI, Palanisamy V, et al. Structural-mechanical characterization of nanoparticle exosomes in human saliva, using correlative AFM, FESEM, and force spectroscopy. *ACS Nano*. 2010;4(4):1921-1926. doi:10.1021/nn901824n

135. Beekman P, Enciso-Martinez A, Rho HS, et al. Immuno-capture of extracellular vesicles for individual multi-modal characterization using AFM, SEM and Raman spectroscopy. *Lab on a Chip*. 2019;19(15):2526-2536. doi:10.1039/c9lc00081j

136. Yuana Y, Oosterkamp TH, Bahatyrova S, et al. Atomic force microscopy: A novel approach to the detection of nanosized blood microparticles. *Journal of Thrombosis and Haemostasis*. 2010;8(2):315-323. doi:10.1111/j.1538-7836.2009.03654.x

137. Obeid S, Sung PS, le Roy B, et al. NanoBioAnalytical characterization of extracellular vesicles in 75-nm nanofiltered human plasma for transfusion: A tool to improve transfusion safety. *Nanomedicine: Nanotechnology, Biology, and Medicine*. 2019;20:101977. doi:10.1016/j.nano.2019.02.026

138. Obeid S. Analyses quantitative et qualitative sur puce de vésicules extracellulaires en milieux complexes au sein d ’ une plateforme nanobioanalytique. Published online 2017:1-198.

139. Morales-Kastresana A, Musich TA, Welsh JA, et al. High-fidelity detection and sorting of nanoscale vesicles in viral disease and cancer. *Journal of Extracellular Vesicles*. 2019;8(1). doi:10.1080/20013078.2019.1597603

140. van der Pol E, Coumans FAW, Grootemaat AE, et al. Particle size distribution of exosomes and microvesicles determined by transmission electron microscopy, flow cytometry, nanoparticle tracking analysis, and resistive pulse sensing. *Journal of Thrombosis and Haemostasis*. 2014;12(7):1182-1192. doi:10.1111/jth.12602

141. Maguire CM, Rösslein M, Wick P, Prina-Mello A. Characterisation of particles in solution–a perspective on light scattering and comparative technologies. *Science and Technology of Advanced Materials*. 2018;19(1):732-745. doi:10.1080/14686996.2018.1517587

142. Mihály J, Deák R, Szigyártó IC, Bóta A, Beke-Somfai T, Varga Z. Characterization of extracellular vesicles by IR spectroscopy: Fast and simple classification based on amide and C[sbnd]H stretching vibrations. *Biochimica et Biophysica Acta - Biomembranes*. 2017;1859(3):459-466. doi:10.1016/j.bbamem.2016.12.005

143. Zhang H, Silva AC, Zhang W, Rutigliano H, Zhou A. Raman Spectroscopy characterization extracellular vesicles from bovine placenta and peripheral blood mononuclear cells. *PLoS ONE*. 2020;15(7):e0235214. doi:10.1371/journal.pone.0235214

144. Chalapathi D, Padmanabhan S, Manjithaya R, Narayana C. Surface-Enhanced Raman Spectroscopy as a Tool for Distinguishing Extracellular Vesicles under Autophagic Conditions: A Marker for Disease Diagnostics. *Journal of Physical Chemistry B*. 2020;124(48):10952-10960. doi:10.1021/acs.jpcb.0c06910

145. Yanase Y, Hiragun T, Ishii K, et al. Surface Plasmon Resonance for Cell-Based Clinical Diagnosis. *Sensors*. 2014;14(3):4948-4959. doi:10.3390/s140304948

146. Gool EL, Stojanovic I, Schasfoort RBM, et al. Surface plasmon resonance is an analytically sensitive method for antigen profiling of extracellular vesicles. *Clinical Chemistry*. 2017;63(10):1633-1641. doi:10.1373/clinchem.2016.271049

147. Suthar J, Parsons ES, Hoogenboom BW, Williams GR, Guldin S. Acoustic Immunosensing of Exosomes Using a Quartz Crystal Microbalance with Dissipation Monitoring. *Analytical Chemistry*. 2020;92(5):4082-4093. doi:10.1021/acs.analchem.9b05736

148. Stratton D, Lange S, Kholia S, Jorfi S, Antwi-Baffour S, Inal J. Label-free real-time acoustic sensing of microvesicle release from prostate cancer (PC3) cells using a Quartz Crystal Microbalance. *Biochemical and Biophysical Research Communications*. 2014;453(3):619-624. doi:10.1016/j.bbrc.2014.09.132

149. Mathew DG, Beekman P, Lemay SG, Zuilhof H, le Gac S, van der Wiel WG. Electrochemical Detection of Tumor-Derived Extracellular Vesicles on Nanointerdigitated Electrodes. *Nano Letters*. 2020;20(2):820-828. doi:10.1021/acs.nanolett.9b02741

150. Xu L, Shoaie N, Jahanpeyma F, Zhao J, Azimzadeh M, Al−Jamal KT. Optical, electrochemical and electrical (nano)biosensors for detection of exosomes: A comprehensive overview. *Biosensors and Bioelectronics*. 2020;161. doi:10.1016/j.bios.2020.112222

151. Logozzi M, Milito A de, Lugini L, et al. High Levels of Exosomes Expressing CD63 and Caveolin-1 in Plasma of Melanoma Patients. *PLOS ONE*. 2009;4(4):e5219. doi:10.1371/JOURNAL.PONE.0005219

152. Logozzi M, di Raimo R, Mizzoni D, Fais S. Immunocapture-based ELISA to characterize and quantify exosomes in both cell culture supernatants and body fluids. *Methods in Enzymology*. 2020;645:155-180. doi:10.1016/BS.MIE.2020.06.011

153. Nguyen VVT, Witwer KW, Verhaar MC, Strunk D, van Balkom BWM. Functional assays to assess the therapeutic potential of extracellular vesicles. *Journal of Extracellular Vesicles*. 2020;10(1):e12033. doi:10.1002/jev2.12033

154. Bandu R, Oh JW, Kim KP. Mass spectrometry-based proteome profiling of extracellular vesicles and their roles in cancer biology. *Experimental and Molecular Medicine*. 2019;51(3):1-10. doi:10.1038/s12276-019-0218-2

155. Remy-Martin F, el Osta M, Lucchi G, et al. Surface plasmon resonance imaging in arrays coupled with mass spectrometry (SUPRA-MS): Proof of concept of on-chip characterization of a potential breast cancer marker in human plasma. *Analytical and Bioanalytical Chemistry*. 2012;404(2):423-432. doi:10.1007/s00216-012-6130-4

156. Remy-Martin F, Osta M el, Lucchi G, et al. Automated Cancer Marker Characterization in Human Plasma Using SUrface PLASMON Resonance in Array combined with Mass Spectrometry (SUPRA-MS). *Procedia Chemistry*. 2012;6:11-19. doi:10.1016/j.proche.2012.10.125

157. Lin HC, Chang HW, Hsiao SH, Chou ML, Seghatchian J, Burnouf T. Platelet-derived microparticles trigger THP-1 monocytic cell aggregation and release of pro-coagulant tissue factor-expressing microparticles *in* vitro. *Transfusion and Apheresis Science*. 2015;53(2):246-252. doi:10.1016/j.transci.2015.10.002

158. Coulter WH. Means for counting particles suspended in a fluid. US Patent, 2656508. *United States Patent Office Patentiert am*. 1953;20:1953.

159. Smith PK, Krohn RI, Hermanson GT, et al. Measurement of protein using bicinchoninic acid. *Analytical Biochemistry*. 1985;150(1):76-85. doi:10.1016/0003-2697(85)90442-7

160. Wood RW. XLII. On a remarkable case of uneven distribution of light in a diffraction grating spectrum. *Philosophical Magazine Series 6*. 1902;4(21):396-402. doi:10.1080/14786440209462857

161. Fano U. The Theory of Anomalous Diffraction Gratings and of Quasi-Stationary Waves on Metallic Surfaces (Sommerfeld's Waves). *Journal of the Optical Society of America*. 1941;31(3):213. doi:10.1364/josa.31.000213

162. Otto A. Excitation of nonradiative surface plasma waves in silver by the method of frustrated total reflection. *Zeitschrift für Physik*. 1968;216(4):398-410. doi:10.1007/BF01391532

163. Kretschmann E, Raether H. Radiative Decay of Non Radiative Surface Plasmons Excited by Light. *Zeitschrift fur Naturforschung - Section A Journal of Physical Sciences*. 1968;23(12):2135-2136. doi:10.1515/zna-1968-1247

164. Liedberg B, Nylander C, Lunström I. Surface plasmon resonance for gas detection and biosensing. *Sensors and Actuators*. 1983;4(C):299-304. doi:10.1016/0250-6874(83)85036-7

165. Yu H, Halonen MJ, Pepper IL. *Immunological Methods*. Elsevier Inc.; 2015. doi:10.1016/B978-0-12-394626-3.00012-0

166. Shrivastav AM, Cvelbar U, Abdulhalim I. A comprehensive review on plasmonic-based biosensors used in viral diagnostics. *Communications Biology*. 2021;4(1):1-12. doi:10.1038/s42003-020-01615-8

167. Bellassai N, D'Agata R, Jungbluth V, Spoto G. Surface Plasmon Resonance for Biomarker Detection: Advances in Non-invasive Cancer Diagnosis. *Frontiers in Chemistry*. 2019;7:570. doi:10.3389/fchem.2019.00570

168. Abdulhalim I, Zourob M, Lakhtakia A. Surface plasmon resonance for biosensing: A mini-review. *Electromagnetics*. 2008;28(3):214-242. doi:10.1080/02726340801921650

169. Tang Y, Zeng X, Liang J. Surface plasmon resonance: An introduction to a surface spectroscopy technique. *Journal of Chemical Education*. 2010;87(7):742-746. doi:10.1021/ed100186y

170. Barnes WL. Surface plasmon-polariton length scales: A route to sub-wavelength optics. *Journal of Optics A: Pure and Applied Optics*. 2006;8(4):S87. doi:10.1088/1464-4258/8/4/S06

171. Stenberg E, Persson B, Roos H, Urbaniczky C. Quantitative determination of surface concentration of protein with surface plasmon resonance using radiolabeled proteins. *Journal of Colloid And Interface Science*. 1991;143(2):513-526. doi:10.1016/0021-9797(91)90284-F

172. Binnig G, Quate CF, Gerber C. Atomic force microscope. *Physical Review Letters*. 1986;56(9):930-933. doi:10.1103/PhysRevLett.56.930

173. Binnig G, Rohrer H. Scanning tunneling microscopy. *Surface Science*. 1983;126(1-3):236-244. doi:10.1016/0039-6028(83)90716-1

174. Bottomley LA, Coury JE, First PN. *Scanning Probe Microscopy*. American Chemical Society ; 1996. doi:10.1021/A1960008+

175. Sharma S, Leclaire M, Gimzewski JK. Ascent of atomic force microscopy as a nanoanalytical tool for exosomes and other extracellular vesicles. *Nanotechnology*. 2018;29(13):132001. doi:10.1088/1361-6528/aaab06

176. Li M, Xi N, Wang Y, Liu L. Progress in Nanorobotics for Advancing Biomedicine. *IEEE Transactions on Biomedical Engineering*. 2021;68(1):130-147. doi:10.1109/TBME.2020.2990380

177. Li M. Introduction to Atomic Force Microscopy-Based Nanorobotics for Biomedical Applications. In: Springer, Singapore; 2018:1-20. doi:10.1007/978-981-10-6829-4_1

178. Rémy-Martin F. Développement d'une plateforme pour l'analyse sur puce d'un biomarqueur par couplage des technologies de résonance des plasmons de surface et de spectrométrie de masse. *http://www.theses.fr*. Published online July 4, 2013. Accessed April 18, 2021. http://www.theses.fr/2013BESA2043

179. Sebaihi N, de Boeck B, Yuana Y, Nieuwland R, Pétry J. Dimensional characterization of extracellular vesicles using atomic force microscopy. *Measurement Science and Technology*. 2017;28(3):034006. doi:10.1088/1361-6501/28/3/034006

180. YUANA Y, OOSTERKAMP TH, BAHATYROVA S, et al. Atomic force microscopy: a novel approach to the detection of nanosized blood microparticles. *Journal of Thrombosis and Haemostasis*. 2010;8(2):315-323. doi:10.1111/j.1538-7836.2009.03654.x

181. Coumans FAW, van der Pol E, Böing AN, et al. Reproducible extracellular vesicle size and concentration determination with tunable resistive pulse sensing. *Journal of Extracellular Vesicles*. 2014;3(1):25922. doi:10.3402/jev.v3.25922

182. Lane RE, Korbie D, Anderson W, Vaidyanathan R, Trau M. Analysis of exosome purification methods using a model liposome system and tunable-resistive pulse sensing. *Scientific Reports*. 2015;5(1):1-7. doi:10.1038/srep07639

183. Vogel R, Willmott G, Kozak D, et al. Quantitative sizing of nano/microparticles with a tunable elastomeric pore sensor. *Analytical Chemistry*. 2011;83(9):3499-3506. doi:10.1021/ac200195n

184. Armbruster DA, Pry T. Limit of blank, limit of detection and limit of quantitation. *The Clinical biochemist Reviews*. 2008;29 Suppl 1(Suppl 1):S49-52. Accessed April 19, 2021. http://www.ncbi.nlm.nih.gov/pubmed/18852857

185. Kilic T, Valinhas ATDS, Wall I, Renaud P, Carrara S. Label-free detection of hypoxia-induced extracellular vesicle secretion from MCF-7 cells. *Scientific Reports*. 2018;8(1):1-9. doi:10.1038/s41598-018-27203-9

186. Priglinger E, Strasser J, Buchroithner B, et al. Comprehensive label-free characterization of extracellular vesicles and their surface proteins. *bioRxiv*. Published online December 28, 2020:2020.12.28.424566. doi:10.1101/2020.12.28.424566

187. Zhu S, Li H, Yang M, Pang SW. Highly sensitive detection of exosomes by 3D plasmonic photonic crystal biosensor. *Nanoscale*. 2018;10(42):19927-19936. doi:10.1039/c8nr07051b

188. Sina AAI, Vaidyanathan R, Dey S, Carrascosa LG, Shiddiky MJA, Trau M. Real time and label free profiling of clinically relevant exosomes. *Scientific Reports*. 2016;6(1):1-9. doi:10.1038/srep30460

189. Picciolini S, Gualerzi A, Vanna R, et al. Detection and Characterization of Different Brain-Derived Subpopulations of Plasma Exosomes by Surface Plasmon Resonance Imaging. *Analytical Chemistry*. 2018;90(15):8873-8880. doi:10.1021/acs.analchem.8b00941

190. Flaumenhaft R, Koseoglu S. Platelet contents. In: *Molecular and Cellular Biology of Platelet Formation: Implications in Health and Disease*. Springer International Publishing; 2017:133-152. doi:10.1007/978-3-319-39562-3_6

191. Weibrich G, Kleis WKG, Hafner G, Hitzler WE. Growth factor levels in platelet-rich plasma and correlations with donor age, sex, and platelet count. *Journal of Cranio-Maxillofacial Surgery*. 2002;30(2):97-102. doi:10.1054/jcms.2002.0285

192. Doucet C, Ernou I, Zhang Y, et al. Platelet lysates promote mesenchymal stem cell expansion: A safety substitute for animal serum in cell-based therapy applications. *Journal of Cellular Physiology*. 2005;205(2):228-236. doi:10.1002/jcp.20391

193. Thieme D, Reuland L, Lindl T, Kruse F, Fuchsluger T. Optimized human platelet lysate as novel basis for a serum-, xeno-, and additive-free corneal endothelial cell and tissue culture. *Journal of Tissue Engineering and Regenerative Medicine*. 2018;12(2):557-564. doi:10.1002/term.2574

194. Mojica-Henshaw MP, jacobson P, Morris J, et al. Serum-converted platelet lysate can substitute for fetal bovine serum in human mesenchymal stromal cell cultures. *Cytotherapy*. 2013;15(12):1458-1468. doi:10.1016/j.jcyt.2013.06.014

195. Bernardi M, Albiero E, Alghisi A, et al. Production of human platelet lysate by use of ultrasound for ex vivo expansion of human bone marrow-derived mesenchymal stromal cells. *Cytotherapy*. 2013;15(8):920-929. doi:10.1016/j.jcyt.2013.01.219

196. Shih DTB, Burnouf T. Preparation, quality criteria, and properties of human blood platelet lysate supplements for ex vivo stem cell expansion. *New Biotechnology*. 2015;32(1):199-211. doi:10.1016/j.nbt.2014.06.001

197. Burnouf T, Tseng YH, Kuo YP, Su CY. Solvent/detergent treatment of platelet concentrates enhances the release of growth factors. *Transfusion*. 2008;48(6):1090-1098. doi:10.1111/j.1537-2995.2008.01691.x

198. Kocaoemer A, Kern S, Klüter H, Bieback K. Human AB Serum and Thrombin-Activated Platelet-Rich Plasma Are Suitable Alternatives to Fetal Calf Serum for the Expansion of Mesenchymal Stem Cells from Adipose Tissue. *Stem Cells*. 2007;25(5):1270-1278. doi:10.1634/stemcells.2006-0627

199. Dichtelmüller HO, Biesert L, Fabbrizzi F, et al. Robustness of solvent/detergent treatment of plasma derivatives: A data collection from Plasma Protein Therapeutics Association member companies. *Transfusion*. 2009;49(9):1931-1943. doi:10.1111/j.1537-2995.2009.02222.x

200. Burnouf T, Strunk D, Koh MBC, Schallmoser K. Human platelet lysate: Replacing fetal bovine serum as a gold standard for human cell propagation? *Biomaterials*. 2016;76:371-387. doi:10.1016/j.biomaterials.2015.10.065

201. Bieback K, FERNANDEZ-MUÑOZ B, PATI S, SCHÄFER R. Gaps in the knowledge of human platelet lysate as a cell culture supplement for cell therapy: a joint publication from the AABB and the International Society for Cell & Gene Therapy. *Cytotherapy*. 2019;21(9):911-924. doi:10.1016/j.jcyt.2019.06.006

202. Nebie O, Devos D, Vingtdeux V, et al. The neuroprotective activity of heat-treated human platelet lysate biomaterials manufactured from outdated pathogen-reduced (amotosalen/UVA) platelet concentrates. *Journal of biomedical science*. 2019;26(1):89. doi:10.1186/s12929-019-0579-9

203. Burnouf T, Goubran HA, Chen TM, Ou KL, El-Ekiaby M, Radosevic M. Blood-derived biomaterials and platelet growth factors in regenerative medicine. *Blood Reviews*. 2013;27(2):77-89. doi:10.1016/j.blre.2013.02.001

204. Nebie O, Carvalho K, Barro L, et al. Human platelet lysate biotherapy for traumatic brain injury: preclinical assessment. *Brain*. doi:10.1093/brain/awab205/6292079

205. Burnouf T, Goubran HA, Chen TM, Ou KL, El-Ekiaby M, Radosevic M. Blood-derived biomaterials and platelet growth factors in regenerative medicine. *Blood Reviews*. 2013;27(2):77-89. doi:10.1016/j.blre.2013.02.001

206. Morel O, Toti F, Hugel B, et al. Procoagulant microparticles: Disrupting the vascular homeostasis equation? *Arteriosclerosis, Thrombosis, and Vascular Biology*. 2006;26(12):2594-2604. doi:10.1161/01.ATV.0000246775.14471.26

207. Delila L, Wu YW, Nebie O, et al. Extensive characterization of the composition and functional activities of five preparations of human platelet lysates for dedicated clinical uses. *Platelets*. 2021;32(2):259-272. doi:10.1080/09537104.2020.1849603

208. Engeland M van, Nieland LJW, Ramaekers FCS, Schutte B, Reutelingsperger CPM. Annexin V-Affinity Assay: A Review on an Apoptosis Detection System Based on Phosphatidylserine Exposure. 1998; 9:1-9.

209. Koopman G, Reutelingsperger CP, Kuijten GA, Keehnen RM, Pals ST, van Oers MH. Annexin V for flow cytometric detection of phosphatidylserine expression on B cells undergoing apoptosis. *Blood*. 1994;84(5):1415-1420. http://www.ncbi.nlm.nih.gov/pubmed/8068938

210. Kunicki TJ. Platelet membrane glycoproteins and their function: An overview. *Blut*. 1989;59(1):30-34. doi:10.1007/BF00320245

211. Cleator JH, Zhu WQ, Vaughan DE, Hamm HE. Differential regulation of endothelial exocytosis of P-selectin and von Willebrand factor by protease-activated receptors and cAMP. *Blood*. 2006;107(7):2736-2744. doi:10.1182/blood-2004-07-2698

212. Yun SH, Sim EH, Goh RY, Park JI, Han JY. Platelet activation: The mechanisms and potential biomarkers. *BioMed Research International*. 2016;2016. doi:10.1155/2016/9060143

213. Butenas S. Tissue Factor Structure and Function. *Scientifica*. 2012;2012:1-15. doi:10.6064/2012/964862

214. Mackman N. Role of tissue factor in hemostasis, thrombosis, and vascular development. *Arteriosclerosis, Thrombosis, and Vascular Biology*. 2004;24(6):1015-1022. doi:10.1161/01.ATV.0000130465.23430.74

215. Shen M, Di K, He H, et al. Progress in exosome associated tumor markers and their detection methods. *Molecular Biomedicine*. 2020;1(1):1-25. doi:10.1186/s43556-020-00002-3

216. Vermes I, Haanen C, Steffens-Nakken H, Reutellingsperger C. A novel assay for apoptosis Flow cytometric detection of phosphatidylserine expression on early apoptotic cells using fluorescein labelled Annexin V. *Journal of Immunological Methods*. 1995;184(1):39-51. doi:10.1016/0022-1759(95)00072-I

217. van Engeland M, Nieland LJW, Ramaekers FCS, Schutte B, Reutelingsperger CPM. *Annexin V-Affinity Assay: A Review on an Apoptosis Detection System Based on Phosphatidylserine Exposure*. doi:10.1002/(SICI)1097-0320(19980101)31:1

218. Webber J, Clayton A. How pure are your vesicles? *Journal of Extracellular Vesicles*. 2013;2(1). doi:10.3402/jev.v2i0.19861

219. Nieuwland R, Falcón-Pérez JM, Théry C, Witwer KW. Rigor and standardization of extracellular vesicle research: Paving the road towards robustness. *Journal of Extracellular Vesicles*. 2020;10(2). doi:10.1002/jev2.12037

220. Coumans FAW, Brisson AR, Buzas EI, et al. Methodological guidelines to study extracellular vesicles. *Circulation Research*. 2017;120(10):1632-1648. doi:10.1161/CIRCRESAHA.117.309417

221. Geeurickx E, Tulkens J, Dhondt B, et al. The generation and use of recombinant extracellular vesicles as biological reference material. *Nature Communications*. 2019;10(1):1-12. doi:10.1038/s41467-019-11182-0

222. Valkonen S, van der Pol E, Böing A, et al. Biological reference materials for extracellular vesicle studies. *European Journal of Pharmaceutical Sciences*. 2017;98:4-16. doi:10.1016/j.ejps.2016.09.008

223. van Deun J, Mestdagh P, Agostinis P, et al. EV-TRACK: Transparent reporting and centralizing knowledge in extracellular vesicle research. *Nature Methods*. 2017;14(3):228-232. doi:10.1038/nmeth.4185

224. Szabo G, Momen-Heravi F. Extracellular vesicles in liver disease and potential as biomarkers and therapeutic targets. *Nature Reviews Gastroenterology and Hepatology*. 2017;14(8):455-466. doi:10.1038/nrgastro.2017.71

225. Mathieu M, Martin-Jaular L, Lavieu G, Théry C. Specificities of secretion and uptake of exosomes and other extracellular vesicles for cell-to-cell communication. *Nature Cell Biology*. 2019;21(1):9-17. doi:10.1038/s41556-018-0250-9

226. Obeid S. Analyse quantitative et qualitative sur puce de vésicules extracellulaires en milieux complexes au sein d ’ une plateforme nanobioanalytique Sameh Obeid To cite this version : HAL Id : tel-01785472 Analyses quantitative et qualitative sur puce de vésicule. Published online 2018.